Adsorption of Alkanes on the Platinum Surface: Density Functional Theory compared to the Random Phase Approximation

DISSERTATION

Zur Erlangung des akademischen Grades
Doctor rerum naturalium
(Dr. rer. nat.)

im Fach Chemie

eingereicht an der
Mathematisch-Naturwissenschaftlichen Fakultät
der Humboldt-Universität zu Berlin

von

Christopher Sheldon

Präsidentin der Humboldt-Universität zu Berlin
Prof. Dr. Julia von Blumenthal

Dekanin der Mathematisch-Naturwissenschaftlichen Fakultät
Prof. Dr. Caren Tischendorf

Gutachter: 1. Prof. Joachim Sauer
2. Dr. Joachim Paier
3. Prof. Karsten Reuter

Tag der mündlichen Prüfung: 01.06.2023

“What then?” sang Plato’s ghost.

William Butler Yeats

Abstract

Catalysis is crucial in many reactions in the chemical industry. The presence of a heterogeneous catalyst is often required. For example, in the reformation reaction, the dehydrogation of alkanes occurs on the platinum surface. Solid surfaces prove to be a significant computational challenge. Conventionally, they are studied using Density Functional Theory (DFT). It performs well (in many cases) but fails to account for the dispersion interaction, important for the adsorption of alkanes. To describe the dispersion, these density functionals must be augmented via a kernel (vdW-functionals) or by additive, dispersion corrections (DFT+D). This is reasonable for many systems, such as zeolites, and metal organic frameworks. However, for metal surfaces they break down, failing to accurately describe the dispersion interaction. Post-HF methods have shown promise here, with recent advances in computational power making them affordable. One suitable method is the Random Phase Approximation (RPA). The adsorption of alkanes on the Pt(111) surface is studied using RPA.

RPA is first benchmarked with respect to technical parameters and tested for methane adsorption on Pt(111). It is found to perform well relative to the Perdew–Burke–Ernzerhof (PBE) functional augmented with the many-body dispersion scheme of Tkatchenko (PBE+MBD). It also compares well relative to experimentally derived adsorption energies at physically relevant coverages. RPA correctly assigns the adsorption of methane to the hcp (hexagonal close packed) hollow tripod site, matching vibrational spectra, whereas PBE+MBD found another site. Adsorption energies within chemical accuracy (±4 kJ mol^{-1}) of experiment are found.

Given the high cost of periodic RPA, a high-level: low-level QM:QM (QM = quantum mechanics) hybrid approach is applied using RPA (RPA:PBE(+D)), which has also been tested with several dispersion corrections, with RPA:PBE and RPA:PBE+MBD performing best. This extends the QM:QM hybrid approach to the study of adsorption on metal surfaces, resulting in high accuracy at significantly reduced cost.

Finally we test the performance of the low-scaling RPA algorithm of Kresse and co-workers. This algorithm enables the study of larger systems and is applied to the first four n-alkanes (C1-C4) on the Pt(111) surface. Comparison against experiment indicates that RPA offers the best agreement, consistently better than any studied DFT+D or vdW-functional. RPA underbinds slightly but is still found to be the best method for studying adsorption on metal surfaces and is the current benchmark for such systems.

Kurzzusammenfassung

Katalyse ist wichtig für viele Reaktionen in der chemischen Industrie. Oft werden Feststoff–Katalysatoren verwendet, z.B. im *Reforming*-Prozess, in dem Alkane an der Platinoberfläche dehydriert werden. Die Beschreibung von Oberflächen ist eine enorme Herausforderung für gängige Rechenmethoden (der Quantenchemie). Normalerweise wird Dichtefunktionaltheorie (DFT) verwendet. Diese funktioniert meist gut, beschreibt z.B. aber nicht die London-Dispersion, die bei der Adsorption der Alkane einen großen Einfluss hat. Um Dispersionseffekte einzubeziehen, müssen die Dichtefunktionale entweder mit einem Integraloperator (vdW-Funktionale) oder einer additiven Dispersionskorrektur (DFT+D) erweitert werden. Diese Korrekturen sind für viele Systeme hinreichend genau, z.B. Zeolithe und metallorganische Gerüstverbindungen. Allerdings scheitern sie an Metalloberflächen, für die sie nur eine schlechte Beschreibung der Dispersion liefern. Post-Hartree-Fock-Methoden sind eine vielversprechende Alternative, besonders weil sie durch Fortschritte in der verfügbaren Rechenleistung besser zugänglich werden. Eine geeignete Methode ist die *Random-Phase-Approximation* (RPA). Die Alkanadsorption an der Pt(111)-Oberfläche wird mit RPA untersucht.

RPA wird zuerst im Hinblick auf relevante technische Parameter evaluiert und für die Methanadsorption an der Pt(111)-Oberfläche getestet. Im Vergleich zum Perdew-Burke-Ernzerhof-Funktional (PBE) mit Tkatchenkos *Many-Body*-Dispersionskorrektur (PBE+MBD) liefert RPA gute Ergebnisse. Auch reproduziert RPA experimentelle Adsorptionsenergien bei verschiedenen, physikalisch sinnvollen Beladungsstufen der Pt(111) Oberfläche mit Alkanmolekülen. Für Platin in der hexagonal dichtesten Kugelpackung sagt RPA richtigerweise die Methanadsorption an der *hollow-tripod*-Stelle voraus, während mit PBE+MBD die Adsorption an einer anderen Stelle bevorzugt wäre. Dies geht aus Schwingungsspektren hervor. Die berechneten Adsorptionsenergien erreichen chemische Genauigkeit, d.h. weniger als ±4 kJ mol^{-1} Abweichung zu experimentellen Werten.

Da periodisches RPA sehr rechenaufwändig ist, wird ein QM:QM Hybridansatz (QM=Quantenmechanik) angewendet, wobei periodisches PBE(+D) mithilfe von RPA Rechnungen an Clustern korrigiert wird (RPA:PBE(+D)). In einem Test verschiedener Dispersionskorrekturen schneiden RPA:PBE und RPA:PBE+MBD am besten ab. Diese Arbeit ist wegbereitend für die Anwendung des QM:QM Hybridansatzes zur Beschreibung der Adsorptionsprozesse an Metalloberflächen – bei hoher Genauigkeit und deutlich verringertem Rechenaufwand.

Auch Kresses *low-scaling* RPA Algorithmus wird getestet. Dieser Algorithmus ermöglicht, große Systeme, wie z.B. die Methan-, Ethan-, Propan- und n-Butanadsorption an Pt(111), zu untersuchen. Der Vergleich mit experimentellen Daten zeigt, dass mit RPA stets die beste

Übereinstimmung erreicht wird. Dabei wird eine deutliche Verbesserung gegenüber allen untersuchten DFT+D oder vdW-Funktionalen erzielt. Obwohl Bindungen mit RPA etwas zu schwach vorhergesagt werden, ist es die derzeit beste Methode zur Untersuchung der Adsorption an Metalloberflächen und damit der *Benchmark* für diese Systeme.

Table of Contents

Abstract V

Kurzzusammenfassung VI

Table of Contents IX

Introduction 1

Theory and Implementation of the Random Phase Approximation in VASP 6

1. Adsorption of CH_4 on the Pt(111) Surface: Random Phase Approximation Compared to Density Functional Theory 17

- 1.1 Introduction 21
- 1.2 Comparison with Experiment: Heats of Adsorption and Coverage 23
- 1.3 Models 24
- 1.4 DFT Calculations 25
- 1.5 RPA Calculations 27
- 1.6 Conclusions 38
- 1.7 References 39
- 1.8 Supplementary Material 44

2. Hybrid RPA and DFT: Embedding for Adsorption on Pt(111) 59

- 2.1 Introduction 62
- 2.2 Models and Methods 63
- 2.3 Computational Details 66
- 2.4 Results and Discussion 68
- 2.5 Conclusion 80
- 2.6 References 81
- 2.7 Supplementary Material 87

3. A Study of Dispersion: Alkanes on the Pt(111) Surface using DFT and RPA 103

- 3.1 Introduction 106
- 3.2 Models and Methods 108
- 3.3 Results and Discussion 110
- 3.4 Conclusion 122
- 3.5 References 124
- 3.6 Supplementary Material 131

Summary 162

Appendix 1: Theory of the Random Phase Approximation 165

Appendix 2: RPA Adsorption Energy Summary for Adsorption on Surfaces 176

Acknowledgements 184

Selbstständigkeitserklärung 186

Introduction

Investigating reactions between molecules is the crux of chemistry. The experimentalist does this by transforming simple, precursors into complex molecules, whether those be medicines, or materials, or any manufactured component that makes up our modern world. Theory tries to make sense of the observation of experimentalists, whether that is an unexpected reaction product or unusual lines in a spectrum. The reverse can also be true, with theory predicting a reaction and experiment confirming or disproving this. In this sense, experiment tests theory and theory describes experiment, this being the realm of "normal science".[1] One without the other, leaves both lacking, while their inverse is also true, complementing each other and progressing the field as a whole. In the adapted words of Kant, "*experiment* without theory is blind, but theory without *experiment* is mere intellectual play." Often seen antagonistically, the greatest success is achieved when they are viewed as inseparable converses. The chief goal of theoretical chemistry is to model reactions to sufficient accuracy that the results are then useful to experimentalists to, known as chemical accuracy (± 4 kJ mol^{-1}). Quantum chemistry may be applied to model useful chemical problems. This is done by accurately modelling the wave function (or its square, the density) of electrons interacting with each other and with nuclei. Many approximations must be made and the problem split up into manageable components. The starting point for much of quantum chemistry is the Hartree-Fock method, where non-interacting particles are taken and their pairwise interactions are averaged out iteratively.[2] This approximation works reasonably well for the simplest systems but can quickly break down, even for small molecules, as not all the energy is considered. This missing *correlation* energy is described by the so-called post-HF methods. These apply various perturbations to the HF wavefunction and enable accurate description of many chemical systems. This accuracy comes at a cost. Even the simplest post-HF method, MP2 (Second-order Møller-Plesset Perturbation Theory) scales at a rate of $O(N^5)$ where N is the indicative of the size of the system, making it challenging to apply to large molecules or periodic systems, while the current "gold standard", CCSD(T) (Coupled Cluster Singles, Doubles, and Perturbative Triples) scales at $O(N^7)$, infeasible for even many mid-sized systems. Periodic systems introduce its own set of problems. A good solution is to consider the electron density directly instead of the wave function. This is the basis of Density Functional Theory (DFT) and enables the study of large systems that would be otherwise infeasible, with scaling beginning at a more reasonable $O(N^3)$, less than even the $O(N^4)$ seen for HF. It is particularly suitable for application to metals, which opens up much of surface chemistry.

Many processes in the chemical industry benefit greatly from the presence of a catalyst. One of the most common, the reformation reaction (used in fuel refinery) dehydrogenates alkanes on the (111) surface of platinum. The first step of this process is the adsorption of the alkane onto the Pt(111) surface. Alkanes adsorb largely via the dispersion interaction. This is not accounted for by HF or DFT. This is resolved by modifying the density functional, which may be done in two ways One, by adding a posteriori the sum over interactions between pairs of atom-centred dipoles Eq. (1)

$$E_{disp} = -\sum_{i}^{\mathrm{N_{at}}-1} \sum_{j=i+1}^{\mathrm{N_{at}}} f_{damp}(R_{ij}) \frac{C_6^{ij}}{R_{ij}^6} \tag{1}$$

where E_{disp} is the dispersion energy, N_{at} is the number of atoms, i and j are pairs of atoms, $f_{damp}(R_{ij})$ is a damping function to avoid excessive repulsion in the already well-described short-range, C_6^{ij} is a dipole-dipole dispersion coefficient, and R_{ij} is the distance between two atoms.

This is the basis for many dispersion corrections (+D) added to DFT, hence DFT+D. It is a simple pairwise summation of the system's atoms. This describes the dispersion interaction well for many organic molecules, with D2 being one of the most prevalent.[3] Alternative methods may also include dipole-quadrupole terms, quadrupole-quadrupole terms, corresponding to C_8 and C_{10} coefficients;[4] The rapid decay of these terms R^{-8} and R^{-10}, respectively, makes it possible to omit these terms. Alternatively, more than pairwise terms may be included, such as 3-body,[5] or as many as N-body.[6]

The other DFT approach is to modify the density functional to directly take the dispersion interaction into account. This is done by calculating the non-local correlation energy E_c^{nl}

$$E_c^{nl}[n] = \int d^3\boldsymbol{r} \int d^3\boldsymbol{r}' n(\boldsymbol{r}) \Phi(\boldsymbol{r}, \boldsymbol{r}') n(\boldsymbol{r}') \tag{2}$$

where $n(\boldsymbol{r})$ is the electron density and $\Phi(\boldsymbol{r}, \boldsymbol{r}')$ is a non-local interaction kernel.

The various vdW-functionals differ by the underlying density functional and including additional terms in Eq. (2).

Alternatively to DFT, post-HF methods may be used. Metals are difficult to model with them due to their delocalised electrons and zero-width band gap. In particular he zero-width band gap means that applying any finite-order perturbative method (e.g. MP2) will result in divergent correlation energies.[7,8] However, suitable post-HF methods, such as the Random Phase Approximation (RPA), which will be use in this thesis, have shown promising results. The correlation energy is derived from the response of the electrons to an electric field (i.e. other electrons), via the non-interacting density-density response function χ_0 (typically using DFT orbitals), and applying the Adiabatic Connection Fluctuation-Dissipation Theorem (ACFDT), cf. Eq. (3)

$$E_C = \int_0^{\infty} \frac{d\omega}{2\pi} \mathrm{Tr}\{\ln[1 - \chi_0(i\omega)\nu] + \chi_0(i\omega)\nu\} \tag{3}$$

where E_C is the RPA correlation energy, ω is the frequency, and ν is the Coulomb interaction.

It may be conceived of in several ways: in terms of Time-Dependent DFT with the exchange-correlation kernel set to zero, as an approximation of ring Coupled Cluster Doubles (rCCD), or in terms of collective plasmonic oscillations of electrons. An overview of the theory is given in Appendix 1. RPA has already been successfully applied to solve the "CO adsorption problem?",[9] with RPA able to correctly distinguish between the top and hcp (hexagonal cubic packed) adsorption sites of CO on Pt(111), which non-hybrid DFT had previously failed to do.[10] The adsorption of several small molecules has also been studied,[11] as well as benzene on several transition metal surfaces.[12] A summary of RPA adsorption is given in Appendix 2.

In this thesis, the dispersive adsorption of alkanes on the Pt(111) surface is studied using DFT and RPA.

In **Chapter 1,** RPA is benchmarked for the adsorption of methane on Pt(111). It is found to perform well relative to the Perdew–Burke–Ernzerhof (PBE) functional with dispersion corrections (PBE+D). Two physically relevant coverages are examined and calculated adsorption energies are compared directly to experiment, with thermal and Zero-Point Vibrational Energy (ZPVE) corrections being made. The adsorption of methane is assigned to the hcp (hexagonal close packed) hollow tripod site, in agreement with vibrational spectra, whereas PBE+D struggled to distinguish between two sites of similar energy. Convergence is achieved with respect to the plane wave energy cutoff, *k*-point mesh, vacuum height, and number of platinum layers, resulting in RPA adsorption energies within chemical accuracy of experiment.

In **Chapter 2,** the strengths ofRPA and DFT+D are combined, by taking a hybrid of the two methods. A metal cluster is taken from the surface to apply a high-level, RPA correction to the low-level, PBE+D periodic surface-adsorbate system. This high-level:low-level, QM:QM hybrid approach is applied to study the adsorption of methane, ethane, and carbon monoxide on the Pt(111) surface. The RPA:PBE hybrid is found to offer significantly improved description of methane and ethane adsorption relative to PBE+MBD (Many-Body Dispersion),[6] reproducing periodic RPA values almost exactly, at significantly reduced cost. RPA:PBE+MBD is found to reproduce experiment to within chemical accuracy. CO/Pt(111) adsorption is also qualitatively described using RPA:PBE, with the top site correctly described as the minimum, agreeing with experiment. The hybrid approach is thus extended to metal surfaces.

The adsorption of the C1-C4 *n*-alkanes (methane, ethane, propane, and *n*-butane) on the Pt(111) surface is investigated in **Chapter 3.** RPA is applied using a recently released, low-scaling implementation.[13-15] This is used as a reference to compare other methods to when experimental data is unavailable. Experimental adsorption energies are derived to enable better comparison with theory. Potential energy surfaces (PES) were produced for RPA, with the minimum point obtained by fitting to modified Lennard-Jones type potentials. This indicated that RPA underbinds slightly with respect to experimental energies. Various DFT+D and vdW-functionals are studied and compared. DFT+D is found to consistently overbind, as well as underestimating the platinum-carbon distance. The vdW-functionals are found to be more variable, with most overbinding energetically while underestimating the distance. No vdW-functional is found to match well with experiment or RPA for both energy and distance. RPA is confirmed to be the best method currently available.

Tables, Figures, Equations, References, and Supporting Information are labelled separately for each section for readability's sake. All structures, input and output files are available online.

References

1. Kuhn, T. S., *The Structure of Scientific Revolutions*. University of Chicago Press: Chicago, 2012.
2. Szabo, A.; Ostlund, N. S., *Modern Quantum Chemistry*. Dover Publications Inc.: Mineola, 1996.
3. Grimme, S., Semiempirical GGA-type density functional constructed with a long-range dispersion correction. *J. Comput. Chem.* **2006,** *27*, 1787-1799, https://doi.org/10.1002/jcc.20495.
4. Steinmann, S. N.; Corminboeuf, C., A generalized-gradient approximation exchange hole model for dispersion coefficients. *J. Chem. Phys.* **2011,** *134*, 044117, https://doi.org/10.1063/1.3545985.

5. Grimme, S.; Antony, J.; Ehrlich, S.; Krieg, H., A consistent and accurate ab initio parametrization of density functional dispersion correction (DFT-D) for the 94 elements H-Pu. *J. Chem. Phys.* **2010,** *132*, 154104, https://doi.org/10.1063/1.3382344.

6. Tkatchenko, A.; DiStasio, R. A.; Car, R.; Scheffler, M., Accurate and Efficient Method for Many-Body van der Waals Interactions. *Phys. Rev. Lett.* **2012,** *108*, 236402, https://doi.org/10.1103/PhysRevLett.108.236402.

7. Paier, J.; Ren, X.; Rinke, P.; Scuseria, G. E.; Grüneis, A.; Kresse, G.; Scheffler, M., Assessment of correlation energies based on the random-phase approximation. *New J. Phys.* **2012,** *14*, 043002, https://doi.org/10.1088/1367-2630/14/4/043002.

8. F. E. Harris; H. J. Monkhorst; Freeman, D. L., *Algebraic and Diagrammatic Methods in Many-Fermion Theory*. Oxford University Press: New York, Oxford, 1992.

9. Feibelman, P. J.; Hammer, B.; Nørskov, J. K.; Wagner, F.; Scheffler, M.; Stumpf, R.; Watwe, R.; Dumesic, J., The CO/Pt(111) Puzzle. *J. Phys. Chem. B* **2001,** *105*, 4018-4025, https://doi.org/10.1021/jp002302t.

10. Stroppa, A.; Kresse, G., The shortcomings of semi-local and hybrid functionals: what we can learn from surface science studies. *New J. Phys.* **2008,** *10*, 063020, https://doi.org/10.1088/1367-2630/10/6/063020.

11. Schmidt, P. S.; Thygesen, K. S., Benchmark Database of Transition Metal Surface and Adsorption Energies from Many-Body Perturbation Theory. *J. Phys. Chem. C* **2018,** *122*, 4381-4390, https://doi.org/10.1021/acs.jpcc.7b12258.

12. Garrido Torres, J. A.; Ramberger, B.; Früchtl, H. A.; Schaub, R.; Kresse, G., Adsorption energies of benzene on close packed transition metal surfaces using the random phase approximation. *Phys. Rev. Mater.* **2017,** *1*, 060803, https://doi.org/10.1103/PhysRevMaterials.1.060803.

13. Kaltak, M.; Kresse, G., Minimax isometry method: A compressive sensing approach for Matsubara summation in many-body perturbation theory. *Phys. Rev. B* **2020,** *101*, 205145, https://doi.org/10.1103/PhysRevB.101.205145.

14. Kaltak, M.; Klimeš, J.; Kresse, G., Cubic scaling algorithm for the random phase approximation: Self-interstitials and vacancies in Si. *Phys. Rev. B* **2014,** *90*, 054115, https://doi.org/10.1103/PhysRevB.90.054115.

15. Kaltak, M.; Klimeš, J.; Kresse, G., Low Scaling Algorithms for the Random Phase Approximation: Imaginary Time and Laplace Transformations. *J. Chem. Theory Comput.* **2014,** *10*, 2498-2507, https://doi.org/10.1021/ct5001268.

Theory and Implementation of the Random Phase Approximation in VASP

1. Introduction

The Random Phase Approximation (RPA) originated in the early days of electronic structure theory and was first applied to describe the free electron gas, and metals shortly thereafter.[1-4] The idea was that, with interacting particles, the motion of the individual particles is essentially *random*, such that, with sufficiently many particles interacting, the relative *phase* of their individual motion averages out to zero.[2] This is the *Random Phase Approximation*. We discuss here some of the theory of RPA, in particular those parts relevant to its implementation in the Vienna Ab Initio Simulation Package (VASP); for a more detailed analysis of the theory an how it relates to other methods, we refer the interested reader to Appendix 1. RPA has been applied to various problems by the VASP developers, including graphite sheets, lattice constants, and atomisation energies.[5,6] These were all performed using an algorithm that scales at $O(N_G^4)$, where N_G is the number of plane waves, which hereafter referred to as the *original* algorithm.[7,8] This enabled correct assignment of the adsorption of CO to the top site on the Pt(111) surface,[9] solving the problem proposed by Feibelman.[10] It also indicated that RPA offered a significantly improved description of the dispersion interaction for noble gases.[8] However, its high cost limited its usability to small test systems. In this work, we apply it to the adsorption of CH_4 on Pt(111) (cf. Chapter 1) and it has been applied by another group to the adsorption of H on Pt(111).[11] The release of a newer algorithm that scales at $O(N_G^3)$, hereafter referred to as the *low-scaling* algorithm, opens up many new possibilities.[12,13] It has, at present, been applied to Si defects and vacancies,[12] while in this work, we apply it to the adsorption of the first for *n*-alkanes (cf. Chapter 3). We shall go through the theory of the two algorithms, starting with the original algorithm, and then the low-scaling algorithm.

2. Original RPA Algorithm

This takes the ground state as non-interacting particles and then turn on the interaction via a coupling strength parameter λ scaling the non-interacting ($\lambda = 0$) to the fully-interacting ($\lambda = 1$) system.[14] This is the Adiabatic Connection. When combined with fluctuations in the density, this results in the Adiabatic Connection-Fluctuation Dissipation Theorem (ACFDT), which enables the calculation of the correlation energy.[14] The coupling strength parameter may be integrated over analytically,[15] resulting in a correlation energy E_C expressed by an integral over the KS density-density response function χ_0

$$E_C[\rho] = \int_0^\infty \frac{d\omega}{2\pi} \mathrm{Tr}\{\ln[1 - \chi_0(i\omega)v] + \chi_0(i\omega)v\} \tag{1}$$

where v is the Coulomb potential $(1/|\boldsymbol{r} - \boldsymbol{r}'|)$ and the trace is defined as[8]

$$\mathrm{Tr}\{\mathrm{A}(\mathbf{q})\mathrm{B}(\mathbf{q})\} \coloneqq \sum_{\mathbf{q}\in BZ} \mathrm{g}_\mathbf{q} \sum_{\substack{|\mathbf{g}+\mathbf{q}|<G_{cut}^{\chi} \\ |\mathbf{g}'+\mathbf{q}|<G_{cut}^{\chi}}} A_{\mathbf{g}\mathbf{g}'}(\mathbf{q}) B_{\mathbf{g}'\boldsymbol{g}}(\mathbf{q}) \tag{2}$$

where $\mathbf{q}$ are the crystal momentum vectors within the first Brillouin zone inside the cell of volume V, $\mathbf{g}$ is the reciprocal lattice vector, $\mathrm{g}_\mathbf{k}$ are the *k*-point weights, and G_{cut}^{χ} is the maximum reciprocal lattice vector used to evaluate the response function.

χ_0 is relatively easy to express under periodic boundary conditions, with the Adler-Wiser formula typically being used[5,16]

$$\chi_{0,\mathbf{GG}'}(i\omega, \mathbf{q}) = \frac{1}{V} \sum_{nn'\mathbf{k}} 2\mathrm{g}_\mathbf{k}(f_{n'\mathbf{k+q}} - f_{n\mathbf{k}}) \frac{\langle \psi_{n'\mathbf{k+q}} | e^{i(\mathbf{q+G})\mathbf{r}} | \psi_{n\mathbf{k}} \rangle \langle \psi_{n\mathbf{k}} | e^{-i(\mathbf{q+G}')\mathbf{r}'} | \psi_{n'\mathbf{k+q}} \rangle}{\epsilon_{n'\mathbf{k+q}} - \epsilon_{n\mathbf{k}} - i\omega} \tag{3}$$

where $\mathbf{G}$ is the reciprocal lattice vector, $\mathrm{g}_\mathbf{k}$ are the *k*-point weights, $f_{n\mathbf{k}}$, $\psi_{n\mathbf{k}}$, and $\epsilon_{n\mathbf{k}}$ are the occupancies, KS one-electron orbitals, and the energies of state n, respectively, and $\mathbf{k}$ and $\mathbf{q}$ are crystal momentum vectors within the first Brillouin zone within the cell of volume V.

The evaluation of χ_0 is rate-limiting step of the implementation and results in a scaling of $O(N_\omega N_G^4 N_k^2)$, where N_ω, N_G, and N_k are the number of frequency integration points, plane waves, and *k*-points. This evaluation of χ_0 is where differences with the low-scaling implementation originate.

The integration of Eq. (1) over imaginary frequency is done using a Gaussian-Legendre with typically fewer than 20 frequency integration points. Achieving convergence of E_{corr} with respect to the number of frequency points is important, although rarely difficult. Greater numbers of frequency points are required for conductors than insulators (cf. VASP keyword: NOMEGA).[17] When integrating, it is not over χ_0 directly, instead it is re-expressed

$$\begin{aligned} &\mathrm{Tr}\{\ln[1 - \chi_0 v] + \chi_0 v\} \\ &= \mathrm{Tr}\left\{\ln\left[1 - v^{\frac{1}{2}}\chi_0 v^{\frac{1}{2}}\right] + v^{\frac{1}{2}}\chi_0 v^{\frac{1}{2}}\right\} \end{aligned}$$

$$= \sum_{\mathrm{i}} \ln[1 - \bar{\varepsilon}_{\mathrm{i}}] + \bar{\varepsilon}_{\mathrm{i}} \tag{4}$$

where $\bar{\varepsilon}_{\mathrm{i}}$ are the eigenvalues of the Hermitian matrix $\nu^{\frac{1}{2}}\chi_0\nu^{\frac{1}{2}}$

Convergence must be tested with respect to several other parameters beyond the number of frequency points. In practice, these are found to be the more significant. When calculating χ_0, one must integrate over the wave function $\psi_{n\mathbf{k}}$, which is modelled using a plane wave basis. These, unlike LCAOs (Linear Combination of Atomic Orbitals), are independent of atomic position. Instead of there being a defined set of functions within a basis set, an infinite number may be chosen. A plane wave has a momentum, which may be expressed as an energy. Plane waves of energies less than the energy cut-off E_{cut} (cf. ENCUT in VASP) are then used.[17] These are used to describe only the valence electrons in a periodic system, as the core would require so many plane waves as to become inefficient. Instead, the core electrons up to a certain radius are modelled by a core-centred potential (cf. POTCAR).[18-20] In VASP, GW Projector Augmented Wave (PAW) with improved scattering properties for unoccupied states are used.[21] Integration must also be performed over the first Brillouin zone, the primitive cell in reciprocal space. This is done using a set of points known as *k*-points, cf. Eq. (3). As χ_0 is a density-density response, this must be done for each set of densities to get the full response, resulting in integration at each *k*-point $\mathbf{q}$ over another *k*-point grid $\mathbf{k}$. This also requires integration over an auxiliary set of plane waves E_{cut}^{χ}, which is extrapolated to the infinite basis set, as E_{corr} is strongly dependent on,[5]

$$E_{corr}\left(E_{cut}^{\chi}\right) = E_{corr}^{\infty} + \frac{A}{\left(G_{cut}^{\chi}\right)^3} = E_{corr}^{\infty} + \frac{A'}{\left(E_{cut}^{\chi}\right)^{3/2}} \tag{5}$$

where E_{corr}^{∞} is the correlation energy with a complete basis set, A and A' are constants, and E_{cut}^{χ} is the auxiliary plane wave basis set, where the requirement for the maximum reciprocal lattice vector in Eq. (5) is defined as

$$\frac{\hbar^2}{2\mathrm{m}}(\mathbf{G} + \mathbf{q})^2 < E_{cut}^{\chi} \coloneqq \frac{\hbar^2}{2\mathrm{m}}\left(G_{cut}^{\chi}\right)^2 \tag{6}$$

E_{corr} is then evaluated at several different E_{cut}^{χ} and a linear regression using Eq. (5) applied to obtain E_{corr}^{∞}.[16] After extrapolation, the correlation energy obtained is converged with respect to the auxiliary plane wave basis set. When it is converged with the k-point mesh, plane wave energy cut-off, and frequency points, the correlation energy is reliable and the energies obtained may be relied upon as precise RPA energies. We perform such convergences for CH_4/Pt(111) in Chapter 1 of this work.

3. Low-Scaling RPA Algorithm

As mentioned previously, the original RPA algorithm has found only limited application, due to its high computational cost. By changing the equation by which the response function is calculated (cf. Eq. (3)), the scaling may be reduced to $O(N_\omega N_G^3 N_k)$. This is done by calculating the response function from Green's functions G.[12,13] Eq. (7) is valid for all coupling strength, but we choose to express it for the non-interacting, KS system here for the sake of consistency.

$$\chi(i\tau, \boldsymbol{r}, \boldsymbol{r}') = -G(i\tau, \boldsymbol{r}, \boldsymbol{r}')G^*(-i\tau, \boldsymbol{r}', \boldsymbol{r}) \tag{7}$$

where $i\tau$ is imaginary time and the $\boldsymbol{r}$ is real space.

This is only true in space-time domain, which makes it inappropriate to use for calculating the correlation energy. Instead, several steps must be performed to obtain the reciprocal space-frequency domain required by Eq. (1). This consists of several Fourier transformations and a "Cosine transformation", as illustrated by Figure 1.

$$\begin{tikzcd}
G_{\boldsymbol{k}}(\boldsymbol{g}, \boldsymbol{g}', i\tau) \arrow[r, "FFT"] & G(\boldsymbol{r}, \boldsymbol{r}', i\tau) \arrow[d, "GG"] \\
\chi(\boldsymbol{g}, \boldsymbol{g}', i\tau) \arrow[d, "CT"'] & \chi(\boldsymbol{r}, \boldsymbol{r}', i\tau) \arrow[l, "FFT"'] \\
\chi(\boldsymbol{g}, \boldsymbol{g}', i\omega) \arrow[r, "ACFDT"] & E_{corr}
\end{tikzcd}$$

Figure 1. Scheme for calculating the RPA correlation energy E_{corr}, via Fast Fourier Transforms (FFT – Eq. (11) and Eq. (12)), contraction of Green's functions (GG – Eq. (7)), Cosine Transformation (CT – Eq. (9)), and the Adiabatic Connection-Fluctuation Dissipation Theorem (ACFDT – Eq. (1)). This is a reproduction of Figure 1 in Ref. [12].

3.1 Cosine Transformation

The Cosine transformation recognises that χ is an even function with respect to time and frequency, i.e. $\chi(i\tau) = \chi(-i\tau)$ and $\chi(i\omega) = \chi(-i\omega)$, so the Fourier transformation between the two[13]

$$\chi(i\omega) = \int_{-\infty}^{\infty} d\tau\, \chi(i\tau)\, \mathrm{e}^{i\tau\omega} \tag{8}$$

may be written in terms of only cosine

$$\chi(i\omega) = 2\int_{0}^{\infty} d\tau\, \chi(i\tau)\cos(\tau\omega) \tag{9}$$

This is integrated numerically using the non-uniform cosine transformation.[13] Since this is an automated procedure, we will not dwell on it here but instead refer the curious reader to Ref. [13] for details.

3.2 Fast Fourier Transformations

The two Fast Fourier Transformations (FFT) in Figure 1 are analogous but, being inverses of one another, require slightly different equations. The first, from Green's function in reciprocal space $G(\boldsymbol{g}, \boldsymbol{g}', i\tau)$ to real space $G(\boldsymbol{r}, \boldsymbol{r}', i\tau)$, and the second from the response function in real space $\chi(\boldsymbol{r}, \boldsymbol{r}', i\tau)$ to reciprocal space $\chi(\boldsymbol{g}, \boldsymbol{g}', i\tau)$.

The implementation uses supercells (or "superlattices") in real and reciprocal space, as this enables a reduction in scaling with respect to the number of *k*-points from quadratic to linear.[12] The real space superlattice Green's function $G(\boldsymbol{R}, \boldsymbol{R}')$ is expressed directly as a reduced strip $G(\boldsymbol{r}, \boldsymbol{R}')$ directly from $G(\boldsymbol{r}, \boldsymbol{r}')$

$$G(\boldsymbol{r}, \boldsymbol{R}') = e^{-i\boldsymbol{k}\boldsymbol{a}} G_{\boldsymbol{k}}(\boldsymbol{r}, \boldsymbol{r}') \tag{10}$$

where $\boldsymbol{a}$ is the lattice parameter and $\boldsymbol{R}' = \boldsymbol{r}' + \boldsymbol{a}$

The Fourier transformation is then done one variable at a time

$$G(\boldsymbol{r}, \boldsymbol{G}') = \sum_{\boldsymbol{g}} G_{\boldsymbol{k}}(\boldsymbol{g}, \boldsymbol{g}') e^{-i\boldsymbol{k}\boldsymbol{a}} \tag{11a}$$

$$G(\boldsymbol{r}, \boldsymbol{R}') = \sum_{\boldsymbol{G}'} e^{-i\boldsymbol{G}'\boldsymbol{R}} G(\boldsymbol{r}, \boldsymbol{G}')$$

(11b)

where $\boldsymbol{G}' = \boldsymbol{k} + \boldsymbol{g}'$, and $G_{\boldsymbol{k}}$ is the Green's function within the primitive cell.

This is the first Fourier transformation in Figure 1, the second, for the response function χ, may be obtained by analogous equations

$$\chi(\boldsymbol{r}, \boldsymbol{G}') = \sum_{\boldsymbol{R}'} \chi(\boldsymbol{r}, \boldsymbol{R}') e^{i\boldsymbol{G}'\boldsymbol{R}'}$$

(12a)

$$\chi_{\boldsymbol{k}}(\boldsymbol{g}, \boldsymbol{g}') = \sum_{\boldsymbol{r}} e^{-i\boldsymbol{G}\boldsymbol{r}} \chi(\boldsymbol{r}, \boldsymbol{G}')$$

(12b)

where $\chi_{\boldsymbol{k}}$ is the response function within the primitive cell.

This completes all of the steps in Figure 1 for calculating the correlation energy. The only remaining difficulty remains in calculating the Green's and response functions in the PAW basis.

3.3 Evaluating Green's Functions in the PAW Basis

One recalls that within the PAW, the all-electron orbitals $|\psi_i\rangle$ are represented via pseudo-orbitals $|\tilde{\psi}_i\rangle$ which interact with the augmentation sphere Ω_R (the pseudopotential surrounding the nuclei).

$$|\psi_i\rangle = |\tilde{\psi}_i\rangle + \sum_{\mu} (|\phi_\mu\rangle - |\tilde{\phi}_\mu\rangle)\langle \tilde{p}_\mu | \tilde{\psi}_i \rangle$$

(13)

where $|\phi_\mu\rangle$ are the solutions for an isolated atom to the Schrödinger equation with respect to μ ($\boldsymbol{R}_\mu, n_\mu, l_\mu$, and $m_{l,\mu}$, the atomic site, and principle, orbital angular momentum, and magnetic quantum numbers), $|\tilde{\phi}_\mu\rangle$ are the solutions only outside of Ω_R, and $\langle \tilde{p}_\mu|$ are the projectors within Ω_R. N.B. $\langle \tilde{p}_\mu | \tilde{\phi}_\nu \rangle = \delta_{\mu\nu}$, i.e. are dual, cf. Ref. [18,20] for further details.

The evaluation of the response function then becomes more complex, with the all-electron (bra-ket) terms in Eq. (3) being evaluated as[12,22]

$$\langle \psi_{n'\mathbf{k+q}} | e^{i(\mathbf{q+g})\mathbf{r}} | \psi_{n\mathbf{k}} \rangle = \langle \tilde{\psi}_{n'\mathbf{k+q}} | e^{i(\mathbf{q+g})\mathbf{r}} | \tilde{\psi}_{n\mathbf{k}} \rangle + \sum_{\boldsymbol{r}} e^{i(\mathbf{q+g})\mathbf{r}} \sum_{\mu\nu} \langle \tilde{\psi}_{n'\mathbf{k+q}} | \tilde{p}_\mu \rangle Q_{\mu\nu}(\boldsymbol{r}) \langle \tilde{p}_\nu | \tilde{\psi}_{n\mathbf{k}} \rangle$$

(14)

where $Q_{\mu\nu}(\boldsymbol{r})$ is the auxiliary function describes the difference between the charge density of the pseudopartial and all-electron partial waves

$$Q_{\mu\nu}(\boldsymbol{r}) = \phi_\mu^*(\boldsymbol{r})\phi_\nu(\boldsymbol{r}) - \tilde{\phi}_\mu^*(\boldsymbol{r})\tilde{\phi}_\nu(\boldsymbol{r})$$

(15)

Fourier transforming the response function from Eq. (3) into real space and imaginary time, and substituting in Eq. (14), gives

$$\chi(\boldsymbol{r}, \boldsymbol{R}', i\tau) = \sum_{j=1}^{4} \chi^{(j)}(\boldsymbol{r}, \boldsymbol{R}', i\tau)$$

(16)

consisting of pseudoterms only $\chi^{(1)}$

$$\chi^{(1)}(\boldsymbol{r}, \boldsymbol{R}', i\tau) \propto \tilde{\psi}_{n'\mathbf{k+q}}(\boldsymbol{r})\tilde{\psi}^*{}_{n'\mathbf{k+q}}(\boldsymbol{R}')\tilde{\psi}^*{}_{n'\mathbf{k}}(\boldsymbol{r})\tilde{\psi}_{n'\mathbf{k}}(\boldsymbol{R}')$$

(17)

consisting of terms with pseudoterms and only one augmentation sphere, $\chi^{(2)}$ and $\chi^{(3)}$

$$\chi^{(2)}(\boldsymbol{r}, \boldsymbol{R}', i\tau) \propto \tilde{\psi}_{n'\mathbf{k+q}}(\boldsymbol{r})\tilde{\psi}^*{}_{n\mathbf{k}}(\boldsymbol{r}) \sum_{\alpha\beta} \langle \tilde{\psi}_{n'\mathbf{k+q}} | \tilde{p}_\alpha \rangle Q_{\alpha\beta}(\boldsymbol{R}') \langle \tilde{p}_\beta | \tilde{\psi}_{n\mathbf{k}} \rangle$$

(18a)

$$\chi^{(3)}(\boldsymbol{r}, \boldsymbol{R}', i\tau) \propto \tilde{\psi}^*{}_{n'\mathbf{k+q}}(\boldsymbol{r})\tilde{\psi}_{n\mathbf{k}}(\boldsymbol{r}) \sum_{\mu\nu} \langle \tilde{\psi}_{n\mathbf{k}} | \tilde{p}_\mu \rangle Q_{\mu\nu}(\boldsymbol{r}) \langle \tilde{p}_\nu | \tilde{\psi}_{n\mathbf{k+q}} \rangle$$

(18b)

and only augmentation spheres $\chi^{(4)}$

$$\chi^{(4)}(\boldsymbol{r}, \boldsymbol{R}', i\tau) \propto \sum_{\mu\nu} \langle \tilde{\psi}_{n\mathbf{k}} | \tilde{p}_\mu \rangle Q_{\mu\nu}(\boldsymbol{r}) \langle \tilde{p}_\nu | \tilde{\psi}_{n\mathbf{k+q}} \rangle \sum_{\alpha\beta} \langle \tilde{\psi}_{n'\mathbf{k+q}} | \tilde{p}_\alpha \rangle Q_{\alpha\beta}(\boldsymbol{R}') \langle \tilde{p}_\beta | \tilde{\psi}_{n\mathbf{k}} \rangle$$

(19)

There is an analogous set of equations for the Green's functions

$$G_{\boldsymbol{k}}^{(1)}(\boldsymbol{g},\boldsymbol{G}',i\tau)=\sum_{n}\langle\tilde{\psi}_{n\boldsymbol{k}}|\boldsymbol{g}\rangle\langle\boldsymbol{G}'|\tilde{\psi}_{n\boldsymbol{k}}\rangle e^{-\epsilon_{n\mathrm{k}}\tau}\qquad G_{\boldsymbol{k}}^{(2)}(\mu,\boldsymbol{G}',i\tau)=\sum_{n}\langle\tilde{\psi}_{n\boldsymbol{k}}|\tilde{p}_{\mu}\rangle\langle\boldsymbol{G}'|\tilde{\psi}_{n\boldsymbol{k}}\rangle e^{-\epsilon_{n\mathrm{k}}\tau}$$

$$G_{\boldsymbol{k}}^{(3)}(\boldsymbol{g},\alpha,i\tau)=\sum_{n}\langle\tilde{\psi}_{n\boldsymbol{k}}|\boldsymbol{g}\rangle\langle\tilde{p}_{\alpha}|\tilde{\psi}_{n\boldsymbol{k}}\rangle e^{-\epsilon_{n\mathrm{k}}\tau}\qquad G_{\boldsymbol{k}}^{(4)}(\mu,\alpha,i\tau)=\sum_{n}\langle\tilde{\psi}_{n\boldsymbol{k}}|\tilde{p}_{\mu}\rangle\langle\tilde{p}_{\alpha}|\tilde{\psi}_{n\boldsymbol{k}}\rangle e^{-\epsilon_{n\mathrm{k}}\tau}$$

(20)

where

$$\langle\tilde{\psi}_{n\boldsymbol{k}}|\boldsymbol{g}\rangle=\sum_{\boldsymbol{r}}\tilde{\psi}_{n\boldsymbol{k}}^{*}(\boldsymbol{r})e^{+i(\boldsymbol{k}+\boldsymbol{g})\boldsymbol{r}}$$

(21a)

$$\langle\tilde{\psi}_{n\boldsymbol{k}}|\boldsymbol{G}'\rangle=\sum_{\boldsymbol{R}'}\tilde{\psi}_{n\boldsymbol{k}}^{*}(\boldsymbol{R}')e^{+i\boldsymbol{G}'\boldsymbol{R}'}$$

(21b)

For each $G^{(j)}$, this is split into occupied $\bar{G}^{(j)}$ and unoccupied states $\bar{\bar{G}}^{(j)}$, evaluated in the negative and positive time axes, respectively, and combine with Eq. (7) to yield

$$\begin{aligned}\chi(\boldsymbol{r},\boldsymbol{R}',i\tau)&=\bar{G}^{(1)}(\boldsymbol{r},\boldsymbol{R}',i\tau)\bar{\bar{G}}^{*(1)}(\boldsymbol{r},\boldsymbol{R}',-i\tau)\\&+\sum_{\mu\nu}\bar{G}^{(2)}(\mu,\boldsymbol{R}',i\tau)\bar{\bar{G}}^{*(2)}(\nu,\boldsymbol{R}',-i\tau)\,Q_{\mu\nu}(\boldsymbol{r})\\&+\sum_{\alpha\beta}\bar{G}^{(3)}(\boldsymbol{r},\alpha,i\tau)\bar{\bar{G}}^{*(3)}(\boldsymbol{r},\beta,-i\tau)\,Q_{\alpha\beta}(\boldsymbol{R}')\\&+\sum_{\mu\nu\alpha\beta}\bar{G}^{(4)}(\mu,\alpha,i\tau)\bar{\bar{G}}^{*(4)}(\nu,\beta,-i\tau)\,Q_{\mu\nu}(\boldsymbol{r})Q_{\alpha\beta}(\boldsymbol{R}')\end{aligned}$$

(22)

N.B. $\boldsymbol{R}_{\mu}$ and $\boldsymbol{R}_{\nu}$ are within the unit cell, while $\boldsymbol{R}_{\alpha}$ and $\boldsymbol{R}_{\beta}$ are within the supercell.

Calculating each $G^{(j)}$ term scales at $O(N_{\omega}N_{G}^{3}N_{k})$, i.e. the overall scaling for the algorithm, it being the limiting step. Eq. (22) is then inserted into Eq. (12a) and (12b) to obtain $\chi_{\boldsymbol{k}}(\boldsymbol{g},\boldsymbol{g}')$ and then the RPA correlation energy from Eq. (1), as for the original algorithm. This reduced scaling is of great benefit, although this is only significant for large cells. The limiting factor for the low-scaling algorithm is not in the scaling of the method but in storing the Green's functions, which are extremely memory intensive.

3.4 Finite-Temperature RPA

The equations thus far are sufficient to calculate the correlation energy for insulators using the low-scaling algorithm at zero-tempterature. For zero- or small band gaps systems, e.g. metal, a finite-temperature form of the algorithm must be used (cf. LFINITE_TEMPERATURE).[23] In this implementation, a compressed Matsubara-frequency grid is used for integrations over frequency in (9), (11), (12), and (20), i.e. the Non-uniform Cosine and Fourier transformations, and calculating the Green's function.[23] The effect of temperature on the population of bands is performed by using a Fermi distribution, which then necessitates the use of Fermi smearing (cf. ISMEAR). Instead of the usual correlation energy, the finite-temperature analogue grand potential Ω_{corr} is calculated. This is similar to Eq. (1) but with an additional factor of reciprocal β and it is expressed as a summation, rather than an integral

$$\Omega_{corr} = \frac{1}{2}\frac{1}{\beta}\sum_{n} \mathrm{Tr}\{\ln[1 - \chi_0(i\omega_n)v] + \chi_0(i\omega_n)v\} \tag{23}$$

where $\beta = 1/k_B T$ with the Boltzmann constant k_B and the temperature T.

This introduces one additional parameter to test convergence against, β. A suitable smearing width (cf. SIGMA) must be determined. A smaller smearing width approximates the zero-temperature algorithm, though this is never exact for narrow gap systems due to issues with the zero-temperature algorithm.[23] A larger smearing width compensates for this but will distort the electronic structure away from the physical system if excessive. A suitable smearing width must be chosen to balance these two competing factors. We have performed this for narrow band-gap systems in the Supplementary Material of Chapter 3. When calculations are performed with the smearing width, frequency grid, *k*-point mesh, and plane wave cut-off correctly tested, converged RPA energies may be calculated and used to test the finite-temperature, low-scaling RPA algorithm itself.

4. Conclusion

We have discussed the different implementations of the original and low-scaling algorithms. The algorithms themselves are identical for the correlation energy equation but differ greatly in the calculation of the response function, with either the Adler-Wiser equation used for the former and the Green's function-approach for the latter. On application to metals, the low-scaling algorithm requires a finite-temperature implementation, which results in a final difference between the two algorithms. Overall, both methods are suitable for broad application. In this work we will apply both of them to the adsorption of alkanes on the Pt(111) surface, and we refer to Chapter 1 and 3, respectively, for details of their testing and their practical application.

5. References

1. Bohm, D.; Pines, D., A Collective Description of Electron Interactions. I. Magnetic Interactions. *Phys. Rev.* **1951,** *82*, 625-634, https://doi.org/10.1103/PhysRev.82.625.
2. Pines, D.; Bohm, D., A Collective Description of Electron Interactions: II. Collective vs Individual Particle Aspects of the Interactions. *Phys. Rev.* **1952,** *85*, 338-353, https://doi.org/10.1103/PhysRev.85.338.
3. Bohm, D.; Pines, D., A Collective Description of Electron Interactions: III. Coulomb Interactions in a Degenerate Electron Gas. *Phys. Rev.* **1953,** *92*, 609-625, https://doi.org/10.1103/PhysRev.92.609.
4. Pines, D., A Collective Description of Electron Interactions: IV. Electron Interaction in Metals. *Phys. Rev.* **1953,** *92*, 626-636, https://doi.org/10.1103/PhysRev.92.626.
5. Harl, J.; Schimka, L.; Kresse, G., Assessing the quality of the random phase approximation for lattice constants and atomization energies of solids. *Phys. Rev. B* **2010,** *81*, 115126, https://doi.org/10.1103/PhysRevB.81.115126.
6. Lebègue, S.; Harl, J.; Gould, T.; Ángyán, J. G.; Kresse, G.; Dobson, J. F., Cohesive Properties and Asymptotics of the Dispersion Interaction in Graphite by the Random Phase Approximation. *Phys. Rev. Lett.* **2010,** *105*, 196401, https://doi.org/10.1103/PhysRevLett.105.196401.
7. Harl, J.; Kresse, G., Accurate Bulk Properties from Approximate Many-Body Techniques. *Phys. Rev. Lett.* **2009,** *103*, 056401, https://doi.org/10.1103/PhysRevLett.103.056401.
8. Harl, J.; Kresse, G., Cohesive energy curves for noble gas solids calculated by adiabatic connection fluctuation-dissipation theory. *Phys. Rev. B* **2008,** *77*, 045136, https://doi.org/10.1103/PhysRevB.77.045136.
9. Schimka, L.; Harl, J.; Stroppa, A.; Grüneis, A.; Marsman, M.; Mittendorfer, F.; Kresse, G., Accurate surface and adsorption energies from many-body perturbation theory. *Nat. Mater.* **2010,** *9*, 741, https://doi.org/10.1038/nmat2806.
10. Feibelman, P. J.; Hammer, B.; Nørskov, J. K.; Wagner, F.; Scheffler, M.; Stumpf, R.; Watwe, R.; Dumesic, J., The CO/Pt(111) Puzzle. *J. Phys. Chem. B* **2001,** *105*, 4018-4025, https://doi.org/10.1021/jp002302t.
11. Yan, L.; Sun, Y.; Yamamoto, Y.; Kasamatsu, S.; Hamada, I.; Sugino, O., Hydrogen adsorption on Pt(111) revisited from random phase approximation. *J. Chem. Phys.* **2018,** *149*, 164702, https://doi.org/10.1063/1.5050830.

12. Kaltak, M.; Klimeš, J.; Kresse, G., Cubic scaling algorithm for the random phase approximation: Self-interstitials and vacancies in Si. *Phys. Rev. B* **2014,** *90*, 054115, https://doi.org/10.1103/PhysRevB.90.054115.

13. Kaltak, M.; Klimeš, J.; Kresse, G., Low Scaling Algorithms for the Random Phase Approximation: Imaginary Time and Laplace Transformations. *J. Chem. Theory Comput.* **2014,** *10*, 2498-2507, https://doi.org/10.1021/ct5001268.

14. Eshuis, H.; Bates, J. E.; Furche, F., Electron correlation methods based on the random phase approximation. *Theor. Chem. Acc.* **2012,** *131*, 1084, https://doi.org/10.1007/s00214-011-1084-8.

15. Niquet, Y. M.; Fuchs, M.; Gonze, X., Exchange-correlation potentials in the adiabatic connection fluctuation-dissipation framework. *Phys. Rev. A* **2003,** *68*, 032507, https://doi.org/10.1103/PhysRevA.68.032507.

16. Schmidt, P. S.; Thygesen, K. S., Benchmark Database of Transition Metal Surface and Adsorption Energies from Many-Body Perturbation Theory. *J. Phys. Chem. C* **2018,** *122*, 4381-4390, https://doi.org/10.1021/acs.jpcc.7b12258.

17. The VASP Manual. https://www.vasp.at/wiki/index.php/The_VASP_Manual.

18. Blöchl, P. E., Projector augmented-wave method. *Phys. Rev. B* **1994,** *50*, 17953, https://doi.org/10.1103/PhysRevB.50.17953.

19. Kresse, G.; Furthmuller, J., Efficient iterative schemes for ab initio total-energy calculations using a plane-wave basis set. *Phys. Rev. B* **1996,** *54*, 11169-11186, https://doi.org/10.1103/PhysRevB.54.11169.

20. Kresse, G.; Joubert, D., From ultrasoft pseudopotentials to the projector augmented-wave method. *Phys. Rev. B* **1999,** *59*, 1758-1775, https://doi.org/10.1103/PhysRevB.59.1758.

21. Shishkin, M.; Kresse, G., Implementation and performance of the frequency-dependent GW method within the PAW framework. *Phys. Rev. B* **2006,** *74*, 035101, https://doi.org/10.1103/PhysRevB.74.035101.

22. Gajdoš, M.; Hummer, K.; Kresse, G.; Furthmüller, J.; Bechstedt, F., Linear optical properties in the projector-augmented wave methodology. *Phys. Rev. B* **2006,** *73*, 045112, https://doi.org/10.1103/PhysRevB.73.045112.

23. Kaltak, M.; Kresse, G., Minimax isometry method: A compressive sensing approach for Matsubara summation in many-body perturbation theory. *Phys. Rev. B* **2020,** *101*, 205145, https://doi.org/10.1103/PhysRevB.101.205145.

Chapter 1

Adsorption of CH_4 on the Pt(111) Surface:

Random Phase Approximation Compared to Density Functional Theory

Reproduced from Sheldon, C.; Paier, J.; Sauer, J., Adsorption of CH_4 on the Pt(111) surface: Random phase approximation compared to density functional theory,. J. Chem. Phys. 2021, 155, 174702, https://doi.org/10.1063/5.0071995, with the permission of AIP Publishing.

Chapter 1: Adsorption of CH_4 on the Pt(111) Surface: Random Phase Approximation Compared to Density Functional Theory

We investigate adsorption of CH_4 on the Pt(111) surface for two adsorption modes, hcp (hexagonal closed packed) hollow tripod and top monopod in a (√3x√3)R30° surface cell which corresponds to experimental surface coverage. Surface structures are optimised with density functional theory using the Perdew-Burke-Ernzerhof (PBE) functional augmented with the Many-Body Dispersion scheme of Tkatchenko (PBE+MBD). Whereas the Random Phase Approximation (RPA) predicts a clear preference of about 5 kJ mol^{-1} for the hcp tripod compared to the top monopod structure, in agreement with vibrational spectra, PBE+MBD predicts about equal stability of the two adsorption structures. For the hcp tripod, RPA yields an adsorption energy of -14.5 kJ mol^{-1}, which is converged to within 1.0±0.5 kJ mol^{-1} with respect to the plane wave energy cut-off (500 eV), the *k*-point mesh (4x4x1), the vacuum layer (about 10.3 Å, with extrapolation to infinite distance), and the number of Pt layers (3). Increments for increasing the number of Pt layers to 4 (+1.6 kJ mol^{-1}) and the *k*-point mesh to 6x6x1 (-0.6 kJ mol^{-1}) yield a final estimate of -13.5±2.1 kJ mol^{-1} which agrees to within 2.2±2.1 kJ mol^{-1} with experiment (-15.7 ± 1.6), well within the chemical accuracy range.

1. Introduction

The initial step in heterogeneous catalysis is adsorption. This directly affects measured rates and reaction barriers, and heats of adsorption are an indispensable input for microkinetic models of catalytic processes, but rarely available from experiment. Here, we are interested in the adsorption of small alkanes on the Pt(111) single crystal surface as the model system of reduced complexity for the industrial dehydrogenation of propane using supported Pt catalysts.[1] This process converts propane as a component of natural/ shale gas into propene - a key chemical intermediate, e.g. for polymerisation.[2]

To be useful, quantum chemical predictions have to reach chemical accuracy (4 kJ mol^{-1}), which is not the case for the "work horse" of computational catalysis, density functional theory (DFT) with some account of dispersion (DFT+D).[3-9] For adsorption and reactions on Pt(111), mean absolute errors (MAE) of about 25 kJ mol^{-1} have been reported,[10] whereas maximum errors (ME) can be as large as 55 kJ mol^{-1}. Even advanced variants like the Bayesian error estimation functional with van der Waals correlation contributions (BEEF–vdW)[11] show MAE of around 30 kJ mol^{-1} for reactions on transition metal surfaces and MEs as large as 115 – 130 kJ mol^{-1}.[10,12] This benchmark set contains experimental adsorption energies that the authors believed to be "particularly accurate" and suitable for "benchmarking theoretical methods" against.[12]

The alternative to modifying DFT+D are post-Hartree-Fock wavefunction methods, which show the correct decay of the binding energy with the molecule-surface distance and do not suffer from the self-interaction errors (SIE). However, they are expensive, prohibitively so for periodic systems with more than a few atoms in the respective cell. Moreover, for metals, any "finite-order" perturbation theory breaks down when applied to systems with vanishing energy gaps.[13,14]

For metallic systems, the Random Phase Approximation (RPA) was developed,[15,16] which represents a subset of coupled-cluster-doubles (CCD) ring-type diagrams.[17] Two recent reviews on RPA-based electronic structure methods (including some post-RPA approaches) have been published by Chen et al. and, with emphasis on material science, Ren et al.[18,19] Our interest in RPA stems from it correctly describing the asymptotic tail of dispersion interactions, where DFT fails;[20] Dobson and Gould published a detailed review on the theory of calculating dispersion energies, which discusses the RPA approximation extensively.[21] RPA has already been applied to adsorption of H,[22] CO,[22-25] Xe,[26] 3,4,9,10-perylene-tetracarboxylic-dianhydride,[26] and C_6H_6[27] on transition metal surfaces, as well as on solids and other surfaces.[28-31]

Our interest in RPA stems from it correctly describing the asymptotic tail of dispersion interactions, where DFT fails.[20] However, its use is not widespread due to its high cost. From a user's perspective, one needs to consider the scaling with respect to system size in terms of the number of plane waves N_G (which is related to the number of atoms, and therefore electrons in the unit cell), as well as the number of *k*-points, N_k. The overall scaling is $O(N_k^2 N_G^4)$, with respect to floating point operations.[32] This is particularly unfortunate for metals, which require dense *k*-point grids to describe the band structure correctly. We would like mention here that, during our study, a newer, low scaling $O(N_k N_G^3)$ algorithm was released and is available as of VASP 6.[33]

In this paper, we study the adsorption of CH_4 on the Pt(111) surface and test the convergence of RPA results with respect to model choice and technical parameters in view of generating a benchmark. Comparison is made with experiment by taking nuclear motion effects into account and agreement is reached within 2.2-2.7 kJ mol^{-1}, well within the 4 kJ mol^{-1} chemical accuracy limits. The RPA calculations on CH_4/Pt(111) used surface structures optimised with Perdew-Burke-Ernzerhof (PBE)[34,35] augmented with the Many-Body Dispersion (MBD) scheme of Tkatchenko (PBE+MBD).[6,7]

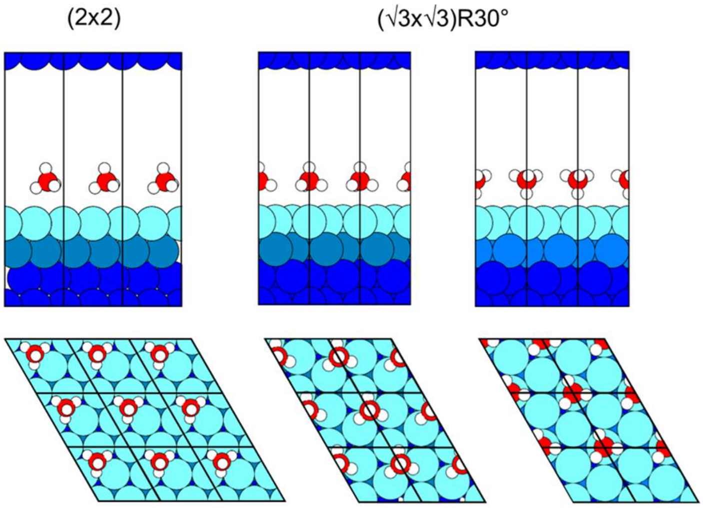

Figure 1. Repeated slab models with (2x2) and (√3x√3)R30° supercells used, including four and three Pt atoms in the surface layer, respectively. With one CH_4 molecule per cell, this corresponds to coverages of $^1/_4$ and $^1/_3$ ML, respectively. The C–C distances are 561 and 485 pm, respectively. The slabs contain four layers of Pt atoms. The hcp tripod (left) and top monopod (right) adsorption modes are shown for the (√3x√3)R30° supercell.

CH_4 can interact with different sites on the Pt(111) surface in different ways. We found that, among the many possible, the hcp (hexagonal closed packed) hollow tripod and the top monopod (see Figure 1) are the two lowest energy structures with the hcp tripod being the most stable; details are given in Sections 4.3 and 5.4. We will use the hcp tripod adsorption structure for studying the RPA adsorption energy.

2. Comparison with Experiment: Coverage and Heats of Adsorption

Surface coverage is an important issue when comparison is made between calculations with periodic boundary conditions as performed here and experiments. We define one monolayer (ML) as one CH_4 molecule per surface Pt atom ($CH_4/Pt_{surface}$) and assume a saturated coverage of $^1/_3$ ML, which corresponds to one molecule in a (√3x√3)R30° supercell (see Figure 1) and matches the value of 0.33±0.05 ML derived from XPS.[36]

Tait et al.[37] report desorption energies as function of coverage with respect to monolayer saturation coverage (Eq. 7 of Ref. [37]). Therefore, $^1/_4$ and $^1/_3$ ML in terms of $CH_4/Pt_{surface}$ will correspond to $^3/_4$ and 1 ML of the saturated coverage reported by Tait et al.,[37] which yields (Eq. 7 of Ref. [37]) observed adsorption enthalpies of -15.5 and -15.7 kJ mol^{-1}, respectively. For visualisation of these coverages, see Figure 1. The result reported in Table III of Ref. [37] (-15.2 kJ mol^{-1}) corresponds to $^1/_6$ ML of $CH_4/Pt_{surface}$ and would require surface cells for which converged RPA results are much harder to obtain than for $^1/_4$ or $^1/_3$ ML of $CH_4/Pt_{surface}$.

For comparison with quantum mechanical energies (i.e. the bottom of the potential energy surface), we firstly need to convert the experimental desorption energies,[37] which represent Arrhenius energies of activation, E_A, into heats of adsorption,[38]

$$\Delta H_{ads}(T) = - E_A(T) + RT \tag{1}$$

where T is the temperature and R the gas constant, and then into “experimentally derived” reference energies,[39]

$$\Delta E_{ref} = \Delta H_{ads}(T) - \Delta E_{ZPV} - \Delta E_{therm}(T) + RT = - E_A(T) - \Delta E_{ZPV} - \Delta E_{therm}(T) + 2\,RT \tag{2}$$

taking the zero-point vibrational energy, ΔE_{ZPV}, and the thermal corrections to the energy, ΔE_{therm}, into account.

We calculated the latter from vibrational partition functions using harmonic frequencies obtained with PBE+MBD (see below). For T = 63 K, this yields (2 RT = 1.04 kJ mol^{-1})

ΔE_{ref} ($^1/_3$ ML) = -15.7 – 0.57 – 0.45 + 1.04 = - 15.7 kJ mol^{-1}
ΔE_{ref} ($^1/_4$ ML) = -15.5 – 0.77 – 0.35 + 1.04 = - 15.6 kJ mol^{-1}

The difference between E_A and E_{ref} is very small, only 0.1 kJ mol^{-1}, but this is not always the case. For example, for adsorption of CH_4 on the MgO(100) surface the difference was - 2.7 kJ mol^{-1}.[38]

3. Models

"Repeated slab" models were produced by cutting an optimised bulk cell along the (111) plane (see Supplementary Material, Section S1 for more information on bulk). Figure 1 shows the (√3x√3)R30°, and (2x2) surface cells studied. If there were one CH_4 in each cell, would correspond to coverages of $^1/_3$, and $^1/_4$ ML, respectively, where one monolayer (ML) is formally defined as one adsorbed molecule per surface Pt atom.

The (1x1) cell was not considered for CH_4 adsorption. In accordance with the experimental saturation coverage of $^1/_3$ ML, the PBE+MBD adsorption energy was +130.2 kJ mol^{-1}, i.e. strongly repulsive, see Supplementary Material, Figure S2.1 and Table S2.2 for more details.

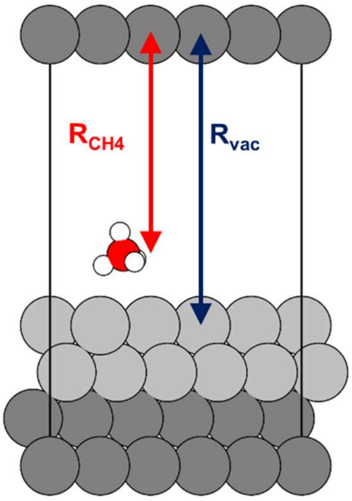

Figure 2. Repeated slab model (only one layer of the upper slab along the 'non-periodic' direction is shown): molecule-surface distance (red), R_{CH4}, and surface-slab distance (blue), R_{vac}.

Figure 2 shows the vacuum height definition between repeated slabs. The molecule-surface distance is shown in red and the surface-slab distance in blue. The positions of the atoms in the bottom two Pt layers were frozen to simulate the bulk, with the remaining free to move; exceptions are specifically noted.

Γ-centred *k*-point meshes were used for the Pt(111) surface calculations. The grids were chosen according to the cell vectors to ensure a sampling with nearly constant *k*-point density along a certain direction in reciprocal space,

$$k_{\text{density}} = N_k \cdot |b|/2\pi \tag{3}$$

where N_k is the number of *k*-points and b is the reciprocal lattice vector.

We also define the *k*-point spacing along a certain direction in reciprocal space:

$$k_{\text{spacing}} = |b|/(N_k \cdot 2\pi) \tag{4}$$

Isolated CH_4 molecules were modelled using cubic cells (20^3 Å^3) to avoid image interactions, unless otherwise indicated, and the calculations used only the Γ-point.

4. DFT Calculations

In addition to the Many-Body Dispersion (MBD) scheme of Tkatchenko,[6,7] the density dependent dispersion correction of Steinmann and Corminbouef (dDsC)[8,9] was used with PBE[34,35] in structure optimisations of the hcp hollow tripod and top monopod structures, see Figure 1. Based on subsequent frequency analysis we assign the structure by comparison with observed IRAS (Infrared Reflection-Adsorption Spectroscopy) spectra.[40,41]

4.1. Computational Details

The calculations were performed using the projector-augmented wave (PAW) method,[42,43] as implemented in the Vienna ab initio simulation package (VASP).[44] The PAW pseudopotential used to describe the electron-ion interaction for Pt includes the 4f electrons resulting in 10 valence electrons: [Xe,$4f^{14}$]$5d^9 6s^1$. Two partial waves were used for each orbital and their cut-off radius was 2.5 au for both the 5d and 6s states. For C, 4 valence electrons ([He]$2s^2 2p^2$) were considered. The partial wave cut-off radii were 1.2 and 1.5 au for 2s and 2p, respectively. For the 1s orbital of H, a partial wave cut-off radius of 1.1 au was used. These pseudopotentials were used for all structural optimisations.

An electronic energy threshold of $1\text{x}10^{-6}$ eV, a 6x6x1 *k*-point mesh, and a plane wave energy cut-off, $E_{\text{cut-off}}$, of 400 eV were applied. N.B., to simplify notation, subsequently we omit the final *k*-point along the 'non-periodic' direction, and write e.g. 8x8x1 as 8x8, 6x6x1 as 6x6. All calculations with dispersion terms used Ewald summations.[45] Calculations involving Pt used 1st order Methfessel-Paxton smearing with a smearing width of 0.2 eV, while those on isolated alkanes used Gaussian smearing with a smearing width of 0.05 eV.

Structure optimisations, unless otherwise stated, were performed until all forces on relaxed atoms were converged to below 0.01 eV Å^{-1} (0.194 mE_h bohr^{-1}). The conjugate gradient method was used with cell shape and volume kept constant. Structure optimisations using the DFT with the density-dependent dispersion correction from Steinmann and Corminboeuf (DFT+dDsC) were performed until an energy difference between structures of $1\text{x}10^{-6}$ eV had been achieved. Vibrational frequencies used central differences for the force derivative with atomic displacements of ±1.5 pm and electronic energy threshold of $1\text{x}10^{-8}$ eV. Frequency calculations were performed using PBE+MBD optimised structures of 4-layered slabs.

4.2. DFT Results

The optimized PBE+MBD structures for the 3-layered (√3x√3)R30° and (2x2) surface cells used for the RPA calculations are given in Table 1, see also Figure 1. Among several possible (top, hcp, fcc) the top and hcp sites were the lowest in energy whereas the monopod and tripod adsorption modes are the only ones compatible with the IRAS results.[40,41]

Table 1. Selected structure parameters of 3-layered, PBE+MBD optimised (√3x√3)R30° and (2x2) cells for the hcp tripod and top monopod adsorption models in pm, lattice parameters, a and c (b=a for hexagonal cells), and bond distances, r(X).[a]

r(X) / pm	hcp tripod		top monopod	
	(√3x√3)R30°	(2x2)	(√3x√3)R30°	(2x2)
a, c	485, 1486	561, 1458	485, 1486	561, 1458
r(Pt-C)	385, 381, 387	385, 386, 387	357	348
r(Pt-H)	344, 338, 344	324, 325, 326	246	237

[a] For all systems the distance between Pt atoms in the fixed, bottom layer is 281 pm and the distance between Pt atoms of the surface and first subsurface layer is 279 pm.

Table 2 shows the PBE+MBD and PBE+dDsC adsorption energies for the (√3x√3)R30° cell. With either DFT+D method, the energies of the two structures differ less than 1 kJ mol^{-1}, but the energetically favoured structure depends on which dispersion correction is applied.

Table 2. Adsorption energy, ΔE_{ads} (kJ mol^{-1}) of the top monopod and hcp tripod structures (PBE and dispersion contributions in parentheses) for a 4-layered (√3x√3)R30° slab optimized with the respective method,[a] see Figure 1 for details.

Method	top monopod	hcp tripod
PBE+dDsC	-21.3 (-0.3; -21.0)	-22.0 (+0.9; -22.9)
PBE+MBD	-17.9 (-0.5; -17.4)	-16.9 (+1.2; -18.1)

[a] A $E_{\text{cut-off}}$ of 400 eV, a 6x6 k mesh, and 14.0 Å vacuum height.

Determining which structure is physically favoured requires careful analysis of the available experimental data. Small redshifts of ~20 cm^{-1} for C-H vibrational modes have been reported for alkane monolayers on Pt(111).[46] Unlike other alkanes,[40,46] CH_4 only shows a small redshift upon adsorption on Pt(111). The T_d symmetry of the isolated CH_4 reduces to C_{3v} on the surface, making the IR-inactive symmetric stretch mode ν_1 IRAS active, associated with a shift of 37 cm^{-1} from 2917 cm^{-1} to 2882 cm^{-1}.[40,41]

We performed frequency calculations with PBE+MBD for the top monopod and hcp tripod structures, which yielded scaled redshifts of 101 cm^{-1} and 17 cm^{-1}, respectively. For scaling, f = ν_{exp}/ν_{calc} =0.984, we have used the symmetric (in-phase) C-H stretch of gas phase CH_4.[40] The experimental red-shift of 37 cm^{-1} differs significantly from the top monopod's predicted 101 cm^{-1}, while being far closer to the hcp tripod's 17 cm^{-1}. This indicates that the hcp tripod structure is observed physically, but not the top monopod. This conclusion does not agree with the study of Öström et al. who assigned their angle-resolved x-ray adsorption spectrum (XAS) of CH_4/Pt(977) to the top monopod structure.[47] Their assignment was based on BP86[48,49] calculations on a Pt_{10} cluster model of the Pt(111) surface. The transition moments between the 1s orbital and the virtual states have been calculated (IGLO-III basis set) by putting "half an electron charge" in the 1s orbital.[50] They investigated the monopod and tripod configurations at the top site, but the limited cluster size did not allow them to investigate the hcp tripod structure.

5. RPA Calculations

5.1. Computational Details

The RPA calculations were performed using the projector-augmented wave (PAW) method,[42,43] as implemented in the Vienna ab initio simulation package (VASP).[44] All calculations used an electronic energy threshold of 1x10^{-8} eV and a $E_{cut\text{-}off}$ of 500 eV, unless otherwise specified. Calculations involving Pt used 1st order Methfessel-Paxton smearing with a smearing width of 0.2 eV, while those on isolated alkanes used Gaussian smearing with a smearing width of 0.05 eV.

For RPA, *GW* PAW pseudopotentials[51] were used with identical core and valence definitions as the above but improved scattering properties for unoccupied states (PBE cores, as of VASP 5.4). These pseudopotentials have thus slightly higher minimally required energy cut-offs, e.g. 413 eV for C, rather than 400 eV. Being aware of that, we began our convergence tests with 400 eV, but also included 500 and 600 eV which are well above the minimal technical boundary. For Pt, the partial wave cut-off radii were 2.4 au for both the 5d and 6s states. For C, the partial wave cut-off radii were 1.2 and 1.5 au for 2s and 2p, respectively. For the 1s orbital of H, a cut-off radius of 0.95 au was used.

RPA calculations were performed in four steps, following the VASP manual.[52] Initially, a PBE calculation was performed to obtain orbitals and orbital energies. A Hartree-Fock energy calculation was performed using these orbitals, leaving them unchanged. All of the virtual states are then obtained by diagonalisation of the Fock operator. Finally, the ACFDT-RPA (Adiabatic Connection Fluctuation-Dissipation Theorem - Random Phase Approximation) correlation energy[53-55] is calculated. A frequency integration grid density containing 18 points was required for technical convergence for Pt calculations, while a grid of 12 points was sufficient for isolated CH_4. The correlation energy in VASP is automatically extrapolated to convergence with respect to the auxiliary plane wave basis set used for calculating the response function; these correlation energies have been used consistently throughout. All calculations, besides CH_4, neglected the long-wavelength contributions to speed up *k*-point convergence.[28] The number of plane waves is set by the number of maximal plane waves in the step generating the orbitals. Additionally, we include the contribution of the automated VASP extrapolation with respect to the auxiliary plane wave basis set used for calculating the response function $E^{\chi}_{cut-off}$.[32]

5.2. RPA Calculations for the Pt(111) Surface

Using surface structures optimised with PBE+MBD, we investigated the convergence of the RPA surface energy with respect to the number of Pt layers, the distance between periodic images, the number of *k*-points and the plane wave energy cut-off, $E_{cut\text{-}off}$.

The surface energy is defined as

$$\gamma_{surf} = ½\cdot(E_{surf} - N_{at}\cdot E_{bulk})/A \tag{5}$$

where N_{at} is the number of atoms in the surface model. E_{surf} and E_{bulk} are the electronic energies of the metal surface with N_{at} atoms and of the primitive bulk unit cell (single atom), respectively. A is one of the two (relaxed and unrelaxed) surface areas of the cell.

Table 3. Dependence of the PBE and RPA surface energies (J m^{-2}) on the number of Pt layers, N_{layer}, for the (1x1) slab model.[a] PBE+MBD optimised structures were used in both cases.

N_{layer}	PBE	RPA
2	1.58	2.01
3	1.61	2.02
4	1.57	1.98
	1.58[23, b]	2.03[23, b]
5	1.63	1.96
6	1.65	2.01
Obsd.[c]	2.49[c]	

[a] $E_{cut\text{-}off}$: 500 eV; 8x8 *k*-point mesh; vacuum height: 10.3 Å.

[b] Converted from eV $atom^{-1}$ to J m^{-2}.

[c] Observed value.[56]

For the (1x1) cell, Table 3 shows that there is no significant effect of the number of Pt layers on the surface energy. The PBE and RPA results vary over 0.08 and 0.06 J m^{-2}, respectively, without a systematic trend with increasing number of layers.

Our results for the 4-layered slab, 1.57 and 1.98 J m^{-2} for PBE and RPA, respectively, are in close agreement with the results of Kresse and co-workers,[23] 1.58 and 2.03 J m^{-2}, respectively. The results of Olsen and Thygesen,[57] 1.35 and 2.20 J m^{-2}, respectively, show much larger deviations (about 0.2 J m^{-2}) from both our and Kresse's results, which reflects the sensitivity of RPA with respect to the choice of computational parameters.

Usually, in DFT slab calculations, four layers are used to mimic the metal surface, with the two bottom-most being frozen in the positions of the bulk solid. However, the cost of RPA is high, scaling at $O(N^4)$ relative to PBE with $O(N^3)$, in addition to a much larger pre-factor. We therefore decided that three layers of Pt atoms are sufficient and can be used without compromising on accuracy as Table 3 shows.

Both PBE and RPA significantly underestimate the observed surface energy which is measured at the melting point (2.20 J m^{-2}) and then extrapolated to absolute zero.[56] PBE underestimates the surface energy more than RPA.

Table 4. Dependence of surface energy γ_{surf} (J m^{-2}) on vacuum height R_{vac} (Å) for a 3-layered, PBE+MBD (1x1) cell.[a]

R_{vac}	PBE	RPA
4.0	1.54	1.70
5.0	1.61	1.91
6.0	1.61	1.96
7.0	1.61	1.99
8.0	1.61	2.00
10.0	1.61	2.02
12.0	1.61	2.03
14.0	1.61	2.04
16.0	1.61	2.05
18.0	1.61	2.06

[a] A $E_{cut\text{-}off}$ of 500 eV and an 8x8 *k*-point mesh were used.

We tested the impact of the *k*-point density on the surface energy (see Table S3.1) and found an 8x8 mesh was sufficient to achieve convergence, and so it was chosen as standard for use with the (1x1) cell. Additionally, the $E_{cut\text{-}off}$ was found to have virtually no impact on the surface energy (Supplementary Material, Table S3.2).

The larger the cell, the costlier the calculation, so it is of interest to minimise this, where possible. The surface area must be kept constant, being dependent on the repeated surface image. However, the vacuum height of the cell (see Figure 2) can be modified. Table 4 shows that, once the vacuum height has reached ~10 Å, the surface energy is well-converged for RPA and fully so for PBE. This results from PBE to failing to properly describe long-range interactions. Beyond 10 Å, little additional precision can be obtained but at increasingly high cost, and we have chosen this value as a suitable vacuum height.

These preliminary investigations on the (1x1) cell have been useful for determining suitable settings but the cell is too small for application to surface chemistry. Therefore, we performed further convergence tests for the (√3x√3)R30° supercell. The change of the surface energy was below 0.01 J m $^{-2}$ when the $E_{cut\text{-}off}$ was varied between 400 and 600 eV for the settings of Table 4 with 4x4 k points, see Supplementary Material, Table S3.2.

The dependence on the *k*-point grid (Table 5) is stronger than for the (1x1) cell. This is due to the differences in *k*-point density, with much higher densities (0.045 Å^{-1} for the 8x8 mesh) more readily affordable for the (1x1) cell. While passing from a 4x4 to a 6x6 mesh changes the RPA surface energy by as much as 0.26 J m^{-2} (towards experiment), the corresponding change of the CH_4 adsorption energy is much smaller, just 0.2 kJ mol^{-1} for a 500 eV $E_{cut\text{-}off}$, see Table 6 below.

Table 5. Surface energy of a 3-layered (√3x√3)R30° cell, γ_{surf} (J m^{-2}), for different *k*-point meshes.[a] The linear *k*-point density[b] and the k-point spacing[c] are given in Å^{-1}.

k-points	$k_{density}$[b]	$k_{spacing}$[c]	γ_{surf}	
			PBE	RPA
2x2	0.476	0.119	2.12	1.56
4x4	0.952	0.060	1.50	1.68
6x6	1.428	0.040	1.54	1.94

[a] 10.3 Å vacuum height, 500 eV $E_{cut\text{-}off}$; [b] Eq. 3; [c] Eq. 4

5.3. RPA Results for CH_4 Adsorbed on the Pt(111) Surface

Having investigated the convergence of technical settings for the Pt(111) surface energy, and for the energy of the isolated CH_4 molecule, see Supplementary Material, Section S5 for details, we turn to the adsorption of CH_4. Our RPA calculations on CH_4/Pt(111) use surface structures optimised with PBE+MBD.

Table 6 shows the variation of the adsorption energy, ΔE_{ads}, with the $E_{cut\text{-}off}$ and *k*-point meshes. The adsorption energy changed significantly between the 2x2 and 4x4 *k*-point meshes, but there is little effect between the denser 4x4 and 6x6 meshes. Hence, the 4x4 *k*-

point mesh is chosen in further calculations. Table 6 also confirms that adsorption energies are sufficiently converged for a $E_{\text{cut-off}}$ of 500 eV.

Table 6. RPA adsorption energies, ΔE_{ads}, as well as their Hartree-Fock, ΔE_{HF}, and correlation energy components, ΔE_{corr}, in kJ mol^{-1} for different $E_{\text{cut-off}}$ (eV) and *k*-point meshes.[a]

	k_{density}[b]	k_{spacing}[c]	ΔE_{ads}			ΔE_{HF}			ΔE_{corr}		
$E_{\text{cut-off}}$			400[d]	500	600	400[d]	500	600	400[d]	500	600
2x2	0.476	0.119	-24.2	-24.7	-24.7	-0.2	-0.6	-0.6	-24.0	-24.0	-24.1
4x4	0.952	0.060	-16.7	-17.1	-17.1	9.4	9.0	9.1	-26.1	-26.1	-26.1
6x6	1.428	0.040	-17.2	-17.3	-	9.1	8.9	8.9	-26.3	-26.2	-

[a] A 3-layered (√3x√3)R30° cell with 10.3 Å vacuum height was used; [b] Eq. 3; [c] Eq. 4; [d] For limitations of 400 eV, see the computational section.

The RPA adsorption energy can be split into the Hartree-Fock energy, E_{HF}, (including the energy corrections[28] relating to partial occupancies in the metal) and correlation energy components, E_{corr}. Table 6 shows that the effect of increasing *k*-point meshes is not uniform for these two parts. Whereas the correlation energy is converged within ~2 kJ mol^{-1} using only a, relatively sparse, 2x2 *k*-point mesh, the Hartree-Fock component requires the denser 4x4 mesh at least. For both components though, passing from the 4x4 to the 6x6 *k*-point mesh offers only a small change, of the order of 0.1 kJ mol^{-1}. The adsorption energy is suitably converged to within 0.5 kJ mol^{-1} by the 4x4 mesh (Table 6). Additionally, the $E_{\text{cut-off}}$ has limited impact on the correlation energy and only a slightly more significantly one of ~0.5 kJ mol^{-1} on E_{HF} between 400 and 500 eV, after which convergence has been reached to within 0.1 kJ mol^{-1}. With this, we have converged the settings in terms of the ab initio parameters, i.e. the $E_{\text{cut-off}}$ and *k*-point density, at 500 eV and 0.95 Å^{-1}, respectively.

Table 7. RPA adsorption energy, ΔE_{ads} (kJ mol^{-1}), for varying number of Pt layers, N_{layer}, and surface coverage θ (ML).[a]

Cell	(√3x√3)R30°	(2x2)
θ	$^1/_3$	$^1/_4$
$k_{density}$[b]	0.952	0.823
N_{layer}	ΔE_{ads}	
2	-10.6	-11.2
3	-17.1	-16.8
4	-15.9	-

[a] Both cells use a 4x4 *k*-point mesh, 500 eV $E_{cut\text{-}off}$, and a 10.3 Å vacuum height; the k-point density is given in Å^{-1}; [b] Eq. 3

The parameters of the slab model need yet to be tested. Thus far, we have used 3-layered structures due to cost but, if fewer layers were suitable, it would enable the study of larger cells and so the coverage effect on the adsorption could be investigated. In this vein, we have calculated the adsorption energies for the (2x2) and (√3x√3)R30° cells, corresponding to $^1/_4$ and $^1/_3$ ML a coverages, respectively. The latter matches the observed saturated coverage, see Section 2.[36] Although two layers were sufficient for convergence with respect to the surface energy (cf. Table 3), Table 7 shows that this is not the case for the adsorption energy. We find three layers to be an acceptable compromise between accuracy and computational cost. However, there is still a difference of ~1 kJ mol^{-1} between three and four layers, which should be included in the final quantum mechanical estimate.

The other parameter that defines the slab model is the vacuum height. The results plotted in Figure 3a show a more significant dependence of the adsorption energy on the vacuum height than previously observed for the *k*-point mesh or the $E_{cut\text{-}off}$, cf. Table 6. The surface energy was virtually converged by a vacuum height of ~7 Å, whereas the adsorption energy still shows a noticeable difference between 10.3 Å and 14.3 Å. This reflects the fact that the surface energy is essentially unaffected by dispersion interactions whereas the adsorption energy of CH_4/Pt(111) is chiefly a dispersive effect. At a vacuum height of ~10 Å the adsorption energy is converged to within ~2 kJ mol^{-1} only which is insufficient for a benchmark study.

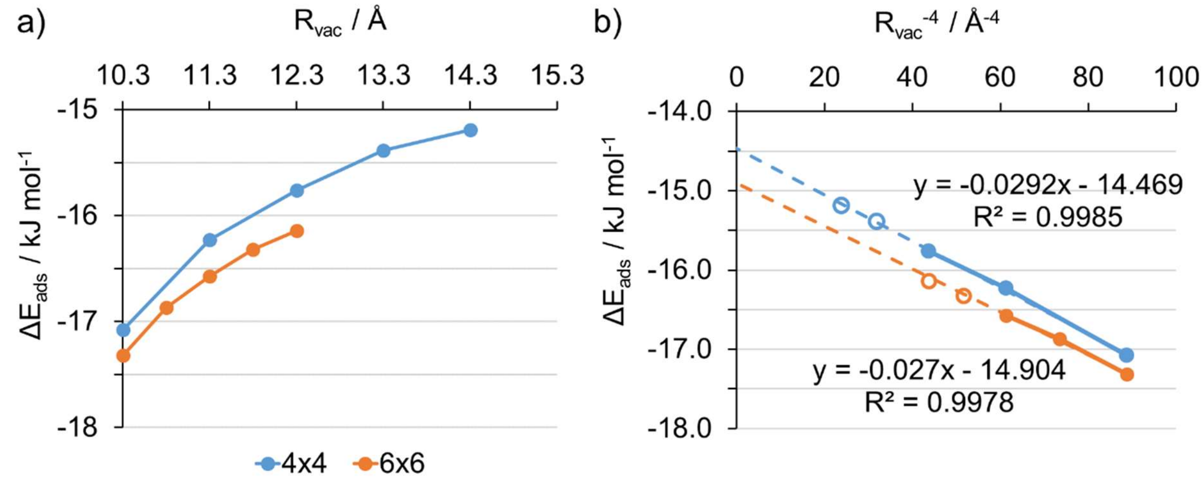

Figure 3. RPA adsorption energy ΔE_{ads} for the (√3x√3)R30° cell with given *k*-point meshes plotted **a)** against the surface-slab vacuum height R_{vac} . **b)** against the reciprocal vacuum height raised to the fourth power R_{vac}^{-4}; extrapolations are shown based on the three shaded points. See Table S6.1 for tabulated values and Section S6 for additional extrapolations.

To find the adsorption energy limit for slab models with large ("infinite") vacuum height, we attempted a linear extrapolation of the adsorption energy with respect to a reciprocal power, R^{-n}, of the vacuum height. For the dispersion interaction between metal slabs, theory[58] suggests a decay with $R^{-2.5}$,[58] but we saw the best fitting for R^{-4}, in line with the reported R^{-4} dependence of the RPA energy between graphene sheets, which dominates at short distances.[59,60] We show the R^{-4} extrapolation in Figure 3b.

If we instead extrapolate with respect to the height from the CH_4 centre (C nucleus) to the repeated Pt slab (the top of the supercell), R_{CH4} (Figure 2), we achieve the best fitting for R_{CH4}^{-3}, with R^2 =0.9992 (Figure S6.1). The R^{-3} dependence matches the power law theory suggests for the interaction between a neutral atom and the solid surface.[61] Both of these extrapolations yield virtually identical "infinite" vacuum values, -14.47 and -14.57 kJ mol^{-1} for the R^{-4} and R^{-3} extrapolations, respectively (Section S6), and we arrive at -14.5±0.1 kJ mol^{-1} as average value for the adsorption energy.

Since the calculations for the cells with the largest vacuum height are the computationally most demanding (13.3. and 14.3 Å) we tested if only three distances, 10.3, 11.3 and 12.3 Å, are sufficient for the extrapolation. The results, -14.46 and -14.62 kJ mol^{-1} for the R^{-4} and R^{-3} extrapolations, respectively, are virtually identical which is an important finding in view of future applications to larger adsorbates. It made it also possible to extrapolate the adsorption energy obtained with a 6x6 *k*-point mesh for R_{vac} =10.3, 10.8 and 11.3 Å, see Figure 3b and Supplementary Material, Figure S6.2. The R_{vac}^{-4} and R_{CH4}^{-3} extrapolations yield -14.90 and -15.12 kJ mol^{-1}, respectively, for "infinite" vacuum adsorption energy, with -15.0±0.1 kJ mol^{-1} as average.

For the (2x2) cell, using a 4x4 *k*-point mesh extrapolated with respect to the vacuum height gave values of -13.8 and -13.9 kJ mol^{-1} for the R_{vac}^{-4} and R_{CH4}^{-3}, respectively (see Table S6.2), averaging to 13.8 kJ mol^{-1}.

Table 8 summarizes the results of our convergence studies. We found that a 4x4 *k*-point mesh is sufficient for both (√3x√3)R30° and (2x2) cells. A *k*-point density of 0.95 and 0.82 Å^{-1}, respectively, was found to be converged. Further, we recommend $E_{cut\text{-}off}$ = 500 eV. The slab model should consist of at least three layers of Pt atoms for a dispersion-bound adsorbate like methane, and extrapolation with respect to vacuum height beyond 10.3 Å for the surface slab distance should be performed. This requires two additional calculations with 11.3 and 12.3 Å vacuum heights.

Table 8. Dependence of the RPA adsorption energies (kJ mol^{-1}) on the *k*-point mesh, the number of Pt layers of the slab, N_{layer}, and the vacuum height, R_{vac}, for a $E_{cut\text{-}off}$ of 500 eV.

cell	*k* points	N_{layer}	R_{vac}		
			10.3 Å	∞	
(√3x√3)R30°	4x4	3	-17.1	-14.5	Figure 3
		4	-15.9	-12.9	Table S6.3
Δlayer			+1.2	+1.6	
	6x6	3	-17.3	-15.1	Figure 3
Δ*k*-points			-0.2	-0.6	
estimated				-13.5±0.5	
(2x2)	4x4	3	-16.8	-13.8	Table 7
estimated				-12.8±0.5	

Adding a fourth Pt layer to the slab for the (√3x√3)R30° cell changes the adsorption energy by +1.2 and 1.6 kJ mol^{-1} for R_{vac} = 10.3 Å and ∞ (extrapolated), respectively. Passing from a 4x4 to a 6x6 k-point mesh changes the result for R_{vac} = 10.3 Å and ∞ (extrapolated) by -0.2 and -0.6 kJ mol^{-1}, respectively.

Our best estimate is obtained as:

$\Delta E_{ads} = \Delta E_{ads}$ (500 eV, 4x4, 3 layers, $R_{vac} = \infty$) + Δlayer + Δ*k*-points.

There is a partial compensation between Δlayer and Δ*k*-points which results in the same combined effect (+1.0 kJ mol^{-1}) for both R_{vac} = 10.3 Å and the extrapolated value. This finding may be specific for the chosen slab model. Taking half of this value as uncertainty we get estimates of - 14.5 + 1.0 = - 13.5 ± 0.5 and - 13.8 + 1.0 = - 12.8 ± 0.5 kJ mol^{-1} for the (√3x√3)R30° and (2x2) cells, respectively.

5.4. Lateral Interactions

Adsorption energies have two components: the molecule-surface interactions and the lateral interactions between the adsorbed molecules. The lateral interaction energy, ΔE_{lat}, is defined as:

$$\Delta E_{lat} = [E(M_N//M_N \cdot S) - N_M \cdot E(M)]/N_M$$

(6)

where $E(M_N//M_N \cdot S)$ is the energy of the adsorbate layer at the structure of the adsorbate-surface system, N_M is the number of molecules in that system, and E(M) is the energy of an isolated adsorbate molecule.

Table 9 shows the lateral interaction energies for the (√3x√3)R30° and (2x2) cells. The (1x1) cell showed a PBE+MBD adsorption energy of +130 kJ mol^{-1} and a lateral interaction of 146 kJ mol^{-1} indicating strong repulsion; we will not discuss it further here but this data is presented in the Supplementary Material, Table S2.2. Extrapolation of the adsorption energy to “infinite” vacuum heights was also done for the lateral interactions in z-direction, R_z, i.e., the same direction as when the slab was present. Only the Hartree-Fock component was extrapolated with respect to R_z^{-3}, as the correlation energy component is already well-converged to within 0.1 kJ mol^{-1}, see Supplementary Material, Section S8. For the smallest cells, corresponding to the CH_4/Pt(111) supercells with 10.3 Å vacuum heights, see Supplementary Material, Table S7.1.

Table 9. RPA adsorption, lateral interaction and molecule-slab interaction energies (kJ mol^{-1}),[a] ΔE_{ads}, ΔE_{lat}, and $\Delta E_{M\text{-}slab}$, respectively, extrapolated to “infinite” vacuum height for two surface coverages. The distance between the CH_4 molecules, R_{CC} (pm), is also given.

θ / ML	Cell	*k*-points	R_{CC}	ΔE_{ads}	ΔE_{lat}	$\Delta E_{M\text{-}slab}$
$^1/_3$	(√3x√3)R30°	4x4	485	-14.5	-3.3	-11.2
		6x6	485	-15.1	-2.5	-12.6
$^1/_4$	(2x2)	4x4	561	-13.8	-1.6	-12.2
		6x6	561	-	-1.1	-

[a] 500 eV $E_{cut\text{-}off}$.

For the (√3x√3)R30° cell, with C-C distances of 485 pm between the CH_4 molecules in the adsorbate layer, the lateral interactions contribute 15-20 % to the total adsorption energy. This drops to about 10% if the C-C distance increases to 561 pm for the (2x2) cell. Passing from a 4x4 to a 6x6 *k*-mesh, the lateral interactions become weaker (+0.8 kJ mol^{-1}) whereas the molecule surface interaction become stronger (-1.4 kJ mol^{-1}). There is a partial compensation and the total adsorption energy changes by -0.6 kJ mol^{-1}.

5.5. RPA Adsorption Mode

In Section 4.3, we used DFT+D and compared with experimental vibrational spectra to determine which of the two adsorption structures, top monopod or hcp tripod was likely to be more stable. Table 10 shows RPA results for $^1/_3$ and $^1/_4$ ML coverages which have been obtained at PBE+MBD structures.

Table 10. RPA adsorption energies, ΔE_{ads}, and their Hartree-Fock and correlation energy components (kJ mol^{-1}), ΔE_{HF} and ΔE_{corr}, respectively,[a] for the top monopod and hcp tripod adsorption structures.

θ / ML	Cell	*k*-points	top monopod			hcp tripod		
			ΔE_{ads}	ΔE_{HF}	ΔE_{corr}	ΔE_{ads}	ΔE_{HF}	ΔE_{corr}
$^1/_3$	(√3x√3)R30°	4x4	-12.0	14.1	-26.1	-17.1	9.0	-26.1
$^1/_4$	(2x2)	4x4	-8.3	21.0	-29.3	-16.8	9.0	-25.8

[a] With a 3-layered slab, 500 eV $E_{cut\text{-}off}$, and 10.3 Å vacuum heights.

In contrast to the DFT+D methods which predict about equal energies for both structures, see Table 2, with RPA the hcp tripod is clearly the lower energy structure, favoured 5.1 and 8.5 kJ mol^{-1} for θ = $^1/_3$ and $^1/_4$ ML, respectively.

For (√3x√3)R30 cell, the predicted energy difference between the two structures comes entirely from the Hartree-Fock contribution, whereas for the (2x2) cell the Hartree-Fock difference of 12.0 kJ mol^{-1} is partially compensated by a correlation energy difference of -3.5 kJ mol^{-1}.

5.6. Comparison with Experimental Heats of Adsorption

For comparison with experiment (Table 11) we make use of the experimentally derived adsorption energies, ΔE_{ref}, as defined in Section 2. Table 11 shows the comparison with the final estimate from RPA calculations.

Table 11. Comparison of RPA results with experiment.[37]

Θ	$-E_A$ [a] Obsd.	ΔE_{ZPV} Calcd.	ΔE_{therm} Calcd.	ΔE_{ref} [b] Obsd.[a]	ΔE_{RPA} Calcd.	ΔE_{est} [c] Estd.	$\Delta E_{est} - \Delta E_{ref}$
$^1/_3$	-15.7 ± 1.6	0.57	0.45	-15.7± 1.6	-14.5	-13.5 ± 0.5	+ 2.2 ± 2.1
$^1/_4$	-15.5 ± 1.6	0.77	0.35	-15.6± 1.6	-13.8	-12.8 ± 0.5	+ 2.7 ± 2.1

[a] Ref. [37]; 10% uncertainty of the inversion analysis.[62] [b] Experimentally derived reference energy. [c] cf. Table 8

Our RPA adsorption energy estimates are 2.2 and 2.7 kJ mol^{-1} less binding than the reference energies derived from experiment. This deviation is not much larger than the combined uncertainties of experiment and RPA calculation (2.1 kJ mol^{-1}) and well within chemical accuracy limits of 4 kJ mol^{-1}. Note that the directly calculated RPA adsorption energies, without the correction for 4 layers (instead of 3 slab layers) and a 6x6 k-point mesh (instead of a 4x4 one), with deviations of 1.2 and 1.7 kJ mol^{-1}, are apparently in better agreement with experiment. This underlines the need for convergence studies to get “the right answer for the right reason”.

The RPA results are a substantial improvement compared to DFT+D. Whereas PBE+dDsC correctly predicts the hcp tripod structure, the adsorption energy is 6.3 kJ mol^{-1} more negative than the experimental reference. In contrast, PBE+MBD deviates only 2.2 kJ mol^{-1} from experiment but predicts the wrong adsorption mode (top monopod).

RPA results have been reported for other adsorbates on Pt(111), see Table 12. For benzene on Pt(111), the RPA result (θ= 0.8),[27] -168 kJ mol^{-1}, is also close to experiment, -162 kJ mol^{-1}. In this case, also PBE+dDsC performs very well (-170 kJ mol^{-1}).[10]

The good agreement for CH_4 and benzene indicates that the RPA provides a good description for molecule – surface interactions with dominating dispersive interaction. For CO and H which form chemical bonds with the surface the deviations of the RPA results from experiment are much larger than for CH_4 and benzene, but still a significant improvement over PBE+dDsC. This corroborates the previous finding that RPA underestimates atomisation energies of molecules.[63]

Table 12. RPA and PBE+dDsC energies (kJ mol^{-1}) for adsorption on Pt(111) compared to experiment.

		CH_4	C_6H_6	CO	H
	θ	$^1/_3$	$^1/_9$ (0.8)	$^1/_4$	$^1/_4$
Exp.[a]	$-\Delta E$	15.7	162	117	35
RPA[b]	$-\Delta E$	13.5	168[27]	131[22]	49[22]
PBE+dDsC[c]	$-\Delta E$	22.0	170	179	53

[a] Derived from Ref. [37] using vibrational corrections for CH_4; Ref. [64] without corrections for others.
[b] CO/M(111) values are for top site adsorption.
[c] This work for CH_4/Pt(111), Ref. [10] for others.

6. Conclusions

For adsorption of CH_4 on the Pt(111) surface, RPA yields adsorption energies that are 2.2 – 2.7 kJ mol^{-1} less binding than experimental reference values, well within chemical accuracy limits. This provides further evidence that RPA describes interactions of molecules with metal surfaces such as Pt(111) well when the binding is dominated by dispersion (CH_4, benzene), whereas much larger errors are reported for cases with chemical bonding (H, CO).

For CH_4 on Pt(111), the RPA results are a major improvement over DFT+dispersion approaches. Whereas RPA predicts a clear preference for the hcp tripod structure compared to the top monopod structure, in agreement with vibrational spectra, PBE+MBD and PBE+dDsC predict about equal stability of the two adsorption structures.

Supplementary Material

Details of bulk calculations, DFT optimised structures, Pt(111) surface energies, CH_4 atomisation energies, isolated CH_4 calculations, vacuum height extrapolations, RPA adsorption energy results, and lateral interactions.

Acknowledgements

This work has been supported by German Research Foundation (DFG) with a Reinhart Koselleck grant, as well as by the “Fonds der Chemischen Industrie”. The HLRN is acknowledged for computer time grants (bec00213 and bec00230).

Author Declarations

Conflict of Interest

The authors have no conflicts of interest to disclose.

Data Availability Statements

Data available on request from the authors.

7. References

1. Sauer, J.; Freund, H.-J., Models in Catalysis. *Catal. Lett.* **2015,** *145*, 109-125, https://doi.org/10.1007/s10562-014-1387-1.

2. Sattler, J. J. H. B.; Ruiz-Martinez, J.; Santillan-Jimenez, E.; Weckhuysen, B. M., Catalytic Dehydrogenation of Light Alkanes on Metals and Metal Oxides. *Chem. Rev.* **2014,** *114*, 10613-10653, https://doi.org/10.1021/cr5002436.

3. Wu, X.; Vargas, M. C.; Nayak, S.; Lotrich, V.; Scoles, G., Towards extending the applicability of density functional theory to weakly bound systems. *J. Chem. Phys.* **2001,** *115*, 8748-8757, https://doi.org/10.1063/1.1412004.

4. Grimme, S.; Hansen, A.; Brandenburg, J. G.; Bannwarth, C., Dispersion-Corrected Mean-Field Electronic Structure Methods. *Chem. Rev.* **2016,** *116*, 5105-5154, https://doi.org/10.1021/acs.chemrev.5b00533.

5. Dion, M.; Rydberg, H.; Schröder, E.; Langreth, D. C.; Lundqvist, B. I., Van der Waals Density Functional for General Geometries. *Phys. Rev. Lett.* **2004,** *92*, 246401, https://doi.org/10.1103/PhysRevLett.92.246401.

6. Ambrosetti, A.; Reilly, A. M.; DiStasio, R. A.; Tkatchenko, A., Long-range correlation energy calculated from coupled atomic response functions. *J. Chem. Phys.* **2014,** *140*, 18A508, https://doi.org/10.1063/1.4865104.

7. Bučko, T.; Lebègue, S.; Gould, T.; Ángyán, J. G., Many-body dispersion corrections for periodic systems: an efficient reciprocal space implementation. *J. Phys.: Condens. Matter* **2016,** *28*, 045201, https://doi.org/10.1088/0953-8984/28/4/045201.

8. Steinmann, S. N.; Corminboeuf, C., Comprehensive Benchmarking of a Density-Dependent Dispersion Correction. *J. Chem. Theory Comput.* **2011,** *7*, 3567-3577, https://doi.org/10.1021/ct200602x.

9. Steinmann, S. N.; Corminboeuf, C., A generalized-gradient approximation exchange hole model for dispersion coefficients. *J. Chem. Phys.* **2011,** *134*, 044117, https://doi.org/10.1063/1.3545985.

10. Gautier, S.; Steinmann, S. N.; Michel, C.; Fleurat-Lessard, P.; Sautet, P., Molecular adsorption at Pt(111). How accurate are DFT functionals? *Phys. Chem. Chem. Phys.* **2015,** *17*, 28921-28930, https://doi.org/10.1039/C5CP04534G.

11. Wellendorff, J.; Lundgaard, K. T.; Møgelhøj, A.; Petzold, V.; Landis, D. D.; Nørskov, J. K.; Bligaard, T.; Jacobsen, K. W., Density functionals for surface science: Exchange-correlation model development with Bayesian error estimation. *Phys. Rev. B* **2012,** *85*, 235149, https://doi.org/10.1103/PhysRevB.85.235149.

12. Wellendorff, J.; Silbaugh, T. L.; Garcia-Pintos, D.; Nørskov, J. K.; Bligaard, T.; Studt, F.; Campbell, C. T., A benchmark database for adsorption bond energies to transition metal surfaces and comparison to selected DFT functionals. *Surf. Sci.* **2015,** *640*, 36-44, https://doi.org/10.1016/j.susc.2015.03.023.

13. Paier, J.; Ren, X.; Rinke, P.; Scuseria, G. E.; Grüneis, A.; Kresse, G.; Scheffler, M., Assessment of correlation energies based on the random-phase approximation. *New J. Phys.* **2012,** *14*, 043002, https://doi.org/10.1088/1367-2630/14/4/043002.

14. F. E. Harris; H. J. Monkhorst; Freeman, D. L., *Algebraic and Diagrammatic Methods in Many-Fermion Theory*. Oxford University Press: New York, Oxford, 1992.

15. Bohm, D.; Pines, D., A Collective Description of Electron Interactions. I. Magnetic Interactions. *Phys. Rev.* **1951,** *82*, 625-634, https://doi.org/10.1103/PhysRev.82.625.

16. Bohm, D.; Pines, D., A Collective Description of Electron Interactions: III. Coulomb Interactions in a Degenerate Electron Gas. *Phys. Rev.* **1953,** *92*, 609-625, https://doi.org/10.1103/PhysRev.92.609.

17. Scuseria, G. E.; Henderson, T. M.; Sorensen, D. C., The ground state correlation energy of the random phase approximation from a ring coupled cluster doubles approach. *J. Chem. Phys.* **2008,** *129*, 231101, https://doi.org/10.1063/1.3043729.

18. Chen, G. P.; Voora, V. K.; Agee, M. M.; Balasubramani, S. G.; Furche, F., Random-Phase Approximation Methods. *Annu. Rev. Phys. Chem.* **2017,** *68*, 421-445, https://doi.org/10.1146/annurev-physchem-040215-112308.

19. Ren, X.; Rinke, P.; Joas, C.; Scheffler, M., Random-phase approximation and its applications in computational chemistry and materials science. *J. Mater. Sci.* **2012,** *47*, 7447-7471, https://doi.org/10.1007/s10853-012-6570-4.

20. Furche, F., Molecular tests of the random phase approximation to the exchange-correlation energy functional. *Phys. Rev. B* **2001,** *64*, 195120, https://doi.org/10.1103/PhysRevB.64.195120.

21. Dobson, J. F.; Gould, T., Calculation of dispersion energies. *J. Phys.: Condens. Matter* **2012,** *24*, 073201, https://doi.org/10.1088/0953-8984/24/7/073201.

22. Schmidt, P. S.; Thygesen, K. S., Benchmark Database of Transition Metal Surface and Adsorption Energies from Many-Body Perturbation Theory. *J. Phys. Chem. C* **2018,** *122*, 4381-4390, https://doi.org/10.1021/acs.jpcc.7b12258.

23. Schimka, L.; Harl, J.; Stroppa, A.; Grüneis, A.; Marsman, M.; Mittendorfer, F.; Kresse, G., Accurate surface and adsorption energies from many-body perturbation theory. *Nat. Mater.* **2010,** *9*, 741, https://doi.org/10.1038/nmat2806.

24. Ren, X.; Rinke, P.; Scheffler, M., Exploring the random phase approximation: Application to CO adsorbed on Cu(111). *Phys. Rev. B* **2009,** *80*, 045402, https://doi.org/10.1103/PhysRevB.80.045402.

25. Harl, J.; Kresse, G., Accurate Bulk Properties from Approximate Many-Body Techniques. *Phys. Rev. Lett.* **2009,** *103*, 056401, https://doi.org/10.1103/PhysRevLett.103.056401.

26. Rohlfing, M.; Bredow, T., Binding Energy of Adsorbates on a Noble-Metal Surface: Exchange and Correlation Effects. *Phys. Rev. Lett.* **2008,** *101*, 266106, https://doi.org/10.1103/PhysRevLett.101.266106.

27. Garrido Torres, J. A.; Ramberger, B.; Früchtl, H. A.; Schaub, R.; Kresse, G., Adsorption energies of benzene on close packed transition metal surfaces using the random phase approximation. *Phys. Rev. Mater.* **2017,** *1*, 060803, https://doi.org/10.1103/PhysRevMaterials.1.060803.

28. Harl, J.; Schimka, L.; Kresse, G., Assessing the quality of the random phase approximation for lattice constants and atomization energies of solids. *Phys. Rev. B* **2010,** *81*, 115126, https://doi.org/10.1103/PhysRevB.81.115126.

29. Göltl, F.; Hafner, J., Alkane adsorption in Na-exchanged chabazite: The influence of dispersion forces. *J. Chem. Phys.* **2011,** *134*, 064102, https://doi.org/10.1063/1.3549815.

30. Ma, J.; Michaelides, A.; Alfè, D.; Schimka, L.; Kresse, G.; Wang, E., Adsorption and diffusion of water on graphene from first principles. *Phys. Rev. B* **2011,** *84*, 033402, https://doi.org/10.1103/PhysRevB.84.033402.

31. Kim, H.-J.; Tkatchenko, A.; Cho, J.-H.; Scheffler, M., Benzene adsorbed on Si(001): The role of electron correlation and finite temperature. *Phys. Rev. B* **2012,** *85*, 041403, https://doi.org/10.1103/PhysRevB.85.041403.

32. Harl, J.; Kresse, G., Cohesive energy curves for noble gas solids calculated by adiabatic connection fluctuation-dissipation theory. *Phys. Rev. B* **2008,** *77*, 045136, https://doi.org/10.1103/PhysRevB.77.045136.

33. Kaltak, M.; Klimeš, J.; Kresse, G., Cubic scaling algorithm for the random phase approximation: Self-interstitials and vacancies in Si. *Phys. Rev. B* **2014,** *90*, 054115, https://doi.org/10.1103/PhysRevB.90.054115.

34. Perdew, J. P.; Burke, K.; Ernzerhof, M., Generalized Gradient Approximation Made Simple. *Phys. Rev. Lett.* **1996,** *77*, 3865-3868, https://doi.org/10.1103/PhysRevLett.77.3865.

35. Perdew, J. P.; Burke, K.; Ernzerhof, M., Generalized Gradient Approximation Made Simple [Phys. Rev. Lett. 77, 3865 (1996)]. *Phys. Rev. Lett.* **1997,** *78*, 1396-1396, https://doi.org/10.1103/PhysRevLett.78.1396.

36. Matsumoto, Y.; Gruzdkov, Y. A.; Watanabe, K.; Sawabe, K., Laser-induced photochemistry of methane on Pt(111): Excitation mechanism and dissociation dynamics. *J. Chem. Phys.* **1996,** *105*, 4775-4788, https://doi.org/10.1063/1.472316.

37. Tait, S. L.; Dohnálek, Z.; Campbell, C. T.; Kay, B. D., n-alkanes on Pt(111) and on C(0001)/Pt(111): Chain length dependence of kinetic desorption parameters. *J. Chem. Phys.* **2006,** *125*, 234308, https://doi.org/10.1063/1.2400235.

38. Tosoni, S.; Sauer, J., Accurate quantum chemical energies for the interaction of hydrocarbons with oxide surfaces: CH(4)/MgO(001). *Phys. Chem. Chem. Phys.* **2010,** *12*, 14330-40, https://doi.org/10.1039/c0cp01261k.

39. Sauer, J., Ab Initio Calculations for Molecule–Surface Interactions with Chemical Accuracy. *Acc. Chem. Res.* **2019,** *52*, 3502-3510, https://doi.org/10.1021/acs.accounts.9b00506.

40. Shimanouchi, T., *Tables of Molecular Vibrational Frequencies: Consolidated Volume 1*. National Standard Reference Data System: Washington, 1972.

41. Yoshinobu, J.; Ogasawara, H.; Kawai, M., Symmetry Controlled Surface Photochemistry of Methane on Pt(111). *Phys. Rev. Lett.* **1995,** *75*, 2176-2179, https://doi.org/10.1103/PhysRevLett.75.2176.

42. Blöchl, P. E., Projector augmented-wave method. *Phys. Rev. B* **1994,** *50*, 17953-17979, https://doi.org/10.1103/PhysRevB.50.17953.

43. Kresse, G.; Joubert, D., From ultrasoft pseudopotentials to the projector augmented-wave method. *Phys. Rev. B* **1999,** *59*, 1758-1775, https://doi.org/10.1103/PhysRevB.59.1758.

44. Kresse, G.; Furthmuller, J., Efficient iterative schemes for ab initio total-energy calculations using a plane-wave basis set. *Phys. Rev. B* **1996,** *54*, 11169-11186, https://doi.org/10.1103/PhysRevB.54.11169.

45. Kerber, T.; Sierka, M.; Sauer, J., Application of semiempirical long-range dispersion corrections to periodic systems in density functional theory. *J. Comput. Chem.* **2008,** *29*, 2088-2097, https://doi.org/https://doi.org/10.1002/jcc.21069.

46. Chesters, M. A.; Gardner, P.; McCash, E. M., The reflection-absorption infrared spectra of n-alkanes adsorbed on Pt(111). *Surf. Sci.* **1989,** *209*, 89-99, https://doi.org/https://doi.org/10.1016/0039-6028(89)90060-5.

47. Öström, H.; Ogasawara, H.; Näslund, L. Å.; Andersson, K.; Pettersson, L. G. M.; Nilsson, A., Geometric and electronic structure of methane adsorbed on a Pt surface. *J. Chem. Phys.* **2007,** *127*, 144702, https://doi.org/10.1063/1.2781470.

48. Perdew, J. P., Density-functional approximation for the correlation energy of the inhomogeneous electron gas. *Phys. Rev. B* **1986,** *33*, 8822-8824, https://doi.org/10.1103/PhysRevB.33.8822.

49. Becke, A. D., Density-functional exchange-energy approximation with correct asymptotic behavior. *Phys. Rev. A* **1988,** *38*, 3098-3100, https://doi.org/10.1103/PhysRevA.38.3098.

50. Triguero, L.; Pettersson, L. G. M.; Ågren, H., Calculations of near-edge x-ray-absorption spectra of gas-phase and chemisorbed molecules by means of density-functional and transition-potential theory. *Phys. Rev. B* **1998,** *58*, 8097-8110, https://doi.org/10.1103/PhysRevB.58.8097.

51. Shishkin, M.; Kresse, G., Implementation and performance of the frequency-dependent GW method within the PAW framework. *Phys. Rev. B* **2006,** *74*, 035101, https://doi.org/10.1103/PhysRevB.74.035101.

52. Hehre, W. J.; Radom, L.; Schleyer, P. v. R.; Pople, J. A., *Ab initio Molecular Orbital Theory*. Wiley: New York, 1986.

53. Langreth, D. C.; Perdew, J. P., Exchange-correlation energy of a metallic surface: Wave-vector analysis. *Phys. Rev. B* **1977,** *15*, 2884-2901, https://doi.org/10.1103/PhysRevB.15.2884.

54. Langreth, D. C.; Perdew, J. P., The exchange-correlation energy of a metallic surface. *Solid State Commun.* **1975,** *17*, 1425-1429, https://doi.org/https://doi.org/10.1016/0038-1098(75)90618-3.

55. Furche, F.; Van Voorhis, T., Fluctuation-dissipation theorem density-functional theory. *J. Chem. Phys.* **2005,** *122*, 164106, https://doi.org/10.1063/1.1884112.

56. Tyson, W. R.; Miller, W. A., Surface free energies of solid metals: Estimation from liquid surface tension measurements. *Surf. Sci.* **1977,** *62*, 267-276, https://doi.org/https://doi.org/10.1016/0039-6028(77)90442-3.

57. Olsen, T.; Thygesen, K. S., Accurate Ground-State Energies of Solids and Molecules from Time-Dependent Density-Functional Theory. *Phys. Rev. Lett.* **2014,** *112*, 203001, https://doi.org/10.1103/PhysRevLett.112.203001.

58. Boström, M.; Sernelius, B. E., Fractional van der Waals interaction between thin metallic films. *Phys. Rev. B* **2000,** *61*, 2204-2210, https://doi.org/10.1103/PhysRevB.61.2204.

59. Gould, T.; Simpkins, K.; Dobson, J. F., Theoretical and semiempirical correction to the long-range dispersion power law of stretched graphite. *Phys. Rev. B* **2008,** *77*, 165134, https://doi.org/10.1103/PhysRevB.77.165134.

60. Lebègue, S.; Harl, J.; Gould, T.; Ángyán, J. G.; Kresse, G.; Dobson, J. F., Cohesive Properties and Asymptotics of the Dispersion Interaction in Graphite by the Random Phase Approximation. *Phys. Rev. Lett.* **2010,** *105*, 196401, https://doi.org/10.1103/PhysRevLett.105.196401.

61. Zaremba, E.; Kohn, W., Van der Waals interaction between an atom and a solid surface. *Phys. Rev. B* **1976,** *13*, 2270-2285, https://doi.org/10.1103/PhysRevB.13.2270.

62. Tait, S. L.; Dohnálek, Z.; Campbell, C. T.; Kay, B. D., n-alkanes on MgO(100). I. Coverage-dependent desorption kinetics of n-butane. *J. Chem. Phys.* **2005,** *122*, 164707, https://doi.org/10.1063/1.1883629.

63. Paier, J.; Janesko, B. G.; Henderson, T. M.; Scuseria, G. E.; Grüneis, A.; Kresse, G., Hybrid functionals including random phase approximation correlation and second-order screened exchange. *J. Chem. Phys.* **2010,** *132*, 094103, https://doi.org/10.1063/1.3317437.

64. Silbaugh, T. L.; Campbell, C. T., Energies of Formation Reactions Measured for Adsorbates on Late Transition Metal Surfaces. *J. Phys. Chem. C* **2016,** *120*, 25161-25172, https://doi.org/10.1021/acs.jpcc.6b06154.

Chapter 1: Supplementary Material

S1. Bulk Calculations

Method Details

Primitive fcc unit cells were used for all Pt bulk calculations. The calculations were performed using the projector-augmented wave (PAW) method,[1,2] as implemented in the Vienna ab initio simulation package (VASP).[3] All calculations used an electronic energy threshold of 1×10^{-8} eV and a plane wave energy cut-off, $E_{\text{cut-off}}$, of 500 eV. Calculations used 1st order Methfessel-Paxton smearing with a smearing width of 0.2 eV. Γ-centred *k*-point meshes were used throughout. 16x16x16 *k*-point meshes were used for all calculations on the primitive bulk unit cell.

Bulk Platinum

The Pt bulk was optimised by taking six frozen cell parameters around the observed lattice parameter (three either side and the observed value itself) and then performing a Murnaghan fit.[4] For PBE, two additional points were taken above the observed lattice parameter to improve the symmetry of the plot. This determined the optimised lattice parameter for the primitive fcc cell. Using PBE, we performed this and obtained a lattice parameter of 3.969 Å, close to the literature PBE value of 3.965 Å.[5] PBE overbinds relative to the observed lattice parameter of 3.921 Å (corrected for anharmonic expansion).[6,7] RPA gave a lattice parameter of 3.939 Å, once again close to the literature RPA value of 3.936 Å.[8] Even when using PBE orbitals, RPA can be seen to offer a significant improvement over PBE.

In addition to RPA and PBE,[9,10] the SCAN,[11] PBE0,[12] and HSE06[13] density functionals were used. The optimised lattice constants obtained are compiled in Table S1.1 and the Murnaghan plots are shown in Figure S1.1. In Table S1.1, the observed value has been corrected for the anharmonic expansion, as in Equation 18 of Ref. [14]. The observed bulk modulus B_0 and its first derivative with respect to pressure B_1, a_0, and the Debye temperature Θ_D taken Ref. [15], Ref. [6], and Ref. [16], respectively. We find good comparison to literature, usually within only a few mÅ of the literature calculation.

Table S1.1. Murnaghan fitted lattice constants, a_0 (Å) for different functionals compared to that observed.

Method	This work	Literature
Obsd.[b]	-	3.921[6,7]
PBE	3.969	3.965[5]
PBE0	3.930	3.932[5]
HSE06	3.928	3.927[17]
SCAN	3.899	3.919[18]
RPA	3.939	3.936[8]

[a] $E_{cut\text{-}off}$: 500 eV, 16x16x16 *k*-point mesh.

[b] The observed value has been corrected for the anharmonic expansion removed, following Ref. [14].

Murnaghan equation of state fitted plots for PBE, PBE0, HSE06, SCAN, and RPA, a-e, respectively.

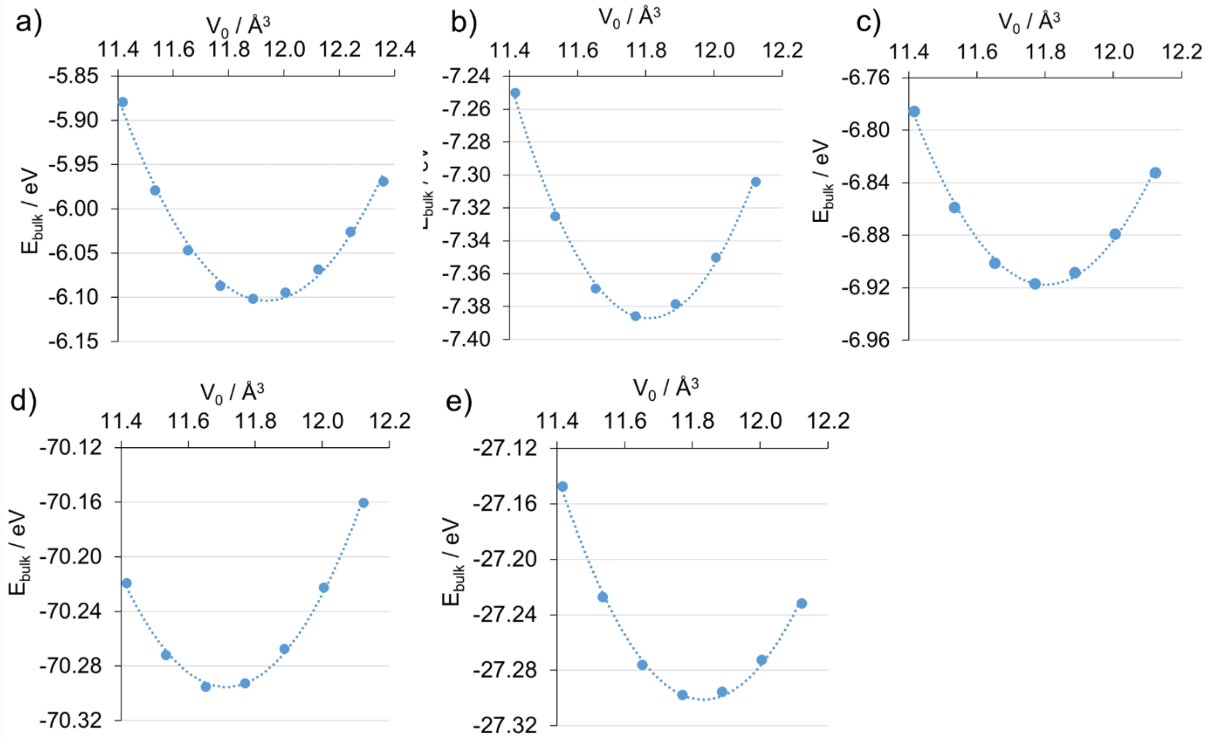

Figure S1.1. Energy of the bulk E_{bulk} against unit cell volume per atom V_0 PBE, PBE0, HSE06, SCAN, and RPA, a-e, respectively. Seven points have been plotted to fit to the Murnaghan equation of state.

S2. DFT Optimisation

The series of different surface cells studied is shown in Figure S2.1.

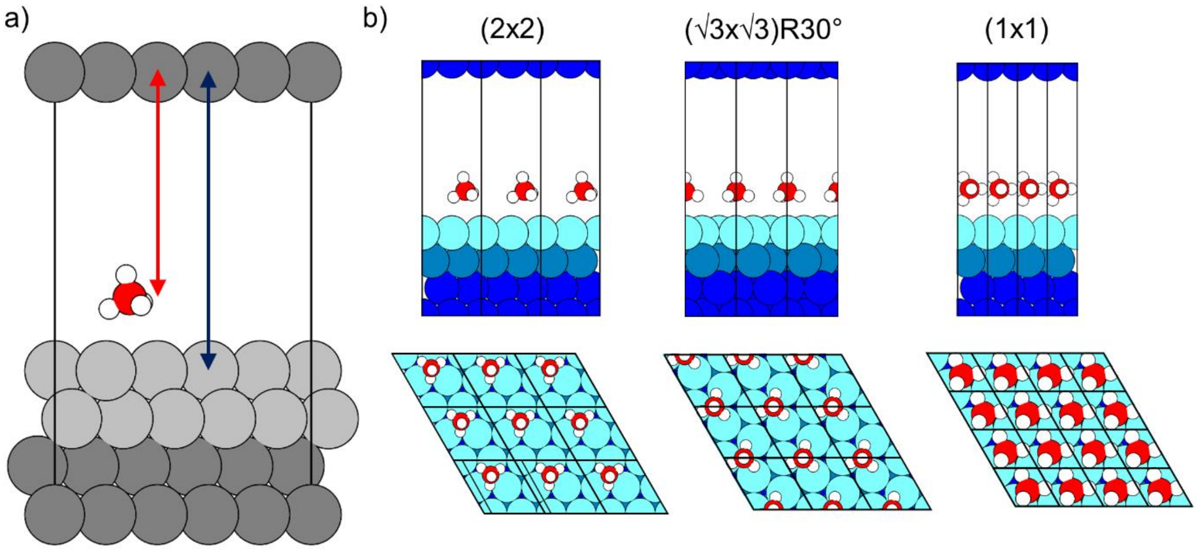

Figure S2.1. a) The vacuum height definition: surface-slab distance (red) and the molecule-slab distance (blue). **b)** Repeated slab model with (2x2), (√3x√3)R30°, and (1x1) supercells used, corresponding to $^1/_4$, $^1/_3$, and 1 ML respectively. The C – C distances are 561, 485, and 280 pm, respectively. The supercells shown contain four layers of Pt atoms.

The key hcp tripod and top monopod, 4-layered, (√3x√3)R30° cell distances are presented in Table S2.1.

Table S2.1. Pt-C and Pt-H distances r(X) (in pm) for PBE+D at the top monopod and hcp tripod adsorption sites. Pt-Pt distances are the same as for Table S2.1. See DFT section for calculation details. These correspond to the structures used in Figure 2 and Table 10.

	r(Pt-C)		r(Pt-H)	
	top monopod	hcp tripod	top monopod	hcp tripod
PBE+dDsC	352	377, 378, 380	241	314, 314, 314
PBE+MBD	353	376, 376, 376	242	311, 312, 312

Table S2.2 presents a breakdown of the PBE+MBD adsorption energy with respect to the lateral interaction for the (1x1), (√3x√3)R30°, and (2x2) cells.

Table S2.2. PBE+MBD adsorption energies, ΔE_{ads}, and lateral interaction energies, ΔE_{lat}, for surface coverages θ = 1, $^{1}/_{3}$, and $^{1}/_{4}$ monolayers. All energies are in kJ mol^{-1}. The distance between the CH_4 molecules, R_{CC} (Å), is also given.[a]

θ / ML	Cell	*k*-points	R_{CC} / Å	ΔE_{ads}	ΔE_{lat}	ΔE_{lat} %
1	(1x1)	6x6	3.97	+130.2	+146.0	112.2
$^{1}/_{3}$	(√3x√3)R30°	6x6	4.85	-16.9	-3.3	19.2
$^{1}/_{4}$	(2x2)	6x6	5.61	-14.7	-1.2	7.9

[a] 4-layered cells with a 400 eV $E_{cut\text{-}off}$ were used.

S3. Surface Energy

The surface energy convergence for (1x1) cells of Pt(111) with respect to *k*-points and $E_{cut\text{-}off}$ are shown in Tables S3.1 and S3.2, respectively. Table S3.2 also contains comparison to a (√3x√3)R30° cell.

Table S3.1. Surface energy γ_{surf} for a 3-layered (1x1) cell using different *k*-point meshes.[a] The linear *k*-point density and the k-point spacing (in reciprocal space) are also shown.

			γ_{surf} / J m^{-2}	
k-points	*k*-density / Å^{-1}	*k*-spacing / Å^{-1}	PBE	RPA
4x4	1.426	0.089	1.01	0.91
6x6	2.140	0.059	1.46	1.75
8x8	2.853	0.045	1.61	2.02
10x10	3.566	0.036	1.56	2.03

[a] A 500 eV $E_{cut\text{-}off}$ and a 10.3 Å vacuum height were used.

Table S3.2. Surface energy γ_{surf} / J m^{-2} as function of the $E_{cut\text{-}off}$ / eV for a 3-layered (1x1) and (√3x√3)R30° cells.[a]

	(1x1) cell[a]		(√3x√3)R30° cell[b]	
$E_{cut\text{-}off}$	PBE	RPA	PBE	RPA
400	1.60	2.02	1.50	1.67
500	1.61	2.02	1.50	1.68
600	1.60	2.03	1.50	1.68

[a] 8x8 *k*-point mesh and a 10.0 Å vacuum height; [b] 4x4 *k*-point mesh; and a 10.3 Å vacuum height.

S4. CH_4 Atomisation Energies

The so-called "hard" pseudopotentials were used here. Three partial waves were used for each orbital, with cut-off radii of 1.0 and 1.1 au for the 2s and 2p states of carbon, respectively. For the 1s orbital of hydrogen, a partial wave cut-off radius of 0.8 au was used. A $E_{cut\text{-}off}$ of 1000 eV was used and the non-spherical contributions to the exchange-correlation potential in the PAW spheres was included. Spin-polarised calculations were performed for the carbon and hydrogen atoms. Due to C and H atoms being open-shell, orthorhombic cells were used for RPA correlation calculations.

The Hartree-Fock, using PBE orbitals, energy E_{HF} was extrapolated for the three different species with respect to the inverse cell volume. The energies are given in Table S4.1 and the extrapolations are shown in Figure S4.1. Large cubic cells were required to perform these extrapolations, so the open-shell occupancies were fixed for the PBE and HF calculations, while this is not an option for RPA.

Table S4.1. Hartree-Fock, using PBE orbitals, energies E_{HF} for C, H, and CH_4 in cubic cells with given volume, V. Extrapolation of E_{HF} for each species was done against V^{-1} and the extrapolated values are given at the bottom of the table. These extrapolations are shown in Figure S4.1 below.[a]

V / Å^3	E_{HF} / eV		
	C	H	CH_4
216	-10.30929	-3.70241	-
343	-10.17190	-3.64417	-
512	-10.08911	-3.61634	-
729	-10.03769	-3.60031	-38.59606
1000	-10.00408	-3.59016	-38.53461
1331	-9.981707	-3.58338	-38.49346
1728	-	-	-38.46487
2744	-	-	-38.42937
Extrapolated	-9.92109	-3.55853	-38.36911

[a] A 1000 eV $E_{cut\text{-}off}$ was used.

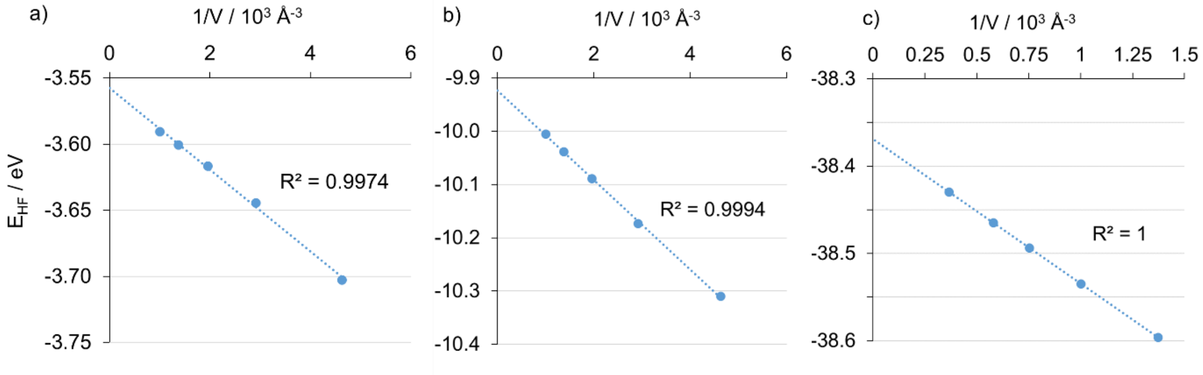

Figure S4.1. Extrapolation of E_{HF} against the reciprocal volume for H, C, and CH_4 (a, b, and c, respectively).

The RPA correlation energy E_{corr} for each species is shown in Table S4.2, with the energy difference ΔE_{corr} extrapolated against the inverse volume squared V^{-2} to give a value of -3.37223 eV, as shown in Figure S4.2. *N.B.* in contrast to the Hartree-Fock energy, extrapolation was done against correlation energy *differences* and not the correlation energy itself, as in Ref. [19].

Table S4.2. RPA correlation energies E_{corr} in eV for orthorhombic cells. The dimensions and the volume of the cell are given in each case.[a]

		E_{corr} / eV		
Cell	Volume / Å^3	C	H	CH_4
5.0x5.5x6.0	125.000	-5.27844	-0.57382	-11.02706
5.5x6.0x6.5	166.375	-5.28799	-0.57354	-10.99842
6.0x6.5x7.0	216.000	-5.29288	-0.57316	-10.98584
6.5x7.0x7.5	274.625	-5.29537	-0.57287	-10.98009

[a] A 1000 eV $E_{cut\text{-}off}$ was used.

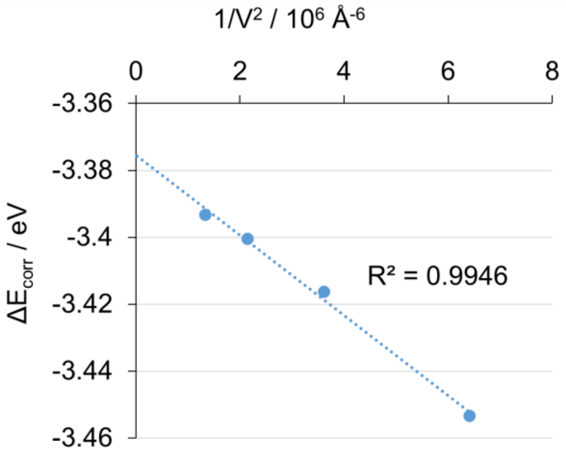

Figure S4.2. Correlation energy difference against inverse volume squared.

The atomisation energy ΔE_{atom} for methane extrapolated to infinite volume is shown in Table S4.3, along with its constituent parts. The atomisation energy being the difference between the

Table S4.3. The Hartree-Fock energy, using PBE orbitals, E_{HF} is given for each of the species. The RPA correlation energy difference ΔE_{corr} is also given (i.e. the RPA correlation energy contribution to the atomisation energy), as well as the atomisation energy ΔE_{atom} between CH_4 and its constituent atoms. All energies in eV, except for ΔE_{atom} in eV and kJ mol^{-1}. All values are for the extrapolated infinite-volume limit.

C	H	CH_4		CH_4 – 4H - C	
E_{HF} / eV			ΔE_{corr} / eV	ΔE_{atom} / eV	ΔE_{atom} / kJ mol^{-1}
-9.92109	-3.55853	-38.36911	-3.37223	-17.58611	-1696.79583

S5. Isolated Methane

For calculating the adsorption energy, the energy of an isolated CH_4 molecule is required. To test the accuracy of the RPA calculations, the bond dissociation energy of the CH_4 molecule with respect to separate atoms, *i.e*. the atomisation energy, was computed at the PBE+MBD structure. The RPA results use supercell volume, V_{cell}, extrapolations for the Hartree-Fock energy E_{HF} ("$1/V_{cell}$") and the RPA correlation energy difference contribution ("$1/V_{cell}^2$"). We found an atomisation energy of -1697 kJ mol^{-1}, see S4 for the extrapolations, comparable to those obtained by atom-centred Gaussian-type basis sets -1693 kJ mol^{-1} (see supplementary material of Ref. [20]). This shows that close agreement between plane wave and pseudopotential and Gaussian basis sets can be achieved if both are converged with respect to computational parameters. The remaining difference can be attributed to the extrapolation procedure.

For the total energy of CH_4 supercell volume extrapolation has been done for the Hartree-Fock energy. The correlation energy was not extrapolated ("$1/V_{cell}^2$"), as no linear relationship was seen, in contrast to the atomisation energy.[19] Instead, the correlation energy of the largest affordable cell (10x10x10 Å^3) was used. Correlation energy differences showed a linear relationship with $1/V^2$ for atomisation energies but we did not see this for the surface, so we did not extrapolate.

E_{HF} and E_{corr} values with extrapolated E_{HF} for $E_{cut\text{-}off}$ of 400, 500, and 600 eV in Tables S5.1, S5.2, and S5.3, respectively. All are for cubic supercells.

Table S5.1. E_{HF} energy and E_{corr} for difference cells for methane with a 400 eV $E_{cut\text{-}off}$.[a]

Volume / Å^3	E_{HF} / eV	E_{corr} / eV
125.000	-	-10.89867
166.375	-	-10.88015
216.000	-	-10.83767
274.625	-	-10.83777
343.000	-	-10.81775
1000.000	-40.39765	-10.81913
1728.000	-40.33688	-
2744.000	-40.30152	-
4096.000	-40.27782	-
Extrapolated	-40.24285	-

[d] For limitations of 400 eV, see the main computational section.

Table S5.2. E_{HF} energy and correlation energy E_{corr} for difference cells for methane with a 500 eV $E_{cut\text{-}off}$.

Volume / Å^3	E_{HF} / eV	E_{corr} / eV
125.000	-	-10.95272
166.375	-	-10.87645
216.000	-	-10.86247
274.625	-	-10.84833
343.000	-	-10.84162
1000.000	-40.46711	-10.83787
1728.000	-40.39682	-
2744.000	-40.36192	-
4096.000	-40.34146	-
Extrapolated	-40.30108	-

Table S5.3. E_{HF} energy and correlation energy for difference cells for methane with a 600 eV $E_{cut\text{-}off}$.

Volume / Å^3	E_{HF} / eV	E_{corr} / eV
125.000	-	-10.94330
166.375	-	-10.88700
216.000	-	-10.86078
274.625	-	-10.84634
343.000	-	-10.84518
1000.000	-40.48294	-10.83891
1728.000	-40.41325	-
2744.000	-40.37762	-
4096.000	-40.35761	-
Extrapolated	-40.31720	-

S6. Extrapolation of Adsorption Energy with Respect to the Vacuum Height

The adsorption energy ΔE_{ads} was calculated at various vacuum heights and shown in Figure 3 of the main text. The adsorption energies are presented in Table S6.1.

Table S6.1. RPA adsorption energy ΔE_{ads} with respect to vacuum height R_{vac} and *k*-point mesh.[a] The linear *k*-point density and the k-point spacing (in reciprocal space) are given in $Å^{-1}$, see Eq. (1) and (2) in the main text for their respective definitions.

R_{vac} / Å	ΔE_{ads}	
	k-points	
	4x4	6x6
10.3	-17.1	-17.3
10.8	-	-16.9
11.3	-16.2	-16.6
11.8	-	-16.3
12.3	-15.8	-16.1
13.3	-15.4	-
14.3	-15.2	-

[a] A 3-layered (√3x√3)R30° cell was used with a $E_{cut\text{-}off}$ of 500 eV.

The adsorption energy for the (√3x√3)R30° cell was extrapolated against the reciprocal slab-surface distance to the fourth power R_{vac}^{-4} and the reciprocal molecule-slab distance to the third power R_{CH4}^{-3} (cf. Figure 1a). The slab-surface distance extrapolation for a 4x4 *k*-point mesh is given in Figure 4 of the main text, while the molecule-slab distance is presented in Figure S6.1 below. Figure S6.2 shows the same extrapolations for the 6x6 *k*-point mesh.

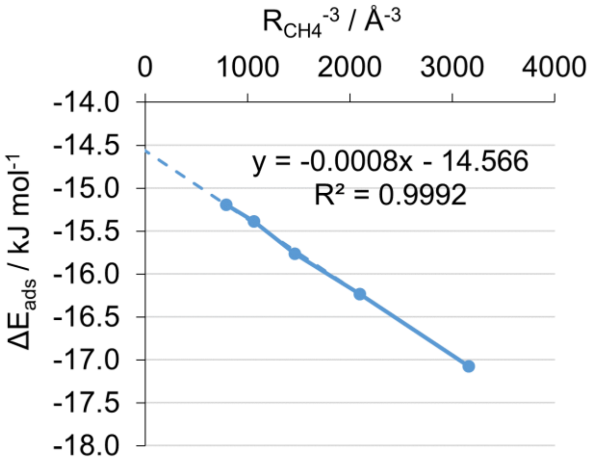

Figure S6.1. Adsorption energy ΔE_{ads} against the reciprocal molecule-slab distance raised to the third power R_{CH4}^{-3} for the (√3x√3)R30° cell with a 4x4 *k*-point mesh.

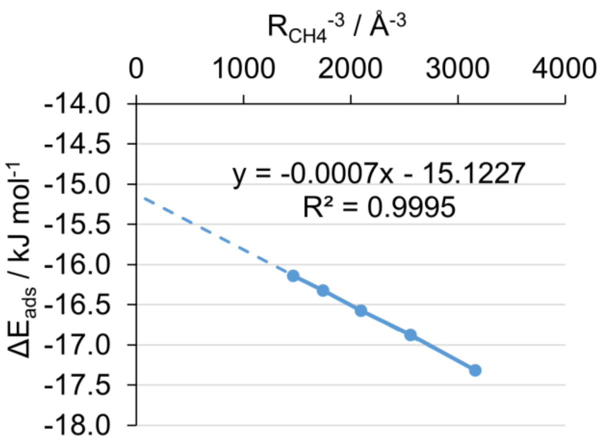

Figure S6.2. Adsorption energy ΔE_{ads} against the reciprocal molecule-slab distance raised to the third power R_{CH4}^{-3} for the (√3x√3)R30° cell with a 6x6 *k*-point mesh.

The adsorption energies in a (2x2) cell have been extrapolated with respect to the vacuum height and molecule-slab distance; this is shown in Table S6.2.

Table S6.2. RPA adsorption energy ΔE_{ads} for a (2x2) cell with respect to surface-slab R_{vac} and molecule-slab distance R_{CH4}, extrapolated to the reciprocal fourth and reciprocal third powers, respectively.[a]

ΔE_{ads} / kJ mol^{-1}	R_{vac} / Å	R_{CH4} / Å
-16.8	10.3	6.8
-16.2	11.3	7.8
-15.8	12.3	8.8
-15.4	13.3	9.8
-15.2	14.3	10.8
Extrapolated ΔE_{ads}	-13.8	-13.9
R^2	0.9966	0.9958

[a] A 3-layered cell and a 500 eV $E_{cut\text{-}off}$ were used.

The adsorption energies for 3- and 4-layered (√3x√3)R30° cells have been extrapolated with respect to the vacuum height and molecule-slab distance; this is shown in Table S6.3.

Table S6.3. RPA adsorption energy ΔE_{ads} for 3- and 4-layered (√3x√3)R30° cells with respect to vacuum height, R_{vac}, and molecule-slab distance, R_{CH4}, extrapolated to the reciprocal fourth and reciprocal third powers, respectively.[a]

3-layered			4-layered		
ΔE_{ads} / kJ mol^{-1}	R_{vac} / Å	R_{CH4} / Å	ΔE_{ads} / kJ mol^{-1}	R_{vac} / Å	R_{CH4} / Å
-17.1	10.3	6.8	-15.9	10.3	6.8
-16.2	11.3	7.8	-14.9	11.3	7.8
-15.8	12.3	8.8	-14.3	12.3	8.8
-15.4	13.3	9.8	-	-	-
-15.2	14.3	10.8	-	-	-
Extrapolated ΔE_{ads}	-14.5	-14.6		-12.8	-13.0
R^2	0.9991	0.9947		0.9998	1.0000

[a] 4x4 *k*-point meshes and a 500 eV $E_{cut\text{-}off}$ were used.

S7. RPA Summary

The RPA adsorption energies and lateral interactions before extrapolation (~10 Å surface-slab distance and equivalent cell for lateral interactions) are presented in Table S7.1, cf. Table 8 for extrapolated results.

Table S7.1. RPA adsorption energy, ΔE_{ads} (kJ mol^{-1}), and the lateral interactions, ΔE_{lat} (in kJ mol^{-1}), for surface coverages θ = $^1/_3$ and $^1/_4$ monolayers.[a]

θ / ML	Cell	*k*-points	ΔE_{ads}	ΔE_{lat}	ΔE_{lat} %
$^1/_3$	(√3x√3)R30°	4x4	-17.1	-4.5	26.3
		6x6	-17.3	-3.0	17.3
$^1/_4$	(2x2)	4x4	-16.8	-2.6	6.5
		6x6	-	-1.5	-

[a] 3-layered cells, a 500 eV $E_{cut\text{-}off}$, and 10.3 Å vacuum heights were used.

S8. Lateral Interactions

The lateral interaction energies in (√3x√3)R30° and (2x2) cells have been extrapolated with respect to the vacuum height and molecule-slab distance; these are shown in Table S8.1 and S8.2.

Table S8.1. HF component $\Delta E_{HF\text{-}lat}$ of the RPA lateral interaction energy ΔE_{lat} for (√3x√3)R30° cell with respect to the distance between molecules R_z, extrapolated to the reciprocal fourth power, and the *k*-point mesh. The correlation energy component $\Delta E_{corr\text{-}lat}$ is also shown, for the sake of reference but only the longest distance was used. All energies are in kJ mol^{-1}.

R_z / Å	4x4		6x6	
	$\Delta E_{HF\text{-}lat}$	$\Delta E_{corr\text{-}lat}$	$\Delta E_{HF\text{-}lat}$	$\Delta E_{corr\text{-}lat}$
14.9	-2.05	-2.47	-0.17	-2.82
15.9	-1.82	-2.51	-0.09	-2.85
16.9	-1.64	-2.56	-0.01	-2.87
17.9	-1.45	-2.59	0.07	-2.88
18.9	-1.34	-2.64	0.14	-2.90
Extrapolated ΔE_{ads}	-0.66	-	0.42	-
R^2	0.9976	-	0.9886	-

[a] A 500 eV $E_{cut\text{-}off}$ were used.

Table S8.2. HF component $\Delta E_{HF\text{-}lat}$ of the RPA lateral interaction energy ΔE_{lat} for (2x2) cell with respect to distance between molecules R_z, extrapolated to the reciprocal fourth power, and the *k*-point mesh. The correlation energy component $\Delta E_{corr\text{-}lat}$ is also shown, for the sake of reference but only the longest distance was used. All energies are in kJ mol^{-1}.

R_z / Å	4x4		6x6	
	$\Delta E_{HF\text{-}lat}$	$\Delta E_{corr\text{-}lat}$	$\Delta E_{HF\text{-}lat}$	$\Delta E_{corr\text{-}lat}$
14.9	-1.91	-0.65	-0.51	-0.94
15.9	-1.73	-0.69	-0.45	-0.98
16.9	-1.58	-0.71	-0.39	-0.99
17.9	-1.45	-0.73	-0.32	-0.99
18.9	-1.37	-0.78	-0.27	-1.01
Extrapolated ΔE_{ads}	-0.85	-	-0.05	-
R^2	0.9987	-	0.9838	-

[a] A 500 eV $E_{cut\text{-}off}$ were used.

References

1. Blöchl, P. E., Projector augmented-wave method. *Phys. Rev. B* **1994,** *50*, 17953, https://doi.org/10.1103/PhysRevB.50.17953.
2. Kresse, G.; Joubert, D., From ultrasoft pseudopotentials to the projector augmented-wave method. *Phys. Rev. B* **1999,** *59*, 1758-1775, https://doi.org/10.1103/PhysRevB.59.1758.

3. Kresse, G.; Furthmuller, J., Efficient iterative schemes for ab initio total-energy calculations using a plane-wave basis set. *Phys. Rev. B* **1996,** *54*, 11169-11186, https://doi.org/10.1103/PhysRevB.54.11169.

4. Murnaghan, F. D., The Compressibility of Media under Extreme Pressures. *Proc. Natl. Acad. Sci. U.S.A.* **1944,** *30*, 244, https://doi.org/10.1073/pnas.30.9.244.

5. Stroppa, A.; Termentzidis, K.; Paier, J.; Kresse, G.; Hafner, J., CO adsorption on metal surfaces: A hybrid functional study with plane-wave basis set. *Phys. Rev. B* **2007,** *76*, 195440, https://doi.org/10.1103/PhysRevB.76.195440.

6. Swanson, H. E.; Tagte, E., Standard X-ray Diffraction Powder Patterns. *Natl. Bur. Stand. U.S. Circ.* **1953,** *539*, 1, https://doi.org/https://doi:10.6028/NBS.CIRC.539v1.

7. Ozoliņš, V.; Körling, M., Full-potential calculations using the generalized gradient approximation: Structural properties of transition metals. *Phys. Rev. B* **1993,** *48*, 18304-18307, https://doi.org/10.1103/PhysRevB.48.18304.

8. Schimka, L.; Gaudoin, R.; Klimeš, J.; Marsman, M.; Kresse, G., Lattice constants and cohesive energies of alkali, alkaline-earth, and transition metals: Random phase approximation and density functional theory results. *Phys. Rev. B* **2013,** *87*, 214102, https://doi.org/10.1103/PhysRevB.87.214102.

9. Perdew, J. P.; Burke, K.; Ernzerhof, M., (PBE) Generalized Gradient Approximation made simple. *Phys. Rev. Lett.* **1996,** *77*, 3865-3868, https://doi.org/10.1103/PhysRevLett.77.3865.

10. Perdew, J. P.; Burke, K.; Ernzerhof, M., Erratum. *Phys. Rev. Lett.* **1997,** *78*, 1396, https://doi.org/10.1103/PhysRevLett.78.1396.

11. Sun, J.; Ruzsinszky, A.; Perdew, J. P., Strongly Constrained and Appropriately Normed Semilocal Density Functional. *Phys. Rev. Lett.* **2015,** *115*, 036402, https://doi.org/10.1103/PhysRevLett.115.036402.

12. Perdew, J. P.; Ernzerhof, M.; Burke, K., Rationale for mixing exact exchange with density functional approximations. *J. Chem. Phys.* **1996,** *105*, 9982-9985, https://doi.org/10.1063/1.472933.

13. Krukau, A. V.; Vydrov, O. A.; Izmaylov, A. F.; Scuseria, G. E., Influence of the exchange screening parameter on the performance of screened hybrid functionals. *J. Chem. Phys.* **2006,** *125*, 224106, https://doi.org/10.1063/1.2404663.

14. Staroverov, V. N.; Scuseria, G. E.; Tao, J.; Perdew, J. P., Tests of a ladder of density functionals for bulk solids and surfaces. *Phys. Rev. B* **2004,** *69*, 075102, https://doi.org/10.1103/PhysRevB.69.075102.

15. Dewaele, A.; Loubeyre, P.; Mezouar, M., Equations of state of six metals above 94 GPa. *Phys. Rev. B* **2004,** *70*, 094112, https://doi.org/10.1103/PhysRevB.70.094112.

16. Berg, W. T., The low temperature heat capacity of platinum. *J. Phys. Chem. Solids* **1969,** *30*, 69-72, https://doi.org/https://doi.org/10.1016/0022-3697(69)90340-0.

17. Janthon, P.; Luo, S.; Kozlov, S. M.; Viñes, F.; Limtrakul, J.; Truhlar, D. G.; Illas, F., Bulk Properties of Transition Metals: A Challenge for the Design of Universal Density Functionals. *J. Chem. Theory Comput.* **2014,** *10*, 3832-3839, https://doi.org/10.1021/ct500532v.

18. Patra, A.; Bates, J. E.; Sun, J.; Perdew, J. P., Properties of real metallic surfaces: Effects of density functional semilocality and van der Waals nonlocality. *Proc. Natl. Acad. Sci. U.S.A.* **2017,** *114*, E9188, https://doi.org/10.1073/pnas.1713320114.

19. Harl, J.; Kresse, G., Cohesive energy curves for noble gas solids calculated by adiabatic connection fluctuation-dissipation theory. *Phys. Rev. B* **2008,** *77*, 045136, https://doi.org/10.1103/PhysRevB.77.045136.

20. Paier, J.; Janesko, B. G.; Henderson, T. M.; Scuseria, G. E.; Grüneis, A.; Kresse, G., Hybrid functionals including random phase approximation correlation and second-order screened exchange. *J. Chem. Phys.* **2010,** *132*, 094103, https://doi.org/10.1063/1.3317437.

Chapter 2

Hybrid RPA and DFT: Embedding for Adsorption on Pt(111)

This chapter is intended for publication.

Authors: Christopher Sheldon, Joachim Paier, Denis Usvyat, and Joachim Sauer

Chapter 2: Hybrid RPA and DFT: Embedding for Adsorption on Pt(111)

The hybrid QM:QM approach is extended to metal surfaces via the application of metal clusters. The Random Phase Approximation (RPA) is used as a high-level method and combines with density functional theory both with and without dispersion corrections (PBE(+D)) as a low-level method. RPA:PBE(+D) is applied to methane, ethane, and CO adsorption on the Pt(111) surface. Experimental adsorption energies at physically meaningful coverages are compared to calculated values and quantitatively reproduce experiment for methane and ethane, while qualitative prediction of the top-site is shown with CO. Calculated hybrid RPA:PBE for methane show agreement with periodic RPA at equilibrium (RPA:PBE – -14.3 kJ mol^{-1}; RPA – -13.8 kJ mol^{-1}) at significantly reduced computational cost. Final adsorption energies for RPA:PBE (CH_4 – -14.3 kJ mol^{-1}; C_2H_6 – -17.8 kJ mol^{-1}) indicate a slight underbinding relative to experiment (CH_4 – -15.6 kJ mol^{-1}; C_2H_6 – -27.2 kJ mol^{-1}), while RPA:PBE+MBD matches experiment well (CH_4 – -16.0 kJ mol^{-1}; C_2H_6 – -24.9 kJ mol^{-1}). Experimental energies are derived from measured desorption energies of activation and corrected for zero point vibrational energy (ZPVE) and thermal enthalpic contributions.

1. Introduction

Modelling chemical reaction from first principles is a chief goal of quantum chemistry. This can be a challenge for some of the most useful reactions in the chemical industry, e.g. those on metal surfaces. Such heterogeneous catalytic reactions occur at the surface, the interface between the solid and gas phase. Good methods exist for both of these but the space where they meet remains elusive. For solids, Density Functional Theory (DFT) well describes solids, in particular the bulk metal. Generally, DFT offers a reasonable description of many properties at low cost, while wave function methods offer a better description but at an increased cost. This is particularly acute for periodic systems, where the cost of wave function methods is so prohibitive that only a few special cases exist.[1] This limits the accuracy and, therefore, the reliability of results in the solid phases.

A solution arises in the form of a hybrid approach, however, where the efficiency of DFT can be applied to the whole system, and a subset taken of the surface in the form of a cluster to which higher level methods may be applied. This is known as hybrid QM:QM and has been successfully applied to many periodic systems.[2,3] This offers an improved description at relatively low cost, with MP2:DFT offering equivalent accuracy as periodic MP2 but with a 3 order magnitude reduction in cost.[4,5] Such “mechanical” embedding may be readily applied to covalent systems or those containing only a few heavier atoms but great difficulty comes as soon as more metal atoms are added, where many spin states may lie close in energy, necessitating even more costly multi-reference methods.

This preclusion of metals is unfortunate, as many important chemical reactions occur on metal surfaces. One exemplar reaction is the reformation process, the dehydrogenation step of which occurs on the Pt(111) surface. To model this, the alkane must first adsorb, chiefly through the dispersion interaction, which is unaccounted for by standard DFT. One way to include this is to apply additive, post-SCF dispersion corrections (+D),[6,7] or to amend the density functional to include them (i.e. vdW-functionals).[8,9] These offer a reasonable description but fail to reach the accuracies required for application to reaction kinetics, which exponentially magnify difference. Generally, chemical accuracy (±4 kJ mol^{-1}) is required for such problems, well beyond the current capability of DFT+D.

We propose using a hybrid QM:QM scheme for metal clusters. This immediately creates problems. Metals have, by definition, a zero-width band-gap, with many close-lying energy levels. For any “finite-order” perturbative method, the correlation energy diverges for zero-width energy gaps.[10,11] However, suitable methods do exist. One such method is the Random Phase Approximation (RPA).[12-15] We have previously applied this method to the study of CH_4 on the Pt(111) surface and successfully obtained chemical accuracy for two, physically relevant, coverages.[16] However, we were limited from studying larger systems due to the computational cost, scaling at $O(N^4)$ with respect to the number of plane waves and $O(N^2)$ with respect to *k*-points.[1,17] Other implementations have similar high costs,[18] though the O(N^3) algorithm is a noteworthy exception.[19]

In this paper, we apply an RPA:DFT+D hybrid scheme to study the adsorption of CH_4 and C_2H_6 on Pt(111), for which reliable experimental data is available.[20] We use this to calculate the Potential Energy Surface (PES) of the hybrid, corrected for Basis Set Superposition Error (BSSE). The CH_4/Pt(111) structures are identical to our previous work, allowing us to assess the accuracy of our approach relative to periodic RPA.[16] We also study the adsorption of CO on Pt(111) to test our hybrid method with respect to chemisorption, specifically against the famous "CO/Pt(111) puzzle",[21] which was answered using periodic RPA.[22]

2. Models and Methods

2.1 Hybrid QM:QM calculations with counterpoise correction and complete basis set extrapolation

In our QM:QM hybrid approach, we amend periodic boundary conditions (PBC)[23] using the subtractive scheme.[23-25] The hybrid energy $E_{HL:LL}$(pbc) is:

$$E_{HL:LL}(\mathrm{pbc}) = E_{LL}(\mathrm{pbc}) - E_{LL}(\mathrm{C}) + E_{HL}(\mathrm{C}) \tag{1}$$

where E_{LL}(pbc) is the energy of the periodic system using the low-level method, E_{LL}(C) is the energy of the cluster using a low-level method, and E_{HL}(C) is the energy of the cluster using a high-level method, both using a finite-cluster model. The hybrid energy may be conceived of as a high-level correction Δ_{HL}(C) to the energy of the periodic system using a low-level method low-level:

$$E_{HL:LL}(\mathrm{pbc}) = E_{LL}(\mathrm{pbc}) + \Delta_{HL}(\mathrm{C}) = E_{HL}(\mathrm{C}) + \Delta_{LR}(\mathrm{pbc, C}) \tag{2}$$

$$\Delta_{HL}(\mathrm{C}) = E_{HL}(\mathrm{C}) - E_{LL}(\mathrm{C}) \tag{3}$$

Alternatively, but entirely equivalently, the hybrid energy may be conceived of as a long-range correction Δ_{LR}(C) to the energy of the cluster using a high-level method:

$$\Delta_{LR}(\mathrm{pbc, C}) = E_{LL}(\mathrm{pbc}) - E_{LL}(\mathrm{C}) \tag{4}$$

For cluster calculations, and any system using finite basis sets, there will always be the need to correct for the basis set superposition error (BSSE).[26] The interaction energy between two monomers A and B is defined as:

$$\Delta E = E(\mathrm{A{\cdot}B}) - E(\mathrm{A}) - E(\mathrm{B}) \tag{5}$$

We correct for the BSSE by using the Counterpoise Correction (CPC) scheme:[26]

$$\varepsilon = [E(\mathrm{A//A{\cdot}B}) - E(\mathrm{A\{B\}//A{\cdot}B})] - [E(\mathrm{B//A{\cdot}B}) - E(\mathrm{\{A\}B//A{\cdot}B})] \tag{6}$$

where "//" denotes "at the structure of", meaning that the energies of the two monomers are computer at the structure of the A·B complex. The $E(\mathrm{A\{B\}//A{\cdot}B})$ and $E(\mathrm{\{A\}B//A{\cdot}B})$ refer to the A and B monomers, respectively, in the full basis of the A·B complex. The BSSE correction is the obtained by:

$$\Delta E_{\mathrm{CPC}} = \Delta E + \varepsilon \tag{7}$$

2.2 Hybrid QM:QM adsorption energies

The adsorption energy per molecule for an adsorbate layer of N molecules per unit cell is defined as:

$$\Delta E = [E(\mathrm{M}_N{\cdot}\mathrm{S}) - E(\mathrm{S}) - N{\cdot}E(\mathrm{M})]/\mathrm{N} \tag{8}$$

where $\mathrm{M}_N{\cdot}\mathrm{S}$ is the adsorbate-surface system, S is the bare surface, and M is the molecule in the gas phase, each at their equilibrium structure. The adsorption energy can be divided into the adsorbate-surface interaction ΔE^* and the lateral interactions ΔE_{L}:

$$\Delta E = \Delta E^* + \Delta E_{\mathrm{L}} \tag{9}$$

according to:

$$\Delta E^* = [E(\mathrm{M}_N{\cdot}\mathrm{S}) - E(\mathrm{S}) - E(\mathrm{M}_N//\mathrm{M}_N{\cdot}\mathrm{S})]/\mathrm{N}$$

(10)

and

$$\Delta E_\mathrm{L} = [E(\mathrm{M}_N//\mathrm{M}_N\cdot\mathrm{S}) - E(\mathrm{S}) - N\cdot E(\mathrm{M})]/\mathrm{N} \tag{11}$$

where $E(\mathrm{M}_N//\mathrm{M}_N\cdot\mathrm{S})$ is the energy of the adsorbate layer at the structure of the adsorbate-surface system $\mathrm{M}_N\cdot\mathrm{S}$. With decreasing coverage, the lateral interaction tends towards zero and the adsorption energy is exclusively defined by the adsorbate-surface interaction.

For the energies in Eq. 8-11, the hybrid QM:QM values are computed by applying the QM:QM subtractive scheme of Eq. 1 to each of these equations:

$$\Delta E_\mathrm{HL:LL} = [E_\mathrm{HL:LL}(\mathrm{M}_N\cdot\mathrm{S}) - E_\mathrm{HL:LL}(\mathrm{S}) - N\cdot E_\mathrm{HL:LL}(\mathrm{M})]/\mathrm{N} \tag{12}$$

2.3. Models

Clusters were cut from a PBE+MBD-optimised (2x2) Pt(111) cells. For CH_4/Pt(111), this was a 3-layered cell that we have previously used for studying RPA at $^1/_4$ ML coverage,[16] where one monolayer (ML) is formally defined as one adsorbed molecule per surface Pt atom. For C_2H_6/Pt(111) and CO/Pt(111), these were 4-layered cells. The CO was adsorbed at the top and hcp (hexagonal close-packed) sites. We present images of these in Figure 1, below.

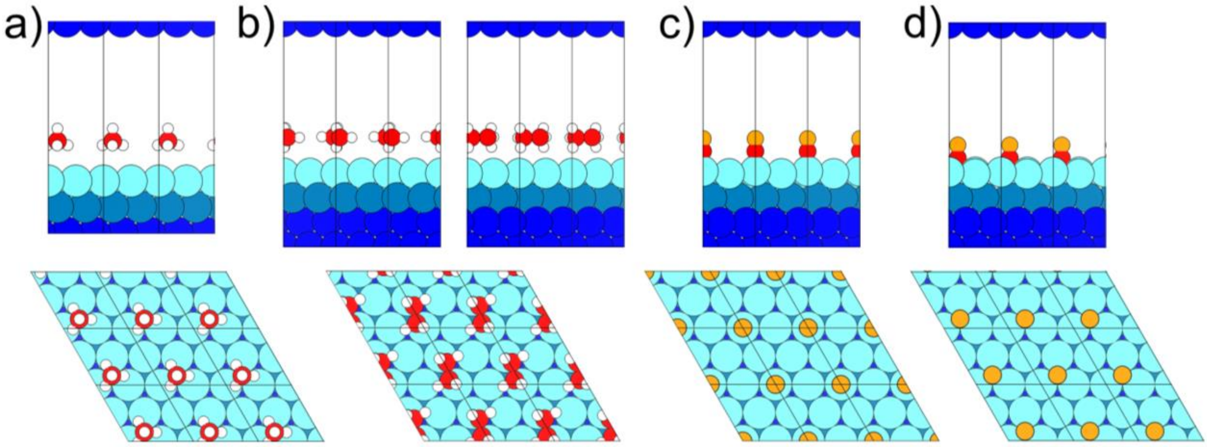

Figure 1. Pt(111) surface ((2x2) cells) with $^1/_4$ ML coverage adsorbate taken from above and below: a) CH_4, b) C_2H_6 (two from above – rotate 90°), c) CO (top site), d) CO (hcp site). Colour code: platinum – blue (light – first layer cluster atoms, turquoise – second layer cluster atoms, dark – third and fourth layer atoms), carbon – red, oxygen – orange, and hydrogen – white.[27]

The Pt_{19} cluster embedded in the Pt(111) surface is shown in Figure 2 (see S1 for all clusters). They are named according to the following convention: Pt_n(A,B,…), where n is the number of platinum atoms in the cluster, A is the number in the top layer of the cluster, B is the number in the second layer, and so on. The same structures were used for calculations both with and without periodic boundary conditions (non-PBC). For those with PBC, these were placed in 20^3 $Å^3$ cubic cells, which was found to be sufficiently large to avoid image interaction (cf. S2.1 for testing of cell size). Likewise, isolated, gaseous alkane molecules were modelled using identical cells (20^3 $Å^3$). All periodic calculations use a 14 Å vacuum height (i.e. the distance between the slab surface and the repeated image).

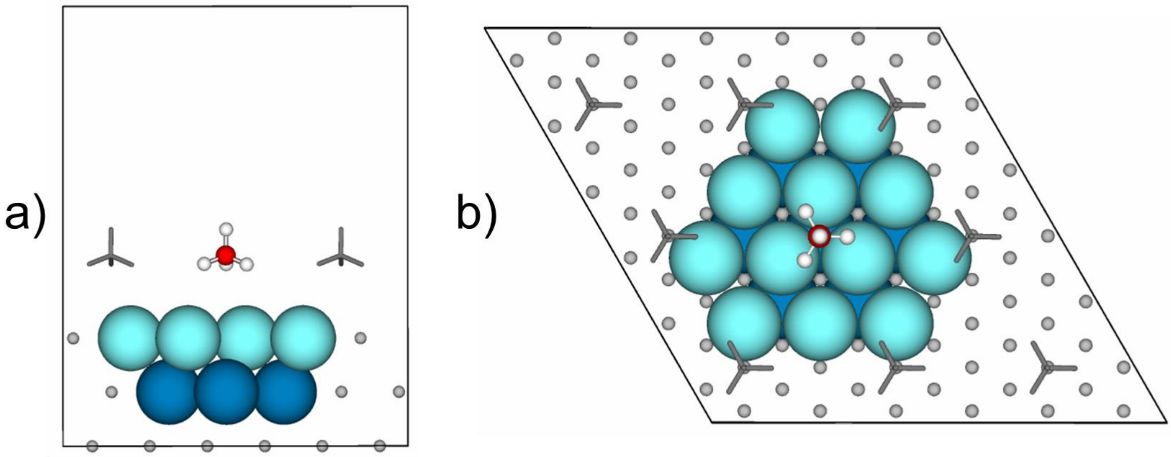

Figure 2. CH_4/Pt_{19}(12,7) cluster embedded in the Pt(111) surface at $^1/_4$ ML coverage viewed from the side (a) and above (b). Colour code: platinum – light blue (first layer) and turquoise (second layer); carbon – red; hydrogen – white.[28]

3. Computational Details

3.1 VASP

3.1.1 DFT

Plane wave DFT calculations were performed using the projector-augmented wave (PAW) method,[29,30] as implemented in the Vienna ab initio simulation package (VASP).[31] The PAW pseudopotential used to describe the electron-ion interaction for Pt includes the 4f electrons resulting in 10 valence electrons: $[Xe,4f^{14}]5d^{9}6s^{1}$. Two partial waves were used for each orbital and their cut-off radius was 2.5 au for both the 5d and 6s states. For C, 4 valence electrons ($[He]2s^{2}2p^{2}$) were considered. The partial wave cut-off radii were 1.2 and 1.5 au for 2s and 2p, respectively. For O, 6 valence electrons ($[He]2s^{2}2p^{4}$) were considered. The partial wave cut-off radii were 1.2 and 1.52 au for 2s and 2p, respectively. For the 1s orbital of H, a partial wave cut-off radius of 1.1 au was used. These pseudopotentials were used for all structural optimisations.

An electronic energy threshold of $1x10^{-6}$ eV, a 6x6x1 *k*-point mesh, and a plane wave energy cut-off, $E_{cut-off}$, of 400 eV were applied. Calculations involving Pt used 1st order Methfessel-Paxton smearing with a smearing width of 0.2 eV, while those on isolated alkanes used Gaussian smearing with a smearing width of 0.05 eV. For the isolated alkanes and clusters, only the Γ-point was sampled. To enable more direct comparison with Gaussian basis set calculations, spin-polarised calculations were performed (N.B. the difference with non-spin-polarised is generally less than 0.1 kJ mol^{-1} and at most 0.4 kJ mol^{-1} for $Pt_{27,19,12}$, cf. Table S2.2).

Structure optimisations, were performed until all forces on relaxed atoms were converged to below 0.01 eV $Å^{-1}$ (0.194 mE_h $bohr^{-1}$). The conjugate gradient method was used with cell shape and volume kept constant.

The PBE[32,33] density functional was used throughout with dispersion corrections D denoted by PBE+D. The Grimme D2[34] and D3,[6] Tkatchenko-Scheffler's Many-Body Dispersion (MBD),[35] and Steinmann-Corminbouef's dDsC[36,37] dispersion corrections were used.

3.1.2 RPA

The periodic RPA calculations (CH_4/Pt(111)) were performed according to Ref. [16] using the projector-augmented wave (PAW) method,[29,30] as implemented in the Vienna ab initio simulation package (VASP).[31] All calculations used an electronic energy threshold of $1x10^{-8}$ eV and a $E_{cut-off}$ of 500 eV. Calculations involving Pt used 1st order Methfessel-Paxton smearing with a smearing width of 0.2 eV, while those on isolated alkanes used Gaussian smearing with a smearing width of 0.05 eV.

For RPA, *GW* PAW pseudopotentials[38] were used with identical core and valence definitions as the above but improved scattering properties for unoccupied states (PBE cores, as in VASP 5.4). For Pt, the partial wave cut-off radii were 2.4 au for both the 5d and 6s states. For C, the partial wave cut-off radii were 1.2 and 1.5 au for 2s and 2p, respectively. For the 1s orbital of H, a cut-off radius of 0.95 au was used. A frequency integration grid density containing 18 and 12 points were used for Pt and isolated CH_4 calculations, respectively. For greater details of RPA, see Ref. [16].

3.2 TURBOMOLE

3.2.1 DFT

DFT calculations were performed using the resolution of identity (RI)-DFT module[39,40] available in 7.3.1 version of the TURBOMOLE program.[41] Additionally, Effective Core Potentials (def2-ECPs) were used for the core 60 electrons of platinum.[42] For C, H, and Pt atoms, def2-QZVPP basis sets were used, with the corresponding auxiliary bases.[42-44]

Energies were converged to within 10^{-7} Ha. Virtual orbitals were shifted by 0.4 eV and heavy damping was applied to aid SCF convergence.

3.2.2 RPA

RPA using orbitals from the aforementioned DFT calculations were performed using the resolution of identity (RI)-RPA module.[45,46] The "frozen-core" approximation was applied, with orbitals below 2 Ha considered to be core. (RI)-MP2 and (RI)-CC def2-QZVPP auxiliary, correlation basis sets[42] were used, as recommended in the literature.[47,48] Counterpoise corrections (CPC) were performed on all cluster calculations.[26] The number of integration points necessary for calculating the RPA correlation energy depended on the cluster size; 100 and 220 integrations points were required to achieve 0.1 kJ mol^{-1} convergence in adsorption energy for Pt_{19} and Pt_{28}, respectively. Additionally, the DFT orbitals were used to obtain their corresponding Hartree-Fock energy, performing a single elementary step, as implemented in the dscf module.[49]

4. Results and Discussion

4.1 Clusters under PBC

We investigated the adsorption energy with respect to cluster size and different dispersion corrections. We found it useful to split this into the total adsorption energy and the dispersive contribution, as shown in Figure 3a and 3b, respectively.

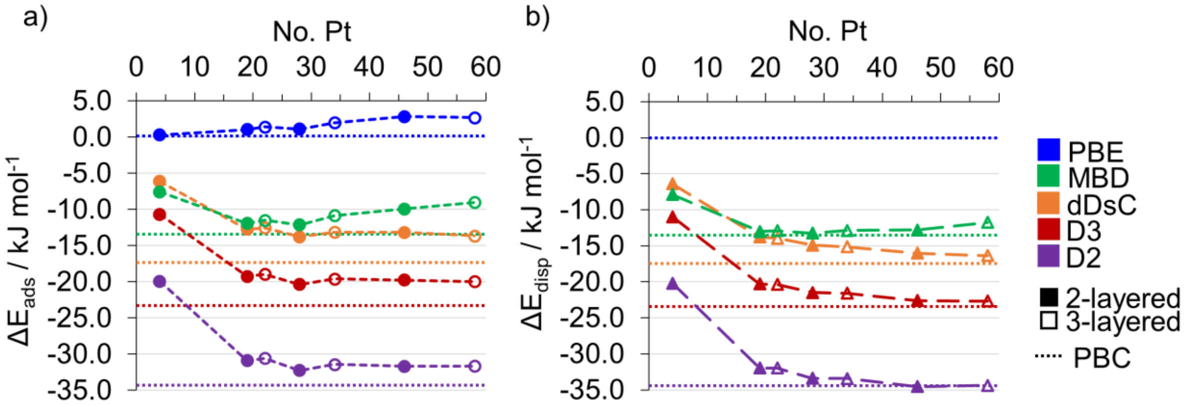

Figure 3. Adsorption energy plots for CH_4 on Pt_n clusters for different sized clusters. a) Circles show the total adsorption energy ΔE_{ads}, while b) triangles show the dispersive component ΔE_{disp}. Full and hollow markers are for 2- and 3-layered clusters, respectively. Periodic values are straight, dashed lines (with lateral interactions removed, cf. Eq. 11). Tabulated values given in Table S2.2 and S2.3.

It is clear from Figure 3a that there is gradual convergence with respect to the total adsorption energy towards the PBC values, regardless of which dispersion correction was used.

However, there is a noticeable dip from the final cluster ($Pt_{27,19,12}$) and the periodic value. Analysis of the PBE adsorption energy sheds some light as to why. Although the binding becomes stronger with cluster size when dispersion is included, the PBE component alone becomes increasingly repulsive. It was expected that properties would approach the bulk with increasing size, so this is somewhat surprising but, given that this is only ~2 kJ mol^{-1}, this is a minor divergence.

To get a better impression of the dispersive contribution, we removed PBE energy and show only the dispersive component in Figure 3b, which is easily done being only a post-SCF calculation. This shows improved convergence, with convergence virtually achieved by Pt_{19} for the MBD and Pt_{28} for the other dispersion corrections. While the final cluster slightly bucks the trend for MBD, we do not consider this to be significant as we will not be using such large clusters for our hybrid calculations.

We can see that there is little difference between the 2- and 3-layered clusters for either the total adsorption energy or for the purely dispersive component. We conclude that there is little to no gain from using 3-layered clusters over 2-layered. There is a far more significant effect from expanding the clusters laterally than vertically. A final point of note is that the adsorption energy of the Pt_4 cluster is far from convergence. This is not surprising as it is far too small to capture most of the dispersion. Nonetheless, it remains a useful first point in the convergence series. Overall, the convergence with respect to cluster size validates the use of clusters for the metal surface, as the periodic value will be matched, if a sufficiently large cluster is used.

We briefly comment on the accuracy of the different dispersion corrections, although we save the main discussion for later. The experimental-derived adsorption energy is -15.5 kJ mol^{-1} at $^{1}/_{4}$ ML coverage,[16] which the dDsC and MBD dispersion corrections approach with PBC adsorption energies of -18.9 and -14.7 kJ mol^{-1} each, respectively. The D2 and D3, however, significantly overbind (at -35.6 and -24.9 kJ mol^{-1} each, respectively), with the D2 functional doing more so and the D3 to a lesser degree. This is well-known in the literature and they are only included for the sake of comparison.[50] We put the success of the dDsC and MBD functionals down to their taking the electron density into account, enabling improved descriptions of the dispersion interaction.

4.2 Hybrid RPA:DFT

4.2.1 Methane

We selected the Pt_{19} cluster in the singlet state for our hybrid scheme (cf. Section S3 for details of PBE and RPA tests), with PBE+D as the low-level method and RPA as the high-level method. We did this according to Eq. 12, and present this breakdown using the Pt_{19} cluster in the singlet state in Table 1. We also tried Pt_{19} in the triplet and Pt_{28} in the quintet states but these did not perform sufficiently well as due to additional repulsion from the surface, see Tables S4.1 and S4.2, respectively.

Table 1. Adsorption energy $\Delta E_{HL:LL,\ CPC}$(pbc) of CH_4/Pt(111) for the hybrid scheme, with RPA as the high-level method and PBE(+D) as the low-level method. The Pt_{19} cluster in the singlet state was used. PBE+MBD optimised structures were used. The platinum-carbon height was 350 pm.

ΔE / kJ mol^{-1}	PBE	PBE+MBD	PBE+dDsC	PBE+D3	PBE+D2
ΔE_{LL}(pbc)	-0.4	-14.7	-18.9	-24.9	-35.9
$\Delta E_{LL,\ CPC}$(C)	0.6	0.6	0.6	0.6	0.6
ΔE_{disp}(C, VASP)	0.0	-13.0	-13.8	-20.3	-31.9
$\Delta E_{LL,\ CPC}$(C) + ΔE_{disp}(C, VASP)	0.6	-12.4	-13.2	-19.7	-31.3
$\Delta E_{HL,\ CPC}$(C)	-12.9	-12.9	-12.9	-12.9	-12.9
$\Delta_{HL,\ CPC}$(C)	-13.5	-0.5	0.3	6.8	18.5
Δ_{LR}(pbc, C)	-1.0	-2.3	-5.7	-5.2	-4.6
$\Delta E_{HL:LL,\ CPC}$(pbc)	-13.8	-15.1	-18.6	-18.1	-17.4
ΔE_{RPA}(pbc)	-12.8[16]				
$\Delta E_{obs.}$	-15.6[16]				

From Table 1, it became clear that the hybrid approach broadly works. We then varied the C-Pt distance r(C-Pt) and calculated the hybrid adsorption energy. These are presented in Figure 4 for HL:LL RPA:PBE+D (D2, +D3, and +dDsC) and tabulated in Table S4.3.

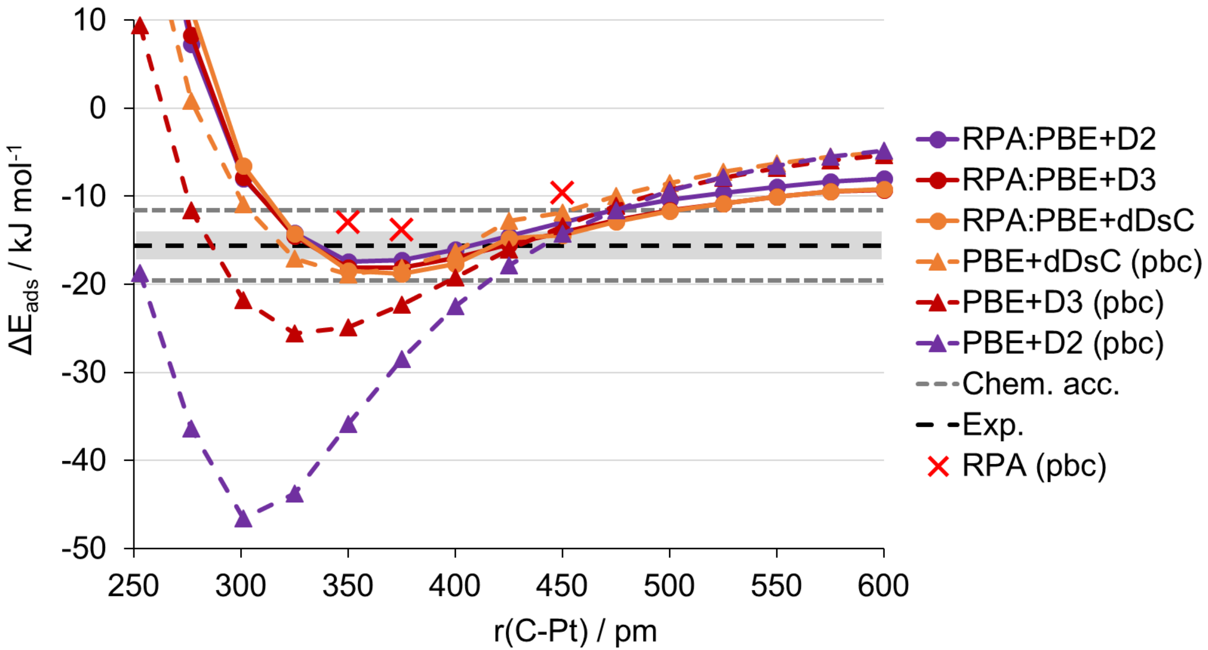

Figure 4. RPA:PBE+D (D2, D3, dDsC) adsorption energy (in kJ mol^{-1}) against Pt-C distance r(C-Pt) in pm for CH_4/Pt(111). Red crosses are periodic RPA values; circles/ full lines are hybrid values; triangles/ dashed lines are periodic values. The experiment is shown by a dashed black line with grey error bars to indicate the range of experimental error; chemical accuracy, ±4 kJ mol^{-1} is shown by dashed darker grey lines. Points are tabulated in Table S4.3.

The hybrid approach gives clear improvement from the base PBE+D approach. For D2 and D3, there is a significant decrease in the strength of adsorption and the overbinding characteristic of most dispersion corrections on metal surfaces disappears.[50] This effect is far small for dDsC, which already performed reasonably for adsorption energy. One thing that is seen for all three, is a lengthening of r(C-Pt). This is most pronounced for D2, where r(C-Pt) increases from ~300 pm to 375 pm, but is still visible for D3 (325 pm to 375 pm) and dDsC (350 pm to 375 pm). The merits of the hybrid approach are clear from these low-level methods, however, we choose to focus on PBE and PBE+MBD as the low-level methods for deeper analysis, as these perform best. We present these in Figure 5.

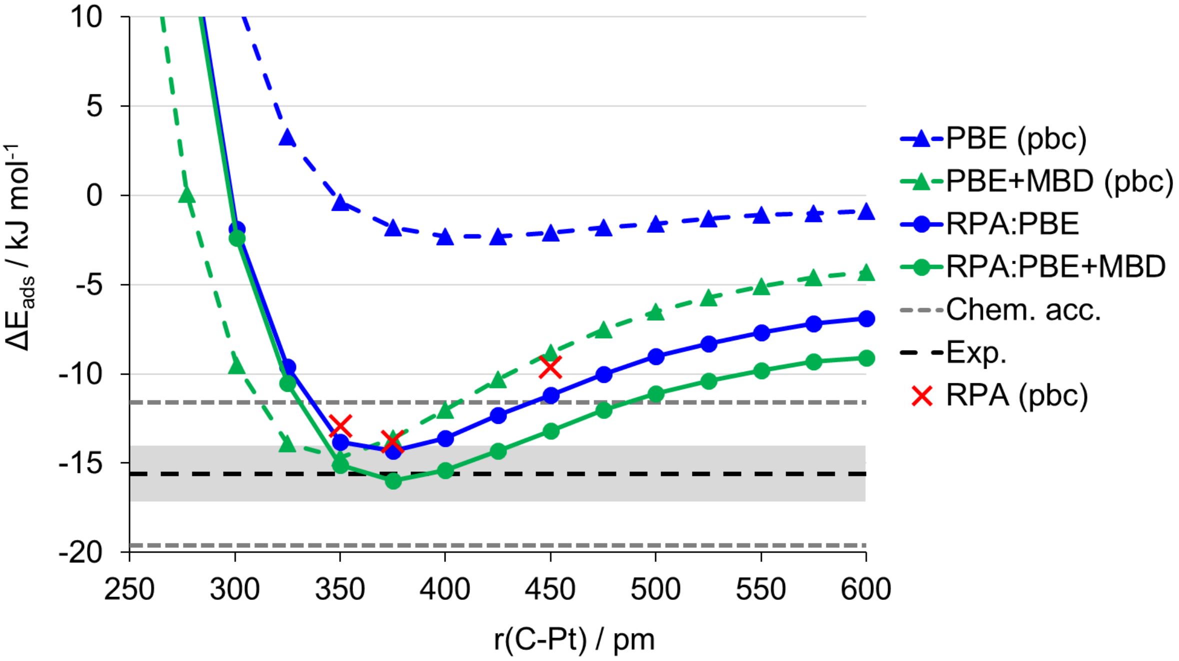

Figure 5. RPA:PBE and RPA:PBE+MBD adsorption energy (in kJ mol^{-1}) against Pt-C distance r(C-Pt) in pm for CH_4/Pt(111). Red crosses are periodic RPA values; circles/ full lines are hybrid values; triangles/ dashed lines are periodic values. The experiment is shown by a dashed black line with grey error bars to indicate the range of experimental error; chemical accuracy, ±4 kJ mol^{-1} is shown by dashed darker grey lines. Points are tabulated in Table S4.3.

It is immediately clear that RPA:PBE introduces dispersion to PBE where there was none before, even to the point of being within the experimental error and well within chemical accuracy. We see that the r(C-Pt) decreases from 400 pm to 375 pm, shifting towards a more reasonable distance. These are clear indicators of the success of the method. Additionally, we see for RPA:PBE+MBD that there is a slight increase in the adsorption strength towards experiment. The r(C-Pt) also increases from 350 pm to 375 pm, matching the RPA:PBE distance, along with the other hybrid methods. On a first analysis, we see that RPA:PBE still underbinds relative to experiment , whereas RPA:PBE+MBD exactly matches experiment. However, this is misleading, as it is better to compare the hybrid directly to the periodic RPA that it is approximating. When we do this, it becomes clear that RPA:PBE offers a better description, with the points around the equilibrium giving virtually identical adsorption energies to the periodic RPA. This indicates that the hybrid approach offers a very good approximation to the high-level method. With a difference of less than 2 kJ mol^{-1} at equilibrium, it is difficult to determine much between the two hybrid methods, beyond that PBE+MBD binds slightly stronger, presumably as, by already accounting for some dispersion, some is already accounted for in addition to that provided by RPA. We present a breakdown of the cluster terms in RPA, PBE, and PBE+MBD contributions in Figure 6 below.

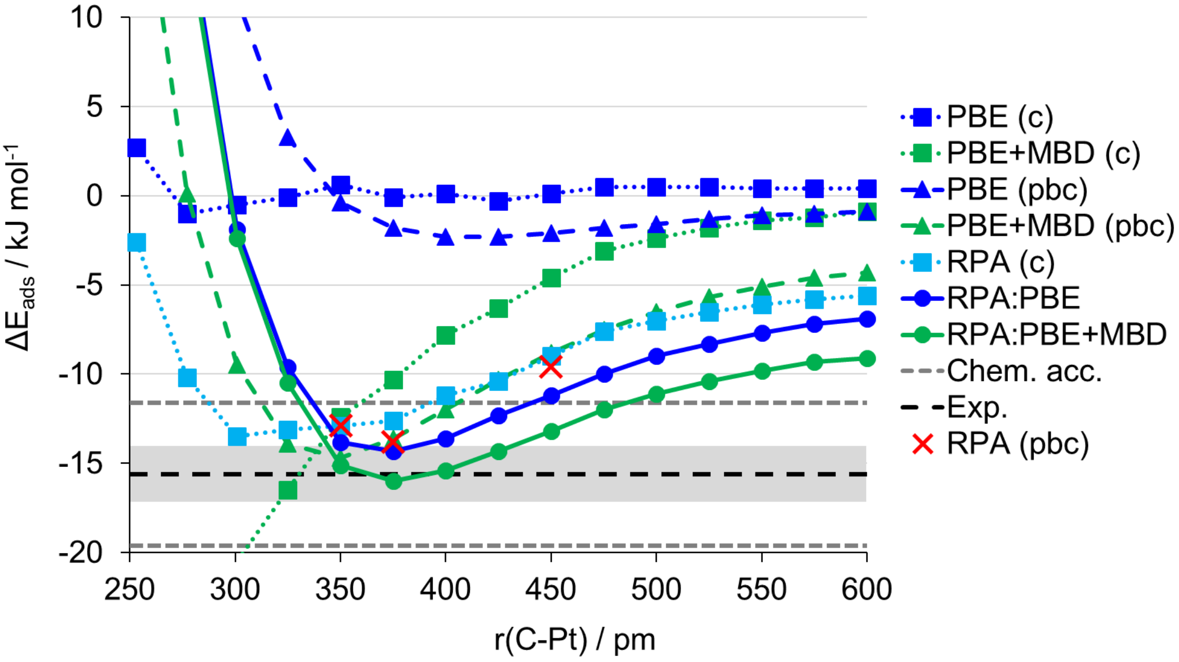

Figure 6. RPA:PBE and RPA:PBE+MBD adsorption energy (in kJ mol^{-1}) against Pt-C distance r(C-Pt) in pm for CH_4/Pt(111), along with breakdown of cluster terms. Red crosses are periodic RPA values; circles/ full lines are hybrid values; triangles/ dashed lines are periodic values; squares are cluster components (c). The experiment is shown by a dashed black line with grey error bars to indicate the range of experimental error; chemical accuracy, ±4 kJ mol^{-1} is shown by dashed darker grey lines. Points are tabulated in Table S4.3.

We can quickly see that the PBE curve for the cluster fails to match that of the periodic value, differing by a few kJ mol^{-1} at long distances and more so at shorter ones. This indicates a limitation of the cluster model to capture the PBE energy. The PBE+MBD cluster component is much stronger and overbinds significantly. It does, however, show a more pronounced minimum at shorter distances than PBE. The cluster is significantly better for RPA, where a repulsive curve is seen at short distances and a more typical tail at longer distances. Particularly encouraging is that the cluster RPA values match very closely to the periodic RPA values, indicating that our cluster model is suitable. In fact, it appears that it is difference between the periodic and cluster PBE that result in differences on the hybrid level of RPA:PBE, not in the RPA term itself. This is extremely encouraging as this similar level of accuracy was obtained at a significantly reduced cost, with each point of the hybrid calculation taking approximately 14 CPU hours, compared to the ~2600 hours per periodic RPA calculation, saving of over a hundred-fold (cf. Table 5). Methane provided a useful case study to test our method. We now apply it to a system where ordinary periodic RPA proved too costly, that of ethane.

4.2.2 Ethane

Having found RPA:PBE and RPA:PBE+MBD to be the better hybrid approaches, we present a breakdown these for ethane on Pt(111) in Table 2.

Table 2. Adsorption energy $\Delta E_{\mathrm{HL:LL,\ CPC}}$(pbc) of C_2H_6/Pt(111) for the RPA:PBE and RPA:PBE+MBD. The Pt_{19} cluster in the singlet state was used. PBE+MBD optimised structures were used. The platinum-carbon height was 335 pm.

ΔE / kJ mol^{-1}	PBE	PBE+MBD
ΔE_{LL}(pbc)	0.3	-34.4
$\Delta E_{\mathrm{LL,\ CPC}}$(C)	-1.8	-1.8
ΔE_{disp}(C, VASP)	0.0	-25.8
$\Delta E_{\mathrm{LL,\ CPC}}$(C) + ΔE_{disp}(C, VASP)	-1.8	-27.6
$\Delta E_{\mathrm{HL,\ CPC}}$(C)	-12.4	-12.4
$\Delta_{\mathrm{HL,\ CPC}}$(C)	-10.5	15.2
Δ_{LR}(pbc, C)	2.1	-6.8
$\Delta E_{\mathrm{HL:LL,\ CPC}}$(pbc)	-10.2	-19.2
$\Delta E_{\mathrm{obs.}}$	-27.2[a]	

[a]Corrected from Tait et al.'s observed activation energy,[20] cf. Table S4.5 for details.

At a first glance, it seems that the reverse trend for methane is seen, with PBE and PBE+MBD performing the worst and D2, D3, and dDsC performing the best. However, on inspecting the r(C-Pt) curves, cf. Figure 7, it becomes clear that RPA:PBE and RPA:PBE+MBD still perform well and it is only a question of distance, with the equilibrium shifting to longer distances (375 pm) distorting the adsorption energy at the PBE+MBD optimised distance (340 pm).

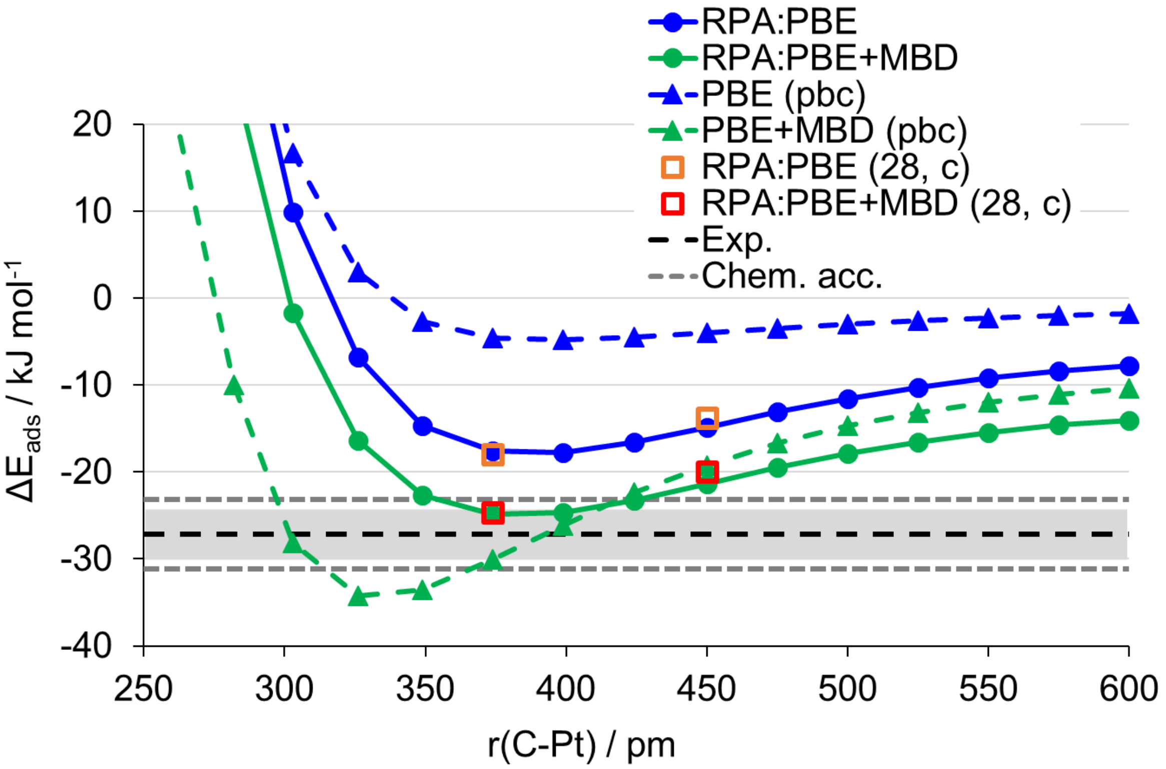

Figure 7. RPA:PBE and RPA:PBE+MBD adsorption energy (in kJ mol^{-1}) against Pt-C distance r(C-Pt) in pm for C_2H_6/Pt(111). Circles/ full lines are hybrid values; triangles/ dashed lines are periodic values; hollow squares use the Pt_{28} cluster in the quintet state. The experiment is shown by a dashed black line with grey error bars to indicate the range of experimental error; chemical accuracy, ±4 kJ mol^{-1} is shown by dashed darker grey lines. Points are tabulated in Table S4.4.

In the periodic case, we see an equivalent picture to methane, with the PBE barely binding, and the PBE+MBD overbinding with respect to experiment. PBE+MBD has a minimum at 340 pm, significantly shorter than PBE at ~400 pm. Once the hybrid approach is applied, they both shift towards a minimum of around 375 pm. Additionally, the overbinding of PBE+MBD and underbinding of PBE are both corrected. The two curves are almost parallel, differing by a near constant ~10 kJ mol^{-1}. Ethane reveals what was suspected for methane, that RPA:PBE underbinds relative to experiment, while RPA:PBE+MBD matches closely. To exposit this discrepancy, we tested the cluster size for RPA by performing the hybrid approach using the Pt_{28} cluster instead. These are shown as squares in Figure 7 and virtually overlap with the two chosen points, indicating that cluster size is not an important factor here, i.e. Pt_{19} is sufficiently large to capture the RPA energy and is suitable for application. Given the closeness of periodic RPA and RPA:PBE seen for methane, this leads us to conclude that RPA underbinds and does not capture the full dispersion interaction. The pre-included dispersion provided from MBD then adds to this to give a value closer to experiment. We feel the need stress here that RPA is more grounded in the physics than MBD and so do not suggest that RPA:PBE+MBD is necessarily superior to RPA, it being an good, additive correction, rather than an ab initio description of the dispersion. We show a breakdown of the cluster components in Figure 8. We have omitted the Pt_{28} terms for clarity, which are given in Table 3.

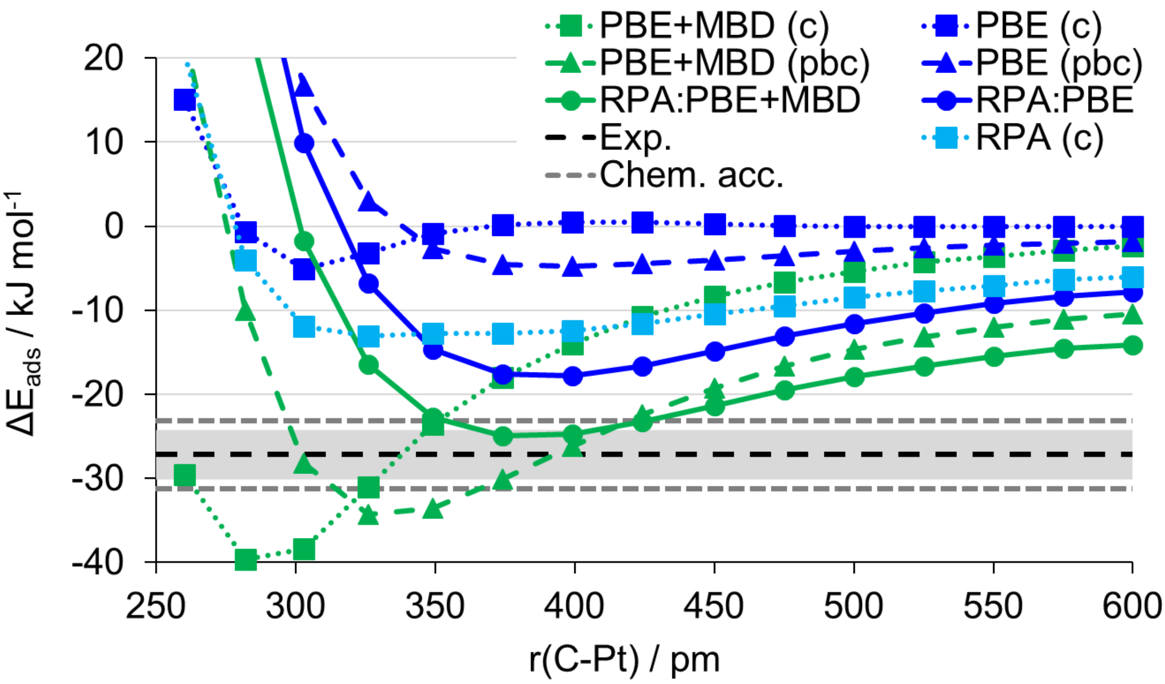

Figure 8. RPA:PBE and RPA:PBE+MBD adsorption energy (in kJ mol^{-1}) against Pt-C distance r(C-Pt) in pm for C_2H_6/Pt(111), along with breakdown of cluster terms. Circles/ full lines are hybrid values; triangles/ dashed lines are periodic values; squares are cluster components (c). The experiment is shown by a dashed black line with grey error bars to indicate the range of experimental error; chemical accuracy, ±4 kJ mol^{-1} is shown by dashed darker grey lines. Points are tabulated in Table S4.4.

We see in Figure 8 that the PBE binds more strongly than methane but, once again, the equilibrium is at significantly shorter distances than the periodic PBE. This implies that this is simply a limitation of the finite cluster approach given that, even with the use of a larger cluster, the energy differences are within a few kJ mol^{-1} (cf. Table 3). The PBE+MBD overbinds significantly in the cluster, as for methane. The RPA component for the cluster is larger than for methane and follows a smooth curve. We expect that the periodic RPA value would lie close to this. At any rate, the correction between high- and low-level proves successful and on breakdown of the terms, we find no indicators otherwise.

Table 3. Breakdown of the adsorption energy $\Delta E_{\text{HL:LL, CPC}}$(pbc) of C_2H_6/Pt(111) for RPA:PBE(+MBD). The Pt_{19} (singlet) and Pt_{28} (quintet) clusters were used. PBE+MBD optimised structures were used.

ΔE / kJ mol^{-1}	r(C-Pt) / pm			
	375		450	
	Pt_{19}	Pt_{28}	Pt_{19}	Pt_{28}
$\Delta E_{\text{PBE, CPC}}$(C)	0.2	2.6	0.3	0.6
$\Delta E_{\text{PBE+MBD, CPC}}$(C)	-18.0	-16.2	-8.4	-8.5
$\Delta E_{\text{RPA, CPC}}$(C)	-12.8	-10.8	-10.5	-9.2
$\Delta E_{\text{RPA:PBE, CPC}}$(pbc)	-17.6	-18.0	-14.9	-13.8
$\Delta E_{\text{RPA:PBE+MBD, CPC}}$(pbc)	-24.9	-24.7	-21.4	-20.0

4.2.3 Carbon Monoxide

We have confirmed our approach to be suitable for the cases where the adsorption is largely through the dispersive interaction. We now take an archetypal example of strong adsorption, that of CO/Pt(111) and apply our method here. We do not test with dispersion as this is dominated by chemisorption, rather than physisorption; we use PBE to optimise structures for this reason. We test the top and hcp sites to determine how our method determines the "CO/Pt(111) puzzle"[21]. We highlight that the BSSE correction is calculated differently here to our previous calculations. We break up the BSSE in terms of binding and relaxation energies, taking the binding energy for the cluster and the relaxation energy for the periodic calculations (cf. Table S4.6). This is due to a slight distortion of the periodic surface on adsorption for the top site, resulting in the top-site platinum protruding slightly from the surface. Platinum clusters, if physically realised and not as models for the surface, are more stable when tending towards the "spherical"[51,52] and so this protrusion results in greater stability for Pt//CO/Pt and destabilises the BSSE. Hence our taking the periodic system's binding energy. We present the results of this for the Pt_{19} (triplet) and Pt_{28} (quintet) clusters in Table 4 below.

Table 4. Breakdown of the adsorption energy $\Delta E_{RPA:PBE,\ CPC}$(pbc) for the top and hcp sites of CO/Pt(111), as well as the energy difference between the two $\Delta E_{top\text{-}hcp}$. Comparison to literature periodic RPA ΔE_{RPA}(pbc) and experiment ΔE_{Exp} are shown. Pt_{19} (triplet) and Pt_{28} (quintet) clusters were used. PBE optimised structures were used.

ΔE / kJ mol^{-1}	Site		$\Delta E_{top\text{-}hcp}$
$\Delta E_{RPA:PBE,\ CPC}$(pbc)	Hcp	top	
Pt_{19}	-76	-152	-76
Pt_{28}	-83	-107	-24
ΔE_{RPA}(pbc)[23]	-119	-126	-7
ΔE_{Exp}[a]	-	-123	-

[a]Single-Crystal Adsorption Calorimetry (SCAC); taken from Ref. [53].

We did not use the singlet state for the Pt_{19} cluster as this was not stable on adsorption of the CO. This indicates to us that the chemisorption of CO results in a significant change of the electronic structure of the cluster. We expect that this would be mitigated by a sufficiently large cluster. This can, in fact, be seen for the top site, where there is a significant jump in adsorption strength once a larger cluster is used. The hcp site is more stable with respect to cluster size, but it is clear that there is significant underbinding using our hybrid approach. We expect that, if a sufficiently large cluster were used, then this would be corrected. We note that this variation with respect to cluster size was not observed for the similar system of CO/Cu(111) by Scheffler and co.,[54] who found that the energy difference between top and hcp sites relative to PBE was stable with respect to cluster size (up to Cu_{27}). Due to our difficulties with correcting for the BSSE, we cannot obtain a direct comparison, so it is not clear to us whether or not we would see a similar convergence with respect to PBE. Through their use of Numeric Atom-Centred Orbitals (NAOs), they avoided such a problem, as well as issues with an incomplete basis set which, though unlikely to be significant due to our use of a large basis, may have an unexpected impact for metals. With so many factors to consider, a one-for-one comparison would be premature at this stage and mere speculative; further study is needed. However, we can safely conclude that our hybrid method works qualitatively by correctly favouring the top site, yet at a significantly reduced computational cost.

4.2.4 Hybrid cost

The hybrid approach has been shown to be successfully in achieving quality comparable to periodic RPA but at lower cost. We compare the computational times in Table 5 for CH_4/Pt(111).

Table 5. CPU times (in hr) for periodic RPA with a 14 Å vacuum (+ with vacuum extrapolation) and RPA:PBE hybrid approach for different clusters/ spin states. All times are for CH_4/Pt(111). RPA (pbc) are from Ref. [16].

Method		Supercell	
		(√3x√3R30°)	(2x2)
RPA (pbc)		245	876
+extrapolation		727	2618
RPA:PBE	Pt_{19} (S)	-	14
	Pt_{19} (T)	-	40
	Pt_{28} (Q)	-	207

We have not presented times for the (√3x√3R30°) supercell but we do not expect these to be very different than those for the (2x2) cell, as the same clusters would be used (excluding minor structural differences). This decrease of cost from 245 hours to ~14 hours would be a comfortable saving alone. An additional benefit is seen in that the cluster calculations effectively already include vacuum extrapolation, so this saving is even greater and in fact amounts to a decrease from 727 hours to 14 hours. The true benefit of this hybrid approach, however, is seen for sparser coverages. Even for a supercell of similar size, the (2x2) cell, the cost for periodic RPA increases by hundreds of CPU hours, to 2618 hours if the vacuum extrapolation is taken into account. Our hybrid approach will remain similar regardless of cell size, enabling the study of sparser cells such as (3x3) and (2√3x2√3R30°), which are too large for the $O(N^4)$ algorithm to study.[17] The low-scaling RPA algorithm $O(N^3)$ algorithm is capable of studying these cells but requires many CPUs and high memory requirements.[19,55] This makes it particularly suitable for High Performance Computing (HPCs). Our approach, on the other hand, is more applicable to the computer clusters available in the typical group, with there being likely little benefit from using HPC facilities. We envisage that the hybrid approach for metals will be useful in applying post-HF methods to metallic systems where such methods are restricted. Post-HF methods have already been applied to metal clusters, where the HOMO-LUMO gap is small but non-zero.[56-62] We do not expect that this is a distant future, having already performed some preliminary Coupled Cluster (CC) calculations in this direction.

5. Conclusions

We have shown that a divide-and-conquer mechanical embedding scheme is appropriate to be applied to platinum clusters. There is difficulty in finding suitable clusters and this will need to be addressed in the future to make the hybrid method more broadly applicable. We have found that relatively small clusters are suitable for studying dispersive adsorption on the platinum surface for methane and ethane. This approximates the periodic RPA result at significantly reduced cost. This has enabled us to study the Pt-C distance and the cases of methane and ethane strongly indicate that the distance is underestimated by current dispersion corrections relative to RPA. Confirmation of this would require suitable experiment data to be produced to compare against. The stronger physical grounding of RPA relative to the dispersion corrections certainly indicates that this is likely a physical effect, however. As it seems that RPA does not fully account for the dispersive interaction, we have used the MBD to account for some of this missing dispersion and achieved results to within experimental error and well within chemical accuracy. This indicates that chemical accuracy on metal surfaces is now possible. The cluster approach, at present, is not suitable for a quantitative understanding of chemisorption, though it offers a qualitatively correct description. Due to current computational restrictions and time restrictions, we have only studied the RPA as the high-level method but we expect that, in the near future, it will be possible to apply post-HF methods such as the Coupled Cluster methods to small to mid-sized metal clusters to further improve the description of bonding on the metal surfaces and expand beyond the current limitation in periodic systems to DFT and, recently, RPA.

Supplementary Material

Details of clusters in VASP, images of clusters, details of clusters using a Gaussian basis, and tables used for graphs.

Acknowledgements

This work has been supported by German Research Foundation (DFG) with a Reinhart Koselleck grant, as well as by the “Fonds der Chemischen Industrie”, and the Fritz-Haber Institute in the form of external PhD funding. The HLRN is acknowledged for computer time grant (bec00230).

Author Declarations

Conflict of Interest

The authors have no conflicts of interest to disclose.

Data Availability Statements

Data available on request from the authors.

6. References

1. Harl, J.; Kresse, G., Accurate Bulk Properties from Approximate Many-Body Techniques. *Phys. Rev. Lett.* **2009,** *103*, 056401, https://doi.org/10.1103/PhysRevLett.103.056401.
2. Tuma, C.; Sauer, J., A hybrid MP2/planewave-DFT scheme for large chemical systems: proton jumps in zeolites. *Chem. Phys. Lett.* **2004,** *387*, 388-394, https://doi.org/https://doi.org/10.1016/j.cplett.2004.02.056.
3. Tuma, C.; Sauer, J., Treating dispersion effects in extended systems by hybrid MP2:DFT calculations—protonation of isobutene in zeolite ferrierite. *Phys. Chem. Chem. Phys.* **2006,** *8*, 3955-3965, https://doi.org/10.1039/B608262A.
4. Piccini, G.; Alessio, M.; Sauer, J.; Zhi, Y.; Liu, Y.; Kolvenbach, R.; Jentys, A.; Lercher, J. A., Accurate Adsorption Thermodynamics of Small Alkanes in Zeolites. Ab initio Theory and Experiment for H-Chabazite. *J. Phys. Chem. C* **2015,** *119*, 6128-6137, https://doi.org/10.1021/acs.jpcc.5b01739.
5. Piccini, G.; Alessio, M.; Sauer, J., Ab Initio Calculation of Rate Constants for Molecule–Surface Reactions with Chemical Accuracy. *Angew. Chem. Int. Ed.* **2016,** *55*, 5235-5237, https://doi.org/10.1002/anie.201601534.
6. Grimme, S.; Antony, J.; Ehrlich, S.; Krieg, H., A consistent and accurate ab initio parametrization of density functional dispersion correction (DFT-D) for the 94 elements H-Pu. *J. Chem. Phys.* **2010,** *132*, 154104, https://doi.org/10.1063/1.3382344.
7. Gautier, S.; Steinmann, S. N.; Michel, C.; Fleurat-Lessard, P.; Sautet, P., Molecular adsorption at Pt(111). How accurate are DFT functionals? *Phys. Chem. Chem. Phys.* **2015,** *17*, 28921-28930, https://doi.org/10.1039/C5CP04534G.
8. Dion, M.; Rydberg, H.; Schröder, E.; Langreth, D. C.; Lundqvist, B. I., Van der Waals Density Functional for General Geometries. *Phys. Rev. Lett.* **2004,** *92*, 246401, https://doi.org/10.1103/PhysRevLett.92.246401.
9. Lee, K.; Morikawa, Y.; Langreth, D. C., Adsorption of n-butane on Cu(100), Cu(111), Au(111), and Pt(111): Van der Waals density-functional study. *Phys. Rev. B* **2010,** *82*, 155461, https://doi.org/10.1103/PhysRevB.82.155461.

10. Paier, J.; Ren, X.; Rinke, P.; Scuseria, G. E.; Grüneis, A.; Kresse, G.; Scheffler, M., Assessment of correlation energies based on the random-phase approximation. *New J. Phys.* **2012,** *14*, 043002, https://doi.org/10.1088/1367-2630/14/4/043002.

11. F. E. Harris; H. J. Monkhorst; Freeman, D. L., *Algebraic and Diagrammatic Methods in Many-Fermion Theory*. Oxford University Press: New York, Oxford, 1992.

12. Bohm, D.; Pines, D., A Collective Description of Electron Interactions. I. Magnetic Interactions. *Phys. Rev.* **1951,** *82*, 625-634, https://doi.org/10.1103/PhysRev.82.625.

13. Pines, D.; Bohm, D., A Collective Description of Electron Interactions: II. Collective vs Individual Particle Aspects of the Interactions. *Phys. Rev.* **1952,** *85*, 338-353, https://doi.org/10.1103/PhysRev.85.338.

14. Bohm, D.; Pines, D., A Collective Description of Electron Interactions: III. Coulomb Interactions in a Degenerate Electron Gas. *Phys. Rev.* **1953,** *92*, 609-625, https://doi.org/10.1103/PhysRev.92.609.

15. Pines, D., A Collective Description of Electron Interactions: IV. Electron Interaction in Metals. *Phys. Rev.* **1953,** *92*, 626-636, https://doi.org/10.1103/PhysRev.92.626.

16. Sheldon, C.; Paier, J.; Sauer, J., Adsorption of CH4 on the Pt(111) surface: Random phase approximation compared to density functional theory. *J. Chem. Phys.* **2021,** *155*, 174702, https://doi.org/10.1063/5.0071995.

17. Harl, J.; Kresse, G., Cohesive energy curves for noble gas solids calculated by adiabatic connection fluctuation-dissipation theory. *Phys. Rev. B* **2008,** *77*, 045136, https://doi.org/10.1103/PhysRevB.77.045136.

18. Olsen, T.; Thygesen, K. S., Accurate Ground-State Energies of Solids and Molecules from Time-Dependent Density-Functional Theory. *Phys. Rev. Lett.* **2014,** *112*, 203001, https://doi.org/10.1103/PhysRevLett.112.203001.

19. Kaltak, M.; Klimeš, J.; Kresse, G., Low Scaling Algorithms for the Random Phase Approximation: Imaginary Time and Laplace Transformations. *J. Chem. Theory Comput.* **2014,** *10*, 2498-2507, https://doi.org/10.1021/ct5001268.

20. Tait, S. L.; Dohnálek, Z.; Campbell, C. T.; Kay, B. D., n-alkanes on Pt(111) and on C(0001)/Pt(111): Chain length dependence of kinetic desorption parameters. *J. Chem. Phys.* **2006,** *125*, 234308, https://doi.org/10.1063/1.2400235.

21. Feibelman, P. J.; Hammer, B.; Nørskov, J. K.; Wagner, F.; Scheffler, M.; Stumpf, R.; Watwe, R.; Dumesic, J., The CO/Pt(111) Puzzle. *J. Phys. Chem. B* **2001,** *105*, 4018-4025, https://doi.org/10.1021/jp002302t.

22. Schimka, L.; Harl, J.; Stroppa, A.; Grüneis, A.; Marsman, M.; Mittendorfer, F.; Kresse, G., Accurate surface and adsorption energies from many-body perturbation theory. *Nat. Mater.* **2010,** *9*, 741, https://doi.org/10.1038/nmat2806.

23. Eichler, U.; Kölmel, C. M.; Sauer, J., Combining ab initio techniques with analytical potential functions for structure predictions of large systems: Method and application to crystalline silica polymorphs. *J. Comput. Chem.* **1997,** *18*, 463-477, https://doi.org/10.1002/(SICI)1096-987X(199703)18:4<463::AID-JCC2>3.0.CO;2-R.

24. Humbel, S.; Sieber, S.; Morokuma, K., The IMOMO method: Integration of different levels of molecular orbital approximations for geometry optimization of large systems: Test for n-butane conformation and SN2 reaction: RCl+Cl−. *J. Chem. Phys.* **1996,** *105*, 1959-1967, https://doi.org/10.1063/1.472065.

25. Bakowies, D.; Thiel, W., Hybrid Models for Combined Quantum Mechanical and Molecular Mechanical Approaches. *J. Phys. Chem.* **1996,** *100*, 10580-10594, https://doi.org/10.1021/jp9536514.

26. Boys, S. F.; Bernardi, F., The calculation of small molecular interactions by the differences of separate total energies. Some procedures with reduced errors. *Mol. Phys.* **1970,** *19*, 553-566, https://doi.org/10.1080/00268977000101561.

27. Momma, K.; Izumi, F., VESTA 3 for three-dimensional visualization of crystal, volumetric and morphology data. *J. Appl. Crystallogr.* **2011,** *44*, 1272-1276, https://doi.org/10.1107/S0021889811038970

28. Schrödinger, L., The PyMol Molecular Graphics System, Version 2.0. 2015.

29. Blochl, P. E., Projector augmented-wave method. *Phys. Rev. B: Condens. Matter* **1994,** *50*, 17953-17979, https://doi.org/10.1103/physrevb.50.17953.

30. Kresse, G.; Joubert, D., From ultrasoft pseudopotentials to the projector augmented-wave method. *Phys. Rev. B* **1999,** *59*, 1758-1775, https://doi.org/10.1103/PhysRevB.59.1758.

31. Kresse, G.; Furthmuller, J., Efficient iterative schemes for ab initio total-energy calculations using a plane-wave basis set. *Phys. Rev. B* **1996,** *54*, 11169-11186, https://doi.org/10.1103/PhysRevB.54.11169.

32. Perdew, J. P.; Burke, K.; Ernzerhof, M., (PBE) Generalized Gradient Approximation made simple. *Phys. Rev. Lett.* **1996,** *77*, 3865-3868, https://doi.org/10.1103/PhysRevLett.77.3865.

33. Perdew, J. P.; Burke, K.; Ernzerhof, M., Erratum. *Phys. Rev. Lett.* **1997,** *78*, 1396, https://doi.org/10.1103/PhysRevLett.78.1396.

34. Grimme, S., Semiempirical GGA-type density functional constructed with a long-range dispersion correction. *J. Comput. Chem.* **2006,** *27*, 1787-1799, https://doi.org/10.1002/jcc.20495.

35. Bučko, T.; Lebègue, S.; Gould, T.; Ángyán, J. G., Many-body dispersion corrections for periodic systems: an efficient reciprocal space implementation. *J. Phys.: Condens. Matter* **2016,** *28*, 045201, https://doi.org/10.1088/0953-8984/28/4/045201.

36. Steinmann, S. N.; Corminboeuf, C., Comprehensive Benchmarking of a Density-Dependent Dispersion Correction. *J. Chem. Theory Comput.* **2011,** *7*, 3567-3577, https://doi.org/10.1021/ct200602x.

37. Steinmann, S. N.; Corminboeuf, C., A generalized-gradient approximation exchange hole model for dispersion coefficients. *J. Chem. Phys.* **2011,** *134*, 044117, https://doi.org/10.1063/1.3545985.

38. Shishkin, M.; Kresse, G., Implementation and performance of the frequency-dependent GW method within the PAW framework. *Phys. Rev. B* **2006,** *74*, 035101, https://doi.org/10.1103/PhysRevB.74.035101.

39. Eichkorn, K.; Treutler, O.; Öhm, H.; Häser, M.; Ahlrichs, R., Auxiliary basis sets to approximate Coulomb potentials. *Chem. Phys. Lett.* **1995,** *240*, 283-290, https://doi.org/https://doi.org/10.1016/0009-2614(95)00621-A.

40. Eichkorn, K.; Weigend, F.; Treutler, O.; Ahlrichs, R., Auxiliary basis sets for main row atoms and transition metals and their use to approximate Coulomb potentials. *Theor. Chem. Acc.* **1997,** *97*, 119-124, https://doi.org/10.1007/s002140050244.

41. Ahlrichs, R.; Bär, M.; Häser, M.; Horn, H.; Kölmel, C., Electronic structure calculations on workstation computers: The program system turbomole. *Chem. Phys. Lett.* **1989,** *162*, 165-169, https://doi.org/https://doi.org/10.1016/0009-2614(89)85118-8.

42. Weigend, F.; Ahlrichs, R., Balanced basis sets of split valence, triple zeta valence and quadruple zeta valence quality for H to Rn: Design and assessment of accuracy. *Phys. Chem. Chem. Phys.* **2005,** *7*, 3297-3305, https://doi.org/10.1039/B508541A.

43. Weigend, F., Accurate Coulomb-fitting basis sets for H to Rn. *Phys. Chem. Chem. Phys.* **2006,** *8*, 1057-1065, https://doi.org/10.1039/b515623h.

44. Hellweg, A.; Hättig, C.; Höfener, S.; Klopper, W., Optimized accurate auxiliary basis sets for RI-MP2 and RI-CC2 calculations for the atoms Rb to Rn. *Theor. Chem. Acc.* **2007,** *117*, 587-597, https://doi.org/10.1007/s00214-007-0250-5.

45. Eshuis, H.; Yarkony, J.; Furche, F., Fast computation of molecular random phase approximation correlation energies using resolution of the identity and imaginary frequency integration. *J. Chem. Phys.* **2010,** *132*, 234114, https://doi.org/10.1063/1.3442749.

46. Eshuis, H.; Bates, J. E.; Furche, F., Electron correlation methods based on the random phase approximation. *Theor. Chem. Acc.* **2012,** *131*, 1084, https://doi.org/10.1007/s00214-011-1084-8.

47. Waitt, C.; Ferrara, N. M.; Eshuis, H., Thermochemistry and Geometries for Transition-Metal Chemistry from the Random Phase Approximation. *J. Chem. Theory Comput.* **2016,** *12*, 5350-5360, https://doi.org/10.1021/acs.jctc.6b00756.

48. Chedid, J.; Ferrara, N. M.; Eshuis, H., Describing transition metal homogeneous catalysis using the random phase approximation. *Theor. Chem. Acc.* **2018,** *137*, 158, https://doi.org/10.1007/s00214-018-2369-y.

49. Häser, M.; Ahlrichs, R., Improvements on the direct SCF method. *J. Comput. Chem.* **1989,** *10*, 104-111, https://doi.org/10.1002/jcc.540100111.

50. Andersson, M. P., Density functional theory with modified dispersion correction for metals applied to molecular adsorption on Pt(111). *Phys. Chem. Chem. Phys.* **2016,** *18*, 19118-19122, https://doi.org/10.1039/C6CP03289C.

51. Li, L.; Larsen, A. H.; Romero, N. A.; Morozov, V. A.; Glinsvad, C.; Abild-Pedersen, F.; Greeley, J.; Jacobsen, K. W.; Nørskov, J. K., Investigation of Catalytic Finite-Size-Effects of Platinum Metal Clusters. *J. Phys. Chem. Lett.* **2013,** *4*, 222-226, https://doi.org/10.1021/jz3018286.

52. Chaves, A. S.; Piotrowski, M. J.; Da Silva, J. L. F., Evolution of the structural, energetic, and electronic properties of the 3d, 4d, and 5d transition-metal clusters (30 TMn systems for n = 2–15): a density functional theory investigation. *Phys. Chem. Chem. Phys.* **2017,** *19*, 15484-15502, https://doi.org/10.1039/C7CP02240A.

53. Schießer, A.; Hörtz, P.; Schäfer, R., Thermodynamics and kinetics of CO and benzene adsorption on Pt(111) studied with pulsed molecular beams and microcalorimetry. *Surf. Sci.* **2010,** *604*, 2098-2105, https://doi.org/10.1016/j.susc.2010.09.001.

54. Ren, X.; Rinke, P.; Scheffler, M., Exploring the random phase approximation: Application to CO adsorbed on Cu(111). *Phys. Rev. B* **2009,** *80*, 045402, https://doi.org/10.1103/PhysRevB.80.045402.

55. Kaltak, M.; Klimeš, J.; Kresse, G., Cubic scaling algorithm for the random phase approximation: Self-interstitials and vacancies in Si. *Phys. Rev. B* **2014,** *90*, 054115, https://doi.org/10.1103/PhysRevB.90.054115.

56. Heilingbrunner, A.; Stollhoff, G., Ab initio correlation calculation for metallic lithium. *J. Chem. Phys.* **1993,** *99*, 6799-6809, https://doi.org/10.1063/1.465823.

57. Olson, R. M.; Gordon, M. S., Isomers of Au8. *J. Chem. Phys.* **2007,** *126*, 214310, https://doi.org/10.1063/1.2743005.

58. Johansson, M. P.; Lechtken, A.; Schooss, D.; Kappes, M. M.; Furche, F., 2D-3D transition of gold cluster anions resolved. *Phys. Rev. A* **2008,** *77*, 053202, https://doi.org/10.1103/PhysRevA.77.053202.

59. Drebov, N.; Weigend, F.; Ahlrichs, R., Structures and properties of neutral gallium clusters: A theoretical investigation. *J. Chem. Phys.* **2011,** *135*, 044314, https://doi.org/10.1063/1.3615501.

60. Drebov, N.; Ahlrichs, R., Small clusters of aluminum and tin: Highly correlated calculations and validation of density functional procedures. *J. Chem. Phys.* **2011,** *134*, 124308, https://doi.org/10.1063/1.3571596.

61. Voloshina, E.; Paulus, B., Wave-function-based ab initio method for metals: Application of the incremental scheme to magnesium. *Phys. Rev. B* **2007,** *75*, 245117, https://doi.org/10.1103/PhysRevB.75.245117.

62. Voloshina, E.; Paulus, B., First Multireference Correlation Treatment of Bulk Metals. *J. Chem. Theory Comput.* **2014,** *10*, 1698-1706, https://doi.org/10.1021/ct401040t.

Chapter 2: Supplementary Material

S1 – Cluster models

The clusters used in this study are presented in Figures S1.1, respectively. They are named in the following style: Pt_n(A,B,…), where n is the number of platinum atoms in the cluster, A is the number in the top layer of the cluster, B is the number in the second layer, and so on.

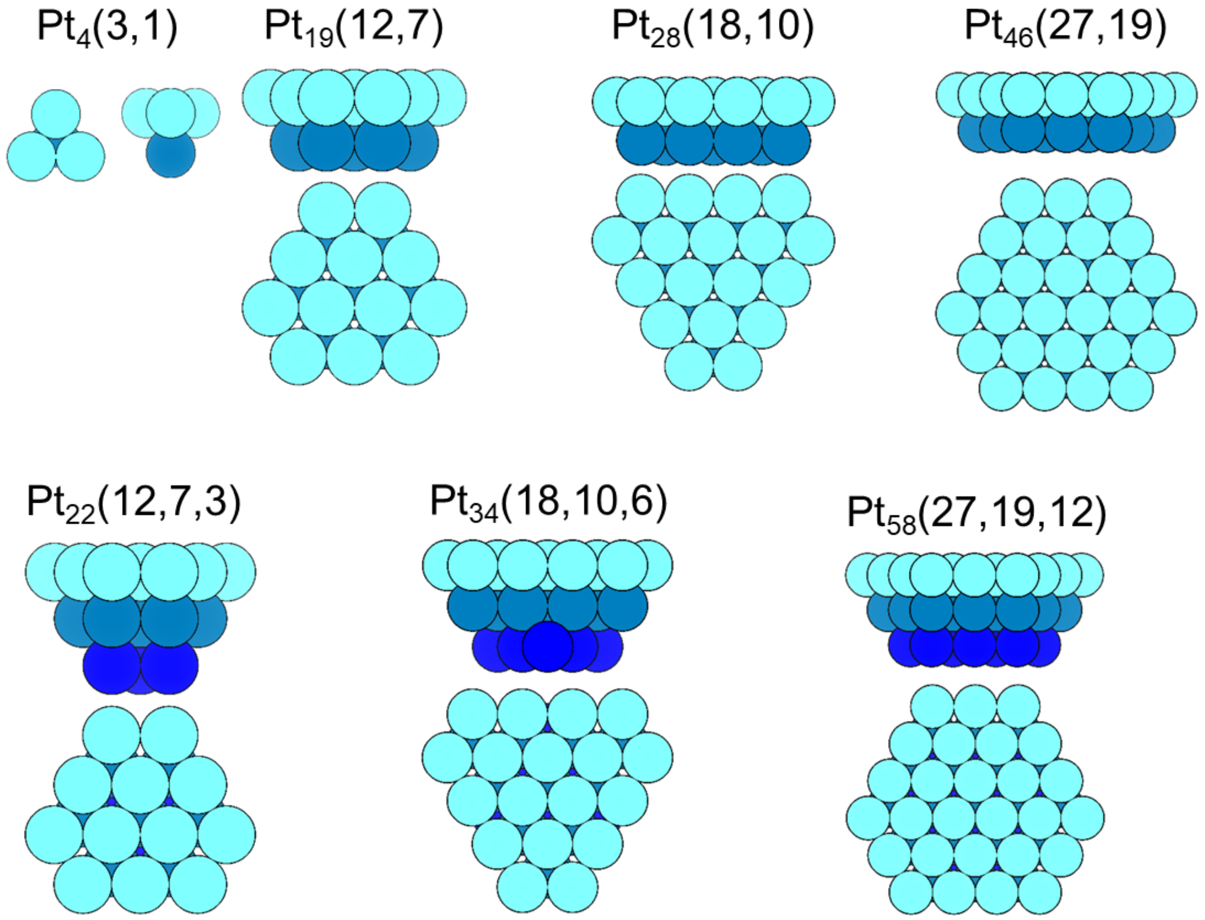
Pt_4(3,1)
Pt_{19}(12,7)
Pt_{28}(18,10)
Pt_{46}(27,19)
Pt_{22}(12,7,3)
Pt_{34}(18,10,6)
Pt_{58}(27,19,12)

Figure S1.1. Cluster models of the surface. Light, middle, and dark blue indicate atoms in the first, second, and third layer of the cluster, respectively.[1]

S2 – Clusters under PBC

The clusters shown in S1 were placed into cubic cells under PBC. We show the adsorption energies for the cluster in 20 Å^3 and 25 Å^3 cells below in Table S2.1.

Table S2.1. Adsorption energy ΔE_{ads} (in kJ mol^{-1}) of CH_4 on platinum clusters Pt_n(A,B,C) for PBE+MBD in 20^3 and 25^3 Å^3 cells. Where n denotes the total number of Pt atoms, A the number in the first layer, B the number in the second layer, and C the number in the third layer.

Cluster	ΔE_{ads} / kJ mol^{-1}	
	20^3	25^3
Pt_4(3,1)	-7.6	-7.6
Pt_{19}(12,7)	-11.9	-12.0
Pt_{22}(12,7,3)	-11.5	-11.5
Pt_{28}(18,10)	-12.1	-12.2
Pt_{34}(18,10,6)	-10.8	-10.9
Pt_{46}(27,19)	-9.9	-10.1
Pt_{58}(27,19,12)	-9.0	-9.1

We present the adsorption energies with and without spin-polarisation in Table S2.2 below. As the D2 and D3 dispersion corrections are post-SCF additive and not density-dependent, they are not impacted by spin polarisation besides the change in the PBE component.

Table S2.2. Spin-polarised (SP) and non-spin-polarised (non-SP) adsorption energy ΔE_{ads} (in kJ mol^{-1}) of CH_4 on platinum clusters Pt_n(A,B,C) for PBE with dispersion corrections (dDsC, and MBD).

Cluster	ΔE_{ads} / kJ mol^{-1}					
	PBE		dDsC		MBD	
	SP	Non-SP	SP	Non-SP	SP	Non-SP
Pt_4(3,1)	0.3	0.3	-6.1	-6.1	-7.6	-7.6
Pt_{19}(12,7)	1.1	1.0	-12.7	-12.9	-11.9	-12.1
Pt_{22}(12,7,3)	1.4	1.5	-12.5	-12.5	-11.5	-11.4
Pt_{28}(18,10)	1.1	1.0	-13.8	-13.9	-12.1	-12.3
Pt_{34}(18,10,6)	2.0	2.0	-13.1	-13.2	-10.8	-10.9
Pt_{46}(27,19)	2.8	2.5	-13.2	-13.5	-9.9	-10.3
Pt_{58}(27,19,12)	2.7	2.5	-13.6	-13.9	-9.0	-9.4

The adsorption energies for the clusters with spin-polarisation under PBC (see Figure S1.1) are presented in Table S2.3 and S2.4.

Table S2.3. Adsorption energy ΔE_{ads} (in kJ mol^{-1}) of CH_4 on platinum clusters $Pt_n(A,B,C)$ for PBE with dispersion corrections (D2, D3, dDsC, and MBD). Where n denotes the total number of Pt atoms, A the number in the first layer, B the number in the second layer, and C the number in the third layer. The periodic calculation is for the 3-layered (2x2) cell with lateral interactions removed, $PBC_{no\ lat}$.

Cluster	ΔE_{ads} / kJ mol^{-1}				
	PBE	D2	D3	dDsC	MBD
$Pt_4(3,1)$	0.3	-19.9	-10.7	-6.1	-7.6
$Pt_{19}(12,7)$	1.1	-30.9	-19.2	-12.7	-11.9
$Pt_{22}(12,7,3)$	1.4	-30.6	-18.9	-12.5	-11.5
$Pt_{28}(18,10)$	1.1	-32.3	-20.4	-13.8	-12.1
$Pt_{34}(18,10,6)$	2.0	-31.4	-19.6	-13.1	-10.8
$Pt_{46}(27,19)$	2.8	-31.7	-19.8	-13.2	-9.9
$Pt_{58}(27,19,12)$	2.7	-31.6	-20.0	-13.6	-9.0
PBC_{lat}	-0.4	-35.6	-24.9	-18.9	-14.7
ΔE_{lat}	-0.5	-1.3	-1.6	-1.6	-1.24
$PBC_{no\ lat}$	0.1	-34.3	-23.3	-17.3	-13.4

Table S2.4. Dispersion contribution to the adsorption energy ΔE_{disp} (in kJ mol^{-1}) of CH_4 on platinum clusters $Pt_n(A,B,C)$ for PBE with dispersion corrections (D2, D3, dDsC, and MBD). The periodic calculation is for the 3-layered (2x2) cell with lateral interactions removed, $PBC_{no\ lat}$.

Cluster	ΔE_{disp} / kJ mol^{-1}				
	PBE	D2	D3	dDsC	MBD
$Pt_4(3,1)$	0.0	-20.2	-11.0	-6.4	-7.9
$Pt_{19}(12,7)$	0.0	-31.9	-20.3	-13.8	-13.0
$Pt_{22}(12,7,3)$	0.0	-32.0	-20.4	-14.0	-12.9
$Pt_{28}(18,10)$	0.0	-33.4	-21.5	-14.9	-13.2
$Pt_{34}(18,10,6)$	0.0	-33.4	-21.6	-15.0	-13.1
$Pt_{46}(27,19)$	0.0	-34.5	-22.6	-16.0	-12.8
$Pt_{58}(27,19,12)$	0.0	-34.4	-22.7	-16.4	-11.7
$PBC_{no\ lat}$	0.0	-34.4	-23.4	-17.5	-13.5

S3 – Clusters using a Gaussian Basis

S3.1 DFT

We have shown that using plane waves, i.e. a near complete basis set is appropriate for describing clusters and converges towards to PBC values. However, this corroboration does not necessarily extend smoothly to Gaussian basis sets. To investigate this, we calculated the adsorption energy for the seven different clusters using PBE with a large, Gaussian basis. The choice of state then becomes important. We chose to investigate the singlet state, as this is the physical state of bulk platinum, lacking any magnetic dipole, and the lowest energy spin state, which as commonly been used in the literature.[2] We neglect the bond-prepared states of Siegbahn, as we have not used symmetry in our calculations and no chemical bond is formed between the CH_4 and the platinum cluster with which to match symmetries. The adsorption energies are plotted against the number of Platinum atoms in the cluster in Figure S3.1. The adsorption energies were obtained using PBE/def2-QZVPP and the Basis Set Superposition Error (BSSE) was accounted for using the Counterpoise Correction (CPC).

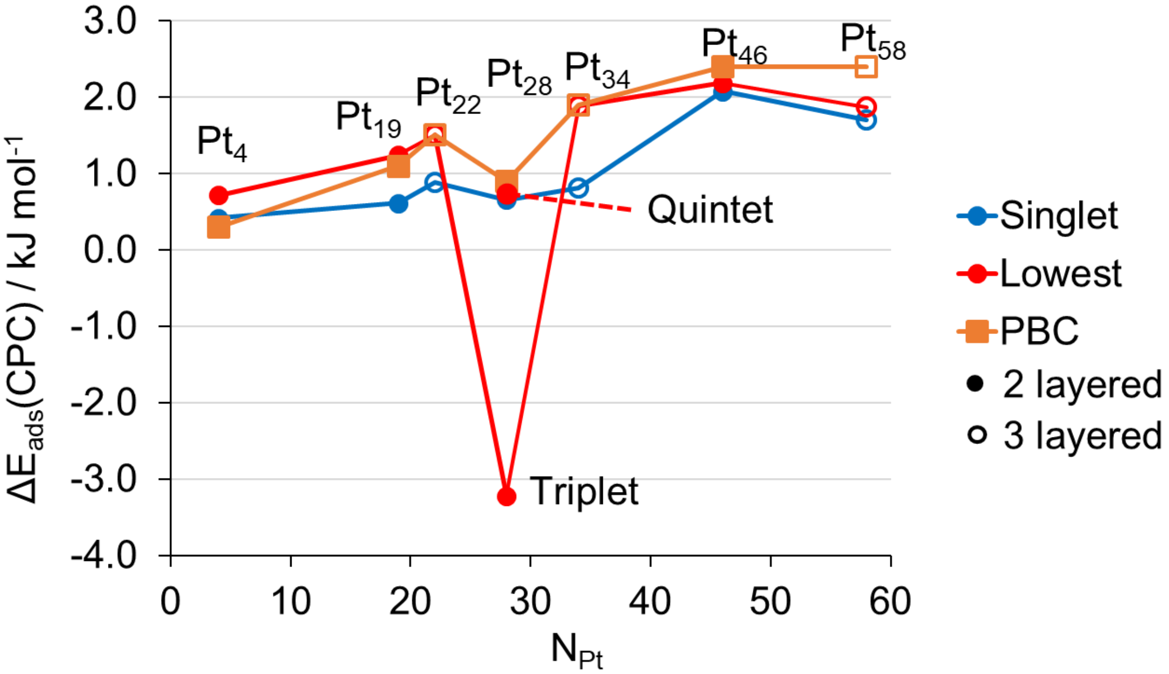

Figure S3.1. Adsorption energy plots for CH_4 on Pt_n clusters for different sized clusters in the singlet (blue) and lowest spin (red) states using Gaussian basis sets. Circles show the total adsorption energy, while triangles show the dispersive component. Full markers are for 2-layered clusters, while empty show the markers are for 3-layered clusters. Plane wave values from Figure 2 are shown for reference (orange squares). Tabulated values given in Table S3.1. The adsorption energies were obtained using PBE/def2-QZVPP and BSSE-corrected with the Counterpoise Correction (CPC).

The difference between the adsorption energies for the singlet and lowest spin states is not significant, varying by less than 1 kJ mol^{-1} with the singlet state being consistently lower in energy. We checked the adsorption energy up to the 39-tet state for Pt_{19} and found that it did not change significantly with multiplet state, see Figure S3.3 and Table S3.2, with only a few minor deviations. We expect that this difference from the older literature, where different states gave very different adsorption energies, was due to their use of the Hartree-Fock method, which is poor for delocalised systems, such as metal clusters.[2-6] By using DFT, one can compensate for this and make the clusters suitable for describing adsorption on surfaces.[7,8]

One important exception is for the $Pt_{18,10}$ cluster, where the lowest energy spin state (the triplet in this case) is significantly lower in energy. Upon investigation, it became clear that this is due to close-lying triplet states that are difficult to distinguish. Instead, we show the quintet state for this is far closer to the singlet state and does not significantly deviate, so we will use this in subsequent calculations on this cluster.

Once again, we see little difference between the 2- and 3-layered clusters, generally less than 0.5 kJ mol^{-1}, confirming our suspicion that there is no real benefit in the use of additional layers, so we will not consider additional layers further. The general trend of adsorption energies with respect to cluster size is similar for both the singlet and lowest spin states, showing similar curves. This is matched by the trend for those adsorption energies obtained from the plane wave basis set, which indicates that they describe the electronic structure similarly. This corroborates that either a plane wave or atom-centred, Gaussian is suitable for the description of these platinum clusters using DFT(+D). This makes it appropriate to use as the low-level method in a hybrid scheme.

3.2.2 RPA

Few post-HF methods are suitable for studying metals, due to their zero band-gap. One such method is the Random Phase Approximation (RPA). This has successfully been applied to several systems with adsorption on surfaces under periodic settings.[9-11] Alternatively, clusters may be used.[8] As these are only mimics for the surface, they do not have an exactly zero band-gap, so other methods may also be suitable, if they were also computationally feasible. We have applied RPA to the metal clusters investigated previously and encountered additional problems. Although the band-gap is not as severe an issue as might have been expected, there is nonetheless great difficulty in finding a suitable spin state for calculating. Above we tested the singlet and the lowest energy spin states and found that they worked well for DFT. We then took these PBE orbitals and used them for RPA. We found that there is a strong dependence on the HOMO-LUMO gap,[12,13] the non-periodic analogue of the band-gap. To test this, we took a cluster that performed well, the singlet state of the Pt_{19} cluster and set the HOMO-LUMO gap to a set value by shifting all the energy of the virtual orbitals by the same amount, then performed RPA calculations. N.B. the PBE orbitals remained otherwise unchanged. We show the adsorption energy against the HOMO-LUMO gap for CH_4/Pt_{19} using RPA in Figure S3.2.

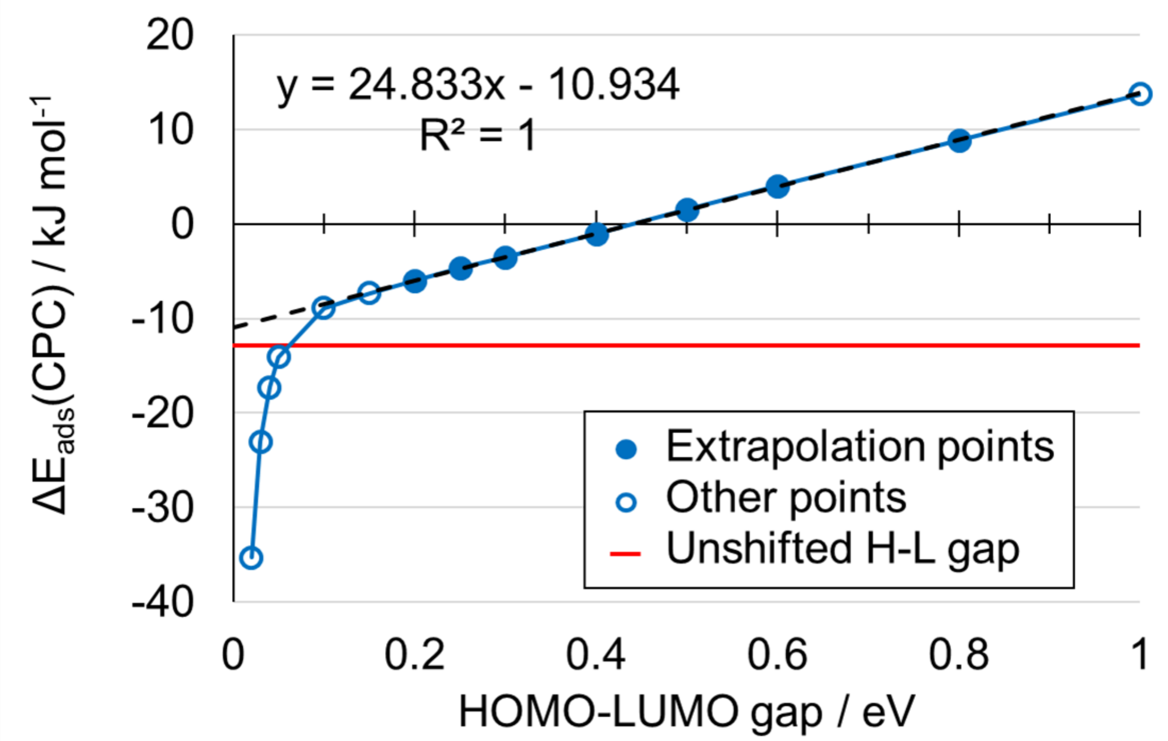

Figure S3.2. RPA adsorption energy (in kJ mol^{-1}) against the HOMO-LUMO gap (in eV) for singlet CH_4/Pt_{19}. Points are tabulated in Table S3.3. The red line is the adsorption energy without any shifting of the HOMO-LUMO gap.

It is clear from Figure 3.2 that the adsorption energy is linear with respect to the HOMO-LUMO gap beyond 0.2 eV, leading us to wonder whether this could be extrapolated to a “zero-gap” value to better mimic the metal surface. This did not match the unshifted HOMO-LUMO gap value (-12.9 kJ mol^{-1}), however, instead underestimating it by 2 kJ mol^{-1}. Additionally, it is clear that this implementation of RPA (as an approximation of ring CCD)[14] is not immune from the zero-gap issue, unlike periodic RPA. Instead, the adsorption energy becomes increasingly strong as the HOMO-LUMO gap tends towards zero, resulting in unphysically strong binding. However, so long as a small, non-zero HOMO-LUMO gap is found for the cluster, good RPA adsorption energies may still be performed.

We tested the HOMO-LUMO gaps for all our clusters and found that, with the exception of the Pt_{19} cluster, the singlet state resulted in a negative HOMO-LUMO gap, i.e. a non-Aufbau population, and making it inappropriate for further use. This can be amended by forcing a final diagonalisation of the Fock matrix. However, this introduces an artificially large HOMO-LUMO gap, rendering the RPA adsorption energies meaningless (cf. dependency of ΔE_{ads} in Figure S3.2 and Table S3.4). This is due to doubly-degenerate orbitals being populated preferentially before singly degenerate, resulting in a hole in the orbital population. However, the singlet state of the Pt_{19} cluster is suitable, due to the HOMO being singly, rather than doubly, degenerate. Additionally, triplet and other multiplet states are suitable in every case. However, due to RPA calculations becoming computationally intractable for the larger clusters, we limit ourselves to the Pt_{19} and Pt_{28} clusters. The adsorption energies for different clusters using a Gaussian basis (Figure 3.1) are presented in Table S3.1.

Table S3.1. Adsorption energy ΔE_{ads} (in kJ mol^{-1}) for CH_4 on platinum clusters Pt_n(A,B,C) in the singlet states and the lowest energy spin states using PBE/def2-QZVPP, and the plane wave (PW) value. The lowest energy spin state multiplicity $(2S+1)_{low}$, Counterpoise-corrected (CPC) adsorption energies, and the Basis Set Superposition Error (BSSE) are given. Additionally, the values for the quintet state of Pt_{28} are shown.

Cluster	$(2S+1)_{low}$	ΔE_{ads} / kJ mol^{-1}				
		Singlet		Lowest		PW
		CPC	BSSE	CPC	BSSE	
Pt_4(3,1)	3	0.4	-0.3	0.7	-0.3	0.3
Pt_{19}(12,7)	7	0.6	-0.2	1.2	-0.2	1.1
Pt_{22}(12,7,3)	13	0.9	-0.2	1.5	-0.2	1.5
Pt_{28}(18,10)	3	0.7	-0.2	-3.2	-0.2	0.9
(quintet)	(5)	-	-	0.7	-0.2	-
Pt_{34}(18,10,6)	13	0.8	-0.3	1.9	-0.3	1.9
Pt_{46}(27,19)	19	2.1	-0.3	2.2	-0.3	2.4
Pt_{58}(27,19,12)	19	1.7	-0.3	1.9	-0.3	2.4

The adsorption energies for different spin states of Pt_{19} are given in Table S3.2 and shown in Figure S3.3.

Table S3.2. Adsorption energy ΔE_{ads} (in kJ mol^{-1}) for CH_4 on Pt_{19} clusters in multiplet states using PBE/def2-QZVPP. The Counterpoise-corrected (CPC) adsorption energies, and the Basis Set Superposition Error (BSSE) are given.

2S+1	ΔE_{ads}(CPC) / kJ mol^{-1}
1	0.6
3	0.8
5	2.5
7	1.2
9	0.8
11	0.8
13	0.4
15	1.0
17	1.0
19	1.1
21	1.1
23	1.2
25	1.2
27	1.1
29	-0.2
31	0.5
33	0.0
35	4.6
37	3.8
39	5.0

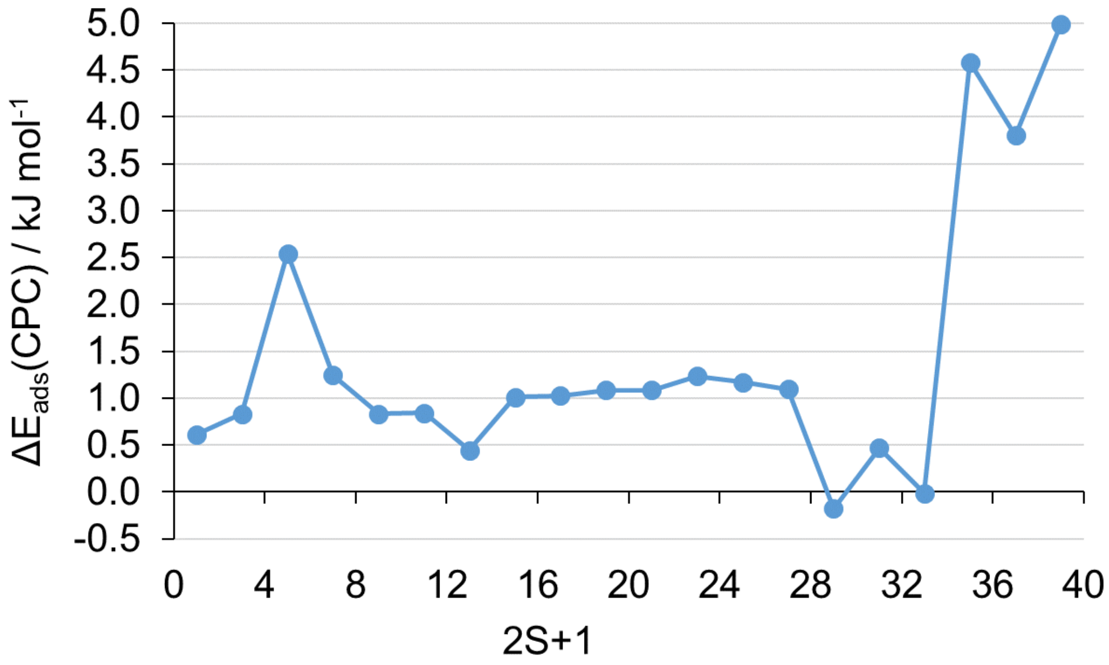

Figure S3.3. Adsorption energy ΔE_{ads} (in kJ mol^{-1}) for CH_4/Pt_{19} against multiplicity using PBE/def2-QZVPP.

The RPA adsorption energies for CH_4/Pt_{19} are presented in Table S3.3. For these calculations, the HOMO-LUMO gap for Pt_{19}, CH_4/Pt_{19}, $Pt_{19}//CH_4/Pt_{19}$, and $Pt_{19}(CH_4)//CH_4/Pt_{19}$ were set to stated value, shifting all the virtual orbitals by the same amount as the LUMO, and then the RPA calculation was performed.

Table S3.3. Adsorption energy ΔE_{ads} (in kJ mol^{-1}) for CH_4/Pt_{19} clusters with set HOMO-LUMO gaps using RPA/def2-QZVPP. BSSE has been done according to CPC.

HOMO-LUMO gap / eV	ΔE_{ads}(CPC) / kJ mol^{-1}
0.01	-274.9
0.02	-35.3
0.03	-23.0
0.04	-17.3
0.05	-14.1
0.1	-8.9
0.15	-7.3
0.2	-6.0
0.25	-4.7
0.3	-3.5
0.4	-1.0
0.5	1.5
0.6	4.0
0.8	8.9
1	13.7
1.25	19.6
1.5	25.5
2	36.9
3	58.7

The HOMO-LUMO gap for cluster calculations, with number of Pt atoms given, is shown in Tables S3.4 for the singlet states.

Table S3.4. HOMO-LUMO gaps (in eV) for PBE/def2-QZVPP for n-atom clusters in the singlet state.

N_{Pt}	HOMO-LUMO Gap / eV			
	Pt_n	Pt_n//CH_4/Pt_n	$Pt_n(CH_4)$//CH_4/Pt_n	CH_4/Pt_n
4	10.37	0.07	8.06	0.07
19	0.05	0.05	0.05	0.05
22	0.24	2.65	0.41	0.06
28	1.14	0.35	1.65	0.01
34	0.13	0.02	0.00	0.00
46	3.59	1.27	5.01	6.32
58	1.45	8.49	0.09	0.03

The HOMO-LUMO gap for cluster calculations against the number of Pt atoms is presented in Table S3.5 and Figure S3.4 for singlet and triplet states.

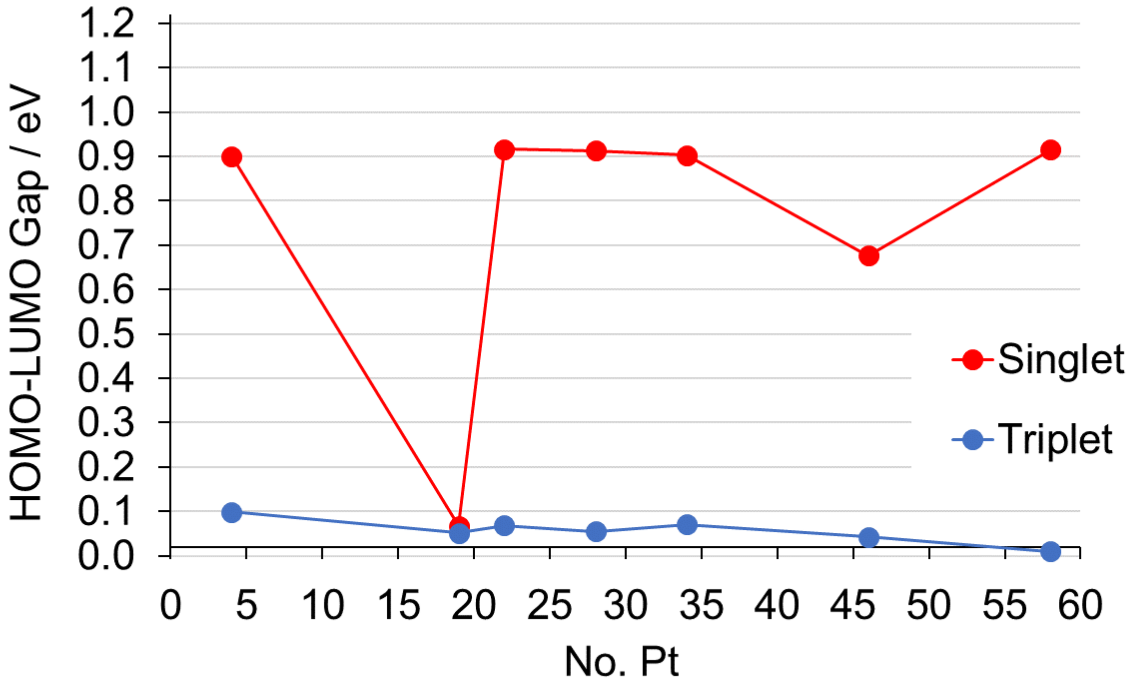

Figure S3.4. HOMO-LUMO gap (in eV) for Pt clusters against number of Pt atoms using PBE/def2-QZVPP for singlet (red) and triplet (blue) states.

Table S3.5. HOMO-LUMO gaps (in eV) for PBE/def2-QZVPP for Pt_n clusters in the singlet and triplet states.

N_{Pt}	Singlet	Triplet
4	0.881	0.079
19	0.897	0.104
22	0.896	0.048
28	0.893	0.035
34	0.883	0.050
46	0.656	0.022
58	0.895	-0.010

S4 – Hybrid RPA:DFT

S4.1 Methane

The hybrid adsorption energies for Pt_{19} in the triplet state are shown and broken down in Table S4.1.

Table S4.1. Hybrid adsorption energy $\Delta E_{HL:LL,\ CPC}$(pbc) for the hybrid scheme, with RPA as the high-level method and PBE(+D) as the low-level method. The Pt_{19} cluster in the triplet state was used. The PBE+MBD optimised structure is used.

ΔE / kJ mol^{-1}	PBE	PBE+MBD	PBE+dDsC	PBE+D3	PBE+D2
ΔE_{LL}(pbc)	0.1	-14.7	-18.9	-24.9	-35.6
$\Delta E_{LL,\ CPC}$(C)	0.3	0.3	0.3	0.3	0.3
ΔE_{disp}(C, VASP)	0.0	-13.0	-13.8	-20.3	-31.9
$\Delta E_{LL,\ CPC}$(C) + ΔE_{disp}(C, VASP)	0.3	-12.7	-13.5	-20.0	-31.7
$\Delta E_{HL,\ CPC}$(C)	-8.5	-8.5	-8.5	-8.5	-8.5
$\Delta_{HL,\ CPC}$(C)	-8.8	4.2	5.0	11.5	23.2
Δ_{LR}(pbc, C)	-0.2	-2.0	-5.4	-4.9	-4.0
$\Delta E_{HL:LL,\ CPC}$(pbc)	-8.6	-10.4	-13.9	-13.4	-12.4
ΔE_{RPA}(pbc)	-12.8[15]				
$\Delta E_{obs.}$	-15.6[15]				

The hybrid adsorption energies for Pt_{28} in the quintet state are shown and broken down in Table S4.2.

Table S4.2. Hybrid adsorption energy $\Delta E_{HL:LL,\ CPC}$(pbc) for the hybrid scheme, with RPA as the high-level method and PBE(+D) as the low-level method. The Pt_{28} cluster in the quintet state was used. The PBE+MBD optimised structure is used.

ΔE / kJ mol^{-1}	PBE	PBE+MBD	PBE+dDsC	PBE+D3	PBE+D2
ΔE_{LL}(pbc)	0.1	-14.7	-18.9	-24.9	-35.6
$\Delta E_{LL,\ CPC}$(C)	0.7	0.7	0.7	0.7	0.7
ΔE_{disp}(C, VASP)	0.0	-13.2	-14.9	-21.5	-33.4
$\Delta E_{LL,\ CPC}$(C) + ΔE_{disp}(C, VASP)	0.7	-12.5	-14.2	-20.8	-32.6
$\Delta E_{HL,\ CPC}$(C)	-8.1	-8.1	-8.1	-8.1	-8.1
$\Delta_{HL,\ CPC}$(C)	-8.8	4.4	6.1	12.7	24.6
Δ_{LR}(pbc, C)	-0.6	-2.2	-4.7	-4.2	-3.0
$\Delta E_{HL:LL,\ CPC}$(pbc)	-8.7	-10.2	-12.8	-12.2	-11.0
ΔE_{RPA}(pbc)	-12.8[15]				
$\Delta E_{obs.}$	-15.6[15]				

The carbon-platinum distance r(C-Pt) was then varied and then reoptimized on the PBE+MBD level with the C atom frozen in place. The adsorption energy using the hybrid structure for these methods is shown in Table S4.3 below.

Table S4.3. Hybrid adsorption energy $\Delta E_{HL:LL,\ CPC}$(pbc) for the hybrid scheme (CH_4/Pt(111)), with RPA as the high-level method and PBE(+D) as the low-level method. The Pt_{19} cluster in the singlet state was used. The PBE+MBD optimised structure is used.

r(C-Pt) / pm	PBE	PBE+ MBD	PBE+ dDsC	PBE+ D3	PBE+ D2	PBE (c)	PBE+ MBD (c)	RPA (c)	RPA (pbc)
253	44.5	42.9	40.6	35.4	33.2	2.7	-25.2	-2.6	-
277	15.6	14.7	11.3	8.3	7.3	-1.0	-24.8	-10.2	-
301	-1.9	-2.4	-6.5	-7.8	-8.0	-0.5	-20.5	-13.5	-
325	-9.6	-10.5	-14.3	-14.5	-14.2	-0.1	-16.5	-13.1	-
350	-13.8	-15.1	-18.5	-18.1	-17.4	0.6	-12.4	-12.9	-12.9
375	-14.3	-16.0	-18.8	-18.1	-17.3	-0.1	-10.3	-12.6	-13.8
400	-13.6	-15.4	-17.7	-17.0	-16.1	0.1	-7.8	-11.2	-
425	-12.3	-14.3	-14.8	-15.5	-14.5	-0.3	-6.3	-10.4	-
450	-11.2	-13.2	-14.4	-14.1	-13.0	0.1	-4.6	-9.0	-9.6
475	-10.0	-12.0	-12.9	-12.7	-11.5	0.5	-3.1	-7.6	-
500	-9.0	-11.1	-11.7	-11.6	-10.4	0.5	-2.4	-7.0	-
525	-8.3	-10.4	-10.8	-10.8	-9.6	0.5	-1.8	-6.5	-
550	-7.7	-9.8	-10.1	-10.1	-8.9	0.4	-1.4	-6.1	-
575	-7.2	-9.3	-9.5	-9.5	-8.3	0.4	-1.2	-5.8	-
600	-6.9	-9.1	-9.2	-9.3	-8.0	0.4	-0.9	-5.6	-

S4.2 Ethane

The carbon-platinum distance r(C-Pt) was then varied and then reoptimized on the PBE+MBD level with the C atom frozen in place. The adsorption energy using the hybrid structure for these methods is shown in Table S4.4 below.

Table S4.4. Hybrid adsorption energy $\Delta E_{\mathrm{HL:LL,\ CPC}}$(pbc) for the hybrid scheme (C_2H_6/Pt(111)), with RPA as the high-level method and PBE(+D) as the low-level method. The Pt_{19} cluster in the singlet state was used. The PBE+MBD optimised structure is used.

r(C-Pt) / pm	PBE	PBE+ MBD	PBE+ dDsC	PBE+ D3	PBE+ D2	PBE (c)	PBE+ MBD (c)	RPA (c)
260	87.9	72.7	73.3	57.9	35.9	15.1	-29.6	20.4
282	39.3	25.7	22.3	14.7	-0.8	-0.7	-39.7	-4.0
303	9.9	-1.7	-5.4	-9.4	-18.3	-5.1	-38.4	-11.9
326	-6.8	-16.4	-22.3	-22.1	-26.4	-3.2	-31.0	-13.1
349	-14.7	-22.7	-31.3	-27.6	-29.3	-0.9	-23.6	-12.8
374	-17.6	-24.9	-33.8	-29.3	-30.1	0.2	-18.0	-12.8
399	-17.8	-24.7	-33.4	-28.7	-29.2	0.5	-14.0	-12.5
424	-16.6	-23.3	-30.3	-27.1	-27.6	0.5	-10.8	-11.6
450	-14.9	-21.4	-26.5	-25.0	-25.6	0.3	-8.4	-10.5
475	-13.1	-19.5	-24.0	-23.0	-23.8	0.1	-6.7	-9.5
500	-11.6	-17.9	-21.9	-21.3	-22.2	0.0	-5.4	-8.5
525	-10.3	-16.6	-22.4	-19.9	-20.9	0.0	-4.3	-7.7
550	-9.2	-15.5	-20.0	-18.7	-19.8	-0.1	-3.6	-7.1
575	-8.4	-14.6	-19.0	-17.8	-19.0	-0.1	-2.9	-6.4
600	-7.8	-14.1	-18.3	-17.2	-18.4	-0.1	-2.4	-6.0

The observed activation energy from Tait et al.[16] was corrected for thermodynamic properties to calculate the adsorption energy. This is according to Eq. (1) below, cf. Eq. (1) and (2) from Sheldon et al. for details.[15]

$$\Delta E_{\mathrm{ref}} = \Delta H_{\mathrm{ads}}(T) - \Delta E_{\mathrm{ZPV}} - \Delta E_{\mathrm{therm}}(T) + RT = -E_A(T) - \Delta E_{\mathrm{ZPV}} - \Delta E_{\mathrm{therm}}(T) + 2\,RT \tag{1}$$

$$\Delta E_{\mathrm{ref}}\,(^{1}/_{4}\ \mathrm{ML}) = -29.4 - 0.68 + 1.17 + 1.76 = -27.2\ \mathrm{kJ\ mol^{-1}}$$

This is presented below in Table S4.5.

Table S4.5. Comparison of RPA results with experiment.[16]

Θ	$- E_A$ [a]	T / K	2RT	ΔE_{ZPV}	ΔE_{therm}	ΔE_{ref} [b]
	Obs.			Calc.	Calc.	Obs.
$^1/_4$	-29.4 ± 2.9	106	1.76	-1.17	0.68	-27.2 ± 2.9

[a] Ref. [16], assuming that $^1/_4$ ML coverage is saturated coverage; 10% uncertainty of the inversion analysis.[17] [b] Experimentally derived reference energy.

S4.3 Carbon Monoxide

We present the breakdown of our hybrid approach for CO/Pt(111) below, and the points for our hybrid approach in Table S4.6 below. $E_{B,\ LL}$ (pbc) is the periodic PBE (i.e. low-level) binding energy ($E_{CO/Pt(111)}$ - $E_{Pt(111)//CO/Pt(111)}$ - $E_{CO//CO/Pt(111)}$), $E_{relax,\ M}$ (pbc) is the periodic PBE relaxation energy for the CO ($E_{CO//CO/Pt(111)}$ - E_{CO}), $E_{relax,\ S}$ (pbc) is the periodic PBE relaxation energy for the Pt ($E_{Pt(111)//CO/Pt(111)}$ - $E_{Pt(111)}$), $E_{B,\ RPA}$ (C) is the cluster RPA binding energy, and $E_{B,\ PBE}$ (C) is the cluster PBE binding energy.

Table S4.6. Binding energies E_B and relaxation energies E_{relax} for the top and hcp sites of CO/Pt(111) using the hybrid RPA:PBE approach, with Pt_{19} in the triplet state and Pt_{28} in the quintet state.

	top		hcp	
	$Pt_{12,7}$ (T)	$Pt_{18,10}$ (Qu)	$Pt_{12,7}$ (T)	$Pt_{18,10}$ (Qu)
$E_{B,\ LL}$ (pbc)	-168.5	-168.5	-188.4	-188.4
$E_{relax,\ M}$ (pbc)	2.4	2.4	13.7	13.7
$E_{relax,\ S}$ (pbc)	11.3	11.3	9.4	9.4
$E_{B,\ RPA}$ (C)	-33.3	-122.1	-128.7	-108.0
$E_{B,\ PBE}$ (C)	-36.2	-169.8	-218.2	-190.1
$E_{HL:LL}$	-151.9	-107.1	-75.8	-83.1

References

1. Momma, K.; Izumi, F., VESTA 3 for three-dimensional visualization of crystal, volumetric and morphology data. *J. Appl. Crystallogr.* **2011,** *44*, 1272-1276, https://doi.org/10.1107/S0021889811038970

2. Panas, I.; Schüle, J.; Siegbahn, P.; Wahlgren, U., On the cluster convergence of chemisorption energies. *Chem. Phys. Lett.* **1988,** *149*, 265-272, https://doi.org/https://doi.org/10.1016/0009-2614(88)85024-3.

3. Nygren, M. A.; Siegbahn, P. E. M., Theoretical study of chemisorption of carbon monoxide on copper clusters. *J. Phys. Chem.* **1992,** *96*, 7579-7584, https://doi.org/10.1021/j100198a018.

4. Pettersson, L. G. M.; Faxen, T., Massively parallel direct SCF calculations on large metal clusters: Ni5-Ni481. *Theor. Chim. Acta* **1993,** *85*, 345-361, https://doi.org/10.1007/BF01113428.

5. Witko, M.; Hermann, K., Site-dependent binding of methoxy on Cu(111): Cluster model studies. *J. Chem. Phys.* **1994,** *101*, 10173-10180, https://doi.org/10.1063/1.468006.

6. Triguero, L.; Wahlgren, U.; Boussard, P.; Siegbahn, P., Calculations of hydrogen chemisorption energies on optimized copper clusters. *Chem. Phys. Lett.* **1995,** *237*, 550-559, https://doi.org/https://doi.org/10.1016/0009-2614(95)00353-6.

7. Gil, A.; Clotet, A.; Ricart, J. M.; Kresse, G.; Garcı; x; a-Hernández, M.; Rösch, N.; Sautet, P., Site preference of CO chemisorbed on Pt(111) from density functional calculations. *Surf. Sci.* **2003,** *530*, 71-87, https://doi.org/https://doi.org/10.1016/S0039-6028(03)00307-8.

8. Ren, X.; Rinke, P.; Scheffler, M., Exploring the random phase approximation: Application to CO adsorbed on Cu(111). *Phys. Rev. B* **2009,** *80*, 045402, https://doi.org/10.1103/PhysRevB.80.045402.

9. Schmidt, P. S.; Thygesen, K. S., Benchmark Database of Transition Metal Surface and Adsorption Energies from Many-Body Perturbation Theory. *J. Phys. Chem. C* **2018,** *122*, 4381-4390, https://doi.org/10.1021/acs.jpcc.7b12258.

10. Schimka, L.; Harl, J.; Stroppa, A.; Grüneis, A.; Marsman, M.; Mittendorfer, F.; Kresse, G., Accurate surface and adsorption energies from many-body perturbation theory. *Nat. Mater.* **2010,** *9*, 741, https://doi.org/10.1038/nmat2806.

11. Garrido Torres, J. A.; Ramberger, B.; Früchtl, H. A.; Schaub, R.; Kresse, G., Adsorption energies of benzene on close packed transition metal surfaces using the random phase approximation. *Phys. Rev. Mater.* **2017,** *1*, 060803, https://doi.org/10.1103/PhysRevMaterials.1.060803.

12. Heßelmann, A.; Görling, A., Correct Description of the Bond Dissociation Limit without Breaking Spin Symmetry by a Random-Phase-Approximation Correlation Functional. *Phys. Rev. Lett.* **2011,** *106*, 093001, https://doi.org/10.1103/PhysRevLett.106.093001.

13. Caruso, F.; Rohr, D. R.; Hellgren, M.; Ren, X.; Rinke, P.; Rubio, A.; Scheffler, M., Bond Breaking and Bond Formation: How Electron Correlation is Captured in Many-Body Perturbation Theory and Density-Functional Theory. *Phys. Rev. Lett.* **2013,** *110*, 146403, https://doi.org/10.1103/PhysRevLett.110.146403.

14. Eshuis, H.; Yarkony, J.; Furche, F., Fast computation of molecular random phase approximation correlation energies using resolution of the identity and imaginary frequency integration. *J. Chem. Phys.* **2010,** *132*, 234114, https://doi.org/10.1063/1.3442749.

15. Sheldon, C.; Paier, J.; Sauer, J., Adsorption of CH4 on the Pt(111) surface: Random phase approximation compared to density functional theory. *J. Chem. Phys.* **2021,** *155*, 174702, https://doi.org/10.1063/5.0071995.

16. Tait, S. L.; Dohnálek, Z.; Campbell, C. T.; Kay, B. D., n-alkanes on Pt(111) and on C(0001)/Pt(111): Chain length dependence of kinetic desorption parameters. *J. Chem. Phys.* **2006,** *125*, 234308, https://doi.org/10.1063/1.2400235.

17. Tait, S. L.; Dohnálek, Z.; Campbell, C. T.; Kay, B. D., n-alkanes on MgO(100). I. Coverage-dependent desorption kinetics of n-butane. *J. Chem. Phys.* **2005,** *122*, 164707, https://doi.org/10.1063/1.1883629.

Chapter 3

A Study of Dispersion:

Alkanes on the Pt(111) Surface using DFT and RPA

This chapter is intended for publication.

Authors: Christopher Sheldon, Joachim Paier, and Joachim Sauer

Chapter 3: A Study of Dispersion: Alkanes on the Pt(111) Surface using DFT and RPA

The low-scaling Random Phase Approximation (RPA) is applied to the adsorption of the first four n-alkanes (C1-C4) on the Pt(111) surface. Experimental measurements at physically relevant coverages are thermodynamically corrected via frequency calculations and compared directly to calculated adsorption energies. RPA Potential Energy Surfaces (PES) are produced and fitted to modified Lennard-Jones potentials. These indicate the slight underbinding of RPA relative to experiment (-40.6 kJ mol^{-1} vs. -45.5 kJ mol^{-1} for n-butane/Pt(111) for RPA and experiment, respectively). The effectiveness of dispersion corrections are studied using the Perdew-Burke-Ernzerhof (PBE) functional, where +D indicates the dispersion correction: PBE+(Grimme's D2, Grimme's D3, Steinmann-Corminboeuf's dDsC, and Tkatchenko's MBD) and are found to consistently overbind energetically and underestimate the platinum-alkane distance. Van der Waals (vdW) density functionals (Perdew's SCAN+rVV10, Michaelides' optB88-vdW, Michaelides' optPBE-vdW, and Lundqvist-Langreth's vdW-DF2) are studied and found to underbind and overbind energetically depending on the individual vdW-functional. Similar variability is found for the platinum-alkane distance. No dispersion correction or vdW-functional is found to consistently repeat the accuracy of RPA in energy and structure. RPA is found to be a suitable method for studying adsorption on metal surfaces and is confirmed as the current benchmark for such systems.

1. Introduction

In the well-known reformation reaction, dehydrogenation of alkanes occurs on the platinum surface. This is chiefly a dispersive interaction and is notoriously tricky to model computationally. Standard Density Functional Theory (DFT) fails to take the dispersion interaction into account, so additional measures must be taken.[1] These come in the form of dispersion corrections (DFT+D) or vdW density functionals.[2,3] The former accounts for the dispersion by means of an additive, post-SCF correction in the form of Eq. (1).

$$E_{disp} = -\sum_{i}^{\mathrm{N_{at}}-1} \sum_{j=i+1}^{\mathrm{N_{at}}} f_{damp}(R_{ij}) \frac{C_6^{ij}}{R_{ij}^6} \tag{1}$$

where E_{disp} is the dispersion energy, N_{at} is the number of atoms, i and j are pairs of atoms, $f_{damp}(R_{ij})$ is a damping function to avoid excessive repulsion at short distances, C_6^{ij} is a dipole-dipole dispersion coefficient, and R_{ij} is the distance between two atoms.

This can be modified in many ways and a plethora of dispersion corrections exists by varying the derivation of the C_6 coefficients and the damping function.[4-7] More sophisticated dispersion corrections include the dipole-quadrupole C_8 coefficients and quadrupole-quadrupole coefficients C_{10},[8-10] or three-body[5] or many-body interactions.[11]

The alternative approach modifies the density functional itself to take the dispersion directly into account. It does this by calculating the non-local correlation energy from the density, shown in Eq. (2).[12]

$$E_c^{nl}[n] = \int d^3\boldsymbol{r} \int d^3\boldsymbol{r}' n(\boldsymbol{r}) \Phi(\boldsymbol{r}, \boldsymbol{r}') n(\boldsymbol{r}') \tag{2}$$

where $E_c^{nl}[n]$ is the non-local correlation energy, $n(\boldsymbol{r})$ is the electron density, and $\Phi(\boldsymbol{r}, \boldsymbol{r}')$ is a non-local interaction kernel.

The vdW-functionals differ by the underlying density functional or by the inclusion of additional terms in the non-local correlation energy.[13-15]

Alternatively, post-Hartree Fock (post-HF) methods may be applied. They account for the dispersion interaction naturally in the correlation energy. However, these are computationally expensive and rarely affordable for large or periodic systems.[16,17] A compromise between cost and accuracy may be made in the hybrid approach, where high accuracy is obtained at significantly reduced cost.[18,19]

The study of metal surfaces, however, introduces further problems in the form of delocalised electrons and a zero-width band gap. The delocalised electrons mean that orbitals cannot be localised, e.g. to Wannier orbitals, for use in a post-HF method requiring them.[16] The zero-width band gap means that, for any finite-order perturbative post-HF method, the correlation energy will diverge.[20,21] One post-HF exception is the Random Phase Approximation (RPA).[22-25] This has been successfully applied to study CO adsorption on metal (111) surfaces,[26] solving the famous "CO/Pt(111) puzzle",[27] as well as several small molecules,[28] and benzene on metal surfaces.[29] We have applied it to CH_4 adsorption on Pt(111) and achieved chemical accuracy (±4 kJ mol^{-1}) for two distinct and physically relevant coverages.[30] RPA calculates the correlation energy using orbitals from an input DFT functional, then derives the non-interacting density-density response function χ_0, which is used to derive the correlation energy via the Adiabatic Connection Fluctuation-Dissipation Theorem (ACFDT), cf. Eq. (3).

$$E_{RPA} = \int_0^\infty \frac{d\omega}{2\pi} \mathrm{Tr}\{\ln[1 - \chi_0(i\omega)\nu] + \chi_0(i\omega)\nu\} \tag{3}$$

where E_{RPA} is the RPA correlation energy, ω is the frequency, and ν is the Coulomb interaction.

With the exception of the benzene study, these have all been using a version of an $O(N^4)$ scaling algorithm,[31,32] where the Alder-Wiser equation is used to calculate the response function.[33,34] This is extremely computationally demanding, scaling at $O(N_G^4 N_k^2)$ where N_G is the number of plane waves (related to the number of atoms in a cell, hence the number of electrons) and N_k is the number of *k*-points, to the extent that it becomes infeasible to study cells with more than ~16 metal atoms.[28,30]

In the case of benzene, a new, low-scaling algorithm was used, where they derived the response function from the Green's function of the occupied and unoccupied states, reducing the scaling to $O(N_G^3 N_k)$, opening up many areas of study.[35,36]

In this paper, we test and apply the low-scaling RPA algorithm to the first four linear alkanes (methane, ethane, propane, and *n*-butane) using the PBE+MBD re-optimised structures of Wellendorff et al.[37] We then calculate the Potential Energy Surface (PES) and compare to thermodynamically-corrected experimental data.[38] We then compare these to adsorption energies calculated by a selection of dispersion corrections (PBE+D2,[4] PBE+D3,[5] PBE+dDsC,[8] and PBE+MBD[11]) and vdW-functionals (vdW-DF2,[12] optB88-vdW,[13] optPBE-vdW,[13] SCAN+rVV10,[15] and BEEF-vdW[14]). Finally, we compare the alkane height above the platinum surface for RPA and compare to the same methods.

2. Models and Methods

2.1. Models

The structures for methane, ethane, propane, and *n*-butane on the Pt(111) surface were taken from Wellendorff et al. and then re-optimised at the PBE+MBD level.[37] The bottom two platinum layers are frozen at the bulk structure, while the top two are free to move. These PBE+MBD structures were subsequently used throughout. We present these in Figure 1 below, along with the definition of vacuum height.

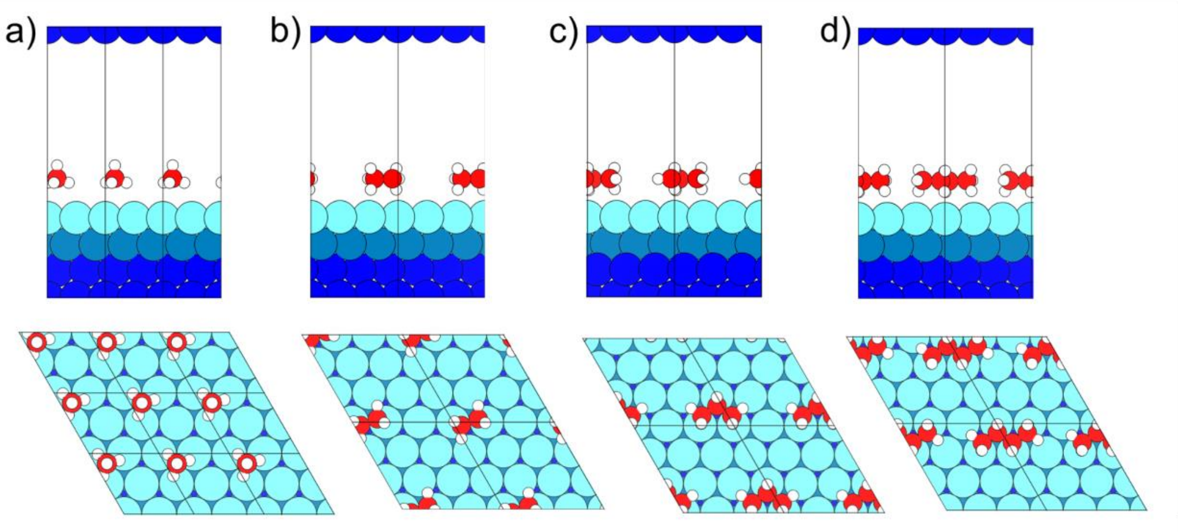

Figure 1. Repeated slab model of methane (a), ethane (b), propane (c), and *n*-butane (d) on Pt(111).[39] Structures are taken from Wellendorff et al. and re-optimised at the PBE+MBD level.[37]

One monolayer (ML) is defined as one adsorbate molecule per surface platinum atom, hence methane is at $^1/_4$ ML coverage and the other three alkanes are at $^1/_9$ ML coverage. N.B. Ref. [37] set the molecule-surface distance and the surface-slab distance to be the same, while we change the molecule-surface distance so that both cells have the same cell parameter orthogonal to the surface, and therefore the same volume, i.e. a vacuum height of ~16 Å. Calculations using RPA have volumes of 14 Å, unless otherwise specified. Isolated alkane molecules were modelled using cubic cells (20^3 Å^3) for DFT calculations. For RPA, this is not routine and requires multiple cells, cf. S1.4 and S1.4.3 for details.

2.2 Methods

The calculations were performed using the projector-augmented wave (PAW) method,[40,41] as implemented in the Vienna ab initio simulation package (VASP).[42] All calculations used a plane wave energy cut-off $E_{cut\text{-}off}$ of 500 eV, unless otherwise specified. Γ-centred meshes were used throughout. For all isolated alkane molecules, only the Γ-point sampling was performed.

2.2.1 DFT calculations

The PAW pseudopotential used to describe the electron-ion interaction for platinum includes the 4f electrons resulting in 10 valence electrons: $[Xe,4f^{14}]5d^96s^1$. Two partial waves were used for each orbital and their cut-off radius was 2.5 au for both the 5d and 6s states. For carbon, 4 ($[He]2s^22p^2$) valence electrons were considered. The partial wave cut-off radii were 1.2 and 1.5 au for 2s and 2p, respectively. For oxygen, 6 ($[He]2s^22p^4$) valence electrons were considered. The partial wave cut-off radii were 1.2 and 1.52 au for 2s and 2p, respectively. For the 1s orbital of hydrogen, a partial wave cut-off radius of 1.1 au was used. These pseudopotentials were used for all structural optimisations.

Calculations involving platinum used 1st order Methfessel-Paxton smearing with a smearing width of 0.2 eV, while those on isolated alkanes used Gaussian smearing with a smearing width of 0.05 eV.

The PBE[43,44] density functional was used, where the presence of a dispersion correction D is denoted as "functional"+D. The Grimme D2[4] and D3,[5] Tkatchenko's Many-Body Dispersion (MBD),[11,45] and Steinmann-Corminboeuf's dDsC[8,46] were used with PBE. Additionally, the non-local vdW density functionals, vdW-DF2,[12] optPBE-vdW,[13] optB88-vdW,[13] and SCAN+rVV10[15,47] were used. The non-spherical contributions relating to the gradient of the density in PAW spheres were calculated when using the vdW-functionals.

All structure optimisations, unless otherwise stated, were performed until all forces on relaxed atoms were converged to below 0.01 eV $Å^{-1}$ (0.194 mE_h $bohr^{-1}$), an electronic energy threshold of $1x10^{-6}$ eV, and a plane wave energy cut-off of 400 eV. The conjugated gradient method was used with cell shape and volume kept constant and only relaxed ions free to move. Structure optimisations using the DFT with the density-dependent dispersion correction from Steinmann and Corminboeuf (DFT+dDsC) were performed until an energy difference between structures of $1x10^{-6}$ eV had been achieved. Vibrational frequencies used central differences for the force derivative with atomic displacements of ±1.5 pm and electronic energy threshold of $1x10^{-8}$ eV. Calculations on the surface used 6x6x1 *k*-point meshes.

The zero point vibrational energy differences and the thermal energy differences were corrected using our MonaLisa program.[48,49]

2.2.2 RPA calculations

All RPA calculations used an electronic energy threshold of 1x10^{-8} eV. For RPA, *GW* PAW pseudopotentials[50] were used with identical core and valence definitions as the above but improved scattering properties for unoccupied states (PBE cores, as of VASP 5.4). For Pt, the partial wave cut-off radii were 2.4 au for both the 5d and 6s states. For C, the partial wave cut-off radii were 1.2 and 1.5 au for 2s and 2p, respectively. For C, the partial wave cut-off radii were 1.2 and 1.52 au for 2s and 2p, respectively. For the 1s orbital of H, a cut-off radius of 0.95 au was used.

RPA calculations were performed in four steps. Initially, a PBE calculation was performed to obtain orbitals and orbital energies. A Hartree-Fock energy calculation was performed using these orbitals, leaving them unchanged. All of the virtual states are then obtained by diagonalisation of the Fock operator. Finally, the ACFDT-RPA (Adiabatic Connection Fluctuation-Dissipation Theorem - Random Phase Approximation) correlation energy[51-53] is calculated. A frequency integration grid density containing 18 points was required for technical convergence for Pt calculations, while a grid of 12 points was sufficient for isolated alkanes. The correlation energy in VASP is automatically extrapolated to convergence with respect to the auxiliary plane wave basis set used for calculating the response function; these correlation energies have been used consistently throughout. All calculations, besides isolated alkanes, neglected the long-wavelength contributions to speed up *k*-point convergence.[54] The number of plane waves is set by the number of maximal plane waves in the step generating the orbitals. Additionally, we include the contribution of the automated VASP extrapolation with respect to the auxiliary plane wave basis set used for calculating the response function $E^{\chi}_{cut-off}$.[31]

We used the low-scaling RPA algorithm throughout.[55] We have used the finite-temperature algorithm as recommended, to avoid the Kohn-Luttinger Conundrum issues due to the metal's zero-width band-gap.[55,56] The finite-temperature algorithm requires the use of Fermi smearing. We tested this and found a smearing width of 0.01 eV to be suitable for use (cf. S1.1-S1.3).

3. Results and Discussion

3.1 Comparison with experiment

3.1.1 Coverage

When comparing to experiment, one must be careful to compare correct coverages, i.e the *theoretician*'s coverage in terms of molecules per surface atom and the *experimentalist*'s coverage in terms of saturation in experiment. We have previously used $^1/_3$ ML coverage as the physical saturated coverage for CH_4/Pt(111), i.e. (√3x√3)R30°;[30] we also studied $^1/_4$ ML coverage, correcting the experimental energy according to Eq (7) in Ref. [38]. For ethane and propane, we assume saturated coverages of $^1/_4$ ML for both, i.e. one molecule per (2x2) cell, as determined by LEED.[57] The case of *n*-butane is more complex, with an ordered monolayer observed at 0.2 ML coverage by LEED (i.e. a ($\sqrt{3}$x$\sqrt{7}$)R30° cell),[57-59] where all chains are lying parallel to the surface; this corresponds to a TPD peak at 186 K or 171 K, Ref. [38] and [59], respectively. As the coverage increases to 0.35 ML (by LEED), a more densely packed ordered phase forms where all chains tilt away from the surface, corresponding to a TPD peak at 98 K.[38,59] These correspond to two distinct phases in the first monolayer (for a detailed discussion of the adsorption of *n*-butane on Pt(111), cf. Ref. [59]). As TPD studies recognise these as distinct peaks, we choose to focus on the higher temperature peak, with the parallel-lying molecules, from which the experimental energy is taken, and take 0.2 ML to be the saturated coverage.

3.1.2 Experimental energies

Besides coverage, it is also important to compare between the correct thermodynamic properties.

Our experimental reference observes the Arrhenius activation energies E_a at temperature.[38] These are distinct from the adsorption energies ΔE_{ads} calculated computationally at absolute zero. We have performed frequency calculations using PBE+MBD to account for the zero point vibrational energy (ZPVE) differences ΔE_{ZPV} and the thermal energy differences ΔE_{therm}, according to Eq. 4:[30,60,61]

$$\Delta E_{ads} = \Delta H_{ads}(T) - \Delta E_{ZPV} - \Delta E_{therm}(T) + RT = - E_A(T) - \Delta E_{ZPV} - \Delta E_{therm}(T) + 2\ RT \tag{4}$$

where $E_a(T)$ is the Arrhenius activation energy, $\Delta H_{ads}(T)$ is the activation enthalpy of adsorption, ΔE_{ads} is the calculated adsorption energy, ΔE_{ZPV} is change in ZPVE on adsorption, $\Delta E_{therm}(T)$ is the thermal energy correction due to temperature T, p is the system pressure, and ΔV is the change of volume during the process.

We present these values in Table 1 at physically meaningful coverages for the first four *n*-alkanes, broken down into the substituents of Eq. 4.[62]

Table 1. Breakdown of terms from Eq. 4 in converting from the observed adsorption activation energy E_a and the observed energy ΔE_{ads}. Structure optimisation and frequency analysis performed at the PBE+MBD level. 1 ML is one molecule per surface atom. A plane wave energy cut-off of 500 eV and a 6x6x1 *k*-point mesh were used.

Alkane	Methane	Ethane	Propane	Butane
Obs. $-E_a$ [38]	-15.5±1.6	-28.7±2.9	-41.3±4.1	-50.7±5.1
θ / ML	$^1/_4$	$^1/_9$	$^1/_9$	$^1/_9$
T / K	63	106	139	171
2RT	1.05	1.76	2.31	2.84
ΔE_{therm}	-0.38	0.51	1.16	1.69
ΔE_{ZPVE}	0.88	-1.88	-3.94	-5.79
Obs. ΔE_{ads}	-14.9±1.6	-25.6±2.9	-36.2±4.1	-43.8±5.1

It should be noted that all ΔE_{ZPV} are negative, except for methane. While uncommon in literature, this is not a unique case.[63-65] Upon analysis of the vibrational modes, many redshifts are seen. Most of these are 10-30 cm^{-1}, matching the 20 cm^{-1} redshift commonly seen in alkane monolayers on metal surfaces.[66] However, particularly strong redshifts (~200 cm^{-1}) are seen for the C-H stretches directed towards surface platinum atoms (see Table S2.1). Using RAIRS (also known as IRAS), strong redshifts have also been observed, notably ν_1, the symmetric CH_3-stretch vibrational mode of ethane, which shifts 101 cm^{-1} from 2954 cm^{-1} in the gas phase[67] to 2853 cm^{-1} upon adsorption.[66] Our scaled, calculated redshift of 187 cm^{-1} qualitatively agrees with this. This red-shifting of alkane vibrational modes upon adsorption is due to charge transfer from the metal surface to the adsorbate.[68-72] The positive ΔE_{ZPVE} seen for methane is indicative that there is no such charge transfer seen and, hence, a much weaker red-shift than for the other alkanes (for further detail, see Ref. [30]).

These corrections to the experimentally observed values allow direct comparison with our calculated energies. However, when comparing computational methods, dispersion corrections and vdW-functionals, it is also beneficial to have a computational reference as well.

3.2 RPA results

In our previous work, we studied the use of the RPA to investigate the adsorption of methane on the Pt(111) surface.[30] We briefly commented there that a newer, lower-scaling algorithm was available at $O(N_k N_G^3)$,[35,36] rather than $O(N_k^2 N_G^4)$ we used.[31] We tested this algorithm on several systems but, for the sake of space, we omit this here and refer those interested to Section S1 of the Supplementary Material. The lower cost of this algorithm, along with the use of supercomputing facilities, enabled us to produced Potential Energy Surfaces (PES) for these four alkanes at different platinum-carbon distances r(Pt-C) above the Pt(111) surface. We present these below in Figure 2.

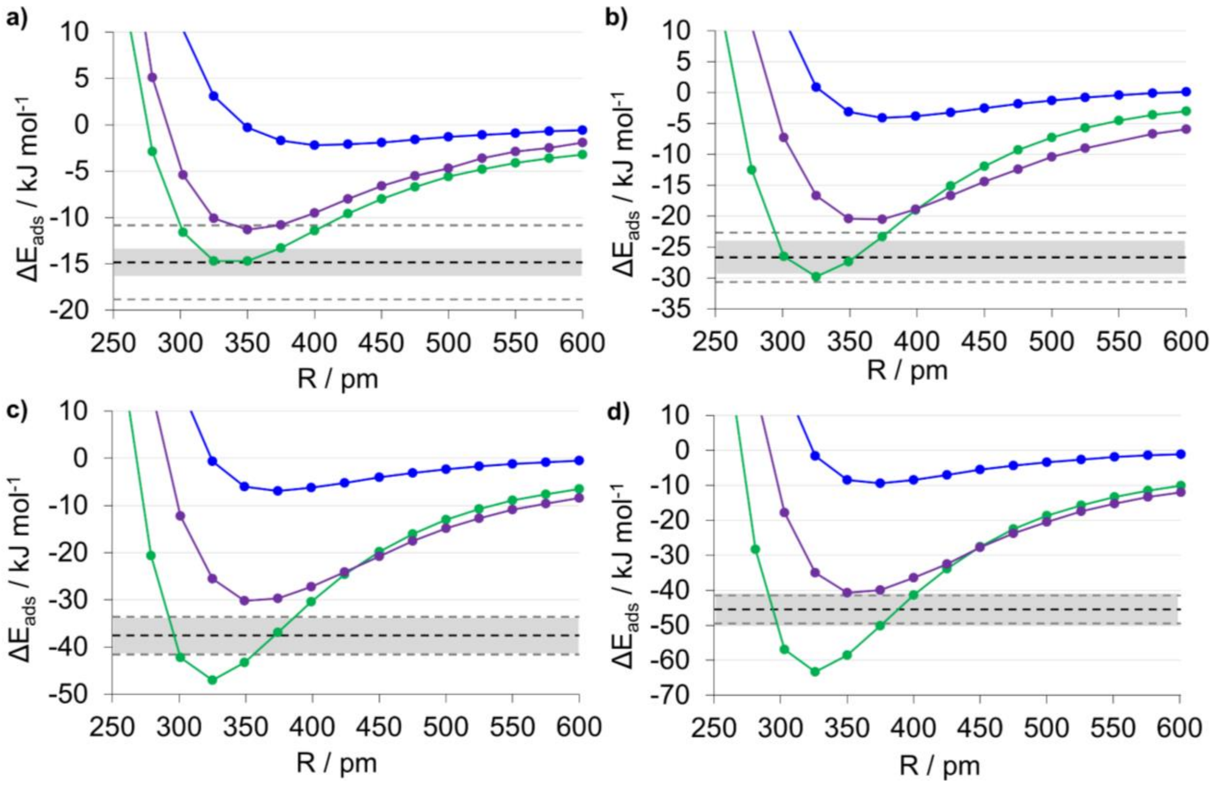

Figure 2. Adsorption energy ΔE$_{ads}$ against platinum-carbon distance r(Pt-C) for methane (a), ethane (b), propane (c), and *n*-butane (d) using PBE, PBE+MBD, and RPA. The carbon atoms were frozen in place and optimised at the PBE+MBD level, then used for all calculations. Experimentally derived adsorption energies with error (cf. Table 1),[38] and chemical accuracy (±4 kJ mol^{-1}) are shown for comparison.

From Figure 2, it is immediately clear that the PBE+MBD and RPA capture the majority of the dispersion, where PBE fails. PBE+MBD always predicts stronger binding than RPA, except at extended distances. For methane, this is not very important, as the difference between the two curves is usually only a few kJ mol^{-1}, although it is clear that RPA is underbinding, scarcely reaching chemical accuracy, the PBE+MBD readily matches with experiment. This is largely in agreement to our previous results. The differences are attributed to the use of Wellendorff et al.'s structure for calculations, never amounting to more than ~1 kJ mol^{-1}.

Starting with ethane, the PBE+MBD and RPA curves begin to diverge more. The PBE+MBD curve overbinds, remaining close to experiment for ethane. This overbinding increases with carbon chain length, such that for propane there is noticeable overbinding, becoming more pronounced for *n*-butane, to the extent that there is a difference of around 20 kJ mol^{-1} with respect to experiment at equilibrium. The RPA curves, on the other hand, consistently underbind by a small degree, 7 kJ mol^{-1} (for ethane and propane) and 5 kJ mol^{-1} (for *n*-butane). This confirms the suitability of RPA for describing the dispersion interaction. We note here that this underbinding appears to be a general feature of the alkanes on metals, as we have also seen this in preliminary investigations of other metal (111) surfaces (see S3.2 for details). This is in contrast to that observed using the same algorithm for benzene on metal surfaces, where there was slight overbinding on the Pt(111) surface, with a slight underbinding for Cu(111), Ag(111), Au(111), and Pd(111).[29]

Additionally, of great interest is the consistency with which the RPA predicts larger platinum-carbon distances. This is only by a few pm for methane but this increases to at least 25 pm for ethane, propane, and *n*-butane. This closer distance is another indicator of noticeable overbinding for PBE+MBD.

3.3 Fitting Adsorption Energy Curves

In an attempt to find the equilibrium distances and energies more precisely, we modified the Lennard-Jones potential to fit to these curves. It is well-known that the R^{-6} decay seen between atoms and molecules in the gas phase is not found for the solid phase, where R^{-3} decay is predicted between a neutral atom and the solid surface from theory,[73] and $R^{-2.5}$ decay is predicted between sheets from theory,[74] (R^{-4} is calculated between graphene sheets for the RPA, which dominates at short distances)[75,76]. Knowing this, we modified the decay of the attractive van der Waals interaction and the repulsive interaction, according to Equation (5):

$$E_{mLJ}(r) = 4\varepsilon[(\sigma/r)^a - (\sigma/r)^b] \tag{5}$$

where E_{mLJ} is the modified Lennard-Jones potential energy, ε is depth of the potential well, σ is the distance at which the potential energy is zero, r is the Pt-C distance, and a and b are fitting constants.

For all RPA results, good fitting was found for a value of 4 for b (i.e. R^{-4} decay) and then used a value of 8 (for methane) or 6 (for ethane, propane, and *n*-butane). The original Lennard-Jones repulsive exponent was without physical justification, so we feel comfortable with modifying it to better fit our PES. In spite of our “manual fit”, we found this to be reasonable for describing the equilibrium, giving an example below in Figure 3. We expect that it is accurate to a few pm for the equilibrium distance r_{eq} and ~0.5 kJ mol^{-1} for the equilibrium energy E_{eq}. The remaining figures are shown in Figure S4.1-S4.3 and the fitting parameters in Table S4.4. N.B. the methane fit was poorer than the other alkanes (cf. Figure S4.1), so the lowest calculated point, lying close to equilibrium, was taken instead; this results in a difference of ~0.1 kJ mol^{-1} in the energy and ~4 pm in the distance.

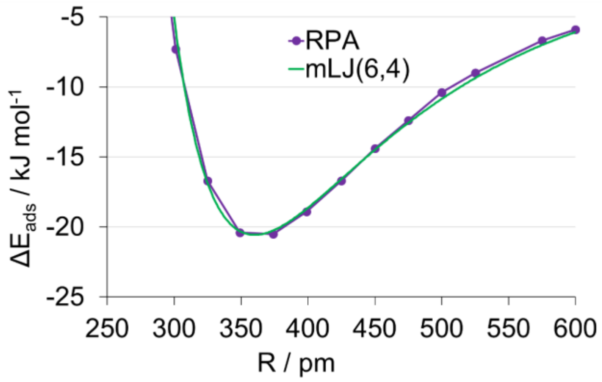

Figure 3. Adsorption energy ΔE_{ads} against platinum-carbon distance r(Pt-C) for ethane using RPA and a modified Lennard-Jones potential.

We also applied this modified Lennard-Jones potential to our previous hybrid RPA:PBE results (see Chapter 2). Here an improved fit could be obtained by allowing free variation of a and b. The figures for these are in S4.2. We report the E_{eq} and r_{eq} for the four alkanes on Pt(111) using RPA and for methane and ethane on Pt(111) using RPA:PBE and RPA:PBE+MBD in Tables 7 and 8 below, respectively.

3.4 Comparing Methods of Dispersion

Having a suitable computational reference, as well as the correct experimental data, it is now appropriate to compare and assess different dispersion corrections and vdW-functionals. We present these in Table 2.

Table 2. Adsorption energy ΔE_{ads} (kJ mol^{-1}) for C1-C4 alkanes with given coverage and dispersion correction for a selection of density functionals. Ref. [37]'s structures were used, then re-optimised. A plane wave energy cut-off $E_{cut\text{-}off}$ of 400 eV, 6x6x1 *k*-mesh, and a 16 Å vacuum height were used.

Alkane	Methane	Ethane	Propane	Butane
θ / ML[a]	$^1/_4$	$^1/_9$	$^1/_9$	$^1/_9$
Cell	(2x2)	(3x3)	(3x3)	(3x3)
Obsd. E_a[38]	-15.5	-28.9	-41.5	-50.9
T / K	63	106	139	171
Obsd. ΔE_{ads}[b]	-14.9	-25.6	-36.2	-43.8
BEEF-vdW[37]	-15	-21	-29	-38
SCAN+rVV10	-43.5	-73.7	-105.9	-137.1
optB88-vdW	-21.9	-36.5	-53.8	-71.3
optPBE-vdW	-23.0	-34.7	-49.6	-65.5
vdW-DF2	-16.8	-37.1	-48.6	-61.1
PBE+dDsC	-18.9	-32.8	-48.0	-64.7
PBE+MBD	-14.9	-31.4	-47.0	-63.3
PBE+D2	-51.1	-78.5	-115.4	-142.7
PBE+D2 (surface)[c]	-40.4	-60.4	-92.1	-114.2
PBE+D2 (Xe)[d]	-25.7	-42.9	-63.5	-82.4
PBE+D3	-26.6	-45.5	-64.9	-86.8
RPA[e]	-11.3[f]	-20.6	-30.1	-40.6
RPA:PBE[g]	-14.4	-17.8	-	-
RPA:PBE+MBD[g]	-15.9	-24.9	-	-

[a] where 1 ML is defined as one molecule per surface atom.

[b] corrected for ZPVE using PBE+MBD, cf. Table 6.

[c] where the C_6 parameter has been set to 0 for all Pt atoms, except for those on the top layer.

[d] where the C_6 parameter for Xe has been used for all Pt atoms.

[e] 14 Å vacuum used.

[f] minimum point, not modified Lennard-Jones potential

[g] cf. Chapter 2 for details.

To allow easier analysis, we split these into vdW-functional and additive dispersion corrections in Figures 4 and 5, respectively, to enable better comparison.

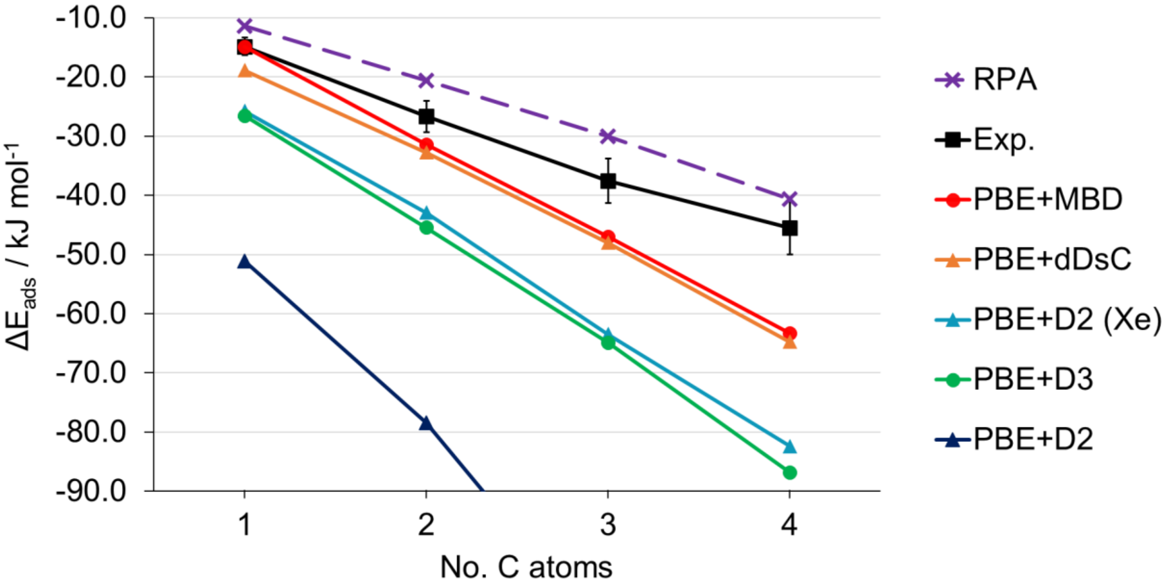

Figure 4. Adsorption energy ΔE_{ads} for the *n*-alkanes on the Pt(111) surface using a selection of dispersion corrections and compared to the experimental energy with experimental error shown.

It is clear from Figure 4 that PBE+D2 overbinds significantly, as has been previously reported in the literature.[5,77] We suspected that this might be in part due to the metal's valence electrons screening the dispersion interaction from platinum atoms below the surface layer. We tested this by setting the C_6 parameters to zero for all platinum atoms, except for those in the surface layer. However, this offers fairly minimal improvement, accounting for only around one-sixth of the discrepancy at most. Changing approach, we followed the assumption of Andersson that the screening of the dispersion interaction by the valence electrons may be adequately described by treating the platinum atoms like hard, noble gas cores.[78] The platinum's C_6 parameter were therefore set to those of Xe, PBE+D2(Xe). This proved successful, shifting all of the adsorption energies to be in line with PBE+D3, indicating that the failure of D2 is due to the C_6 parameter of the metal. While PBE+D3 still overbinds, this is to a lesser extent than PBE+D2.

The PBE+MBD and the PBE+dDsC results are very similar, separated by only a few kJ mol^{-1}, and offer a clear improvement. Both of these dispersion corrections take the electron density into account, allowing the modification of the C_6 parameters (and other parameters unique to each method). We expect that this is to account for the improvement. However, with increasing chain length, the error relative to experiment continues to increase, until it is ~20 kJ mol^{-1} for *n*-butane. It is clear from Figure 4 that different dispersion corrections predict wildly different binding strengths. We save the discussion on RPA for later, noting briefly slight underbinding, which, at a consistent ~7 kJ mol^{-1}, is a significant improvement on any of the dispersion corrections.

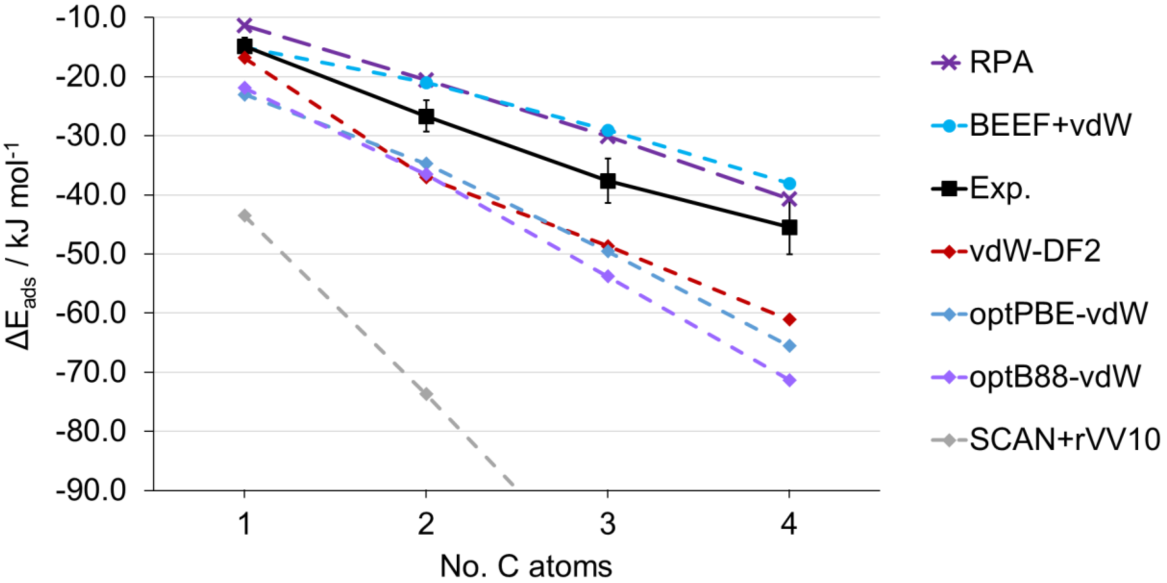

Figure 5. Adsorption energy ΔE_{ads} for the *n*-alkanes on the Pt(111) surface using a selection of dispersion corrections and compared to the experimental energy with experimental error shown.

Figure 5 allows us to compare against vdW density functionals, rather than only the dispersion corrections. It is clear that SCAN+rVV10 overbinds significantly. We expect that this is due to SCAN, like M06,[79] already accounting for a certain amount of mid-range dispersion (cf. Table S5.1). We note that this is in stark contrast to Sun, Perdew, and co. who found that it performed well for benzene and graphene on several metal surfaces.[15] This is in significant contrast to the other vdW functionals, with vdW-DF2, optPBE-vdW, and optB88-vdW all performing similarly, overbinding to a similar degree as PBE+MBD. It is certainly worthy of note that these three density functionals, where the dispersion interaction is directly dependent on the density, matches well to PBE+MBD and PBE+dDsC, where the dispersion is indirectly dependent on the density, indicating a surprising degree of similarity in otherwise conceptually divergent approaches. We include the BEEF-vdW results of Ref. [37], which underbind, though remain consistently close to the RPA values. On analysis of the energies alone, this would imply that BEEF-vdW performed similarly to RPA. We found that RPA consistently underbinds relative to experiment. This is only by a few kJ mol^{-1}, ranging from ~3 kJ mol^{-1} for methane to ~7 kJ mol^{-1} for propane. This indicates that, although RPA accounts for most of the dispersion interaction, a small amount is missing. We now present the optimised platinum-carbon distance r(Pt-C) for the preceding methods in Table 3 below.

Table 3. Platinum-carbon heights r(Pt-C) in pm for C1-C4 alkanes with given coverage and dispersion correction for a selection of density functionals. Averages were taken for the Pt and C heights then subtracted. Ref.[37]'s structures were used, then re-optimised. A plane wave energy cut-off $E_{\text{cut-off}}$ of 400 eV, 6x6x1 *k*-mesh, and a 16 Å vacuum height were used.

Alkane	Methane	Ethane	Propane	Butane
θ / ML[a]	$^1/_4$	$^1/_9$	$^1/_9$	$^1/_9$
Cell	(2x2)	(3x3)	(3x3)	(3x3)
BEEF-vdW[37]	385	390	390	397
SCAN+rVV10	302	302	303	306
optB88-vdW	344	336	338	336
optPBE-vdW	358	351	351	349
vdW-DF2	359	361	362	360
PBE+dDsC	339	332	333	330
PBE+MBD	337	326	325	325
PBE+D2	301	308	310	312
PBE+D2 (surface)[b]	302	313	312	316
PBE+D2 (Xe)[c]	324	327	325	321
PBE+D3	330	326	328	324
RPA[d]	350[e]	360	356	357
RPA:PBE[f]	369	386	-	-
RPA:PBE+MBD[f]	371	381	-	-

[a] where 1 ML is defined as one molecule per surface atom.
[b] where the C_6 parameter has been set to 0 for all Pt atoms, except for those on the top layer.
[c] where the C_6 parameter for Xe has been used for all Pt atoms.
[d] 14 Å vacuum used.
[e] lowest calculated point, not modified Lennard-Jones potential
[f] cf. Chapter 2 for details.

We split these into vdW-functional and additive dispersion corrections in Figures 6 and 7, respectively, to enable better comparison.

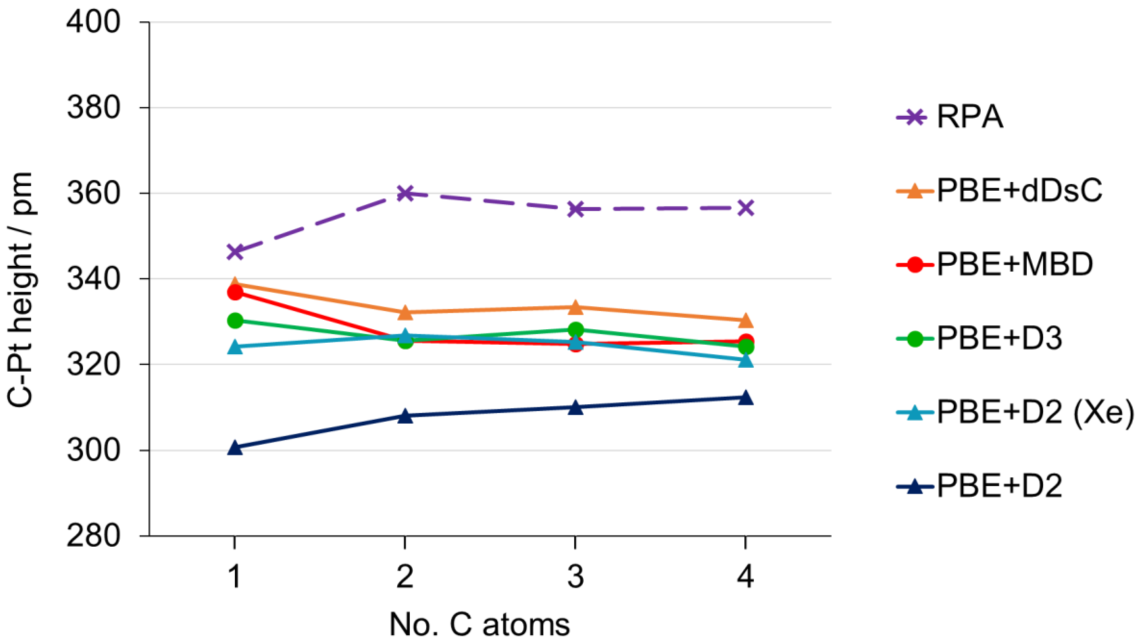

Figure 6. Platinum-carbon heights r(Pt-C) for the *n*-alkanes on the Pt(111) surface using a selection of dispersion corrections and compared to the experimental energy.

It is immediately clear that there is great discrepancy between the dispersion corrections. PBE+D2 predicts distances closest to the surface, which is to be expected given its significant overbinding. PBE+D2(Xe), PBE+D3, and PBE+MBD all give similar distances, with the exception of methane where the variation is over a range of ~15 pm. PBE+dDsC predicts slightly longer distances, though by only around ~5 pm. Due to the sparsity of experimental data for platinum-carbon heights for our system, we compare against the highest level method, that of RPA, which we take as our reference. We expect this to be reasonable, given the accuracy with which RPA metal-carbon distances matched experiment for benzene on Au(111) and Ag(111), within 5 pm of the experimental range.[29] Considering this, it is clear that all of the dispersion corrections tested here, predict alkanes to lie too close to the surface.

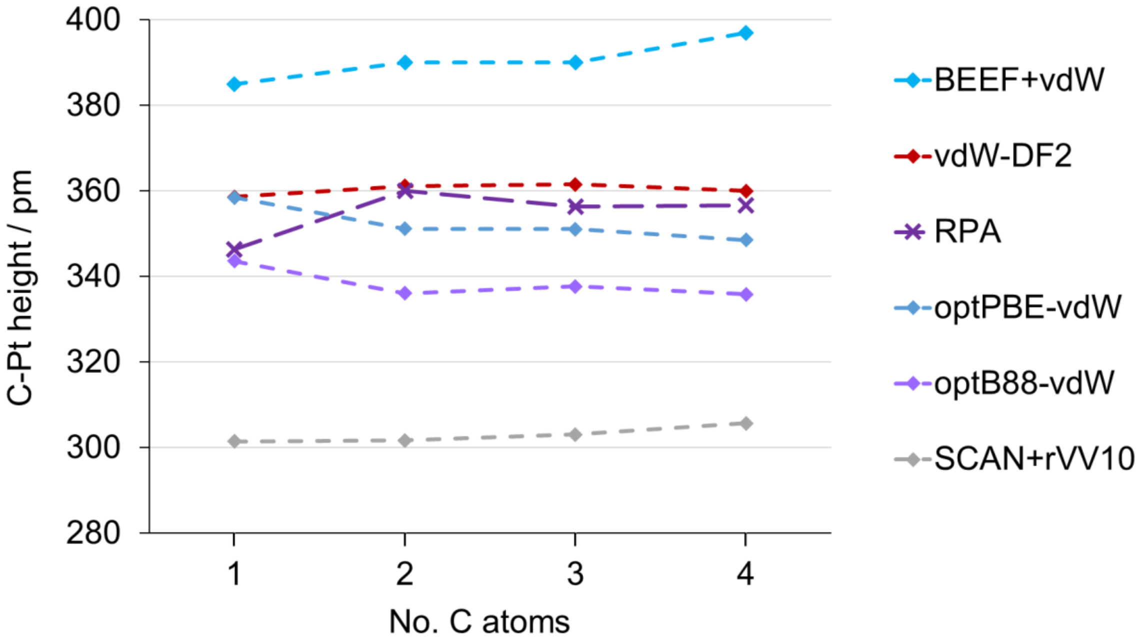

Figure 7. Platinum-carbon heights r(Pt-C) for the *n*-alkanes on the Pt(111) surface using a selection of dispersion corrections and compared to the experimental energy.

There is no significant improvement if we turn to the vdW density functionals. SCAN+rVV10 predicts distances closest to the surface and remains a noticeable outlier. The BEEF-vdW finds distances furthest away, far from those predicted by RPA. This is particularly noteworthy given that the RPA and BEEF-vdW adsorption energies were so close, highlighting the importance of looking at both the energy and structure when comparing methods, as one criterion is insufficient. Additionally, the distance increases noticeably for BEEF-vdW with increasing chain length, which is not seen by the other vdW density functionals (besides SCAN+rVV10) and was only seen for PBE+D2 out of the dispersion corrections. Langreth's vdW-DF2 performs well, matching closely with RPA for all the alkanes, except for methane, and changing by only a small amount with increasing chain length, similarly to RPA. Michaelides' optPBE-vdW and optB88-vdW follow parallel trends, though optPBE-vdW lies much closer to RPA for all alkanes (~350 pm vs ~360 pm), except for methane, where optB88-vdW is almost exactly the same as RPA. However, optB88-vdW diverges from RPA with increasing chain length. The picture is not so clear-cut for the vdW functionals as it was for the dispersion corrections, with no consistent increase or decrease in the platinum-carbon distance relative to RPA. While we do not doubt the ability of RPA to predict adsorbate heights, this could be confirmed by new experimental data, such as by Normal Incidence X-ray Standing Wave (NIXSW).[80]

3.5 Comparison to Hybrid Approach

Having analysed the dispersion corrections and vdW density functionals, we now make a brief comment on our hybrid approach to account for dispersion (cf. Table 2 and Chapter 2). Like RPA, RPA:PBE underbinds relative to experiment. It does not reproduce the periodic RPA value exactly, although it should be stressed that our hybrid results use structures from Chapter 2 and not Wellendorff et al.'s structures as here, so some discrepancies should be expected; additionally, they are at different coverages for ethane ($^1/_4$ vs $^1/_9$ ML for hybrid and RPA, respectively). RPA:PBE predicts adsorption energies 3 kJ mol^{-1} greater for methane and 3 kJ mol^{-1} lesser for ethane than periodic RPA. This indicates that there is a differing gradient with respect to alkane chain length between the two approaches; however, this would require a third point (i.e. propane) at the hybrid level and the same structures to confirm. RPA:PBE+MBD performs better than both RPA and RPA:PBE, lying consistently close to experiment, well within the experimental error. We attribute this to a compensating effect between the underbinding of RPA and the overbinding of PBE+MBD, with RPA over- and PBE+MBD underscreening the dispersion interaction. Overall, the adsorption energies of our hybrid approach are broadly similar to RPA.

We find greater differences in the platinum-carbon distances (cf. Table 3) between periodic RPA and the hybrid approaches. There is not a significant difference (only a few pm) between the two hybrid approaches. Both of these predict carbon heights above the surface ~20 pm greater than RPA. This indicates that our approach correctly predicts the adsorption energy, while underestimating the platinum-carbon distance.

We note here that our hybrid approach saves significant CPU time relative to the low-scaling RPA algorithm (cf. Table S1.13), though with the advent of High Performance Computing (HPC), we confirm the work of Garrido Torres et al.,[29] finding that the wall time is significantly reduced to 3 hours with 384 cores and ~3 TB of RAM. While this cost is significant, it does indicate that such calculations are now within the realm of possibility. We endorse the low-scaling algorithm for use if sufficient resources are available, while finding our hybrid approach to be a reasonable compromise between cost and accuracy.

4. Conclusions

We have found that the low-scaling RPA algorithm is appropriate and readily applicable for the study of molecules adsorbed on the platinum surface. It was found to follow the trend of the experimentally-derived adsorption energy, while consistently underbinding by up to 7 kJ mol^{-1}, indicating that it fails to capture the full dispersion interaction. Relative to experiment, all dispersion corrections were found to overbind, to varying degrees. This becomes increasing significantly with chain length until it is at least ~20 kJ mol^{-1} for *n*-butane. The vdW density functionals also tended to overbind, with the single exception of BEEF-vdW, which matches well to RPA energies.

The height of alkanes above the platinum surface was found to vary significantly, somewhat independent of how the dispersion was described. RPA predicted a platinum-carbon height of ~360 pm, which we take as a benchmark. All dispersion corrections predict alkanes to lie closer to the platinum surface than RPA, not unexpected from the overbinding for each with PBE+D. The vdW functionals vary by more at the extremes, while clustering around the RPA height, and is very dependent on the individual functional. The functional vdW-DF2 shows the best agreement with RPA for platinum-carbon height, while overbinding for the adsorption energies. Conversely, BEEF-vdW showed good agreement with RPA adsorption energies, while overestimating the alkanes' height above the platinum surface.

The RPA:PBE(+MBD) hybrid approach is found to predict adsorption energies well, with RPA:PBE coming close to RPA. With the slight overbinding of PBD+MBD, RPA:PBD+MBD predicts adsorption energies close to experiment. The platinum-carbon height is overestimated relative to RPA.

From the dispersion corrections, we recommend PBE+MBD or PBD+dDsC and, from the vdW density functionals, we recommend optB88-vdW, optPBE-vdW, or vdW-DF2, with the caveat that these will all overbind. However, no dispersion correction or vdW density functional succeeds universally, and a compromise between adsorption energy and structure must be made. RPA and its hybrid derivatives are found to provide the most consistently reliable results.

Supplementary Material

Details of clusters in VASP, images of clusters, details of clusters using a Gaussian basis, and tables used for graphs.

Acknowledgements

This work has been supported by German Research Foundation (DFG) with a Reinhart Koselleck grant, as well as by the "Fonds der Chemischen Industrie", and the Fritz-Haber Institute in the form of external PhD funding. The HLRN is acknowledged for computer time grants (bec00213 and bec00230). We thank F. Studt for providing the Wellendorff et al. structures used in this work and B. Ramberger for useful discussion.

Author Declarations

Conflict of Interest

The authors have no conflicts of interest to disclose.

Data Availability Statements

Data available on request from the authors.

5. References

1. Tang, K. T.; Toennies, J. P., An improved simple model for the van der Waals potential based on universal damping functions for the dispersion coefficients. *J. Chem. Phys.* **1984,** *80*, 3726-3741, https://doi.org/10.1063/1.447150.
2. Grimme, S.; Hansen, A.; Brandenburg, J. G.; Bannwarth, C., Dispersion-Corrected Mean-Field Electronic Structure Methods. *Chem. Rev.* **2016,** *116*, 5105-5154, https://doi.org/10.1021/acs.chemrev.5b00533.
3. Dion, M.; Rydberg, H.; Schröder, E.; Langreth, D. C.; Lundqvist, B. I., Van der Waals Density Functional for General Geometries. *Phys. Rev. Lett.* **2004,** *92*, 246401, https://doi.org/10.1103/PhysRevLett.92.246401.
4. Grimme, S., Semiempirical GGA-type density functional constructed with a long-range dispersion correction. *J. Comput. Chem.* **2006,** *27*, 1787-1799, https://doi.org/10.1002/jcc.20495.
5. Grimme, S.; Antony, J.; Ehrlich, S.; Krieg, H., A consistent and accurate ab initio parametrization of density functional dispersion correction (DFT-D) for the 94 elements H-Pu. *J. Chem. Phys.* **2010,** *132*, 154104, https://doi.org/10.1063/1.3382344.
6. Grimme, S.; Ehrlich, S.; Goerigk, L., Effect of the damping function in dispersion corrected density functional theory. *J. Comput. Chem.* **2011,** *32*, 1456-1465, https://doi.org/10.1002/jcc.21759.
7. Tkatchenko, A.; Scheffler, M., Accurate Molecular Van Der Waals Interactions from Ground-State Electron Density and Free-Atom Reference Data. *Phys. Rev. Lett.* **2009,** *102*, 073005, https://doi.org/10.1103/PhysRevLett.102.073005.
8. Steinmann, S. N.; Corminboeuf, C., A generalized-gradient approximation exchange hole model for dispersion coefficients. *J. Chem. Phys.* **2011,** *134*, 044117, https://doi.org/10.1063/1.3545985.
9. Becke, A. D.; Johnson, E. R., Exchange-hole dipole moment and the dispersion interaction revisited. *J. Chem. Phys.* **2007,** *127*, 154108, https://doi.org/10.1063/1.2795701.
10. Becke, A. D.; Johnson, E. R., A unified density-functional treatment of dynamical, nondynamical, and dispersion correlations. *J. Chem. Phys.* **2007,** *127*, 124108, https://doi.org/10.1063/1.2768530.

11. Tkatchenko, A.; DiStasio, R. A.; Car, R.; Scheffler, M., Accurate and Efficient Method for Many-Body van der Waals Interactions. *Phys. Rev. Lett.* **2012,** *108*, 236402, https://doi.org/10.1103/PhysRevLett.108.236402.

12. Lee, K.; Murray, É. D.; Kong, L.; Lundqvist, B. I.; Langreth, D. C., Higher-accuracy van der Waals density functional. *Phys. Rev. B* **2010,** *82*, 081101, https://doi.org/10.1103/PhysRevB.82.081101.

13. Klimeš, J.; Bowler, D. R.; Michaelides, A., Chemical accuracy for the van der Waals density functional. *J. Phys.: Condens. Matter* **2009,** *22*, 022201, https://doi.org/10.1088/0953-8984/22/2/022201.

14. Wellendorff, J.; Lundgaard, K. T.; Møgelhøj, A.; Petzold, V.; Landis, D. D.; Nørskov, J. K.; Bligaard, T.; Jacobsen, K. W., Density functionals for surface science: Exchange-correlation model development with Bayesian error estimation. *Phys. Rev. B* **2012,** *85*, 235149, https://doi.org/10.1103/PhysRevB.85.235149.

15. Peng, H.; Yang, Z.-H.; Perdew, J. P.; Sun, J., Versatile van der Waals Density Functional Based on a Meta-Generalized Gradient Approximation. *Phys. Rev. X* **2016,** *6*, 041005, https://doi.org/10.1103/PhysRevX.6.041005.

16. Pisani, C.; Maschio, L.; Casassa, S.; Halo, M.; Schütz, M.; Usvyat, D., Periodic local MP2 method for the study of electronic correlation in crystals: Theory and preliminary applications. *J. Comput. Chem.* **2008,** *29*, 2113-2124, https://doi.org/https://doi.org/10.1002/jcc.20975.

17. Alessio, M.; Usvyat, D.; Sauer, J., Chemically Accurate Adsorption Energies: CO and H2O on the MgO(001) Surface. *J. Chem. Theory Comput.* **2019,** *15*, 1329-1344, https://doi.org/10.1021/acs.jctc.8b01122.

18. Piccini, G.; Alessio, M.; Sauer, J.; Zhi, Y.; Liu, Y.; Kolvenbach, R.; Jentys, A.; Lercher, J. A., Accurate Adsorption Thermodynamics of Small Alkanes in Zeolites. Ab initio Theory and Experiment for H-Chabazite. *J. Phys. Chem. C* **2015,** *119*, 6128-6137, https://doi.org/10.1021/acs.jpcc.5b01739.

19. Piccini, G.; Alessio, M.; Sauer, J., Ab Initio Calculation of Rate Constants for Molecule–Surface Reactions with Chemical Accuracy. *Angew. Chem. Int. Ed.* **2016,** *55*, 5235-5237, https://doi.org/10.1002/anie.201601534.

20. Paier, J.; Ren, X.; Rinke, P.; Scuseria, G. E.; Grüneis, A.; Kresse, G.; Scheffler, M., Assessment of correlation energies based on the random-phase approximation. *New J. Phys.* **2012,** *14*, 043002, https://doi.org/10.1088/1367-2630/14/4/043002.

21. F. E. Harris; H. J. Monkhorst; Freeman, D. L., *Algebraic and Diagrammatic Methods in Many-Fermion Theory*. Oxford University Press: New York, Oxford, 1992.

22. Bohm, D.; Pines, D., A Collective Description of Electron Interactions. I. Magnetic Interactions. *Phys. Rev.* **1951,** *82*, 625-634, https://doi.org/10.1103/PhysRev.82.625.

23. Pines, D.; Bohm, D., A Collective Description of Electron Interactions: II. Collective vs Individual Particle Aspects of the Interactions. *Phys. Rev.* **1952,** *85*, 338-353, https://doi.org/10.1103/PhysRev.85.338.

24. Bohm, D.; Pines, D., A Collective Description of Electron Interactions: III. Coulomb Interactions in a Degenerate Electron Gas. *Phys. Rev.* **1953,** *92*, 609-625, https://doi.org/10.1103/PhysRev.92.609.

25. Pines, D., A Collective Description of Electron Interactions: IV. Electron Interaction in Metals. *Phys. Rev.* **1953,** *92*, 626-636, https://doi.org/10.1103/PhysRev.92.626.

26. Schimka, L.; Harl, J.; Stroppa, A.; Grüneis, A.; Marsman, M.; Mittendorfer, F.; Kresse, G., Accurate surface and adsorption energies from many-body perturbation theory. *Nat. Mater.* **2010,** *9*, 741, https://doi.org/10.1038/nmat2806.

27. Feibelman, P. J.; Hammer, B.; Nørskov, J. K.; Wagner, F.; Scheffler, M.; Stumpf, R.; Watwe, R.; Dumesic, J., The CO/Pt(111) Puzzle. *J. Phys. Chem. B* **2001,** *105*, 4018-4025, https://doi.org/10.1021/jp002302t.

28. Schmidt, P. S.; Thygesen, K. S., Benchmark Database of Transition Metal Surface and Adsorption Energies from Many-Body Perturbation Theory. *J. Phys. Chem. C* **2018,** *122*, 4381-4390, https://doi.org/10.1021/acs.jpcc.7b12258.

29. Garrido Torres, J. A.; Ramberger, B.; Früchtl, H. A.; Schaub, R.; Kresse, G., Adsorption energies of benzene on close packed transition metal surfaces using the random phase approximation. *Phys. Rev. Mater.* **2017,** *1*, 060803, https://doi.org/10.1103/PhysRevMaterials.1.060803.

30. Sheldon, C.; Paier, J.; Sauer, J., Adsorption of CH4 on the Pt(111) surface: Random phase approximation compared to density functional theory. *J. Chem. Phys.* **2021,** *155*, 174702, https://doi.org/10.1063/5.0071995.

31. Harl, J.; Kresse, G., Cohesive energy curves for noble gas solids calculated by adiabatic connection fluctuation-dissipation theory. *Phys. Rev. B* **2008,** *77*, 045136, https://doi.org/10.1103/PhysRevB.77.045136.

32. Olsen, T.; Thygesen, K. S., Accurate Ground-State Energies of Solids and Molecules from Time-Dependent Density-Functional Theory. *Phys. Rev. Lett.* **2014,** *112*, 203001, https://doi.org/10.1103/PhysRevLett.112.203001.

33. Adler, S. L., Quantum Theory of the Dielectric Constant in Real Solids. *Phys. Rev.* **1962,** *126*, 413-420, https://doi.org/10.1103/PhysRev.126.413.

34. Wiser, N., Dielectric Constant with Local Field Effects Included. *Phys. Rev.* **1963,** *129*, 62-69, https://doi.org/10.1103/PhysRev.129.62.

35. Kaltak, M.; Klimeš, J.; Kresse, G., Cubic scaling algorithm for the random phase approximation: Self-interstitials and vacancies in Si. *Phys. Rev. B* **2014,** *90*, 054115, https://doi.org/10.1103/PhysRevB.90.054115.

36. Kaltak, M.; Klimeš, J.; Kresse, G., Low Scaling Algorithms for the Random Phase Approximation: Imaginary Time and Laplace Transformations. *J. Chem. Theory Comput.* **2014,** *10*, 2498-2507, https://doi.org/10.1021/ct5001268.

37. Wellendorff, J.; Silbaugh, T. L.; Garcia-Pintos, D.; Nørskov, J. K.; Bligaard, T.; Studt, F.; Campbell, C. T., A benchmark database for adsorption bond energies to transition metal surfaces and comparison to selected DFT functionals. *Surf. Sci.* **2015,** *640*, 36-44, https://doi.org/10.1016/j.susc.2015.03.023.

38. Tait, S. L.; Dohnálek, Z.; Campbell, C. T.; Kay, B. D., n-alkanes on Pt(111) and on C(0001)/Pt(111): Chain length dependence of kinetic desorption parameters. *J. Chem. Phys.* **2006,** *125*, 234308, https://doi.org/10.1063/1.2400235.

39. Momma, K.; Izumi, F., VESTA 3 for three-dimensional visualization of crystal, volumetric and morphology data. *J. Appl. Crystallogr.* **2011,** *44*, 1272-1276, https://doi.org/10.1107/S0021889811038970

40. Blöchl, P. E., Projector augmented-wave method. *Phys. Rev. B* **1994,** *50*, 17953, https://doi.org/10.1103/PhysRevB.50.17953.

41. Kresse, G.; Joubert, D., From ultrasoft pseudopotentials to the projector augmented-wave method. *Phys. Rev. B* **1999,** *59*, 1758-1775, https://doi.org/10.1103/PhysRevB.59.1758.

42. Kresse, G.; Furthmuller, J., Efficient iterative schemes for ab initio total-energy calculations using a plane-wave basis set. *Phys. Rev. B* **1996,** *54*, 11169-11186, https://doi.org/10.1103/PhysRevB.54.11169.

43. Perdew, J. P.; Burke, K.; Ernzerhof, M., (PBE) Generalized Gradient Approximation made simple. *Phys. Rev. Lett.* **1996,** *77*, 3865-3868, https://doi.org/10.1103/PhysRevLett.77.3865.

44. Perdew, J. P.; Burke, K.; Ernzerhof, M., Erratum. *Phys. Rev. Lett.* **1997,** *78*, 1396, https://doi.org/10.1103/PhysRevLett.78.1396.

45. Bučko, T.; Lebègue, S.; Gould, T.; Ángyán, J. G., Many-body dispersion corrections for periodic systems: an efficient reciprocal space implementation. *J. Phys.: Condens. Matter* **2016,** *28*, 045201, https://doi.org/10.1088/0953-8984/28/4/045201.

46. Steinmann, S. N.; Corminboeuf, C., Comprehensive Benchmarking of a Density-Dependent Dispersion Correction. *J. Chem. Theory Comput.* **2011,** *7*, 3567-3577, https://doi.org/10.1021/ct200602x.

47. Sun, J.; Ruzsinszky, A.; Perdew, J. P., Strongly Constrained and Appropriately Normed Semilocal Density Functional. *Phys. Rev. Lett.* **2015,** *115*, 036402, https://doi.org/10.1103/PhysRevLett.115.036402.

48. Bischoff, F.; Alessio, M.; Berger, F.; John, M.; Rybicki, M.; Sauer, J. *Multi-Level Energy Landscapes: The MonaLisa Program (https://www.chemie.hu-berlin.de/de/forschung/quantenchemie/monalisa/)*, Humboldt-University: Berlin, 2019.

49. Alessio, M.; Bischoff, F. A.; Sauer, J., Chemically accurate adsorption energies for methane and ethane monolayers on the MgO(001) surface. *Phys. Chem. Chem. Phys.* **2018,** *20*, 9760-9769, https://doi.org/10.1039/C7CP08083B.

50. Shishkin, M.; Kresse, G., Implementation and performance of the frequency-dependent GW method within the PAW framework. *Phys. Rev. B* **2006,** *74*, 035101, https://doi.org/10.1103/PhysRevB.74.035101.

51. Langreth, D. C.; Perdew, J. P., Exchange-correlation energy of a metallic surface: Wave-vector analysis. *Phys. Rev. B* **1977,** *15*, 2884-2901, https://doi.org/10.1103/PhysRevB.15.2884.

52. Langreth, D. C.; Perdew, J. P., The exchange-correlation energy of a metallic surface. *Solid State Commun.* **1975,** *17*, 1425-1429, https://doi.org/https://doi.org/10.1016/0038-1098(75)90618-3.

53. Furche, F.; Van Voorhis, T., Fluctuation-dissipation theorem density-functional theory. *J. Chem. Phys.* **2005,** *122*, 164106, https://doi.org/10.1063/1.1884112.

54. Harl, J.; Schimka, L.; Kresse, G., Assessing the quality of the random phase approximation for lattice constants and atomization energies of solids. *Phys. Rev. B* **2010,** *81*, 115126, https://doi.org/10.1103/PhysRevB.81.115126.

55. Kaltak, M.; Kresse, G., Minimax isometry method: A compressive sensing approach for Matsubara summation in many-body perturbation theory. *Phys. Rev. B* **2020,** *101*, 205145, https://doi.org/10.1103/PhysRevB.101.205145.

56. Kohn, W.; Luttinger, J. M., Ground-State Energy of a Many-Fermion System. *Phys. Rev.* **1960,** *118*, 41-45, https://doi.org/10.1103/PhysRev.118.41.

57. Carlsson, A. F.; Madix, R. J., Alkane Trapping onto Structured Alkane Monolayers on Pt(111) at Low Temperature. *J. Phys. Chem. B* **2000,** *104*, 12237-12249, https://doi.org/10.1021/jp001655p.

58. Firment, L. E.; Somorjai, G. A., Surface structures of normal paraffins and cyclohexane monolayers and thin crystals grown on the (111) crystal face of platinum. A low-energy electron diffraction study. *J. Chem. Phys.* **1977,** *66*, 2901-2913, https://doi.org/10.1063/1.434360.

59. Weaver, J. F.; Ikai, M.; Carlsson, A.; Madix, R. J., Molecular adsorption and growth of n-butane adlayers on Pt(111). *Surf. Sci.* **2001,** *470*, 226-242, https://doi.org/https://doi.org/10.1016/S0039-6028(00)00863-3.

60. Tosoni, S.; Sauer, J., Accurate quantum chemical energies for the interaction of hydrocarbons with oxide surfaces: CH(4)/MgO(001). *Phys. Chem. Chem. Phys.* **2010,** *12*, 14330-40, https://doi.org/10.1039/c0cp01261k.

61. Sauer, J., Ab Initio Calculations for Molecule–Surface Interactions with Chemical Accuracy. *Acc. Chem. Res.* **2019,** *52*, 3502-3510, https://doi.org/10.1021/acs.accounts.9b00506.

62. Rybicki, M.; Sauer, J., Ab Initio Prediction of Proton Exchange Barriers for Alkanes at Brønsted Sites of Zeolite H-MFI. *J. Am. Chem. Soc.* **2018,** *140*, 18151-18161, https://doi.org/10.1021/jacs.8b11228.

63. Kachel, S. R.; Klein, B. P.; Morbec, J. M.; Schöniger, M.; Hutter, M.; Schmid, M.; Kratzer, P.; Meyer, B.; Tonner, R.; Gottfried, J. M., Chemisorption and Physisorption at the Metal/Organic Interface: Bond Energies of Naphthalene and Azulene on Coinage Metal Surfaces. *J. Phys. Chem. C* **2020,** *124*, 8257-8268, https://doi.org/10.1021/acs.jpcc.0c00915.

64. Kropp, T.; Paier, J., Reactions of Methanol with Pristine and Defective Ceria (111) Surfaces: A Comparison of Density Functionals. *J. Phys. Chem. C* **2014,** *118*, 23690-23700, https://doi.org/10.1021/jp505088b.

65. Hoyt, R. A.; Montemore, M. M.; Sykes, E. C. H.; Kaxiras, E., Anhydrous Methanol and Ethanol Dehydrogenation at Cu(111) Step Edges. *J. Phys. Chem. C* **2018,** *122*, 21952-21962, https://doi.org/10.1021/acs.jpcc.8b06730.

66. Chesters, M. A.; Gardner, P.; McCash, E. M., The reflection-absorption infrared spectra of n-alkanes adsorbed on Pt(111). *Surf. Sci.* **1989,** *209*, 89-99, https://doi.org/https://doi.org/10.1016/0039-6028(89)90060-5.

67. Shimanouchi, T., *Tables of Molecular Vibrational Frequencies: Consolidated Volume 1*. National Standard Reference Data System: Washington, 1972.

68. Fosser, K. A.; Kang, J. H.; Nuzzo, R. G.; Wöll, C., Adsorption of linear alkanes on Cu(111): Temperature and chain-length dependence of the softened vibrational mode. *J. Chem. Phys.* **2007,** *126*, 194707, https://doi.org/10.1063/1.2735595.

69. Wöll, C.; Weiss, K.; Bagus, P. S., Saturated hydrocarbons on a Cu surface: a new type of chemical interaction? *Chem. Phys. Lett.* **2000,** *332*, 553-561, https://doi.org/https://doi.org/10.1016/S0009-2614(00)01308-7.

70. Seki, K., Design of an adsorbent with an ideal pore structure for methane adsorption using metal complexes. *Chem. Commun.* **2001**, 1496-1497, https://doi.org/10.1039/B104204C.

71. Öström, H.; Triguero, L.; Nyberg, M.; Ogasawara, H.; Pettersson, L. G. M.; Nilsson, A., Bonding of Saturated Hydrocarbons to Metal Surfaces. *Phys. Rev. Lett.* **2003,** *91*, 046102, https://doi.org/10.1103/PhysRevLett.91.046102.

72. Öström, H.; Ogasawara, H.; Näslund, L. Å.; Andersson, K.; Pettersson, L. G. M.; Nilsson, A., Geometric and electronic structure of methane adsorbed on a Pt surface. *J. Chem. Phys.* **2007,** *127*, 144702, https://doi.org/10.1063/1.2781470.

73. Zaremba, E.; Kohn, W., Van der Waals interaction between an atom and a solid surface. *Phys. Rev. B* **1976,** *13*, 2270-2285, https://doi.org/10.1103/PhysRevB.13.2270.

74. Boström, M.; Sernelius, B. E., Fractional van der Waals interaction between thin metallic films. *Phys. Rev. B* **2000,** *61*, 2204-2210, https://doi.org/10.1103/PhysRevB.61.2204.

75. Gould, T.; Simpkins, K.; Dobson, J. F., Theoretical and semiempirical correction to the long-range dispersion power law of stretched graphite. *Phys. Rev. B* **2008,** *77*, 165134, https://doi.org/10.1103/PhysRevB.77.165134.

76. Lebègue, S.; Harl, J.; Gould, T.; Ángyán, J. G.; Kresse, G.; Dobson, J. F., Cohesive Properties and Asymptotics of the Dispersion Interaction in Graphite by the Random Phase Approximation. *Phys. Rev. Lett.* **2010,** *105*, 196401, https://doi.org/10.1103/PhysRevLett.105.196401.

77. Bučko, T.; Hafner, J.; Lebègue, S.; Ángyán, J. G., Improved Description of the Structure of Molecular and Layered Crystals: Ab Initio DFT Calculations with van der Waals Corrections. *J. Phys. Chem. A* **2010,** *114*, 11814-11824, https://doi.org/10.1021/jp106469x.

78. Andersson, M. P., Density functional theory with modified dispersion correction for metals applied to molecular adsorption on Pt(111). *Phys. Chem. Chem. Phys.* **2016,** *18*, 19118-19122, https://doi.org/10.1039/C6CP03289C.

79. Grimme, S., Density functional theory with London dispersion corrections. *Wiley Interdiscip. Rev. Comput. Mol. Sci.* **2011,** *1*, 211-228, https://doi.org/10.1002/wcms.30.

80. Woodruff, D. P.; Duncan, D. A., X-ray standing wave studies of molecular adsorption: why coherent fractions matter. *New J. Phys.* **2020,** *22*, 113012, https://doi.org/10.1088/1367-2630/abc63a.

Chapter 3: Supplementary Material

S1 Low-scaling RPA Algorithm

S1.1 Silicon Defects and Vacancy

S1.1.1 Models

A silicon structure (diamond-like) with a lattice parameter of 5.47 Å (derived from volume given in Ref. [1]) was used for the silicon bulk. The dumbbell (X), hexagonal hollow site (H), lower-symmetry sixfold-coordinated position (C_{3v}), and tetragonal (T) defects were studied, along with the vacancy (V), following the nomenclature used in Ref. [1].

S1.1.2 Computational Details

The calculations were performed using the projector-augmented wave (PAW) method,[2,3] as implemented in the Vienna ab initio simulation package (VASP).[4] Γ-centred meshes were used throughout. *GW* PAW pseudopotentials[5] describe the electron-ion interaction for Si considered 4 valence electrons: [Ne]$3s^2 3p^2$. Two partial waves were used for each orbital with cut-off radii of 1.9 au for both the 3s and 3p states. A plane wave energy cut-off of 250 eV was used. These were used for all DFT and RPA calculations.

S1.1.2.1 DFT Calculations

Silicon defects and vacancies were optimised, until all forces on relaxed atoms used convergence to below 0.001 eV $Å^{-1}$ (0.0194 mE_h $bohr^{-1}$) and an electronic energy threshold of $1x10^{-8}$ eV. The conjugated gradient method was used with cell shape and volume kept constant and only relaxed ions free to move. Structure optimisations used the PBE[6,7] density functional and an 8x8x8 *k*-point mesh. Gaussian smearing was used, with a smearing width of 0.05 eV. Only silicon required optimisation.

S1.1.2.2 RPA Calculations

All RPA calculations used an electronic energy threshold of $1x10^{-8}$ eV. RPA calculations were performed in four steps, as detailed in the main paper. A frequency integration grid density containing 16 points was used for Si calculations. 2x2x2, 3x3x3, and 4x4x4 *k*-point meshes were used for silicon. The finite-temperature algorithm version of the low-scaling algorithm was used.[1,8,9] Fermi smearing with 0.001, 0.01, and 0.05 eV smearing widths was used, except where Gaussian smearing (0.05 eV smearing width) is specified.

S1.1.3 Results and Discussion

We tested the low-scaling algorithm of RPA using test systems taken from the literature. The first of these was the defects, following the work of Ref. [1]. We tested the finite-temperature algorithm at three different smearing widths, 0.001, 0.01, and 0.05 eV, which we present in Tables S1.1, S1.2, S1.3.

Table S1.1. The difference between the RPA and PBE formation energies (in eV), E_{RPA} and E_{PBE}, respectively, of the different defects is given for three different *k*-point meshes and a smearing width of 0.05 eV. X(PBE) denotes the PBE formation energy of the dumbell defect. These are presented alognside the literature values.[1]

Defect	$E_{RPA} - E_{PBE}$					
	k-points					
	2x2x2		3x3x3		4x4x4	
	Lit.	Ours	Lit.	Ours	Lit.	Ours
X(PBE)	2.525	2.525	3.481	3.457	3.541	3.533
X	0.824	0.802	0.706	0.660	0.711	0.672
C_{3v}	0.855	0.770	0.800	0.746	0.745	0.696
H	0.830	0.801	0.750	0.709	0.707	0.654
T	0.930	0.922	0.882	0.849	0.868	0.838
V	0.426	0.464	0.444	0.498	0.446	0.419

Table S1.2. The difference between the RPA and PBE formation energies (in eV), E_{RPA} and E_{PBE}, respectively, of the different defects is given for three different *k*-point meshes and a smearing width of 0.01 eV. X(PBE) denotes the PBE formation energy of the dumbell defect. These are presented alognside the literature values.[1]

Defect	$E_{RPA} - E_{PBE}$					
	k-points					
	2x2x2		3x3x3		4x4x4	
	Lit.	Ours	Lit.	Ours	Lit.	Ours
X(PBE)	2.525	2.526	3.481	3.486	3.541	3.542
X	0.824	0.800	0.706	0.690	0.711	0.682
C_{3v}	0.855	0.844	0.800	0.787	0.745	0.736
H	0.830	0.805	0.750	0.725	0.707	0.692
T	0.930	0.925	0.882	0.879	0.868	0.867
V	0.426	0.458	0.444	0.500	0.446	0.510

Table S1.3. The difference between the RPA and PBE formation energies (in eV), E_{RPA} and E_{PBE}, respectively, of the different defects is given for three different *k*-point meshes and a smearing width of 0.001 eV. X(PBE) denotes the PBE formation energy of the dumbell defect. These are presented alognside the literature values.[1]

Defect	$E_{RPA} - E_{PBE}$					
	k-points					
	2x2x2		3x3x3		4x4x4	
	Lit.	Ours	Lit.	Ours	Lit.	Ours
X(PBE)	2.525	2.526	3.481	3.486	3.541	3.542
X	0.824	0.800	0.706	0.699	0.711	0.682
C_{3v}	0.855	0.846	0.800	0.810	0.745	0.748
H	0.830	0.808	0.750	0.724	0.707	0.693
T	0.930	0.924	0.882	0.876	0.868	0.868
V	0.426	0.449	0.444	0.499	0.446	0.514

We find that all smearing widths repeat the literature reasonably X(PBE) energies well, to within 0.03 eV for a smearing width of 0.05 eV; this reduces to 0.005 eV for 0.01 and 0.001 eV smearing widths. The RPA-PBE differences similarly decrease with decreasing smearing width. A width of 0.05 eV results in an average difference with literature of -0.03 eV, while this is reduced to -0.002 and -0.001 eV for smearings of 0.01 and 0.05 eV, respectively. We note that the difference for the vacancy remains larger, though still only 0.05-0.07 eV for each smearing. We note here that the introduction of defects and a vacancy and subsequent change in electronic structure necessitates the use of the finite-temperature algorithm as we found divergences in the zero-temperature algorithm, similar to those seen for metals. A similar result is found if narrower even smearing widths are used. We now compare the 0.001 eV smearing with those of the literature (cf. Table II of Ref. [1]) and present these in Table S1.4 below.

Table S1.4. The difference between the RPA and PBE formation energies (in eV), E_{RPA} and E_{PBE}, respectively, of the different defects is given for three different *k*-point meshes and a smearing width of 0.001 eV. X(PBE) denotes the PBE formation energy of the dumbell defect. The PBE formation energy E_{form} is given for an 8x8x8 *k*-point mesh. The 4x4x4 difference between RPA and PBE is then added to this and presented in the RPA column. All values are presented alognside the literature values.[1]

Defect	*E_{RPA} – E_{PBE} (formation)*						E_{form}			
	k-points									
	2x2x2		3x3x3		4x4x4		PBE (8x8x8)		RPA	
	Lit.	Ours	Lit.	Ours	Lit.	Ours	Lit.	Ours	Lit.	Ours
X(PBE)	2.525	2.526	3.481	3.486	3.541	3.542	3.561	3.559	-	-
X	0.824	0.800	0.706	0.699	0.711	0.682	3.561	3.559	4.27	4.24
C_{3v}	0.855	0.846	0.800	0.810	0.745	0.748	3.644	3.639	4.39	4.39
H	0.830	0.808	0.750	0.724	0.707	0.693	3.740	3.737	4.45	4.43
T	0.930	0.924	0.882	0.876	0.868	0.868	3.659	3.655	4.53	4.52
V	0.426	0.449	0.444	0.499	0.446	0.514	3.023	3.023	3.47	3.54

This shows that the difference in PBE formation energies is never greater than 5 meV, indicating a correct structure, while the RPA agrees to 0.03 eV, with the exception of the vacancy at 0.07 eV. The best agreement for the vacancy with the literature is for a smearing width of 0.05 eV, indicating that the electronic structure of the vacancy is distinct from that of the defects. Given that we used the finite-temperature algorithm, while the literature does not,[1] it having been developed subsequently,[8] we find this our values match well with the literature.

S1.2 Benzene/Pt(111)

S1.2.1 Models

C_6H_6/Pt(111) structures were taken from Ref. [10].

S1.2.2 Computational Details

The calculations were performed using the projector-augmented wave (PAW) method,[2,3] as implemented in the Vienna ab initio simulation package (VASP).[4] Γ-centred meshes were used throughout. *GW* PAW pseudopotentials[5] describe the electron-ion interaction for platinum with 10 valence electrons considered: [Xe]$4f^{14}5d^9 6s^1$; partial wave cut-off radii of 2.3, 2.15, 1.5 au were used the 4f, 5d, and 6s states, respectively. For carbon, 4 ([He]$2s^2 2p^2$) valence electrons were considered. The partial wave cut-off radii were 1.2 and 1.3, and 1.5 au for 2s and 2p, respectively. For the 1s orbital of hydrogen, a partial wave cut-off radius of 0.95 au was used. A plane wave energy cut-off of 400 eV was used.

All RPA calculations used an electronic energy threshold of 1×10^{-8} eV. RPA calculations were performed in four steps, as detailed in the main paper. A frequency integration grid density containing 16 points was used for calculations. A 3x3x1 *k*-point mesh was used. The finite-temperature algorithm version of the low-scaling algorithm was used.[1,8,9] Fermi smearing with 0.001, 0.01, and 0.05 eV smearing widths was used, except where Gaussian smearing (0.05 eV smearing width) is specified.

S1.2.3 Results and Discussion

We present our calculated RPA adsorption energies for benzene on the Pt(111) surface in Table S1.5 below.

Table S1.5. RPA adsorption energies (in eV) with given smearing width σ (in eV) for four different coverages of benzene on the Pt(111) surface. The four supercells are presented in terms of the number of atoms per layer, where 7, 8, 9, and 10 correspond to (2 -1 | 1 3), (3 1 | 1 3), (3 0 | 0 3), and (4 2 | -1 3), respectively. Literature values are given for reference.[10]

Cells	E_{ads} / eV			
	σ / eV			Lit.
N_{Pt}	0.001	0.01	0.05	
7	-1.53	-1.55	-1.52	-1.53
8	-1.65	-1.69	-1.53	-1.68
9	-1.54	-1.86	-1.62	-1.74
10	-1.89	-1.73	-1.47	-1.86

The 0.05 eV width smearing shows the greatest difference from the literature here, ranging from 0.01-0.39 eV. The 0.001 eV smearing similarly ranges from 0.00-0.20 eV, while the 0.01 eV smearing ranges from 0.01-0.13 eV. From these tests, it would seem that the 0.05 eV smearing is too large; this is corroborated by the electronic entropy per atom being in excess of 10 meV atom^{-1}, exceeding the 1 meV atom^{-1} recommended as an upper limit (cf. VASP manual).[4] The 0.001 eV smearing width appears sufficient here, though we do further tests to determine the reliability of this.

S1.3 CH_4/Pt(111)

S1.3.1 Models

CH_4/Pt(111) structures were taken from Ref. [11].

S1.3.2 Computational Details

The calculations were performed using the projector-augmented wave (PAW) method,[2,3] as implemented in the Vienna ab initio simulation package (VASP).[4] Γ-centred meshes were used throughout. For all isolated methane, only the Γ-point sampling was performed. *GW* PAW pseudopotentials[5] describe the electron-ion interaction for platinum with 10 valence electrons considered (the 4f electrons were included in the pseudopotential): [Xe,4f^{14}]5d^{9}6s^1; a partial wave cut-off radii of 2.4 au was used for both 5d and 6s states. For carbon, 4 ([He]2s^{2}2p^2) valence electrons were considered. The partial wave cut-off radii were 1.2 and 1.5 au for 2s and 2p, respectively. For the 1s orbital of hydrogen, a partial wave cut-off radius of 0.95 au was used. A plane wave energy cut-off of 500 eV was used.

All RPA calculations used an electronic energy threshold of 1x10^{-8} eV. RPA calculations were performed in four steps, as detailed in the main paper. A frequency integration grid density containing 18 points was used. 4x4x1 and 6x6x1 *k*-point meshes were used, denoted 4x4 and 6x6, respectively. The low-scaling RPA algorithm is used,[1,8,9] except when specified when the O(N^4) RPA algorithm is explicitly stated.[12] The finite-temperature algorithm version of the low-scaling algorithm was used.[8] Fermi smearing with 0.001, 0.01, and 0.05 eV smearing widths was used, except where Gaussian smearing (0.05 eV smearing width) is specified.

S1.3.3 Results and Discussion

We present the results for adsorption energies in (√3×√3)R30° and (2x2) cells, with a variable number of layers and *k*-point mesh. This is a repeat of Table VIII in Ref. [11] with the low-scaling algorithm results at three different smearing widths. Those for a vacuum height of 10.3 Å are presented in Table S1.6 and for extrapolated vacuum in Table S1.7.

Table S1.6. Dependence of the RPA adsorption energies (in kJ mol^{-1}) on the *k*-point mesh the number of Pt layers of the slab N_{layer}, and the vacuum height R_{vac} (10.3 Å) for a plane wave energy cut-off of 500 eV. The literature values for the original algorithm,[11] and those using the low-scaling algorithm at three different smearing widths is given.

Cell			σ / eV			
	k-points	N_{layer}	Lit.	0.001	0.01	0.05
(√3×√3)R30°	4x4	3	-17.1	-16.1	-17.4	-16.6
		4	-15.9	-15.9	-16.0	-16.6
Δlayer			+1.2	+0.3	+1.4	+0.0
	6x6	3	-17.3	-38.9	-16.4	-16.2
Δk-points			-0.2	-22.8	+1.0	+0.4
(2×2)	4x4	3	-16.8	-15.7	-15.8	-15.5

It is immediately clear that there is fairly minimal disagreement with the literature. The low-scaling algorithm (√3×√3)R30° cell with three and four layers and a 4x4 *k*-point mesh agree to within 1 kJ mol^{-1}, with the best agreement seen for the 0.01 eV smearing width, differing by

0.3 kJ mol^{-1} at most. This smearing width also matches the layer difference to within 0.2 kJ mol^{-1}. A greater difference is seen for the 6x6 *k*-point mesh, although this is still only ~ 1 kJ mol^{-1} for a smearing of 0.01 eV. Interestingly, we observe a non-physical adsorption energy for a smearing width of 0.001 eV for this mesh. From this, we conclude that a smearing width of 0.001 eV is too narrow. Given that 0.05 eV has previously been determined to be too large, we select 0.01 eV as a suitable smearing width for future use. The *k*-point difference is different for all smearing widths from the literature but this is fairly minor in magnitude; additionally, given the lower cost, the *k*-point "correction" necessary for the original algorithm is no longer required for the low-scaling one, as denser *k*-meshes are affordable. The (2x2) cell shows adsorption energies in agreement with literature to 1 kJ mol^{-1}. Adsorption energies for an extrapolated vacuum are shown in Table S1.7.

Table S1.7. Dependence of the RPA adsorption energies (in kJ mol^{-1}) on the *k*-point mesh, the number of Pt layers of the slab N_{layer}, and the vacuum height R_{vac} (∞ Å, i.e. extrapolated) for a plane wave energy cut-off of 500 eV. The literature values for the original algorithm,[11] and those using the low-scaling algorithm at three different smearing widths is given.

Cell			σ / eV			
	k-points	N_{layer}	Lit.	0.001	0.01	0.05
(√3×√3)R30°	4x4	3	-14.5	-13.1	-14.7	-14.1
		4	-12.9	-13.2	-13.3	-14.4
Δlayer			+1.6	-0.1	+1.5	-0.3
	6x6	3	-15.1	+16.0	-14.0	-14.0
Δk-points			-0.6	+29.1	+0.7	+0.1
Estimated			-13.5	+15.8	-12.6	-14.3
(2×2)	4x4	3	-13.8	-13.0	-13.2	-12.9
Estimated			-12.8	+15.9	-11.0	-13.1

We find these to show a similar trend to the 10.3 Å results, but generally differing from the literature by 1-2 kJ mol^{-1} for the 0.01 and 0.05 eV smearing widths. The poor behaviour of 0.001 eV as a smearing width corroborates our selection of 0.01 eV for future calculations. We compare Fermi smearing using the original algorithm and the low-scaling algorithm in Table S1.8 below.

Table S1.8. RPA adsorption energies (in kJ mol^{-1}) for different vacuum heights R_{vac}, along with extrapolation, for the three different smearing widths and Fermi smearing using the original algorithm (O) and low-scaling algorithm (LS). A 4x4 *k*-mesh, (√3×√3)R30° cell, and a plane wave energy cut-off of 500 eV. The literature values using first-order Methfessel-Paxton (M-P) are shown for comparison.[11]

R_{vac} / Å	σ / eV						
	Fermi						M-P
	0.001		0.01		0.05		0.2
	O	LS	O	LS	O	LS	O
10.3	-17.0	-16.4	-17.1	-17.7	-17.2	-16.9	-17.1
10.8	-16.5	-15.7	-16.5	-17.2	-16.7	-16.3	-
11.3	-16.2	-15.4	-16.2	-16.9	-16.3	-16.1	-16.2
11.8	-15.9	-15.1	-16.0	-16.6	-16.1	-15.7	-
12.3	-15.7	-14.8	-15.7	-16.2	-15.9	-15.5	-15.8
Extra.	-14.4	-13.4	-14.5	-15.0	-14.6	-14.3	-14.5

There is a negligible difference between different smearing widths, so we will focus on vacuum height. This differs by less than 0.2 kJ mol^{-1} between the adsorption energies for the Methfessel-Paxton smearing and the Fermi smearing using the original algorithm for a vacuum height of 10.3 Å. This increases to 0.5-0.7 kJ mol^{-1} by 12.3 Å, and vanishes once extrapolated values are compared. The difference between the original algorithm and low-scaling algorithm both using Fermi smearing, however, can vary by up to 1 kJ mol^{-1} and this does not vanish on extrapolation. This indicates that we should expect different, though near identical, adsorption energies between the two algorithms, independent of the smearing.

S1.4 C1-C4 *n*-alkanes/Pt(111)

S1.4.1 Models

The C1-C4 *n*-alkane structures were the PBE+MBD optimised structures used in the main paper. For calculating the correlation energy, isolated alkane molecules were placed in 10^3, 10^2x11.5, 10^2x12.5, and 10^2x13.5 Å^3 cells for methane, ethane, propane, and *n*-butane, respectively. For calculating the Hartree-Fock energy with DFT orbitals, 10^3, 12^3, 14^3, and 16^3 Å^3 cells were used for methane and 12^3, 14^3, 16^3, and 18^3 Å^3 for ethane, propane, and *n*-butane.

S1.4.2 Computational Details

The calculations were performed using the projector-augmented wave (PAW) method,[2,3] as implemented in the Vienna ab initio simulation package (VASP).[4] Γ-centred meshes were used throughout. For all isolated alkanes, only the Γ-point sampling was performed. *GW* PAW pseudopotentials[5] describe the electron-ion interaction for platinum with 10 valence electrons considered (the 4f electrons were included in the pseudopotential): [Xe,4f^{14}]5d^{9}6s^1; a partial wave cut-off radii of 2.4 au was used for both 5d and 6s states. For carbon, 4 ([He]2s^{2}2p^2) valence electrons were considered. The partial wave cut-off radii were 1.2 and 1.5 au for 2s and 2p, respectively. For the 1s orbital of hydrogen, a partial wave cut-off radius of 0.95 au was used. A plane wave energy cut-off of 500 eV was used.

All RPA calculations used an electronic energy threshold of 1x10^{-8} eV. RPA calculations were performed in four steps, as detailed in the main paper. A frequency integration grid density containing 18 points was used. A 6x6x1 *k*-point mesh was used for methane ((2x2) cell) and a 3x3x1 *k*-point mesh was used for the other alkanes ((3x3) cell). The low-scaling RPA algorithm is used.[1,8,9] The finite-temperature algorithm version of the low-scaling algorithm was used.[8] A 0.01 eV Fermi smearing width was used.

S1.4.3 Isolated Alkane Energies

The correlation energy for each isolated alkane is presented in Table S1.9. We also present the Hartree-Fock energies using DFT orbitals for the four different volumes, then extrapolate with respect to the reciprocal volume.[12]

Table S1.9. Hartree-Fock E_{HF} energies for methane, ethane, propane, and *n*-butane for different volumes V (in Å^3), extrapolated E_{HF} (against V^{-1}), and corresponding R^2 values. The RPA correlation energies E_{corr} and RPA energy (E_{HF} + E_{corr}) E_{RPA} are also shown. Energies are given in eV.

V / Å^3	E_{HF} / eV			
	CH_4	C_2H_6	C_3H_8	C_4H_{10}
10^3	-40.46707354	-	-	-
12^3	-40.39682411	-68.09914936	-95.83882732	-123.5749528
14^3	-40.36273538	-68.03756499	-95.75046987	-123.4595788
16^3	-40.34340664	-68.00227070	-95.69523851	-123.3900942
18^3	-	-67.98156997	-95.67101629	-123.3553606
|Extra.|	-40.30300781	-67.93194183	-95.59696580	-123.2602955
|R^2|	0.9998	0.9999(8)	0.9987	0.9995
E_{corr}	-10.84241468	-19.65688628	-28.52361099	-37.39130025
E_{RPA}	-51.14542249	-87.58882810	-124.1205768	-160.6515958

S1.4.4 Results and Discussion

The adsorption energy for methane, ethane, propane, and *n*-butane are presented in Table S1.10, along with 3-point extrapolations.

Table S1.10. RPA adsorption energies (in kJ mol^{-1}) for different vacuum heights R_{vac}, along with extrapolation (using 10.2, 11.2, and 12.2 Å vacuum heights). R^2 values are also presented.

R_{vac} / Å	ΔE_{ads} / kJ mol^{-1}			
	CH_4	C_2H_6	C_3H_8	C_4H_{10}
10.2	-14.0	-19.2	-29.3	-40.2
11.2	-12.6	-18.7	-28.1	-38.7
12.2	-12.7	-18.4	-28.0	-38.0
14.2	-12.1	-16.9	-25.6	-35.1
|Extra.|	-11.3	-17.6	-26.6	-35.8
|R^2|	0.805	0.999	0.896	0.993

The adsorption energies for all alkanes are reasonable. The R^2 value, however, indicates that extrapolation was only successful for ethane and *n*-butane. On close examination, the 11.2 and 12.2 Å points for methane and propane differ by only 0.1 kJ mol^{-1}, which explains the poor extrapolation. When we compare to a 14.2 Å vacuum height, we see that the extrapolation actually overestimates the adsorption energy for all alkanes. In light of this and considering the affordability of larger vacuum heights using the low-scaling algorithm, we will use a 14.2 Å vacuum for all subsequent calculations.

S1.5 Points from RPA

We present below the platinum-carbon distances r(Pt-C) (where the average of each has been taken then subtracted) and the corresponding PBE, PBE+MBD, and RPA adsorption energies for methane and ethane (Table S1.11), and propane and *n*-butane (Table S1.12).

Table S1.11. Adsorption energy ΔE_{ads} (in kJ mol^{-1}) for methane and ethane at different platinum-carbon distances r(Pt-C) (in pm) using PBE, PBE+MBD, and RPA. Structures were optimised at PBE+MBD with frozen C atoms.

methane				ethane			
r(Pt-C) / pm	ΔE_{ads} / kJ mol^{-1}			r(Pt-C) / pm	ΔE_{ads} / kJ mol^{-1}		
	PBE	PBE+MBD	RPA		PBE	PBE+MBD	RPA
257	46.9	14.8	25.7	254	67.8	13.7	39.4
279	23.7	-2.9	5.1	277	34.0	-12.5	10.7
302	10.2	-11.6	-5.4	301	12.0	-26.5	-7.3
325	3.1	-14.7	-10.1	325	0.9	-29.8	-16.7
350	-0.3	-14.7	-11.3	349	-3.1	-27.4	-20.4
375	-1.7	-13.3	-10.8	374	-4.1	-23.3	-20.5
400	-2.2	-11.4	-9.5	399	-3.8	-19.0	-18.9
425	-2.1	-9.6	-8.0	425	-3.2	-15.1	-16.7
450	-1.9	-8.0	-6.6	450	-2.5	-11.9	-14.4
475	-1.6	-6.7	-5.5	475	-1.8	-9.3	-12.4
500	-1.3	-5.6	-4.7	500	-1.3	-7.3	-10.4
525	-1.1	-4.8	-3.6	525	-0.8	-5.7	-9.0
550	-0.9	-4.1	-2.9	550	-0.4	-4.5	-8.3
575	-0.7	-3.6	-2.5	575	-0.1	-3.6	-6.7
600	-0.6	-3.2	-1.9	600	0.1	-3.0	-5.9

Table S1.12. Adsorption energy ΔE_{ads} (in kJ mol^{-1}) for propane and *n*-butane at different platinum-carbon distances r(Pt-C) (in pm) using PBE, PBE+MBD, and RPA. Structures were optimised at PBE+MBD with frozen C atoms.

propane				*n*-butane			
r(Pt-C) / pm	ΔE_{ads} / kJ mol^{-1}			r(Pt-C) / pm	ΔE_{ads} / kJ mol^{-1}		
	PBE	PBE+MBD	RPA		PBE	PBE+MBD	RPA
256	103.1	22.8	60.4	259	134.9	30.0	75.6
279	48.5	-20.6	14.9	281	62.4	-28.3	17.3
301	15.2	-42.2	-12.2	303	18.8	-56.9	-17.8
325	-0.6	-47.0	-25.5	326	-1.6	-63.3	-35.0
349	-6.0	-43.3	-30.2	350	-8.4	-58.5	-40.7
374	-6.9	-36.9	-29.7	375	-9.4	-50.1	-39.9
399	-6.2	-30.4	-27.2	400	-8.4	-41.4	-36.4
424	-5.2	-24.6	-24.1	425	-7.0	-33.8	-32.5
450	-4.0	-19.8	-20.8	450	-5.5	-27.5	-27.7
475	-3.1	-16.0	-17.5	475	-4.3	-22.5	-23.7
500	-2.3	-13.0	-14.8	500	-3.4	-18.7	-20.5
525	-1.7	-10.7	-12.7	526	-2.6	-15.7	-17.4
550	-1.2	-8.9	-10.9	551	-1.9	-13.3	-15.2
575	-0.8	-7.6	-9.6	576	-1.4	-11.5	-13.3
600	-0.5	-6.5	-8.4	601	-1.1	-10.1	-12.0

S1.6 Comparing Periodic RPA and Hybrid Approach Times

We present the CPU times for periodic RPA, both the original and low-scaling algorithms, and our hybrid approach in Table S1.13 below.

Table S1.13. CPU times (in hr) for periodic RPA with a 14 Å vacuum (+ with vacuum extrapolation) and RPA:PBE hybrid approach for different clusters/ spin states. All times are for CH_4/Pt(111). RPA (pbc) are from Ref. [11]. LS indicates the low-scaling algorithm of RPA. The structures from Ref. [11] are used. Cf. S1.3.2 for calculation details (identical to those in Ref. [11]).

Method		Supercell	
		(√3x√3R30°)	(2x2)
RPA (pbc)		245	876
+extrapolation		727	2618
RPA:PBE	Pt_{19} (S)	-	14
	Pt_{19} (T)	-	40
	Pt_{28} (Q)	-	207
RPA (pbc, LS)		428 (1.7)[a]	646 (3.0)[a]

[a] These are the wall times for the low-scaling RPA algorithm using 384 cores and ~3 TB of RAM (4 large96 nodes at the HLRN-IV site in Goettingen, Emmy).

S2 Frequencies

The scaled vibrational frequencies and redshifts calculated for the C-H stretching modes (directed towards surface platinum atoms for all except methane) are presented in Table SI2.1 and SI2.2, respectively for methane, ethane, propane, and *n*-butane. These values have been scaled by taking the ratio of the computed symmetric stretch of gaseous methane (2978 cm^{-1}) to the experimental (2917 cm^{-1}); scaling coefficient: $v_{exp}/v_{calc} = 0.98$).[13]

Table SI2.1. Scaled calculated frequencies (in cm^{-1}) for the C-H stretching modes directed towards the metal surface. These were performed at the PBE+MDB level.

CH-stretch	Methane	Ethane	Propane	*n*-Butane
Symmetric CH_3	2892[a]	2728	2740	2747
Asymmetric CH_3	-	2713	2733	2738
Symmetric CH_2	-	-	2621	2650
Asymmetric CH_2	-	-	-	2630

[a] This C-H stretch does not show any directionality to the surface.

Table SI2.2. Scaled calculated redshifts (in cm^{-1}) for the C-H stretching modes directed towards the metal surface. These were performed at the PBE+MDB level.

CH-stretch	Methane	Ethane	Propane	*n*-Butane
Symmetric CH_3	25[a]	187	167	160
Asymmetric CH_3	-	200	171	169
Symmetric CH_2	-	-	279	246
Asymmetric CH_2	-	-	-	256

[a] This C-H stretch does not show any directionality to the surface.

S3 RPA on M(111)

S3.1. Bulk Calculations

S3.1.1 Models

Primitive fcc unit cells were used for all bulk calculations.

S3.1.2 Method Details

The calculations were performed using the projector-augmented wave (PAW) method,[2,3] as implemented in the Vienna ab initio simulation package (VASP).[4] All calculations used an electronic energy threshold of $1x10^{-8}$ eV was used. Calculations used 1st order Methfessel-Paxton smearing with a smearing width of 0.2 eV. Γ-centred *k*-point meshes were used throughout. 16x16x16 *k*-point meshes were used for all calculations on the primitive bulk unit cell. A plane wave energy cut-off $E_{cut-off}$ of 400 eV was used, well above the minimum recommended values for all the metals.

The PAW pseudopotential used to describe the electron-ion interaction for gold includes the 4f electrons resulting in 11 valence electrons: $[Xe,4f^{14}]5d^{10}6s^1$. Two partial waves were used for each orbital and their cut-off radius was 2.5 au for both the 5d and 6s states. For silver, 11 ($[Kr]4d^{10}5s^1$) valence electrons were considered. Two partial waves were used for each orbital and their cut-off radius was 2.5 au for both the 4d and 5s states. For copper, 11 ($[Ar]3d^{10}4s^1$) valence electrons were considered. Two partial waves were used for each orbital and their cut-off radius was 2.2 au for both the 3d and 4s states. For silver, 10 ($[Kr]4d^9 5s^1$) valence electrons were considered. Two partial waves were used for each orbital and their cut-off radius was 2.4 au for both the 4d and 5s states. For nickel, 10 ($[Ar]3d^9 4s^1$) valence electrons were considered. Two partial waves were used for each orbital and their cut-off radius was 2.3 au for both the 3d and 4s states. For carbon, 4 ($[He]2s^2 2p^2$) valence electrons were considered. The partial wave cut-off radii were 1.2 and 1.5 au for 2s and 2p, respectively. For oxygen, 6 ($[He]2s^2 2p^4$) valence electrons were considered. The partial wave cut-off radii were 1.2 and 1.52 au for 2s and 2p, respectively. For the 1s orbital of hydrogen, a partial wave cut-off radius of 1.1 au was used. These pseudopotentials were used for all structural optimisations.

S3.1.3. Murnaghan Fitting

We optimised the lattice constant for Cu, Ag, Au, Ni, and Pd by recording 7 points and then fitting to the Murnaghan equation. We give these lattice parameters and energies in Table S3.1 below.

Table S3.1. Lattice parameters a and the corresponding PBE energy E for bulk Cu, Ag, Au, Ni, and Pd.

Cu		Ag		Au		Ni		Pd	
a / Å	E / eV	a / Å	E / eV	a / Å	E / eV	a / Å	E / eV	a / Å	E / eV
3.500	-3.653	4.040	-2.685	4.040	-3.156	3.350	-5.259	3.800	-5.107
3.550	-3.701	4.080	-2.706	4.080	-3.194	3.400	-5.344	3.850	-5.174
3.600	-3.725	4.120	-2.717	4.120	-3.215	3.450	-5.394	3.900	-5.209
3.650	-3.729	4.160	-2.719	4.160	-3.220	3.500	-5.413	3.950	-5.217
3.700	-3.716	4.200	-2.712	4.200	-3.213	3.550	-5.407	4.000	-5.203
3.750	-3.689	4.240	-2.699	4.240	-3.195	3.600	-5.379	4.050	-5.170
3.800	-3.650	4.280	-2.680	4.280	-3.167	3.650	-5.333	4.100	-5.121

We present the fitting parameters from the Murnaghan equation (using the points in Table S3.1) in Table S3.2 below.

Table S3.2. Equilibrium lattice parameter a and the equilibrium energy E_0 derived from the Murnaghan equation for bulk Cu, Ag, Au, Ni, and Pd.

	a / Å	E_0 / eV
Cu	3.636	-3.729
Ag	4.148	-2.719
Au	4.157	-3.220
Ni	3.512	-5.414
Pd	3.942	-5.218

S3.2. C1-C4 *n*-alkanes/M(111) Calculations

S3.2.1 Models

Wellendorff et al.'s structures were taken for methane, ethane, propane, and *n*-butane on Pt(111);[14] the lattice parameters were then rescaled to match the appropriate metal (cf. Table S3.2 for lattice parameters for each metal). The vacuum height was set to 16 Å for DFT calculations and 14 for RPA calculations. For details of the isolated alkanes, see S1.4.1.

S3.2.2 Computational Details

The calculations were performed using the projector-augmented wave (PAW) method,[2,3] as implemented in the Vienna ab initio simulation package (VASP).[4] All RPA calculations used an electronic energy threshold of 1×10^{-8} eV was used. RPA calculations were performed in four steps, as detailed in the main paper. A frequency integration grid density containing 18 points was used. The low-scaling RPA algorithm is used.[1,8,9] The finite-temperature algorithm version of the low-scaling algorithm was used.[8] A 0.01 eV Fermi smearing width was used. Γ-centred meshes were used throughout. A 6x6x1 *k*-point mesh was used. For all isolated alkanes, only the Γ-point sampling was performed. A plane wave energy cut-off, $E_{\text{cut-off}}$, of 500 eV was used.

GW PAW pseudopotentials[5] were used with identical core and valence definitions as the above but improved scattering properties for unoccupied states (PBE cores, as of VASP 5.4). For Au, the partial wave cut-off radii were 2.4 au for both the 5d and 6s states. For Ag, the partial wave cut-off radii were 2.4 and 2.5 au, respectively, for the 4d and 5s states. For Cu, the partial wave cut-off radii were 1.85 and 2.2 au, respectively, for the 3d and 4s states. For Pd, the partial wave cut-off radii were 2.4 au for both the 4d and 5s states. For Ni, the partial wave cut-off radii were 2.0 and 2.3 au, respectively, for the 3d and 4s states. For C, the partial wave cut-off radii were 1.2 and 1.5 au for 2s and 2p, respectively. For C, the partial wave cut-off radii were 1.2 and 1.52 au for 2s and 2p, respectively. For the 1s orbital of H, a cut-off radius of 0.95 au was used.

S3.2.2. Results and Discussion

We took the Wellendorf et al.'s structures and scaled them so that the distance between the metal atoms in the frozen layers corresponded to the those in the bulk with lattice constants given in Table S3.2 above. The C1-C4 alkanes were then re-optimised on the M(111) surface using PBE+dDsC. We report the adsorption energies using PBE, PBE+dDsC, and RPA in Table S3.3 for Cu(111).

Table S3.3. Adsorption energy ΔE_{ads} for the C1-C4 linear alkanes on Cu(111). A vacuum height of 16 Å and a plane wave cut-off of 400 eV was used.

alkane	ΔE_{ads} / kJ mol^{-1}			Exp.[a]	
	PBE	PBE+dDsC	RPA	E_a	T / K
methane	2.9	-18.0	-8.6	-	-
ethane	3.3	-30.1	-14.6	-	-
propane	3.7	-44.3	-22.7	-40.2	119
butane	6.4	-58.2	-29.2	-	-

[a]Temperature Programmed Desorption (TPD) – Ref. [15]

These are shown in Figure S3.1 below.

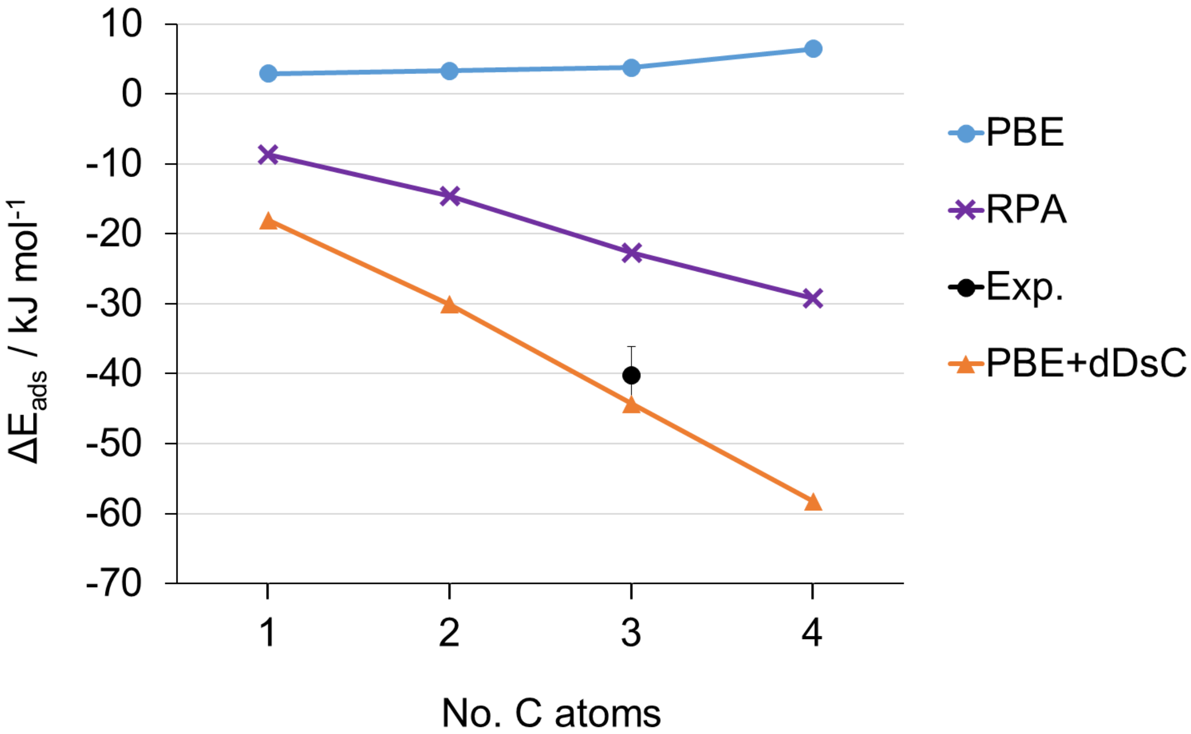

Figure S3.1. The adsorption energies using PBE, PBE+dDsC, and RPA for Cu(111). Experiment is Arrhenius activation energy, not adsorption energy. We have assumed a 10 % error for the TPD experiment.

We report the adsorption energies using PBE, PBE+dDsC, and RPA in Table S3.4 for Ag(111).

Table S3.4. Adsorption energy ΔE_{ads} for the C1-C4 linear alkanes on Ag(111). A vacuum height of 16 Å and a plane wave cut-off of 400 eV was used.

alkane	ΔE_{ads} / kJ mol^{-1}		
	PBE	PBE+dDsC	RPA
methane	1.4	-17.3	-8.4
ethane	1.8	-26.4	-14.8
propane	2.5	-38.1	-21.8
butane	3.6	-50.2	-29.5

These are presented in Figure S3.2 below.

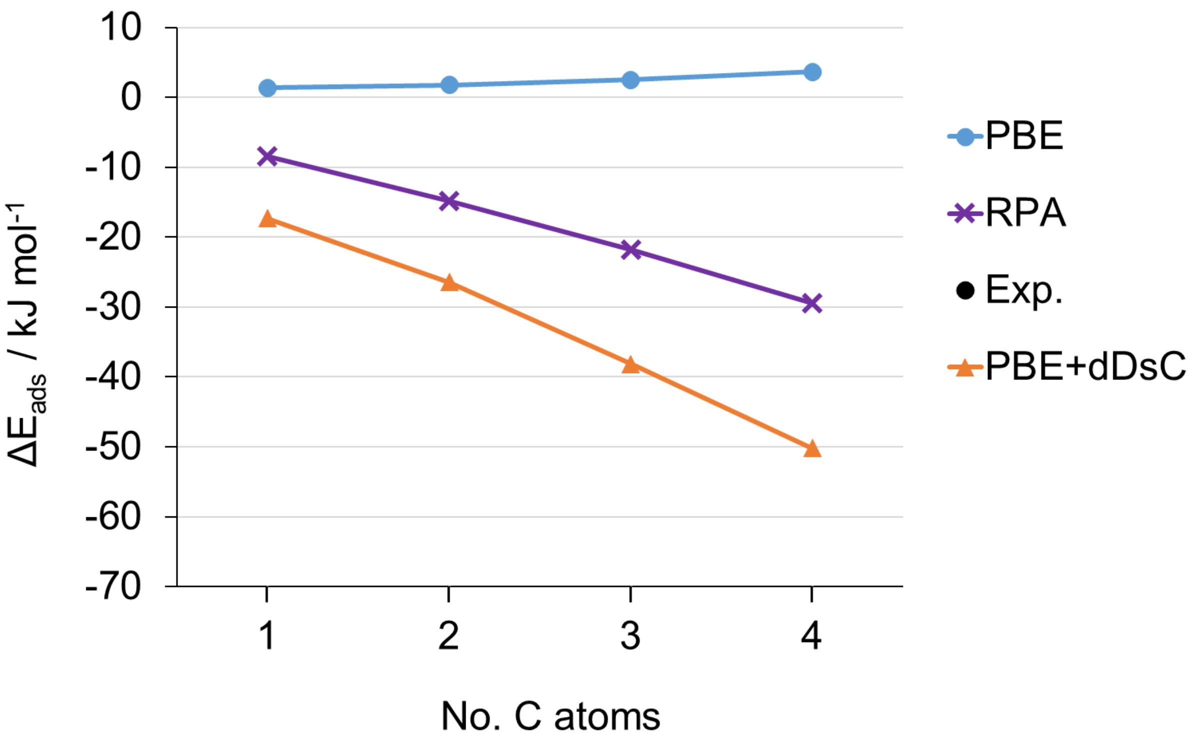

Figure S3.2. The adsorption energies using PBE, PBE+dDsC, and RPA for Ag(111).

We report the adsorption energies using PBE, PBE+dDsC, and RPA in Table S3.5 for Au(111).

Table S3.5. Adsorption energy ΔE_{ads} for the C1-C4 linear alkanes on Au(111). A vacuum height of 16 Å and a plane wave cut-off of 400 eV was used.

alkane	ΔE_{ads} / kJ mol^{-1}			Exp.^{a}	
	PBE	PBE+dDsC	RPA	E_a	T^b / K
methane	1.7	-16.5	-10.5	-14.5	-
ethane	2.1	-27.1	-17.0	-24.1	-
propane	2.7	-39.4	-25.1	-	-
Butane	2.9	-52.4	-34.0	-40.5	-

^{a}Helium Atom Reflectivity – Ref. [16]

^{b}Unreported

These are presented in Figure S3.3 below.

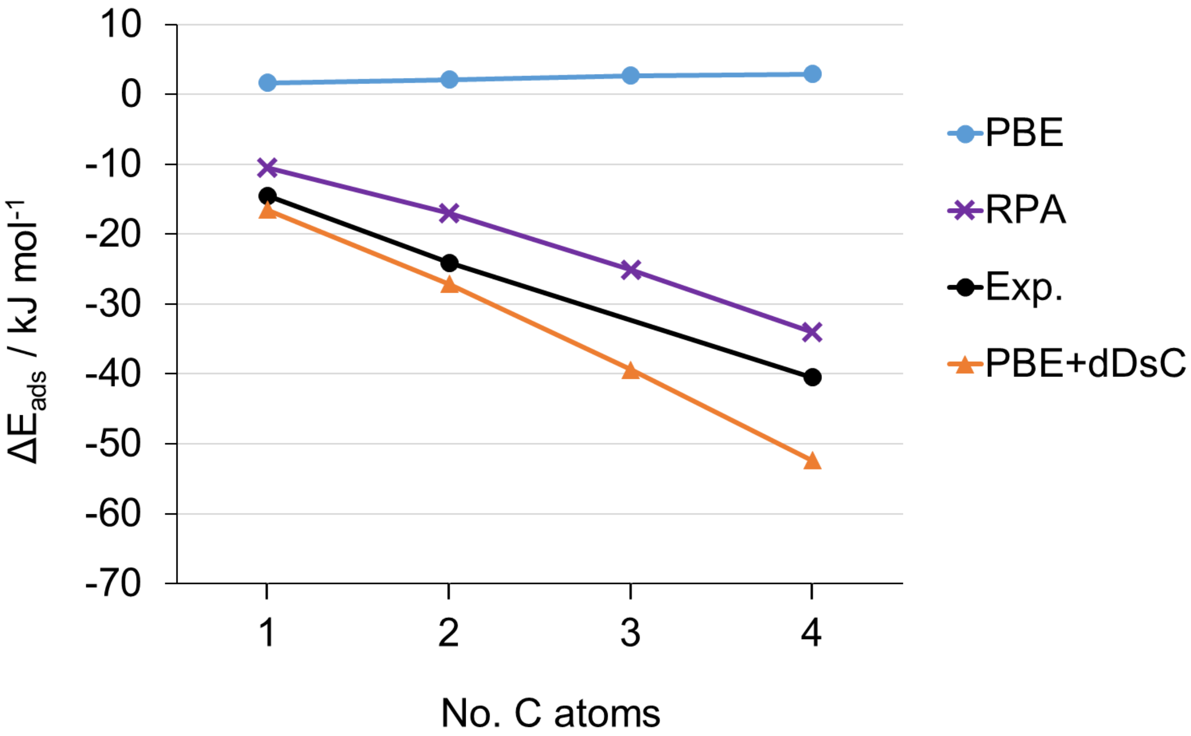

Figure S3.3. The adsorption energies using PBE, PBE+dDsC, and RPA for Au(111). Experiment is Arrhenius activation energy, not adsorption energy. The experimental error bars are shown but are so small (±0.2 kJ mol^{-1}) that they are not visible.

We report the adsorption energies using PBE, PBE+dDsC, and RPA in Table S3.6 for Ni(111).

Table S3.6. Adsorption energy ΔE_{ads} for the C1-C4 linear alkanes on Ni(111). A vacuum height of 16 Å and a plane wave cut-off of 400 eV was used.

alkane	ΔE_{ads} / kJ mol^{-1}			Exp.[a]	
	PBE	PBE+dDsC	RPA	E_a	T / K
methane	2.9	-20.7	-9.5	-12.5	50
ethane	1.9	-35.0	-11.8	-21.3	85
propane	1.7	-51.2	-16.9	-30.0	120
butane	3.7	-67.5	-28.1	-37.0	147

[a] Temperature Programmed Desorption (TPD) – Ref. [17]

These are presented in Figure S3.4 below.

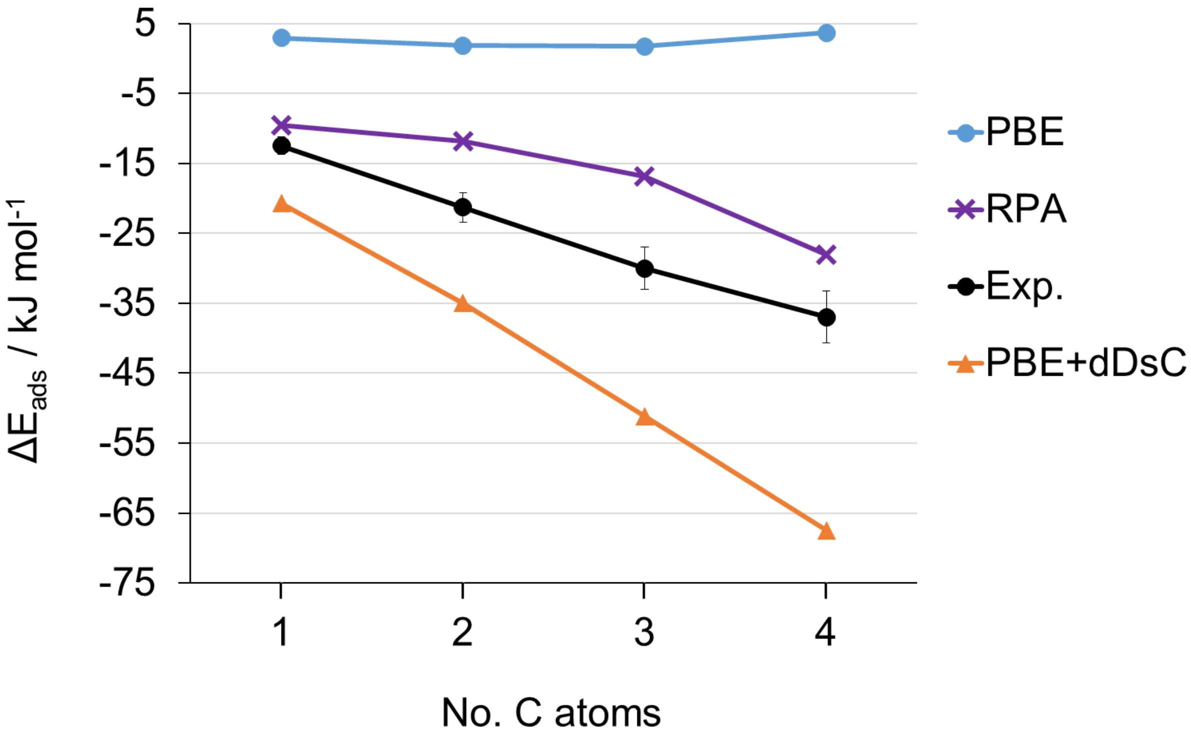

Figure S3.4. The adsorption energies using PBE, PBE+dDsC, and RPA for Ni(111). Experiment is Arrhenius activation energy, not adsorption energy. We have assumed a 10 % error for the TPD experiment.

We report the adsorption energies using PBE, PBE+dDsC, and RPA in Table SIX 1 for Pd(111).

Table S3.7. Adsorption energy ΔE_{ads} for the C1-C4 linear alkanes on Pd(111). A vacuum height of 16 Å and a plane wave cut-off of 400 eV was used.

alkane	ΔE_{ads} / kJ mol^{-1}			Exp.[a]	
	PBE	PBE+dDsC	RPA	E_a	T[b] / K
methane	-0.1	-17.1	-12.6	-16.5	67
ethane	-2.0	-34.3	-26.4	-30.0	120
propane	-3.0	-49.2	-38.7	-41.5	162
butane	-5.2	-65.8	-50.3	-	200

[a] Temperature Programmed Desorption (TPD) – Ref. [16]
[b] TPD from Ref. [16] but reported in Ref. [17] (except for *n*-butane which is only reported in Ref. [17])

These are presented in Figure S3.5 below.

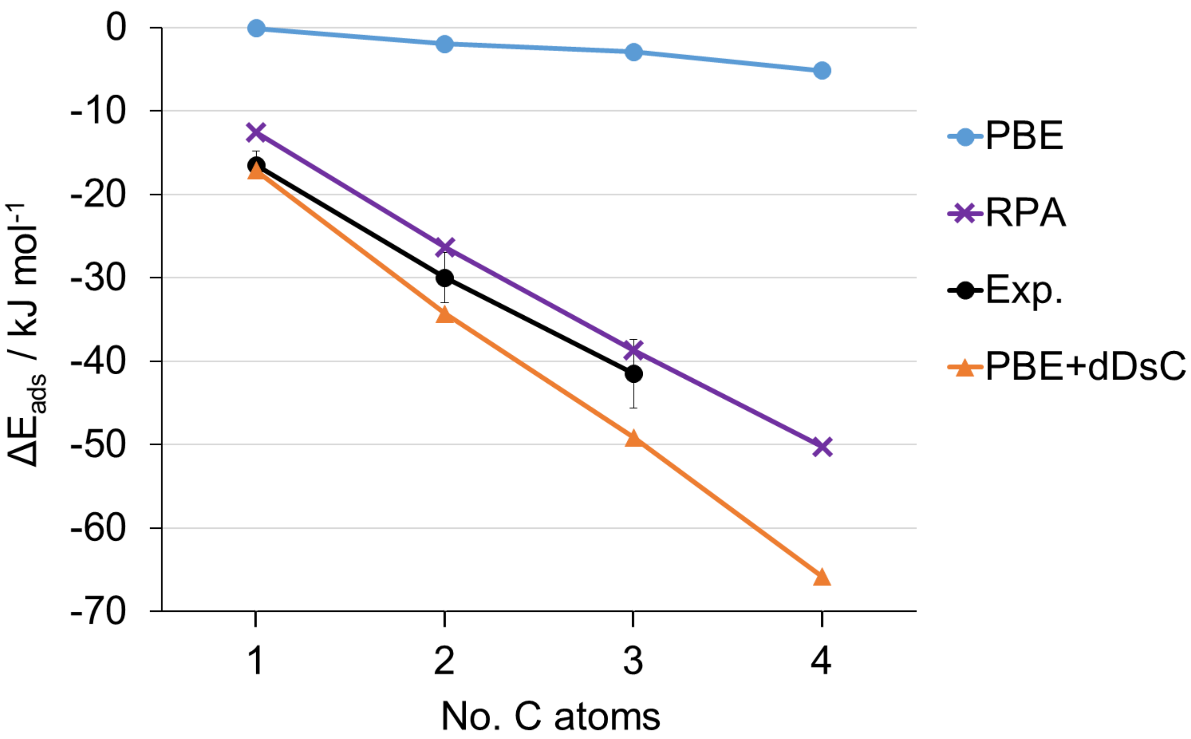

Figure S3.5. The adsorption energies using PBE, PBE+dDsC, and RPA for Pd(111). Experiment is Arrhenius activation energy, not adsorption energy. We have assumed a 10 % error for the TPD experiment.

S4 Modified Lennard-Jones Potential Fitting

S4.1 C1-C4 *n*-alkanes/Pt(111) Fitting

We found a Lennard-Jones potential to be a poor fit for our potential energy curves (PES). Instead we define a modified Lennard-Jones potential in Eq. (1), where the exponents are also variables.

$$V_{mLJ}(r) = 4\varepsilon\left[\left(\frac{\sigma}{r}\right)^{-a} - \left(\frac{\sigma}{r}\right)^{-b}\right] \tag{1}$$

where $V_{mLJ}(r)$ is the modified Lennard-Jones potential, r is the platinum-carbon distance, and ε, σ, a, and b are fitting parameters.

We fitted the modified Lennard-Jones potential with respect to the ε and σ parameters. The a and b parameters are kept constant, except when specifically stated. For each of the fitted parameters, the standard deviation of the fitting is also given. These are presented in Table S4.1 for methane on the Pt(111) surface for PBE, PBE+MBD, and RPA.

Table S4.1. Fitting parameters for PBE, PBE+MBD, and RPA for modified Lennard-Jones potential according to Eq. (1) on the main paper for CH_4/Pt(111). The first and last points used for the fitting are given as r_{start} and r_{end} (in pm). The ε and σ parameters are from the standard Lennard-Jones Potential, while we modify a and b ourselves. We give the equilibrium distance r_{eq} (in pm) and equilibrium energy E_{eq} (in kJ mol^{-1}). The standard deviation for the fitting of a parameter is given as SD(x).

	PBE	PBE+MBD[a]	RPA
r_{start}	350	302	302
r_{end}	600	600	600
r_{eq}	403	335	346
E_{eq}	-2.2	-15.0	-11.4
Epsilon	2.6	15.4	11.4
Sigma	348	279	291
a	9.0	7.6	8.0
b	5.0	3.9	4.0
SD(Epsilon)	0.0	3.0	0.1
SD(Sigma)	0.5	1.0	0.6
SD(a)	-	0.7	-
SD(b)	-	0.2	-

[a] a and b were also fitted

Fitting parameters are presented in Table S4.2 for ethane on the Pt(111) surface for PBE, PBE+MBD, and RPA.

Table S4.2. Fitting parameters for PBE, PBE+MBD, and RPA for modified Lennard-Jones potential according to Eq. (1) in the main paper for C_2H_6/Pt(111). The first and last points used for the fitting are given as r_{start} and r_{end} (in pm). The ε and σ parameters are from the standard Lennard-Jones Potential, while we modify a and b ourselves. We give the equilibrium distance r_{eq} (in pm) and equilibrium energy E_{eq} (in kJ mol^{-1}). The standard deviation for the fitting of a parameter is given as SD(x).

	PBE	PBE+MBD	RPA
r_{start}	325	301	325
r_{end}	500	475	550
r_{eq}	372	321	360
E_{eq}	-4.1	-29.7	-20.6
Epsilon	4.1	35.6	34.7
Sigma	328	273	294
a	11	8	6
b	5.5	4.5	4
SD(Epsilon)	0.1	0.3	0.2
SD(Sigma)	0.5	0.7	0.7

Fitting parameters are presented in Table S4.3 for propane on the Pt(111) surface for PBE, PBE+MBD, and RPA.

Table S4.3. Fitting parameters for PBE, PBE+MBD, and RPA for modified Lennard-Jones potential according to Eq. (1) in the main paper for C_3H_8/Pt(111). The first and last points used for the fitting are given as r_{start} and r_{end} (in pm). The ε and σ parameters are from the standard Lennard-Jones Potential, while we modify a and b ourselves. We give the equilibrium distance r_{eq} (in pm) and equilibrium energy E_{eq} (in kJ mol^{-1}). The standard deviation for the fitting of a parameter is given as SD(x).

	PBE	PBE+MBD[a]	RPA
r_{start}	325	301	325
r_{end}	525	600	550
r_{eq}	370	322	356
E_{eq}	-6.9	-47.2	-30.1
Epsilon	11.6	57.1	50.7
Sigma	323	273	291
a	9.0	7.9	6.0
b	6.0	4.5	4.0
SD(Epsilon)	0.1	7.8	0.3
SD(Sigma)	0.3	0.7	0.8
SD(a)	-	0.4	-
SD(b)	-	0.1	-

[a] a and b were also fitted

Fitting parameters are presented in Table S4.4 for *n*-butane on the Pt(111) surface for PBE, PBE+MBD, and RPA.

Table S4.4. Fitting parameters for PBE, PBE+MBD, and RPA for modified Lennard-Jones potential according to Eq. (1) in the main paper for C_4H_{10}/Pt(111). The first and last points used for the fitting are given as r_{start} and r_{end} (in pm). The ε and σ parameters are from the standard Lennard-Jones Potential, while we modify a and b ourselves. We give the equilibrium distance r_{eq} (in pm) and equilibrium energy E_{eq} (in kJ mol^{-1}). The standard deviation for the fitting of a parameter is given as SD(x).

	PBE	PBE+MBD[a]	RPA
r_{start}	326	281	326
r_{end}	601	526	601
r_{eq}	369	323	357
E_{eq}	-9.4	-63.0	-40.6
Epsilon	10.9	199.0	68.6
Sigma	323	271	291
a	10.0	6.3	6.0
b	5.5	5.1	4.0
SD(Epsilon)	0.1	279.9	0.3
SD(Sigma)	0.3	0.3	0.5
SD(a)	-	1.0	-
SD(b)	-	0.7	-

[a] a and b were also fitted

Using the above parameters, we show the fitted of the modified Lennard-Jones potential to the RPA curves for methane, propane, and *n*-butane in Figures S4.1-S4.4, below. The for methane is not as good as the other alkanes, so we instead take the minimum point, assuming that this is close to equilibrium.

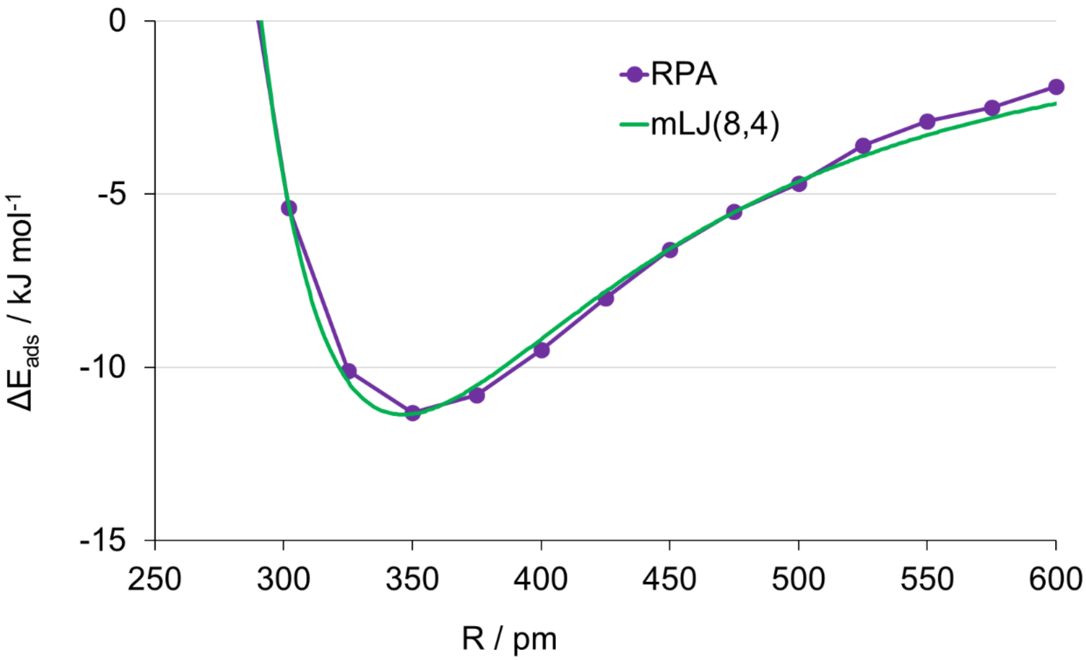

Figure S4.1. Adsorption energy ΔE_{ads} against platinum-carbon distance r(Pt-C) for methane using RPA and a modified Lennard-Jones potential.

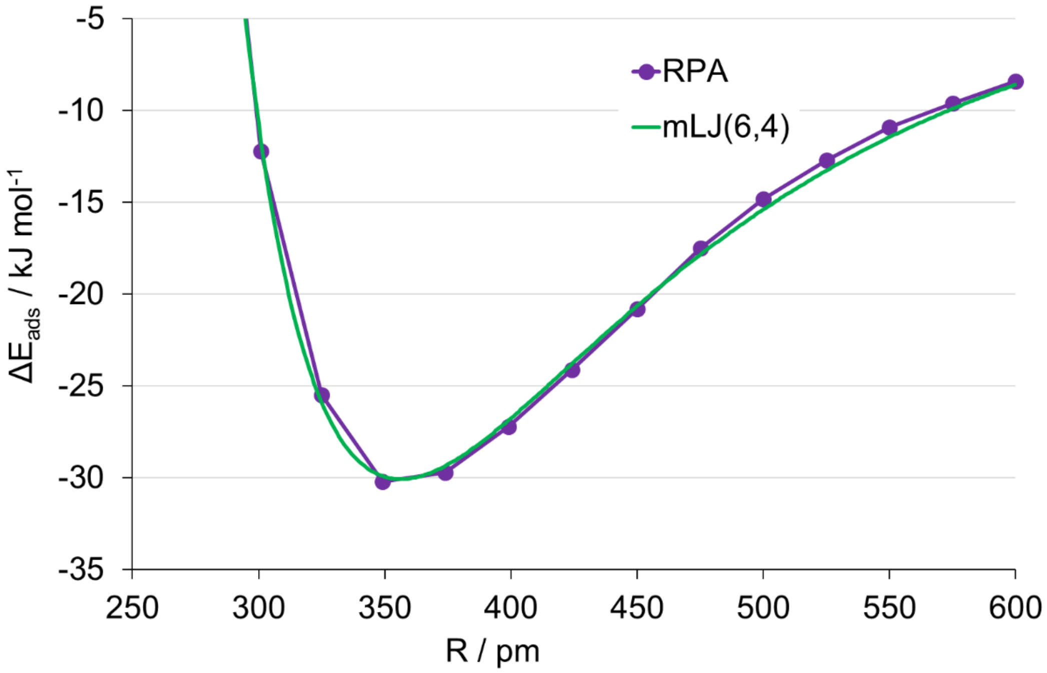

Figure S4.2. Adsorption energy ΔE_{ads} against platinum-carbon distance r(Pt-C) for propane using RPA and a modified Lennard-Jones potential.

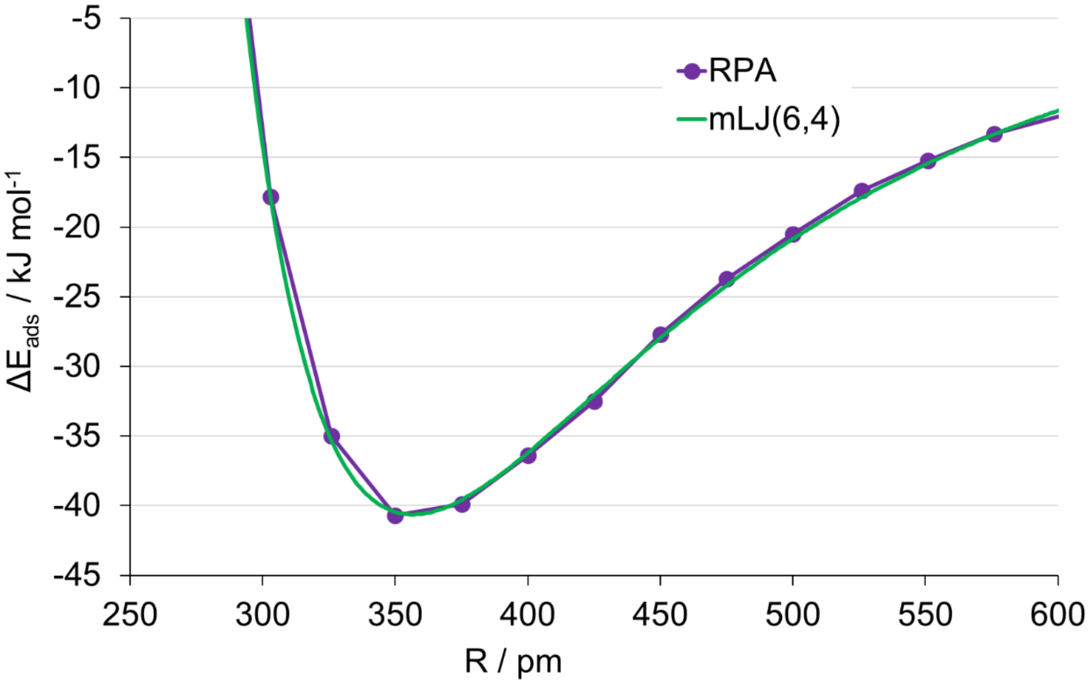

Figure S4.3. Adsorption energy ΔE_{ads} against platinum-carbon distance r(Pt-C) for *n*-butane using RPA and a modified Lennard-Jones potential.

S4.2 Hybrid Approach Fitting

Fitting parameters are presented in Table S4.5 for methane on the Pt(111) surface with the RPA:PBE(+D) hybrid. The fitted data is given in Chapter 2.

Table S4.5. Fitting parameters for RPA:PBE(+D) for modified Lennard-Jones potential according to Eq. (1) in the main paper for CH_4/Pt(111). The first and last points used for the fitting are given as r_{start} and r_{end} (in pm). The ε and σ parameters are from the standard Lennard-Jones Potential; a and b are also free variables. We give the equilibrium distance r_{eq} (in pm) and equilibrium energy E_{eq} (in kJ mol^{-1}). The standard deviation for the fitting of a parameter is given as SD(x).

	PBE	D2	D3	dDsC	MBD
r_{start}	350	325	325	325	325
r_{end}	500	550	550	550	550
r_{eq}	369	358	360	359	371
E_{eq}	-14.4	-17.6	-18.4	-18.9	-15.9
Epsilon	7.0	7.7	7.4	7.2	6.4
Sigma	306	300	302	306	306
a	10.5	12.0	12.9	14.8	11.9
b	2.3	2.1	1.8	1.8	1.7
SD(Epsilon)	0.8	0.5	0.3	0.7	0.3
SD(Sigma)	3.9	1.8	1.4	3.8	1.0
SD(a)	1.6	1.2	1.0	3.5	0.9
SD(b)	0.2	0.1	0.1	0.2	0.1

Fitting parameters are presented in Table S4.6 for methane on the Pt(111) surface with the RPA:PBE(+D) hybrid.

Table S4.6. Fitting parameters for RPA:PBE(+D) for modified Lennard-Jones potential according to Eq. (1) in the main paper for C_2H_6/Pt(111). The first and last points used for the fitting are given as r_{start} and r_{end} (in pm). The ε and σ parameters are from the standard Lennard-Jones Potential; a and b are also free variables. We give the equilibrium distance r_{eq} (in pm) and equilibrium energy E_{eq} (in kJ mol^{-1}). The standard deviation for the fitting of a parameter is given as SD(x).

	PBE	D2	D3	dDsC	MBD
r_{start}	326	326	326	326	326
r_{end}	575	525	575	550	525
r_{eq}	386	367	374	371	381
E_{eq}	-17.8	-30.0	-29.2	-33.7	-24.9
Epsilon	14.3	15.9	12.7	13.8	15.0
Sigma	316	281	298	308	302
a	7.5	6.9	9.5	12.1	7.4
b	3.1	1.7	1.6	1.8	2.2
SD(Epsilon)	2.3	2.4	0.8	2.3	1.9
SD(Sigma)	0.5	3.3	1.9	3.8	1.0
SD(a)	0.6	1.0	0.9	3.3	0.7
SD(b)	0.2	0.2	0.1	0.3	0.2

S5 Modelling Dispersion with PBE and SCAN

S5.1 Models

Primitive fcc unit cells were used for all Pt bulk calculations. The "repeated slab" model for the asymmetric slab models were produced by cutting a PBE-optimised bulk cell along the (111) plane (cf. Ref. [11] for details). Of the four Pt layers, the bottom two were frozen in place to simulate the bulk, with the remaining free to move. A (√3x√3)R30° cell was used, corresponding to a coverage of $^1/_3$ ML, where one monolayer (ML) is defined as one adsorbed molecule per surface Pt atom. The vacuum height, as defined in Figure 1, between repeated surface images is 14 Å.

Isolated methane molecules were modelled using cubic cells (20^3 Å^3) to avoid image interactions, unless otherwise indicated.

S5.2 Computational Details

The calculations were performed using the projector-augmented wave (PAW) method,[2,3] as implemented in the Vienna ab initio simulation package (VASP).[4]

The PAW pseudopotential used to describe the electron-ion interaction for Pt includes the 4f electrons resulting in 10 valence electrons: [Xe,4f^{14}]5d^{9}6s^1. Two partial waves were used for each orbital and their cut-off radius was 2.5 au for both the 5d and 6s states. For carbon, 4 ([He]2s^{2}2p^4) valence electrons were considered. The partial wave cut-off radii were 1.2 and 1.5 au for 2s and 2p, respectively. For the 1s orbital of hydrogen, a partial wave cut-off radius of 1.1 au was used. These pseudopotentials were used for all structural optimisations.

The PBE[6,7] and SCAN[18] density functionals have been used, where the presence of a dispersion correction D is denoted by "functional"+D. The Grimme D2[19] and Tkatchenko's Many-Body Dispersion (MBD)[20] were used with PBE, while D2, MBD and rVV10[21] corrections (using the PBE scaling coefficient for the two former). The non-spherical contributions relating to the gradient of the density in the PAW spheres were included when using the SCAN functional.

All structure optimisations, were performed until all forces on relaxed atoms were converged to below 0.01 eV Å^{-1} (0.194 mE$_h$ bohr^{-1}), an electronic energy threshold of 1x10^{-6} eV, and a plane wave energy cut-off of 400 eV. Calculations on the surface used 6x6x1 *k*-point meshes. For all isolated methane interactions, only the Γ-point sampling was performed. Γ-centred meshes were used throughout. Calculations involving platinum used 1st order Methfessel-Paxton smearing with a smearing width of 0.2 eV, while those on isolated alkanes used Gaussian smearing with a smearing width of 0.05 eV.

S5.3 Results and Discussion

We investigated the PBE functional with a selection of dispersion corrections and compared it to a meta-GGA functional, SCAN,[18] in Table S5.1 for the adsorption of methane in a (√3x√3)R30° cell, i.e. at $^1/_3$ ML coverage. These adsorption energies from the optimised structures conveniently shows the necessity of dispersion corrections, with the PBE functional failing to predict any binding for methane on the Pt(111) surface. The D2 dispersion correction predicts binding but, as has been found previously, it overbinds,[22] significantly so for metals.[23]

Table S5.1. Adsorption energy ΔE_{ads} of CH_4 on Pt(111) for a GGA and meta-GGA functional with different dispersion corrections. The height of the carbon atom above the Pt plane r(C-Pt) is also shown. Calculations performed on a 4-layered (√3x√3)R30° cell ($^1/_3$ ML); a plane wave energy cut-off $E_{cut\text{-}off}$ of 400 eV, 6x6x1 *k*-mesh, and a 14 Å vacuum height were used.

	ΔE_{ads} / kJ mol^{-1}		r(C-Pt) / pm	
Dispersion correction	PBE	SCAN	PBE	SCAN
None	-1.84	-12.3	385	336
D2	-52.9	-72.0*	303	297
MBD	-16.9	-23.7*	339	321
rVV10	-	-31.2	-	334

*using PBE parameter

These introductory results allow us to compare to the SCAN functional, which also requires dispersion corrections to account for the dispersion interaction. However, we found that the SCAN functional does attribute a certain degree of binding methane to the Pt(111) surface, in contrast to PBE. This implies that, like M06, it accounts for the mid-range dispersion correction.[24] In fact, if dispersion corrections are used, this does not offer any improvement, instead significantly overestimating the adsorption energy. This is to be expected for D2, which normally performs poorly for metals but not for MBD, which might be expected to perform better. It is expected tahat this is due to it having been calibrated for PBE, rather than SCAN (cf. s_6 in Eq. 11 of Ref. [19]). However, this cannot account for the poor description when using SCAN+rVV10, it having been specifically calibrated for use with this functional.[21] It seems that the range-separation parameter β (Eq. 7 of Ref. [25]) for SCAN must be quite similar to that of PBE given that which would be optimal for SCAN, as SCAN+MBD performs the best of the SCAN dispersion corrections investigated. It is worth noting that the C-Pt height (i.e. the structure of the adsorbed system) varies significantly here, depending on the dispersion correction and functional used.

References

1. Kaltak, M.; Klimeš, J.; Kresse, G., Cubic scaling algorithm for the random phase approximation: Self-interstitials and vacancies in Si. *Phys. Rev. B* **2014,** *90*, 054115, https://doi.org/10.1103/PhysRevB.90.054115.
2. Blöchl, P. E., Projector augmented-wave method. *Phys. Rev. B* **1994,** *50*, 17953, https://doi.org/10.1103/PhysRevB.50.17953.
3. Kresse, G.; Joubert, D., From ultrasoft pseudopotentials to the projector augmented-wave method. *Phys. Rev. B* **1999,** *59*, 1758-1775, https://doi.org/10.1103/PhysRevB.59.1758.
4. Kresse, G.; Furthmuller, J., Efficient iterative schemes for ab initio total-energy calculations using a plane-wave basis set. *Phys. Rev. B* **1996,** *54*, 11169-11186, https://doi.org/10.1103/PhysRevB.54.11169.
5. Shishkin, M.; Kresse, G., Implementation and performance of the frequency-dependent GW method within the PAW framework. *Phys. Rev. B* **2006,** *74*, 035101, https://doi.org/10.1103/PhysRevB.74.035101.
6. Perdew, J. P.; Burke, K.; Ernzerhof, M., (PBE) Generalized Gradient Approximation made simple. *Phys. Rev. Lett.* **1996,** *77*, 3865-3868, https://doi.org/10.1103/PhysRevLett.77.3865.
7. Perdew, J. P.; Burke, K.; Ernzerhof, M., Erratum. *Phys. Rev. Lett.* **1997,** *78*, 1396, https://doi.org/10.1103/PhysRevLett.78.1396.
8. Kaltak, M.; Kresse, G., Minimax isometry method: A compressive sensing approach for Matsubara summation in many-body perturbation theory. *Phys. Rev. B* **2020,** *101*, 205145, https://doi.org/10.1103/PhysRevB.101.205145.
9. Kaltak, M.; Klimeš, J.; Kresse, G., Low Scaling Algorithms for the Random Phase Approximation: Imaginary Time and Laplace Transformations. *J. Chem. Theory Comput.* **2014,** *10*, 2498-2507, https://doi.org/10.1021/ct5001268.
10. Garrido Torres, J. A.; Ramberger, B.; Früchtl, H. A.; Schaub, R.; Kresse, G., Adsorption energies of benzene on close packed transition metal surfaces using the random phase approximation. *Phys. Rev. Mater.* **2017,** *1*, 060803, https://doi.org/10.1103/PhysRevMaterials.1.060803.
11. Sheldon, C.; Paier, J.; Sauer, J., Adsorption of CH4 on the Pt(111) surface: Random phase approximation compared to density functional theory. *J. Chem. Phys.* **2021,** *155*, 174702, https://doi.org/10.1063/5.0071995.
12. Harl, J.; Kresse, G., Cohesive energy curves for noble gas solids calculated by adiabatic connection fluctuation-dissipation theory. *Phys. Rev. B* **2008,** *77*, 045136, https://doi.org/10.1103/PhysRevB.77.045136.
13. Shimanouchi, T., *Tables of Molecular Vibrational Frequencies: Consolidated Volume 1*. National Standard Reference Data System: Washington, 1972.

14. Wellendorff, J.; Silbaugh, T. L.; Garcia-Pintos, D.; Nørskov, J. K.; Bligaard, T.; Studt, F.; Campbell, C. T., A benchmark database for adsorption bond energies to transition metal surfaces and comparison to selected DFT functionals. *Surf. Sci.* **2015,** *640*, 36-44, https://doi.org/10.1016/j.susc.2015.03.023.

15. Lei, R. Z.; Gellman, A. J.; Koel, B. E., Desorption energies of linear and cyclic alkanes on surfaces: anomalous scaling with length. *Surf. Sci.* **2004,** *554*, 125-140, https://doi.org/10.1016/j.susc.2003.12.058.

16. Kao, C.-L.; Madix, R. J., The Adsorption Dynamics of Molecular Methane, Propane, and Neopentane on Pd(111): Theory and Experiment. *J. Phys. Chem. B* **2002,** *106*, 8248-8257, https://doi.org/10.1021/jp020706a.

17. Kao, C.-L.; Madix, R. J., The adsorption dynamics of small alkanes on (111) surfaces of platinum group metals. *Surf. Sci.* **2004,** *557*, 215-230, https://doi.org/10.1016/j.susc.2004.03.041.

18. Sun, J.; Ruzsinszky, A.; Perdew, J. P., Strongly Constrained and Appropriately Normed Semilocal Density Functional. *Phys. Rev. Lett.* **2015,** *115*, 036402, https://doi.org/10.1103/PhysRevLett.115.036402.

19. Grimme, S., Semiempirical GGA-type density functional constructed with a long-range dispersion correction. *J. Comput. Chem.* **2006,** *27*, 1787-1799, https://doi.org/10.1002/jcc.20495.

20. Bučko, T.; Lebègue, S.; Gould, T.; Ángyán, J. G., Many-body dispersion corrections for periodic systems: an efficient reciprocal space implementation. *J. Phys.: Condens. Matter* **2016,** *28*, 045201, https://doi.org/10.1088/0953-8984/28/4/045201.

21. Peng, H.; Yang, Z.-H.; Perdew, J. P.; Sun, J., Versatile van der Waals Density Functional Based on a Meta-Generalized Gradient Approximation. *Phys. Rev. X* **2016,** *6*, 041005, https://doi.org/10.1103/PhysRevX.6.041005.

22. Bučko, T.; Hafner, J.; Lebègue, S.; Ángyán, J. G., Improved Description of the Structure of Molecular and Layered Crystals: Ab Initio DFT Calculations with van der Waals Corrections. *J. Phys. Chem. A* **2010,** *114*, 11814-11824, https://doi.org/10.1021/jp106469x.

23. Grimme, S.; Antony, J.; Ehrlich, S.; Krieg, H., A consistent and accurate ab initio parametrization of density functional dispersion correction (DFT-D) for the 94 elements H-Pu. *J. Chem. Phys.* **2010,** *132*, 154104, https://doi.org/10.1063/1.3382344.

24. Grimme, S., Density functional theory with London dispersion corrections. *Wiley Interdiscip. Rev. Comput. Mol. Sci.* **2011,** *1*, 211-228, https://doi.org/10.1002/wcms.30.

25. Tkatchenko, A.; DiStasio, R. A.; Car, R.; Scheffler, M., Accurate and Efficient Method for Many-Body van der Waals Interactions. *Phys. Rev. Lett.* **2012,** *108*, 236402, https://doi.org/10.1103/PhysRevLett.108.236402.

Summary

In this work, we have applied quantum chemistry to study dispersive adsorption on metal surfaces. This has been done with the test systems of the C1-C4 *n*-alkanes adsorbing on the Pt(111) surface, where good experimental data was available. We have corrected the energies for thermal contributions and zero point vibrational energies to enable direct comparison between experiment and theory. We have performed fully converged RPA calculations for the C1-C4 *n*-alkanes on Pt(111) (i.e. methane, ethane, propane, and *n*-butane), complete with potential energy surfaces. RPA consistently outperform DFT+D, though RPA's high cost must not be overlooked. To this end, we have developed a more affordable QM:QM hybrid approach based on RPA, which matches RPA in quality while at a significantly reduced cost. This work has successfully applied RPA to metals and achieved chemical accuracy (±4 kJ mol^{-1}) for methane and ethane on the Pt(111) surface. RPA has been found to be an appropriate method to apply to the study of adsorption on metals, while the hybrid approach develops application of post-HF methods to metal surfaces.

In Chapter 1, "Adsorption of CH_4 on the Pt(111) Surface: Random Phase Approximation Compared to Density Functional Theory", RPA was benchmarked with respect to technical parameters for the adsorption of methane on the Pt(111) surface. This was tested with respect to the plane wave energy cutoff, *k*-point mesh, vacuum height, and number of platinum layers and validates the adsorption energies. This was compared against experimental adsorption energies which have been corrected for thermal enthalpic and Zero Point Vibrational Energy (ZPVE) contributions. Experiment and theory were directly compared at identical coverages by analysing experimental data and selecting appropriate cells for calculation. The RPA adsorption energies were found to match the experimental energy to within 2.2 ± 2.1 kJ mol^{-1} at saturated experimental coverage ((√3×√3)R30° surface cell, which corresponds to 1 methane molecule per 3 surface atoms). Additionally, it was possible to distinguish between two adsorption structures, the top monopod and the hcp (hexagonal close packed) tripod. These were predicted to have similar adsorption energies by PBE+MBD and PBE+dDsC, to the extent that each method predicted a different minimum. RPA found the hcp tripod to be the lower energy site, by at least 5 kJ mol^{-1}, and this was corroborated by experiment. RPA was confirmed to accurately describe adsorption when dispersion is the main component.

In Chapter 2, "Hybrid RPA and DFT: Embedding for Adsorption on Pt(111)", RPA was used in tandem with PBE (with and without dispersion corrections, +D), to develop a hybrid QM:QM approach with RPA as the high-level method and PBE(+D) as the low-level method. The hybrid with PBE, RPA:PBE was found to offer a significantly improved description of the relative to

PBE+MBD (the best performing DFT+D method), indicating longer platinum-alkane distances and a slight underbinding. The produced potential energy surface matches well to selected points following from the work of Chapter 1, reproducing RPA values for methane on Pt(111) almost exactly. This indicates that the RPA:PBE adsorption energies calculated for ethane adsorbed on Pt(111) should lie close to those of periodic RPA, were such a calculation affordable. RPA:PBE+MBD was found to lie very close to experiment, reproducing experiment to within chemical accuracy 0.4 and 2.3 kJ mol^{-1} for methane and ethane, respectively. Qualitative adsorption of CO on Pt(111) was also described, with the experimental top site correctly assigned by hybrid RPA:PBE. The hybrid approach applied to metals developed here indicates that RPA is readily applicable to metals and so it is expected that other post-HF methods will be too, in the near future.

In Chapter 3 of this work, “A Study of Dispersion: Alkanes on the Pt(111) Surface using DFT and RPA”, more extensive comparison was made between DFT and RPA. Both DFT+D and vdW density functionals were tested for the C1-C4 *n*-alkanes. RPA was applied using a lower-scaling algorithm, which enabled the study of larger systems and hence sparser coverages. The experimental adsorption energies were corrected for thermal and ZPVE contributions for all four alkanes, at experimentally relevant coverages. RPA potential energy surfaces were produced, with the minimum point obtained by fitting to modified Lennard-Jones type potentials. This indicated a slight underbinding of RPA relative to experimental energies and provided platinum-alkane distances as benchmarks, due to the lack of suitable experimental reference. Optimised DFT+D and vdW density functional structures were then compared. DFT+D was found to consistently overbind relative to experiment and underestimated the RPA distance between alkane molecules and the platinum surface. This varied greatly from the PBE+D2 being completely unphysical to the PBE+MBD being qualitative. The vdW density functionals, on the other hand, were found to be far less consistent than DFT+D. Functionals based on vdW-DF2 (itself, optB88-vdW, and optPBE-vdW) overbound, while predicting platinum-alkane distances relatively close to that of RPA. BEEF-vdW underbound relative to experiment, giving similar values to RPA, while significantly overestimating the platinum-alkane distances. SCAN+rVV10 both significantly overbound and underestimated the platinum-alkane distances. No DFT+D or vdW-functional was found to perform consistently well on both parameters. RPA was found to be the best method to apply to such systems and was taken as a future benchmark.

The application of RPA, a post-HF method to metal surfaces is significant. It enables high accuracy calculations to be performed for the first time. The release of newer, faster algorithms, has opened up the field to the study of large cells previously completely inaccessible at this level of accuracy. The hybrid approach offers this accuracy at lower cost but we also expect that other post-HF methods, such as CCSD(T), will soon be applicable. This will open up the field to accurately study metal surfaces and reactions on them for the first time and provide a suitable complement to already highly-accurate experiment.

Appendix 1. Theory of the Random Phase Approximation

1. Introduction

The Random Phase Approximation (RPA) originated in the early days of electronic structure theory and was first applied to describe the free electron gas, and metals shortly thereafter.[1-4] The idea was that, with interacting particles, the motion of the individual particles is essentially *random*, such that, with sufficiently many particles interacting, the relative *phase* of their individual motion averages out to zero.[2] This is the *Random Phase Approximation*. The cancellation of local terms results in only long-range, collective oscillations in the electron density, i.e. plasmonic oscillations. With the passing decades, it has also become possible to consider RPA from the point of view of Time-Dependent Density Functional Theory (TD-DFT), the Coupled Cluster Approximation, and Many-Body Perturbation Theory (MBPT). The correlation energy is derived from the Adiabatic Connection Fluctuation-Dissipation Theorem (ACFDT), and this shall be discussed first.

N.B. This summary is intended to show the relation between various different methods and RPA, so certain details have been omitted from the derivation. For more in depth analysis of the theory, we recommend the following literature,[5-16] specifically the reviews of Furche and co-workers,[7] and Scheffler and co-workers,[9] or the articles of Furche,[6] and Fuchs and co-workers for details of the theory.[5]

2.1 RPA

The adiabatic connection takes the ground state as non-interacting particles and then turn on the interaction via a coupling strength parameter λ scaling the non-interacting ($\lambda = 0$) to the fully-interacting ($\lambda = 1$) system.[7] The correlation energy E_C may then be expressed by an integral over the coupling strength

$$E_C[\rho] = \int_0^1 d\lambda \, W_C^\lambda[\rho] \tag{1}$$

W_C^λ is the difference between the potential energy of the electron interaction

$$W_C^\lambda[\rho] = \langle \Psi_0^\lambda[\rho] | \hat{V}_{ee} | \Psi_0^\lambda[\rho] \rangle - \langle \Phi_0[\rho] | \hat{V}_{ee} | \Phi_0[\rho] \rangle \tag{2}$$

where $\hat{V}_{ee}$ is the electron-electron interaction operator, $|\Psi_0^\lambda\rangle$ is the interacting, ground-state system, while $|\Psi_0^\lambda\rangle|_{\lambda=0} = |\Phi_0\rangle$, i.e. the Kohn-Sham (KS), ground-state determinant.

W_C^λ may then be expressed in terms of fluctuations in the density[7]

$$W_C^{\lambda} = \frac{\langle \Psi_0^{\lambda} | \Delta\hat{\rho}(\boldsymbol{r_1})\Delta\hat{\rho}(\boldsymbol{r_2}) | \Psi_0^{\lambda} \rangle - \langle \Phi_0 | \Delta\hat{\rho}(\boldsymbol{r_1})\Delta\hat{\rho}(\boldsymbol{r_2}) | \Phi_0 \rangle}{|\boldsymbol{r_1} - \boldsymbol{r_2}|} \tag{3}$$

where $1/|\boldsymbol{r_1} - \boldsymbol{r_2}|$ is the Coulomb potential and $\Delta\hat{\rho}(\boldsymbol{r})$ is the density fluctuation defined as the difference between the one-electron density operator $\hat{\rho}(\boldsymbol{r})$ and the electron density $\rho(\boldsymbol{r})$

$$\Delta\hat{\rho}(\boldsymbol{r}) = \hat{\rho}(\boldsymbol{r}) - \rho(\boldsymbol{r}) \tag{4}$$

The density fluctuation operators may then be given in terms of the one-particle transition densities $\rho_{0n}^{\lambda}(x)$

$$\langle \Psi_0^{\lambda} | \Delta\hat{\rho}(\boldsymbol{r_1})\Delta\hat{\rho}(\boldsymbol{r_2}) | \Psi_0^{\lambda} \rangle = \sum_{n\neq 0} \rho_{0n}^{\lambda}(\boldsymbol{r_1})\rho_{0n}^{\lambda}(\boldsymbol{r_2}) \tag{5}$$

which, in terms of frequency ω and the interacting density-density response function χ_{λ} is

$$\langle \Psi_0^{\lambda} | \Delta\hat{\rho}(\boldsymbol{r_1})\Delta\hat{\rho}(\boldsymbol{r_2}) | \Psi_0^{\lambda} \rangle = -\int_0^{\infty} \frac{d\omega}{\pi} \chi_{\lambda}(i\omega, \boldsymbol{r_1}, \boldsymbol{r_2}) \tag{6}$$

The connection between χ_{λ} and the one-particle transition densities is made by its spectral or Lehmann representation[17]

$$\chi_{\lambda}(i\omega, \boldsymbol{r_1}, \boldsymbol{r_2}) = -\sum_{n\neq 0} \left(\frac{\rho_{0n}^{\lambda}(\boldsymbol{r_1})\rho_{0n}^{\lambda}(\boldsymbol{r_2})}{\Omega_{0n}^{\lambda} - \omega - i\eta} + \frac{\rho_{0n}^{\lambda}(\boldsymbol{r_1})\rho_{0n}^{\lambda}(\boldsymbol{r_2})}{\Omega_{0n}^{\lambda} + \omega + i\eta} \right) \tag{7}$$

where Ω_{0n}^{λ} is an excitation energy, and $i\eta$ is a small contour distortion to make χ_{λ} analytical in the upper complex plane.

Combining Eq. (3), (5), and (7) allows the expression of the correlation energy as

$$E_C[\rho] = -\frac{1}{2}\int_0^1 d\lambda \int_0^{\infty} \frac{d\omega}{\pi} \int d\boldsymbol{r_1} d\boldsymbol{r_2} \frac{\chi_{\lambda}(i\omega, \boldsymbol{r_1}, \boldsymbol{r_2}) - \chi_0(i\omega, \boldsymbol{r_1}, \boldsymbol{r_2})}{|\boldsymbol{r_1} - \boldsymbol{r_2}|} \tag{8a}$$

or

$$E_C[\rho] = -\frac{1}{2}\int_0^1 d\lambda \int_0^{\infty} \frac{d\omega}{\pi} \mathrm{Tr}\{\nu[\,\chi_{\lambda}(i\omega) - \chi_0(i\omega)]\} \tag{8b}$$

where χ_0 is the KS density-density response function, ν is the Coulomb potential $(1/|\boldsymbol{r_1} - \boldsymbol{r_2}|)$ and the trace is defined as[5]

$$\mathrm{Tr}\{\mathrm{A}(i\omega)\mathrm{B}(i\omega)\} = \int d^3\boldsymbol{r_1} d^3\boldsymbol{r_2}\, \mathrm{A}(i\omega, \boldsymbol{r_1}, \boldsymbol{r_2})\mathrm{B}(i\omega, \boldsymbol{r_1}, \boldsymbol{r_2}) \tag{9}$$

χ_0 is rarely expressed in molecular calculations but it is relatively easy to express under periodic conditions, such as the Adler-Wiser formula typically used[12,18]

$$\chi_{0,\mathbf{GG'}}(i\omega, \mathbf{q}) = \frac{1}{V} \sum_{nn'\mathbf{k}} 2\mathrm{g}_{\mathbf{k}}(f_{n'\mathbf{k+q}} - f_{n\mathbf{k}}) \frac{\langle \psi_{n'\mathbf{k+q}} \left| e^{i(\mathbf{q+G})\mathbf{r}} \right| \psi_{n\mathbf{k}} \rangle \langle \psi_{n\mathbf{k}} \left| e^{-i(\mathbf{q+G'})\mathbf{r}'} \right| \psi_{n'\mathbf{k+q}} \rangle}{\epsilon_{n'\mathbf{k+q}} - \epsilon_{n\mathbf{k}} - i\omega} \tag{10}$$

where $\mathbf{G}$ is the reciprocal lattice vector, $\mathrm{g}_{\mathbf{k}}$ are the *k*-point weights, $f_{n\mathbf{k}}$, $\psi_{n\mathbf{k}}$, and $\epsilon_{n\mathbf{k}}$ are the occupancies, KS one-electron orbitals, and the energies of state n, respectively, and $\mathbf{k}$ and $\mathbf{q}$ are crystal momentum vectors within the first Brillouin zone within the cell of volume V.

Alternatively, it may be expressed from Green's functions G_0 for the O(N^3) RPA algorithm.[10,11] Eq. (11) is valid for all coupling strength, but we choose to express it for the non-interacting, KS system here for the sake of consistency.

$$\chi_0(i\tau, \boldsymbol{r_1}, \boldsymbol{r_2}) = -G_0(i\tau, \boldsymbol{r_1}, \boldsymbol{r_2})G_0^*(-i\tau, \boldsymbol{r_2}, \boldsymbol{r_1}) \tag{11}$$

where $i\tau$ indicates that it is over imaginary time and the $\boldsymbol{r}$ indicates that it is over real space. N.B. several Fourier transformations and other steps must be taken to express in the terms used in Eq. (8a), cf. Ref. [10] for details.

The interacting response function χ_λ may be expressed in terms of the non-interacting χ_0 via the Dyson equation[5]

$$\chi_\lambda(i\omega, \boldsymbol{r_1}, \boldsymbol{r_2}) = \chi_0(i\omega, \boldsymbol{r_1}, \boldsymbol{r_2}) + \int d^3\boldsymbol{r}'_1 d^3\boldsymbol{r}'_2 \chi_0(i\omega, \boldsymbol{r_1}, \boldsymbol{r}'_1) K^\lambda_{hxc}(i\omega, \boldsymbol{r}'_1, \boldsymbol{r}'_2) \chi_\lambda(i\omega, \boldsymbol{r}'_2, \boldsymbol{r_2}) \tag{12}$$

where $K^\lambda_{hxc}(i\omega, \boldsymbol{r_1}, \boldsymbol{r_2}) = \lambda v(\boldsymbol{r_1}, \boldsymbol{r_2}) + f^\lambda_{xc}(i\omega, \boldsymbol{r_1}, \boldsymbol{r_2})$ and f^λ_{xc} is the exchange-correlation kernel at coupling strength λ; in RPA, $f^\lambda_{xc} = 0$.

By inserting Eq. (12) in Eq. (8b) and integrating over λ, we obtain a closed expression for the correlation energy[5]

$$E_C[\rho] = \int_0^\infty \frac{d\omega}{2\pi} \mathrm{Tr}\{\ln[1 - \chi_0(i\omega)v] + \chi_0(i\omega)v\} \tag{13}$$

and thus, the correlation energy may be obtained from χ_0. This completes the ACFDT derivation of RPA.

2.2 TD-DFT

Time-Dependent Density Functional Theory (TD-DFT) is a common method for calculating the excitation energies and transition properties of molecules. This somewhat more familiar approach may be used to express RPA. We have previously seen that TD-DFT may be expressed as RPA if $f_{xc}^{\lambda} = 0$. We may derive excitation energies from the familiar eigenvalue equation[6]

$$\Lambda|X_n, Y_n\rangle = \Omega_n \Delta |X_n, Y_n\rangle \tag{14}$$

where X_n and Y_n are the eigenvectors with corresponding eigenvalues Ω_n and

$$\Lambda = \begin{pmatrix} A & B \\ B & A \end{pmatrix} \tag{15a}$$

$$\Delta = \begin{pmatrix} 1 & 0 \\ 0 & -1 \end{pmatrix} \tag{15b}$$

and the orbital rotation Hessians define A and B

$$(A + B)_{ia,jb} = (\epsilon_a - \epsilon_i)\delta_{ij}\delta_{ab} + 2\lambda\langle ij||ab\rangle + \left(f_{xc}^{\lambda}\right)_{ia,jb} \tag{16a}$$

$$(A - B)_{ia,jb} = (\epsilon_a - \epsilon_i)\delta_{ij}\delta_{ab} \tag{16b}$$

where ϵ_p are orbital energies, i and j are occupied molecular orbitals, a and b are virtual molecular orbitals, and $\langle pq||rs\rangle$ is the standard two-electron integral. N.B. we have omitted λ from the eigenvectors and operators for the sake of clarity. In this thesis, we have used only direct RPA. This may be obtained by removing the exchange terms from the two-electron integral (i.e. $\langle pq||rs\rangle \to \langle pq|rs\rangle$).

The transition densities given in Eq. (5) may be written in terms of $\mathbf{X}$ and $\mathbf{Y}$, linking the excitation energy equation to RPA

$$\rho_{0n}^{\lambda}(\boldsymbol{r_1}) = \sum_{ia} (X_n + Y_n)_{ia} \psi_i(\boldsymbol{r_1}) \psi_a(\boldsymbol{r_1}) \tag{17}$$

where $\psi_p(\boldsymbol{r_1})$ is a ground-state KS molecular orbital.

Using Eq. (1), (3), (5), and (17) the correlation energy may be written as

$$E_C = \int_0^1 d\lambda \sum_{iajb} \langle ij||ab\rangle \left(\sum_{n\neq 0} (X_n + Y_n)_{ia} (X_n + Y_n)_{jb} - \delta_{ij}\delta_{ab} \right) \tag{18}$$

An alternative expression for the correlation energy may also be obtained. Firstly, the excitation energies must first be obtained

$$\Omega_n = \langle X_n, Y_n | \Lambda | X_n, Y_n \rangle \tag{19}$$

And their derivative with respect to the coupling constant obtained via the Hellmann-Feynman theorem

$$\frac{d\Omega_n}{d\lambda} = \left\langle X_n, Y_n \middle| \frac{d\Lambda}{d\lambda} \middle| X_n, Y_n \right\rangle \tag{20a}$$

or

$$\frac{d\Omega_n}{d\lambda} = \sum_{iajb} (X_n + Y_n)_{ia} \langle ij||ab\rangle (X_n + Y_n)_{jb} \tag{20b}$$

Quick comparison with Eq. (18) shows obvious similarities and the correlation energy may also be obtained, with Eq. (1), (3), and (5) leading to[6]

$$E_C = \frac{1}{2} \int_0^1 d\lambda \sum_n \left(\frac{d\Omega_n}{d\lambda} - \left.\frac{d\Omega_n}{d\lambda}\right|_{\lambda=0} \right) \tag{21}$$

which is readily integrated to

$$E_C = \frac{1}{2} \sum_n \left(\Omega_n - \Omega_n^{\mathrm{D}} \right) \tag{22}$$

where Ω_n^{D} is the sum of the zero $\Omega_n^{(0)}$ and first order $\left.\frac{d\Omega_n}{d\lambda}\right|_{\lambda=0}$ RPA excitation energies

$$\Omega_n^{\mathrm{D}} = \Omega_n^{(0)} - \left.\frac{d\Omega_n}{d\lambda}\right|_{\lambda=0} \tag{23}$$

N.B. Eq. (22) resembles the expression for the harmonic oscillator.

TD-DFT may thus express the RPA correlation energy via transition densities, cf. Eq. (17) and (18), or excitation energies, cf. Eq. (22).

2.3 Plasmons

The work of Furche links the TD-DFT expressions back to the original plasmonic formulation, where electronic zero point vibration energies (ZPVE) may be expressed[6]

$$\mathrm{ZPVE} = \frac{1}{2}\sum_n \Omega_n \tag{24}$$

This is also the equation for the trace. Keeping this in mind, the first order approximation to RPA Ω_n^{D}, may be expressed in similar terms

$$\mathrm{ZPVE}^{\mathrm{D}} = \frac{1}{2}\sum_n \Omega_n^D = \frac{1}{2}\mathrm{Tr}[A] \tag{25}$$

The eigenvalues of A correspond to the Tamm-Dancoff approximation to the RPA excitation at *full* coupling. Thus, as $\mathrm{ZPVE}^{\mathrm{D}} = \mathrm{ZPVE}^{\mathrm{TDA}}$, Eq. (22) becomes

$$E_C = \frac{1}{2}\sum_n \left(\Omega_n - \Omega_n^{\mathrm{TDA}}\right) = \frac{1}{2}\mathrm{Tr}[\mathbf{\Omega} - \mathbf{A}] \tag{26}$$

This expresses the RPA correlation energy as the electronic ZPVE difference between correlated (RPA) and uncorrelated (TDA) harmonic oscillators, i.e. a difference between an interacting, plasmonic system and a non-interacting KS system.

2.4 Coupled Cluster

A link between coupled cluster and RPA was long suspected, having been indicated numerically by Freeman.[19] This work suggested that RPA was equivalent to ring Coupled Cluster Doubles (rCCD), though this was not proven until relatively recently.[15,16] A similar starting point to TD-DFT is taken, with the eigenvalue equation expressed equivalently to Eq. (14) in Eq. (27)

$$\begin{pmatrix} \mathbf{A} & \mathbf{B} \\ -\mathbf{B} & -\mathbf{A} \end{pmatrix}\begin{pmatrix} \mathbf{X} \\ \mathbf{Y} \end{pmatrix} = \begin{pmatrix} \mathbf{X} \\ \mathbf{Y} \end{pmatrix}\mathbf{\Omega} \tag{27}$$

where

$$(A)_{ia,jb} = (\epsilon_a - \epsilon_i)\delta_{ij}\delta_{ab} + \langle ib||aj\rangle \tag{28a}$$

$$B_{ia,jb} = \langle ij||ab\rangle \tag{28b}$$

Analogy with coupled cluster equations is then taken. The rCCD correlation energy is

$$E_C = \frac{1}{2}\sum_{n} \langle ij||ab\rangle\, t_{ij}^{ab}$$

(29)

and the rCCD amplitude equation

$$0 = \langle ij||ab\rangle + \left(\epsilon_a + \epsilon_b - \epsilon_i - \epsilon_j\right)t_{ij}^{ab} + \langle ic||ak\rangle t_{kj}^{cb} + t_{ik}^{ac}\langle jc||bl\rangle + t_{ik}^{ac}\langle kl||cd\rangle t_{ij}^{db}$$

(30)

These are presented diagrammatically in Figure 1.

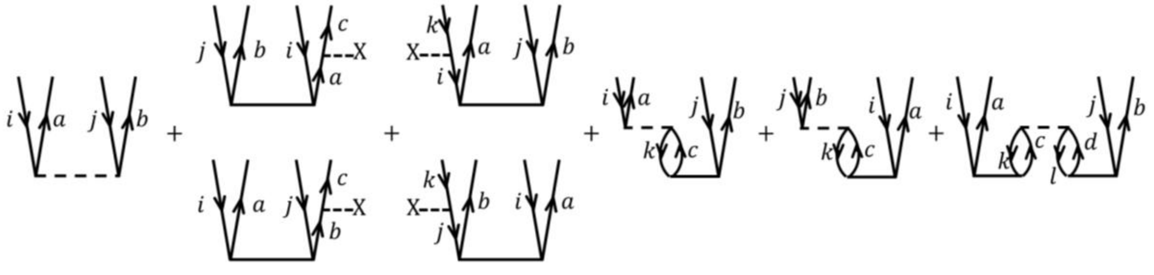

a) $\langle ij||ab\rangle \quad + \quad \left(\epsilon_a + \epsilon_b - \epsilon_i - \epsilon_j\right)t_{ij}^{ab} \quad + \langle ic||ak\rangle t_{kj}^{cb} + t_{ik}^{ac}\langle jc||bl\rangle + t_{ik}^{ac}\langle kl||cd\rangle t_{ij}^{db} = 0$

b) $\langle ij|ab\rangle \quad + \quad \left(\epsilon_a + \epsilon_b - \epsilon_i - \epsilon_j\right)t_{ij}^{ab} \quad + \langle ic|ak\rangle t_{kj}^{cb} + t_{ik}^{ac}\langle jc|bl\rangle + t_{ik}^{ac}\langle kl|cd\rangle t_{ij}^{db} = 0$

Figure 1. Amplitude diagrams for rCCD. The algebraic form for rCCD (a) and direct rCCD (drCCD) (b) are presented beneath the corresponding diagrams.

Defining $t_{ij}^{ab} = T_{ia,jb}$, Eq. (30) may be written:

$$\mathbf{B} + \mathbf{AT} + \mathbf{TA} + \mathbf{TBT} = \mathbf{0}$$

(31)

Also known as the Riccati equation. The rCCD and direct rCCD (drCCD) correlation energy, cf. Eq. (29), may now be expressed

$$E_C^{\mathrm{rCCD}} = \frac{1}{4}\mathrm{Tr}\{\mathbf{BT}\}$$

(32a)

$$E_C^{\mathrm{drCCD}} = \frac{1}{2}\mathrm{Tr}\{\mathbf{BT}\}$$

(32b)

Multiplying Eq. (27) from the right by $\mathbf{X^{-1}}$ results in

$$\begin{pmatrix} \mathbf{A} & \mathbf{B} \\ -\mathbf{B} & -\mathbf{A} \end{pmatrix}\begin{pmatrix} 1 \\ \mathbf{T} \end{pmatrix} = \begin{pmatrix} 1 \\ \mathbf{T} \end{pmatrix}\mathbf{R}$$

(33)

where $\mathbf{T} = \mathbf{YX^{-1}}$ and $\mathbf{R} = \mathbf{X\Omega X^{-1}}$.

Multiplying Eq. (33) from the left by $(\mathbf{T} \quad -1)$ returns Eq. (31). Expanding the first row of Eq. (33) results in

$$\mathbf{A} + \mathbf{BT} = \mathbf{R}$$

(34)

Linking Eq. (32a) and (32b) to Eq. (29)

$$\mathrm{Tr}[\mathbf{BT}] = \mathrm{Tr}[\mathbf{R} - \mathbf{A}] = \mathrm{Tr}[\mathbf{\Omega} - \mathbf{A}]$$

(35)

2.5 MBPT

The link between TD-DFT and Many-Body Perturbation Theory (MBPT) is murky. Expressing RPA in terms of TD-DFT provides clarity to this link.[5] This link begins by expressing RPA in a GW-like way. Similarly to Eq. (10), the response function may be expressed in terms of Green's functions

$$\chi_0(i\omega, \boldsymbol{r_1}, \boldsymbol{r_2}) = 2\int \frac{d\omega}{2\pi} G_0(i\omega + i\omega', \boldsymbol{r_1}, \boldsymbol{r_2}) G_0(i\omega', \boldsymbol{r_2}, \boldsymbol{r_1})$$

(36)

where

$$G_0(i\omega, \boldsymbol{r_1}, \boldsymbol{r_2}) = \sum_j \frac{\psi_j(\boldsymbol{r_1})\psi_j^*(\boldsymbol{r_2})}{i\omega - \epsilon_j}$$

(37)

Inserting Eq. (36) into Eq. (8b) gives

$$E_C[\rho] = \int_0^1 \frac{d\lambda}{\lambda} \int_0^\infty \frac{d\omega}{\pi} \mathrm{Tr}\{\Sigma_c^\lambda(i\omega) G_0(i\omega)\}$$

(38)

where the effective self-energy Σ_c^λ is defined

$$\Sigma_C^\lambda(i\omega, \boldsymbol{r_1}, \boldsymbol{r_2}) = -\int_0^\infty \frac{d\omega}{\pi} G_0(i\omega + i\omega', \boldsymbol{r_1}, \boldsymbol{r_2}) W_\lambda(i\omega', \boldsymbol{r_1}, \boldsymbol{r_2})$$

(39)

where the screened Coulomb interaction W_λ and dielectric function ε_λ are

$$W_\lambda(i\omega) = \lambda\left[\varepsilon_\lambda^{-1}(i\omega) - 1\right]v = \lambda\left[\left(1 - K_{hxc}^\lambda(i\omega)\chi_0(i\omega)\right)^{-1} - 1\right]v$$

(40)

Recalling that $f_{xc}^\lambda = 0$ for RPA, Eq. (38)-(40) may be readily expressed diagrammatically as shown in Figure 2a, 2b, and 2c, for the RPA correlation energy, effective self-energy, and screened Coulomb interaction, respectively, up to the third term.

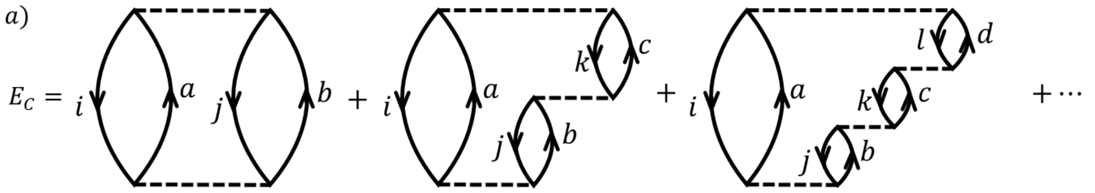

$$E_C = \frac{1}{2}\sum_{\substack{ij\\ab}} \frac{\langle ij|ab\rangle\langle ab|ij\rangle}{E_i^a + E_j^b} + \sum_{\substack{ijk\\abc}} \frac{\langle ij|ab\rangle\langle bk|jc\rangle\langle ac|ik\rangle}{(E_i^a + E_j^b)(E_i^a + E_k^c)} + \sum_{\substack{ijkl\\abcd}} \frac{\langle ij|ab\rangle\langle bk|jc\rangle\langle cl|kd\rangle\langle ad|il\rangle}{(E_i^a + E_j^b)(E_i^a + E_k^c)(E_i^a + E_l^d)} + \cdots$$

$$E_C = \int\left[-\chi_0 v \chi_0 v - \frac{1}{2}\chi_0 v \chi_0 v \chi_0 v - \frac{1}{3}\chi_0 v \chi_0 v \chi_0 v \chi_0 v - \cdots \right] \frac{d\omega}{\pi}\frac{d\omega'}{\pi} d\boldsymbol{r_1} d\boldsymbol{r_2}$$

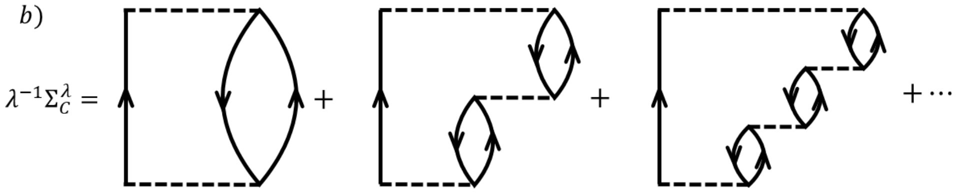

$$\Sigma_C^\lambda = \lambda\int[\, G_0 v \chi_0 v + G_0 v \chi_0 v \chi_0 v + G_0 v \chi_0 v \chi_0 v \chi_0 v + \cdots]\frac{d\omega}{\pi}$$

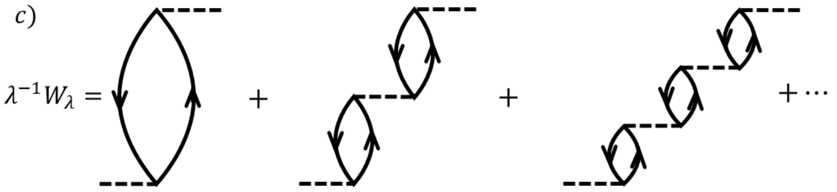

$$W_\lambda = \lambda[v \chi_0 v + v \chi_0 v \chi_0 v + v \chi_0 v \chi_0 v \chi_0 v + \cdots]$$

Figure 2. The direct RPA correlation energy as Goldstone diagrams and algebraically (a), where $E_i^a = \epsilon_i - \epsilon_a$, the effective self-energy as Feynman diagrams and algebraically (b), and the screened Coulomb interaction (c).[5,9,20] Terms up to third order are shown.

RPA may thus be expressed diagrammatically, and linked to the GW approach. We note that the first diagram of the correlation energy is the Coulomb term in MP2.

3. Conclusion

The Random Phase Approximation has been derived via the ACFDT and connected with TD-DFT, plasmon oscillations, ring-CCD, and the GW approach, and illustrated diagrammatically. These points of view all interlink and are all equivalent, the only difference depending on the preference of the reader.

4. References

1. Bohm, D.; Pines, D., A Collective Description of Electron Interactions. I. Magnetic Interactions. *Phys. Rev.* **1951,** *82*, 625-634, https://doi.org/10.1103/PhysRev.82.625.

2. Pines, D.; Bohm, D., A Collective Description of Electron Interactions: II. Collective vs Individual Particle Aspects of the Interactions. *Phys. Rev.* **1952,** *85*, 338-353, https://doi.org/10.1103/PhysRev.85.338.

3. Bohm, D.; Pines, D., A Collective Description of Electron Interactions: III. Coulomb Interactions in a Degenerate Electron Gas. *Phys. Rev.* **1953,** *92*, 609-625, https://doi.org/10.1103/PhysRev.92.609.

4. Pines, D., A Collective Description of Electron Interactions: IV. Electron Interaction in Metals. *Phys. Rev.* **1953,** *92*, 626-636, https://doi.org/10.1103/PhysRev.92.626.

5. Niquet, Y. M.; Fuchs, M.; Gonze, X., Exchange-correlation potentials in the adiabatic connection fluctuation-dissipation framework. *Phys. Rev. A* **2003,** *68*, 032507, https://doi.org/10.1103/PhysRevA.68.032507.

6. Furche, F., Developing the random phase approximation into a practical post-Kohn–Sham correlation model. *J. Chem. Phys.* **2008,** *129*, 114105, https://doi.org/10.1063/1.2977789.

7. Eshuis, H.; Bates, J. E.; Furche, F., Electron correlation methods based on the random phase approximation. *Theor. Chem. Acc.* **2012,** *131*, 1084, https://doi.org/10.1007/s00214-011-1084-8.

8. Chen, G. P.; Voora, V. K.; Agee, M. M.; Balasubramani, S. G.; Furche, F., Random-Phase Approximation Methods. *Annu. Rev. Phys. Chem.* **2017,** *68*, 421-445, https://doi.org/10.1146/annurev-physchem-040215-112308.

9. Ren, X.; Rinke, P.; Joas, C.; Scheffler, M., Random-phase approximation and its applications in computational chemistry and materials science. *J. Mater. Sci.* **2012,** *47*, 7447-7471, https://doi.org/10.1007/s10853-012-6570-4.

10. Kaltak, M.; Klimeš, J.; Kresse, G., Cubic scaling algorithm for the random phase approximation: Self-interstitials and vacancies in Si. *Phys. Rev. B* **2014,** *90*, 054115, https://doi.org/10.1103/PhysRevB.90.054115.

11. Kaltak, M.; Klimeš, J.; Kresse, G., Low Scaling Algorithms for the Random Phase Approximation: Imaginary Time and Laplace Transformations. *J. Chem. Theory Comput.* **2014,** *10*, 2498-2507, https://doi.org/10.1021/ct5001268.

12. Harl, J.; Schimka, L.; Kresse, G., Assessing the quality of the random phase approximation for lattice constants and atomization energies of solids. *Phys. Rev. B* **2010,** *81*, 115126, https://doi.org/10.1103/PhysRevB.81.115126.

13. Harl, J.; Kresse, G., Accurate Bulk Properties from Approximate Many-Body Techniques. *Phys. Rev. Lett.* **2009,** *103*, 056401, https://doi.org/10.1103/PhysRevLett.103.056401.

14. Harl, J.; Kresse, G., Cohesive energy curves for noble gas solids calculated by adiabatic connection fluctuation-dissipation theory. *Phys. Rev. B* **2008,** *77*, 045136, https://doi.org/10.1103/PhysRevB.77.045136.

15. Scuseria, G. E.; Henderson, T. M.; Sorensen, D. C., The ground state correlation energy of the random phase approximation from a ring coupled cluster doubles approach. *J. Chem. Phys.* **2008,** *129*, 231101, https://doi.org/10.1063/1.3043729.

16. Henderson, T. M.; Scuseria, G. E., The connection between self-interaction and static correlation: a random phase approximation perspective. *Mol. Phys.* **2010,** *108*, 2511-2517, https://doi.org/10.1080/00268976.2010.507227.

17. Fetter, A. L.; Walecka, J. D., *Quantum Theory of Many-Particle Systems*. McGraw-Hill Book Company: New York, 1971.

18. Schmidt, P. S.; Thygesen, K. S., Benchmark Database of Transition Metal Surface and Adsorption Energies from Many-Body Perturbation Theory. *J. Phys. Chem. C* **2018,** *122*, 4381-4390, https://doi.org/10.1021/acs.jpcc.7b12258.

19. Freeman, D. L., Coupled-cluster expansion applied to the electron gas: Inclusion of ring and exchange effects. *Phys. Rev. B* **1977,** *15*, 5512-5521, https://doi.org/10.1103/PhysRevB.15.5512.

20. Mattuck, R. D., *A Guide to Feynman Diagrams in the Many-Body Problem*. Dover Publications, Inc.: New York, 1992.

Appendix 2. RPA Adsorption Energy Summary for Adsorption on Surfaces

1. Adsorption Energy Tables

RPA is a computationally expensive method but some calculations on adsorption have been performed. A summary of these are presented in Table 1 with experimental reference. Additional calculations without experimental reference are presented in Table 2.

Table 1. Literature RPA adsorption energy ΔE_{ads} (in kJ mol^{-1}) with experimental adsorption energy.[a] The coverage θ in monolayers (ML), where 1 ML is defined as one adsorbate molecule/ atom per adsorption site (per surface atom for metal surfaces), and the temperature T (in K) are given. In place of experiment, QMC is given where available.

System	Method	Ref.	θ / ML	T / K	ΔH_{ads}	ΔE_{ads}
CO/Cu(111)	Exp. (TREELS)	1	$^{1}/_{4}$	150	-55.2	-53.9
	RPA@LDA	2	$^{1}/_{8}$	-	-	-34
	RPA@PBE	2	$^{1}/_{8}$	-	-	-33
		3	$^{1}/_{4}$[b]	-	-	-41
		4	$^{1}/_{4}$	-	-	-41
		5	$^{1}/_{4}$	-	-	-24
	RPA@PBE0	2	$^{1}/_{8}$	-	-	-36
CO/Pt(111)	Exp. (SCAC)	6	$^{1}/_{4}$	300	-125	-123
	RPA@PBE	5	$^{1}/_{4}$	-	-	-131
		7	$^{1}/_{4}$[c]	-	-	-131
	rALDA	7	$^{1}/_{4}$[c]	-	-	-128
CO/Rh(111)	Exp. (EQBM)	8	$^{1}/_{4}$	477	-139	-135
	RPA@PBE	3	$^{1}/_{4}$[b]	-	-	-139
		5	$^{1}/_{4}$	-	-	-135
CO/Ir(111)	Exp. (TPD)	8	$^{1}/_{4}$	550	-149	-144
	RPA@PBE	5	$^{1}/_{4}$	-	-	-143
CO/Pd(111)	Exp. (EQBM)	9	$^{1}/_{4}$	498	-143	-139
	RPA@PBE	3	$^{1}/_{4}$[b]	-	-	-134
		5	$^{1}/_{4}$	-	-	-152
NO/Pd(111)	Exp. (TPD)	9,10	$^{1}/_{4}$	520	-179	-175
	RPA@PBE	5	$^{1}/_{4}$	-	-	-192
NO/Pt(111)	Exp. (SCAC)	11,12	$^{1}/_{4}$	300	-114[d]	-112
	RPA@PBE	5	$^{1}/_{4}$	-	-	-128
O/Ni(111)	Exp. (SCAC)	9	$^{1}/_{4}$	300	-240	-239
	RPA@PBE	5	$^{1}/_{4}$	-	-	-241
H/Pt(111)	Exp. (TEAS)	13	$^{1}/_{4}$	300	-36	-34
	RPA@PBE	5	$^{1}/_{4}$	-	-	-49
		14	1	-	-	-28.3
H/Ni(111)	Exp. (LITD)	9,15	$^{1}/_{4}$	370	-47	-43
	RPA@PBE	5	$^{1}/_{4}$	-	-	-35
H_2O/Graphene	DMC	16	$^{1}/_{4}$[e]	-	-	-9.5

	RPA	16	$^1/_4{}^e$	-	-	-7.9
H_2O/h-BN	DMC	17	$^1/_{16}$	-	-	-9.2
	LRDMC	17	$^1/_{16}$	-	-	-10.3
	RPA@PBE	17	$^1/_{16}$	-	-	-8.6
	RPA+GWSE	17	$^1/_{16}$	-	-	-10.4
	RPA+GWSE +SOSEX	17	$^1/_{16}$	-	-	-10.9
C_6H_6/Cu(111)	Exp. (TPD)	9,18	$^1/_9$	225	-68	-66
	RPA@PBE	19	$^1/_8$	-	-	-64
		20	0^f	-	-	-9
	RPA+rSE	20	0^f	-	-	-30
C_6H_6/Ag(111)	Exp. (TPD)	9,21	$^1/_9$	210	-63	-61
	RPA@PBE	19	$^1/_8$	-	-	-61
		20	0^f	-	-	-22
	RPA+rSE	20	0^f	-	-	-39
C_6H_6/Au(111)	Exp. (TPD)	9,22	$^1/_9$	230	-72	-70
	RPA@PBE	19	$^1/_8$	-	-	-62
		20	0^f	-	-	-43
	RPA+rSE	20	0^f	-	-	-56
C_6H_6/Pt(111)	Exp. (SCAC)	6,9	$^1/_9$	300	-164	-162
	RPA@PBE	19	$^1/_8$	-	-	-168
CO/MgO(001)	Exp. (TPD)	23,24	$^1/_8$	60	-	-20.6^g
	RPA@PBE	25	$^1/_4$	-	-	-6.9
	RPAh@PBE^h	25	$^1/_4$	-	-	-29.9
NO/MgO(001)	Exp. (TPD)	26	~0.1	75	-21	-20
	RPA@PBE	25	$^1/_4$	-	-	2.8
	RPAh@PBE^h	25	$^1/_4$	-	-	-34.7
CH_4/MgO(001)	Exp. (TPD)	27,28	1	47	-	-15.0^i
	RPA@PBE	25	$^1/_4$	-	-	-8.4
	RPAh@PBE^h	25	$^1/_4$	-	-	-13.5
H_2O/MgO(001)	Exp. (HAS)	24,29	$^1/_8$	203	-50.2^g	-55.8^g
	RPA@PBE	25	$^1/_4$	-	-	-47.5
	RPAh@PBE^h	25	$^1/_4$	-	-	-58.7

[a] Adsorption enthalpies ΔH_{ads} have been corrected to adsorption energies ΔE_{ads} in the scheme used by Silbaugh and Campbell, where the +RT term is included, i.e. a finite temperature correction.[9,30] For TPD, 2RT is added as an activation energy E_a was measured, rather than ΔH_{ads}.[31]

[b] Corrected from $^1/_3$ ML RPA calculation using DFT.

[c] Not explicitly stated. Inferred by close RPA@PBE value to their later 2018 work, Ref. [5], where a near-identical energy was obtained for the same system and a coverage was provided.

[d] Corrected due to an incorrect reflectivity, see Ref. [12].

[e] Corrected with the Hartree-Fock energy from an (8x8) cell, i.e. $^1/_4$ ML (2x2) coverage corrected by $^1/_{64}$ ML coverage.

[f] Performed on M_{22} 2-layered clusters.

[g] Corrected for direct computational comparison in Ref. [32].

[h] Exchange calculated using self-consistent orbitals, cf. Ref [25].

[i] Corrected for direct computational comparison in Ref. [28].

Table 2. Literature computational adsorption energy ΔE_{ads} for given systems (kJ mol^{-1}) without experimental comparison. Coverage θ in monolayers (ML), where 1 ML is one molecule/ atom per surface adsorption site. Papers where RPA calculations were performed but the energies were not reported are given at the end of the table.

System	Method	Ref.	θ / ML	ΔE_{ads} / kJ mol^{-1}
O/CaO(001)	RPA@PBE	25	$^{1}/_{4}$	-56.9
	RPAh@PBE[a]	25	$^{1}/_{4}$	-46.3
O/Mn(111)	RPA@PBE	5	1	-78
	rALDA	5	1	-73
H_2O/NaCl(001)	RPA@PBE	33	1	-37.0
	RPAh@PBE[a]	33	1	-43.4
	RPA+rSE	33	1	-41.5
	RPA+GWSE	33	1	-39.6
H_2O/Fe(001)[b]	RPA@PBE	34	$^{1}/_{9}$	-41.8
N_2/Mn(111)	RPA@PBE	5	1	72
	rALDA	5	1	72
N/Mn(111)	RPA@PBE	5	1	-222
	rALDA	5	1	-222
CH/Mn(111)	RPA@PBE	5	1	346
	rALDA	5	1	349
OH/Mn(111)	RPA@PBE	5	1	120
	rALDA	5	1	131
NO/Mn(111)	RPA@PBE	5	1	-93
	rALDA	5	1	-96
CO/Mn(111)	RPA@PBE	5	1	-14
	rALDA	5	1	-20
CO/Sc(111)	RPA@PBE	5	1	-58
	rALDA	5	1	-59
CO/Ti(111)	RPA@PBE	5	1	-74
	rALDA	5	1	-78
CO/V(111)	RPA@PBE	5	1	-76
	rALDA	5	1	-82
CO/Cr(111)	RPA@PBE	5	1	-33
	rALDA	5	1	-37
CO/Ru(111)	RPA@PBE	3	$^{1}/_{4}$[c]	-136.8
CO/Ni(111)	RPA@PBE	35	$^{1}/_{4}$	N/A[d]
H/Mn(111)	RPA@PBE	5	1	62
	rALDA	5	1	62
$O_2^-/Ca_3O_2Ru_7(001)$	RPA	36	$^{1}/_{9}$	-69.5
N_2/Ru(0001)	RPA@PBE	35	$^{1}/_{3}$	N/A[d]
C_6H_6/Pd(111)	RPA@PBE	19	0.125	-166.0
C_6H_6/Rh(111)	RPA@PBE	19	0.125	-200.7

C_6H_6/Ni(111)	RPA@PBE	[19]	0.125	-140.9
C_6H_6/Si(001)	RPA@PBE	[37]	Low[e]	N/A[f]

[a] Exchange calculated using self-consistent orbitals, cf. Ref [25].

[b] H_2O dissociates on the Fe(001) surface, hence no experimental reference. See paper for reaction pathway using DFT and RPA.

[c] Corrected from $^1/_3$ ML RPA calculation using DFT.

[d] The paper tested RPA while using GPUs and tested these systems without reporting any energies.

[e] Extrapolated to slab from cluster.

[f] Difference between two structures. At 0 K, when temperature is considered it is not meaningful to compare to experiment.

2. Abbreviations

2.1 Experimental

TREELS – Time-Resolved Electron Energy Loss Spectroscopy

SCAC – Single-Crystal Adsorption Calorimetry

EQBM – Equilibrium Measurements of Coverage versus Temperature and Pressure[9]

TPD – Temperature-Programmed Desorption

TEAS – Thermal Energy Helium Atom Scattering

LITD – Laser-Induced Thermal Desorption

HAS – Helium Atom Scattering

2.2 Computational

RPA@X – Random Phase Approximation using orbitals from X

DMC – Diffusion Monte Carlo

LRDMC – Lattice Regularised DMC

GWSE – GW Single Excitations

SOSEX – Second Order Screened Exchange

rSE – Renormalised Single Excitations

rALDA – Renormalised Adiabatic LDA

3. References

1. Hinch, B. J.; Dubois, L. H., First-order corrections in modulated molecular beam desorption experiments. *Chem. Phys. Lett.* **1990,** *171*, 131-135, https://doi.org/10.1016/0009-2614(90)80063-J.

2. Ren, X.; Rinke, P.; Scheffler, M., Exploring the random phase approximation: Application to CO adsorbed on Cu(111). *Phys. Rev. B* **2009,** *80*, 045402, https://doi.org/10.1103/PhysRevB.80.045402.

3. Schimka, L.; Harl, J.; Stroppa, A.; Grüneis, A.; Marsman, M.; Mittendorfer, F.; Kresse, G., Accurate surface and adsorption energies from many-body perturbation theory. *Nat. Mater.* **2010,** *9*, 741, https://doi.org/10.1038/nmat2806.

4. Harl, J.; Kresse, G., Accurate Bulk Properties from Approximate Many-Body Techniques. *Phys. Rev. Lett.* **2009,** *103*, 056401, https://doi.org/10.1103/PhysRevLett.103.056401.

5. Schmidt, P. S.; Thygesen, K. S., Benchmark Database of Transition Metal Surface and Adsorption Energies from Many-Body Perturbation Theory. *J. Phys. Chem. C* **2018,** *122*, 4381-4390, https://doi.org/10.1021/acs.jpcc.7b12258.

6. Schießer, A.; Hörtz, P.; Schäfer, R., Thermodynamics and kinetics of CO and benzene adsorption on Pt(111) studied with pulsed molecular beams and microcalorimetry. *Surf. Sci.* **2010,** *604*, 2098-2105, https://doi.org/10.1016/j.susc.2010.09.001.

7. Olsen, T.; Thygesen, K. S., Accurate Ground-State Energies of Solids and Molecules from Time-Dependent Density-Functional Theory. *Phys. Rev. Lett.* **2014,** *112*, 203001, https://doi.org/10.1103/PhysRevLett.112.203001.

8. Sushchikh, M.; Lauterbach, J.; Weinberg, W. H., Chemisorption of CO on the Ir(111) surface: Adsorption and desorption kinetics measured with in situ vibrational spectroscopy. *J. Vac. Sci. Technol. A* **1997,** *15*, 1630-1634, https://doi.org/10.1116/1.580644.

9. Silbaugh, T. L.; Campbell, C. T., Energies of Formation Reactions Measured for Adsorbates on Late Transition Metal Surfaces. *J. Phys. Chem. C* **2016,** *120*, 25161-25172, https://doi.org/10.1021/acs.jpcc.6b06154.

10. Ramsier, R. D.; Gao, Q.; Waltenburg, H. N.; Lee, K. W.; Nooij, O. W.; Lefferts, L.; Yates, J. T., NO adsorption and thermal behavior on Pd surfaces. A detailed comparative study. *Surf. Sci.* **1994,** *320*, 209-237, https://doi.org/10.1016/0039-6028(94)90310-7.

11. Fiorin, V.; Borthwick, D.; King, D. A., Microcalorimetry of O2 and NO on flat and stepped platinum surfaces. *Surf. Sci.* **2009,** *603*, 1360-1364, https://doi.org/10.1016/j.susc.2008.08.034.

12. Karp, E. M.; Campbell, C. T.; Studt, F.; Abild-Pedersen, F.; Nørskov, J. K., Energetics of Oxygen Adatoms, Hydroxyl Species and Water Dissociation on Pt(111). *J. Phys. Chem. C* **2012,** *116*, 25772-25776, https://doi.org/10.1021/jp3066794.

13. Poelsema, B.; Lenz, K.; Comsa, G., The dissociative adsorption of hydrogen on Pt(111): Actuation and acceleration by atomic defects. *J. Chem. Phys.* **2011,** *134*, 074703, https://doi.org/10.1063/1.3530286.

14. Yan, L.; Sun, Y.; Yamamoto, Y.; Kasamatsu, S.; Hamada, I.; Sugino, O., Hydrogen adsorption on Pt(111) revisited from random phase approximation. *J. Chem. Phys.* **2018,** *149*, 164702, https://doi.org/10.1063/1.5050830.

15. Christmann, K.; Schober, O.; Ertl, G.; Neumann, M., Adsorption of hydrogen on nickel single crystal surfaces. *J. Chem. Phys.* **1974,** *60*, 4528-4540, https://doi.org/10.1063/1.1680935.

16. Ma, J.; Michaelides, A.; Alfè, D.; Schimka, L.; Kresse, G.; Wang, E., Adsorption and diffusion of water on graphene from first principles. *Phys. Rev. B* **2011,** *84*, 033402, https://doi.org/10.1103/PhysRevB.84.033402.

17. Al-Hamdani, Y. S.; Rossi, M.; Alfè, D.; Tsatsoulis, T.; Ramberger, B.; Brandenburg, J. G.; Zen, A.; Kresse, G.; Grüneis, A.; Tkatchenko, A.; Michaelides, A., Properties of the water to boron nitride interaction: From zero to two dimensions with benchmark accuracy. *J. Chem. Phys.* **2017,** *147*, 044710, https://doi.org/10.1063/1.4985878.

18. Xi, M.; Yang, M. X.; Jo, S. K.; Bent, B. E.; Stevens, P., Benzene adsorption on Cu(111): Formation of a stable bilayer. *J. Chem. Phys.* **1994,** *101*, 9122-9131, https://doi.org/10.1063/1.468041.

19. Garrido Torres, J. A.; Ramberger, B.; Früchtl, H. A.; Schaub, R.; Kresse, G., Adsorption energies of benzene on close packed transition metal surfaces using the random phase approximation. *Phys. Rev. Mater.* **2017,** *1*, 060803, https://doi.org/10.1103/PhysRevMaterials.1.060803.

20. Liu, W.; Ruiz, V. G.; Zhang, G.-X.; Santra, B.; Ren, X.; Scheffler, M.; Tkatchenko, A., Structure and energetics of benzene adsorbed on transition-metal surfaces: density-functional theory with van der Waals interactions including collective substrate response. *New J. Phys.* **2013,** *15*, 053046, https://doi.org/10.1088/1367-2630/15/5/053046.

21. Zhou, X. L.; Castro, M. E.; White, J. M., Interactions of UV photons and low energy electrons with chemisorbed benzene on Ag(111). *Surf. Sci.* **1990,** *238*, 215-225, https://doi.org/10.1016/0039-6028(90)90079-N.

22. Syomin, D.; Kim, J.; Koel, B. E.; Ellison, G. B., Identification of Adsorbed Phenyl (C6H5) Groups on Metal Surfaces: Electron-Induced Dissociation of Benzene on Au(111). *J. Phys. Chem. B* **2001,** *105*, 8387-8394, https://doi.org/10.1021/jp012069e.

23. Dohnálek, Z.; Kimmel, G. A.; Joyce, S. A.; Ayotte, P.; Smith, R. S.; Kay, B. D., Physisorption of CO on the MgO(100) Surface. *J. Phys. Chem. B* **2001,** *105*, 3747-3751, https://doi.org/10.1021/jp003174b.

24. Alessio, M.; Usvyat, D.; Sauer, J., Chemically Accurate Adsorption Energies: CO and H2O on the MgO(001) Surface. *J. Chem. Theory Comput.* **2019,** *15*, 1329-1344, https://doi.org/10.1021/acs.jctc.8b01122.

25. Bajdich, M.; Nørskov, J. K.; Vojvodic, A., Surface energetics of alkaline-earth metal oxides: Trends in stability and adsorption of small molecules. *Phys. Rev. B* **2015,** *91*, 155401, https://doi.org/10.1103/PhysRevB.91.155401.

26. Wichtendahl, R.; Rodriguez-Rodrigo, M.; Härtel, U.; Kuhlenbeck, H.; Freund, H. J., Thermodesorption of CO and NO from Vacuum-Cleaved NiO(100) and MgO(100). *Phys. Status Solidi A* **1999,** *173*, 93-100, https://doi.org/10.1002/(SICI)1521-396X(199905)173:1<93::AID-PSSA93>3.0.CO;2-4.

27. Tait, S. L.; Dohnálek, Z.; Campbell, C. T.; Kay, B. D., n-alkanes on MgO(100). II. Chain length dependence of kinetic desorption parameters for small n-alkanes. *J. Chem. Phys.* **2005,** *122*, 164708, https://doi.org/10.1063/1.1883630.

28. Alessio, M.; Bischoff, F. A.; Sauer, J., Chemically accurate adsorption energies for methane and ethane monolayers on the MgO(001) surface. *Phys. Chem. Chem. Phys.* **2018,** *20*, 9760-9769, https://doi.org/10.1039/C7CP08083B.

29. Ferry, D.; Glebov, A.; Senz, V.; Suzanne, J.; Toennies, J. P.; Weiss, H., The properties of a two-dimensional water layer on MgO(001). *Surf. Sci.* **1997,** *377-379*, 634-638, https://doi.org/10.1016/S0039-6028(96)01478-1.

30. Wellendorff, J.; Silbaugh, T. L.; Garcia-Pintos, D.; Nørskov, J. K.; Bligaard, T.; Studt, F.; Campbell, C. T., A benchmark database for adsorption bond energies to transition metal surfaces and comparison to selected DFT functionals. *Surf. Sci.* **2015,** *640*, 36-44, https://doi.org/10.1016/j.susc.2015.03.023.

31. Sauer, J., Ab Initio Calculations for Molecule–Surface Interactions with Chemical Accuracy. *Acc. Chem. Res.* **2019,** *52*, 3502-3510, https://doi.org/10.1021/acs.accounts.9b00506.

32. Bischoff, F.; Alessio, M.; Berger, F.; John, M.; Rybicki, M.; Sauer, J. *Multi-Level Energy Landscapes: The MonaLisa Program (https://www.chemie.hu-berlin.de/de/forschung/quantenchemie/monalisa/)*, Humboldt-University: Berlin, 2019.

33. Klimeš, J.; Kaltak, M.; Maggio, E.; Kresse, G., Singles correlation energy contributions in solids. *J. Chem. Phys.* **2015,** *143*, 102816, https://doi.org/10.1063/1.4929346.

34. Karlický, F.; Lazar, P.; Dubecký, M.; Otyepka, M., Random Phase Approximation in Surface Chemistry: Water Splitting on Iron. *J. Chem. Theory Comput.* **2013,** *9*, 3670-3676, https://doi.org/10.1021/ct400425p.

35. Yan, J.; Li, L.; O'Grady, C., Graphics Processing Unit acceleration of the Random Phase Approximation in the projector augmented wave method. *Comput. Phys. Commun.* **2013,** *184*, 2728-2733, https://doi.org/10.1016/j.cpc.2013.07.014.

36. Halwidl, D.; Mayr-Schmölzer, W.; Setvin, M.; Fobes, D.; Peng, J.; Mao, Z.; Schmid, M.; Mittendorfer, F.; Redinger, J.; Diebold, U., A full monolayer of superoxide: oxygen activation on the unmodified Ca3Ru2O7(001) surface. *J. Mater. Chem. A* **2018,** *6*, 5703-5713, https://doi.org/10.1039/C8TA00265G.

37. Kim, H.-J.; Tkatchenko, A.; Cho, J.-H.; Scheffler, M., Benzene adsorbed on Si(001): The role of electron correlation and finite temperature. *Phys. Rev. B* **2012,** *85*, 041403, https://doi.org/10.1103/PhysRevB.85.041403.

Acknowledgements

Any work is more than just the writer and is made up of the people who contributed and supported throughout. I would like to acknowledge my PhD supervisor, Prof. Dr. Dr. h.c. Joachim Sauer, for his support throughout, and guidance towards the completion of my thesis.

In close second, comes the funding from the “Fonds der Chemischen Industrie”, for funding of the PhD in the form of a Kekulé scholarship. Their funding enabled me to attend several conferences, including the Symposium on Theoretical Chemistry (STC) 2019 and the World Association of Theoretical and Computational Chemists (WATOC) 2020, which were both influential in my development as a scientist. Furthermore, they sponsored me towards and paid for the 70th and 71st Lindau Nobel Laureate meetings, which were excellent opportunities for meeting both enthusiastic young scientists and the most experienced. Thanks is also extended to the organiser of these two meetings in particular for the excellent work that they do encouraging young scientists and connecting people from diverse fields together for everyone’s benefit.

I am also grateful to the Fritz Haber Institute of the Max-Planck-Gesellschaft for external PhD funding for my final year. This allowed for the proper completion of much work that would have been difficult to do otherwise.

I am very thankful to Thomas for his constant upkeep of the machines that made all of this possible. The smooth running of these in spite of challenges over the years was vital. Thank you to Conny, for your constant help with the frequently complex administration at the university and for many enjoyable conversations. Our work would not be possible without you.

Many people have contributed to the fulfilment of the work of this project. Dr Joachim Paier has consistently offered advice on the scientific work and his expertise in the Random Phase Approximation has proven invaluable. I am very grateful for his advice on many manuscripts and abstracts for conferences and papers. This thesis would not be in its complete form without him.

Dr. Denis Usvyat have also been extremely supportive, offering advice when queried and a great deal of support in both the learning of quantum chemistry and my individual project, even when our interests only loosely overlapped. I am also grateful to Dr. Florian Bischoff for his advice when various computational difficulties and curiosities were encountered.

I am especially grateful to Marcin for his constant support and advice both academically and beyond, with his understanding of the difficulties of moving to a foreign country. His support was crucial for the functioning of the group and for the general optimism of the corridor. His scientific expertise was extremely valuable but, beyond that, his gentle manner and unusual kindness shone out wherever he was, exemplifying his personal beliefs. As the late

Edmond Fischer once said, “anyone can be a scientist, what’s important is to be a gentle person,” and Marcin personified this.

There are many other people to thank, including all of the people past and present from the Kneipp (Cecelia, Fani, Sabrina, Tom, Vesna, Victor, Arpad), Sauer (Stephen, Marcel, the Fabians, Henning, Winni, Thais), and Usvyat, Bischoff, and Roemelt groups (Jakob, Alex, Lucas, Mihkel, Philipp, Raunak, Gurjot, Charlotte, Vittorio) who made lunch and conversations very enjoyable over the years and gave life to the corridor. A special mention must be made to the Italians who have shared my office over the years: Maristella, Daria, and Nicole who have been excellent friends throughout and constantly supportive, even when encountering my eccentricities. It has been truly wonderful and I will miss sharing an office with you all. I am very grateful to Denis, Dr. Paier, and Daria for reading through the thesis and for their feedback.

Beyond the university, it would not have been possible to enjoy my time in Berlin without the support of my friends and family. My parents and family were always available for support if I needed it. My friends from over the years, both back in the UK and in Berlin also offered great support. I would like to thank all of them by name but when I started writing them down it rapidly became a long list, so I will instead thank them collectively with thanks to those from church (with special thanks to Matheus and Brandon), York, Harrogate (in particular Michael Mole), and anywhere else that has slipped my mind. It was often crucial to remember the world outside of the ivory tower and the place of it within that.

To anyone that has not been included above, thank you as well!

Selbständigkeitserklärung

Ich, Christopher Sheldon, erkläre, dass ich diese Dissertation selbstständig und nur unter Verwendung der von mir gemäß § 7 Abs. 3 der Promotionsordnung der Mathematisch-Naturwissenschaftlichen Fakultät, veröffentlicht im Amtlichen Mitteilungsblatt der Humboldt-Universität zu Berlin Nr. 42/2018 am 11.07.2018 angegebenen Hilfsmittel angefertigt habe. Diese Dissertation wurde nicht bereits in einem früheren Promotionsverfahren eingereicht und begutachtet.

Statement of Authorship

I, Christopher Sheldon, declare that I have authored this dissertation independently and only by using the specified resources in accordance with § 7 Abs. 3 of the Promotionsordnung of the Faculty of Mathematics and Natural Sciences, published in the official bulletin of Humboldt-Universität zu Berlin No. 42/2018 on 2018/07/11. This dissertation was not submitted and reviewed in an earlier graduation procedure.

08.12.2022, Berlin